

UNCLASSIFIED

AD 419140

**DEFENSE DOCUMENTATION CENTER
FOR
SCIENTIFIC AND TECHNICAL INFORMATION**

CAMERON STATION, ALEXANDRIA, VIRGINIA



UNCLASSIFIED

NOTICE: When government or other drawings, specifications or other data are used for any purpose other than in connection with a definitely related government procurement operation, the U. S. Government thereby incurs no responsibility, nor any obligation whatsoever; and the fact that the Government may have formulated, furnished, or in any way supplied the said drawings, specifications, or other data is not to be regarded by implication or otherwise as in any manner licensing the holder or any other person or corporation, or conveying any rights or permission to manufacture, use or sell any patented invention that may in any way be related thereto.

419140

ASD-TDR-63-865

64-5

INVESTIGATION OF CAPILLARY
EMITTER
THERMIONIC CONVERTERS

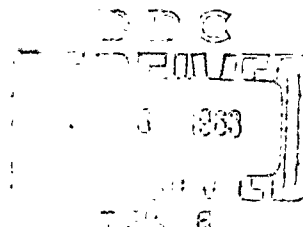
CATALOGED BY DDC
AD No.
AS

TECHNICAL DOCUMENTARY REPORT NO. ASD-TDR-63-865

September 1963

AF Aero-Propulsion Laboratory
Research and Technology Division
Air Force Systems Command
Wright-Patterson Air Force Base, Ohio

Project No. 8173, Task No. 817305-11



419140

(Prepared under Contract No. AF33(616)-8299
by the Allison Division, General Motors Corporation
Indianapolis, Indiana; D. L. Dresser, J. D.
Dunlop, H. Huber, R. LeBihan, V. L. Hill, N.D.
McMurray, and K. E. Muszer, Authors)

NOTICES

When Government drawings, specifications, or other data are used for any purpose other than in connection with a definitely related Government procurement operation, the United States Government thereby incurs no responsibility nor any obligation whatsoever; and the fact that the Government may have formulated, furnished, or in any way supplied the said drawings, specifications, or other data, is not to be regarded by implication or otherwise as in any manner licensing the holder or any other person or corporation, or conveying any rights or permission to manufacture, use, or sell any patented invention that may in any way be related thereto.

Qualified requesters may obtain copies of this report from the Defense Documentation Center (DDC), (formerly ASTIA), Arlington Hall Station, Arlington 12, Virginia.

This report has been released to the Office of Technical Services, U. S. Department of Commerce, Washington 25, D. C., for sale to the general public.

Copies of this report should not be returned to the Aeronautical Systems Division unless return is required by security considerations, contractual obligations, or notice on a specific document.

FOREWORD

This report was prepared by the Research Department of the Allison Division of General Motors Corporation on Air Force Contract AF33(616)-8299, Project No. 8173, "Static Energy Conversion," Task No. 817305-11 (Investigation of Capillary Emitter Thermionic Converters). The work was administered under the direction of the Aero-Propulsion Laboratory, Flight Vehicle Power Division. Mr. G. H. Miller was the Air Force task engineer.

This report covers the period from 15 May 1961 to 15 August 1963. Work began on a basic contract to investigate the feasibility and practicality of a capillary emitter serving the dual role of a cathode surface and a cesium dispenser. Under the basic contract, the theory of the capillary was to be formulated and experiments were to be performed on a monocapillary geometry. A supplementary agreement was reached on 15 November 1961 extending the work to include the design, fabrication, and test of two multicapillary converters. Experimental results from the converters showed no advantage of the capillary concept over conventional devices in the temperature range from 1400 to 1800°K. However, results did indicate that advantages could be obtained by operating at higher temperatures and without cesium flow. Therefore, Allison obtained a no-cost extension to the contract to extend from 15 December 1962 to 15 August 1963 to pursue these additional investigations.

Some of the materials and technology work was done in the Materials Research and Production Laboratories. Other work was accomplished at the Electronic and Corpuscular Physics Research Center of Compagnie générale de télégraphie Sans Fil (CSF) in Paris, France, on a subcontract from Allison. Dr. H. Huber of the CEPEC Laboratory was responsible for this work.

Personnel who participated in this project were:

● Allison

D. L. Dresser	Project Manager
W. G. Laurita	Theory and Cs Flow
K. R. Cross	Cesium Flow
J. D. Dunlop	Converter Test
R. P. Strebe	Converter Test
H. R. Fuquay	Converter Test
R. H. Singleton	Materials and Technology
N. D. McMurray	Vapor Deposition
K. E. Muszer	X-Ray Analysis
V. L. Hill	Recrystallization

● CSF

H. Huber	Converter Theory and Fabrication
----------	-------------------------------------

J. P. Freytag	Converter Design and Fabrication
E. Duval	Design and Fabrication
R. LeBihan	Test and Analysis
P. Dumon	Materials
D. Grauleau	Technology

The following papers were published on results from this project:

1. Laurita, W. G. and Dresser, D. L. "Emission from a Cesiumated Capillary Emitter." Report on Twenty-Third Annual Conference Physical Electronics. Massachusetts Institute of Technology, 20-22 March 1963.
2. Dresser, D. L., Laurita, W. G., Dunlop, J. D., Huber, H., and LeBihan R. Theory and Experiment of a Capillary Emitter in a Thermionic Converter. AIAA Paper No. 63-156.
3. Huber, H. and LeBihan, R. Cesium Ion Capillary Emitter: Application to Thermionic Converters. Presented at the Combustion and Propulsion Panel, AGARD-NATO, Athens, Greece, 15-17 July 1963.
4. Dunlop, J. D. and Schneider, R. T. Spectroscopic Investigation of a Thermionic Capillary Cesium Energy Converter. (Accepted but not yet published as Letter to Journal of Applied Physics.)

Overall management direction was given by H. D. Wilsted, Manager, Engineering Research, and T. F. Nagey, Director of Research.

This is the final report on Contract AF33(616)-8299. The contractor's report number is EDR 3532.

ABSTRACT

A random current theoretical model is formulated to describe the emission of ions and electrons from a capillary thermionic emitter. Extensive experimental results from monocapillary and multicapillary devices are shown to be in good agreement with the theory. Practical power densities of 5 to 15 watts/cm² were obtained between 1900 and 2100°K. A modified capillary emitter in which no cesium flow is required was also investigated and found to agree with the random current model. Ion current measurements, high frequency oscillations, and spectroscopic data are used to interpret the operating conditions of the capillary emitter. Technology developments are reported on the subjects of emitter fabrication and chemical vapor deposition.

PUBLICATION REVIEW

The publication of this technical documentary report does not constitute Air Force approval of the report's findings or conclusions. It is published only for the exchange and stimulation of ideas.

TABLE OF CONTENTS

<u>Section</u>	<u>Title</u>	<u>Page</u>
I	Introduction	1
II	Conclusions	3
III	Theory of the Capillary Emitter	5
	Statement of Problem	5
	Flow Solution	5
	Solutions of Dykman Equation	7
	Predicted Flow Through Multicapillary Emitter	7
	Emission Solution	13
	Sheath Potential Model	13
	Random Current Model	16
	Isothermal Diode Theory	17
	Work Function of Capillary	23
IV	Experimental Devices	27
	Monocapillary	27
	Design	27
	Component Development	29
	Operation and Failure Analysis	29
	Multicapillary	32
	Converter A	33
	Converter B	33
	Converters C and E	35
	Converters D and F	37
	Converter G	37
	Converter I	37
	Supplementary Converters	37
	Converters 1 and 2	40
	Converters 3 and 4	43
	Converters 5 and 6	45
V	Testing and Analyses of Results	49
	Summary of Testing	49
	Monocapillary	49
	Multicapillary	49
	Analyses of Results	49
	Monocapillary	49
	Multicapillary	55
	Supplementary Converters	89

<u>Section</u>	<u>Title</u>	<u>Page</u>
VI	Technology for Thermionic Converters	111
	Machining and Joining	111
	Machining Emitters	111
	Welding Emitters	111
	Seal Development	112
	Cesium Corrosion	113
	Chemical Vapor Deposition of Tungsten	117
	Process Development	118
	Evaluation of Deposits	120
	Free-Standing Structures	125
	Joining Development	126
	Coatings Development	126
	Recrystallization Characteristics of Refractory Metal	
	Thermionic Emitter Materials	129
	Experimental Approach	131
	Emitter Fabrication	133
VII	Suggested Future Work	141
VIII	References	143
	Appendix. Cesium Ion Capillary Emitter: Application to Thermionic Converters	145
	Introduction	149
	Summary	151
	Models of the Capillary Emitter	153
	The Infinitely Long Tube Emitting Electrons or Ions	153
	The Infinitely Long Tube with Simultaneous Emission of Electrons and Ions	155
	The Isothermal Cavity, the Infinitely Long Tube of Large Radius	155
	The Saha Equation	155
	Correlation Between the Charge Densities in the Plasma and the Charge Densities at the Surface	156
	The Plasma Potential	157
	The Electron and Ion Sheaths	158
	Juxtaposition of Current Densities Available in the Cross Section of the Infinitely Long Tube Constituting Either an Electron or Ion Emitter or a Dual Emitter of Electrons and Ions	158

<u>Section</u>	<u>Title</u>	<u>Page</u>
	The Tube of Finite Length with Emission of Electrons and Ions	161
	The Model of the Linear Decrease of Neutral Density Along the Tube	161
	Simplified Model for the Determination of Particle Density Along the Tube	163
	Extraction of Charged Particles	166
	Experimental Work	169
	Monocapillary with an Electrode-Probe	169
	Arrangement and Method of Measurement	169
	Electron Current	172
	Ion Current	173
	Monocapillary with an Extraction Electrode.	174
	Experimental Work on the Monocapillary for Electron Extraction	175
	Experimental Work on the Monocapillary for Ion Extraction	176
	Multicapillary Constituting the Emitter in Thermo-Ionic Converters	176
	Arrangement and Measurements	176
	Electron Current	182
	Ion Current	183
	Comparison Between a Tungsten Multicapillary and a Sintered Tungsten Emitter	183
	Conclusion.	187
	Bibliography	189

LIST OF ILLUSTRATIONS

<u>Figure</u>	<u>Title</u>	<u>Page</u>
1	Capillary Geometry	6
2	Enlarged View of Experimental Multicapillary Geometry	8
3	Increments for Numerical Solution	8
4	Principle of Analog Solution	10
5	Results of Numerical Solution	11
6	Cesium Flow Loop	12
7	Cesium Flow Data	12
8	Comparison Between Theory and Experiment for Cesium Flow Through Multicapillary Emitter	13
9	Local Sheath Potentials in the Capillary	14
10	Comparison of Sheath Model Theory with Experimental Monocapillary Data	15
11	Geometry for Random Current Model	16
12	Isothermal Diode	18
13	Plasma Potential as a Function of T_E and T_{Cs}	19
14	Sheath Conditions in Isothermal Diode	20
15	Capillary Emitter as Isothermal Diode	20
16	Comparison of Random Current to Saturation Current—1600°K	21
17	Comparison of Random Current to Saturation Current—1800°K	22
18	Comparison of Random Current to Saturation Current—2000°K	23
19	Comparison of Random Current to Saturation Current—2200°K	24
20	Random Current Model with Various Area Ratio Limits	25
21	Potential Energy Diagram for Capillary Converter with a High T_E/T_{Cs} Ratio	26
22	Sketch of Monocapillary	28
23	Assembled Layout of First Diode	29
24	Final Heater Design	30
25	Enlarged Sketch of Capillary Structure	30
26	Capillary Emitter, Guard Ring, and Collector Arrangement	31
27	Sketch of Bell Jar Arrangement	32
28	Multicapillary Emitter Structure	33
29	Photographs of Emitter on Collector Surface	34
30	Layout Diagram of Converter C	35
31	Temperature Distribution with Final Heating Design	36
32	Layout Diagram of Converter D	38
33	Parts from Converter G	39
34	Emitter Surface of Converter G	40
35	Sketch of Converter I	41

<u>Figure</u>	<u>Title</u>	<u>Page</u>
36	Sketch of Converter 1	41
37	Picture of Converter 1	42
38	Sketch of Converter 2	42
39	Sketch of Converters 3 and 4	44
40	Temperature Distribution Along Emitter Structure.	45
41	Sketch Showing Blackbody Holes for Temperature Study	46
42	Picture of Excess Area Emitter.	47
43	Test Circuit for Monocapillary Measurements	50
44	Test Circuit for Multicapillary Measurements	50
45	Test Arrangement for Converter C	51
46	Typical I-V Curve from Monocapillary Device	52
47	Pertinent Areas in the Monocapillary Geometry	53
48	Comparison of the Monocapillary Data with the Houston Data for Tantalum	54
49	Maximum Power Measurements from Converter C	56
50	Maximum Power Measurements from Converter G for T_E from 1400 to 1800°K.	56
51	Maximum Power Measurements from Converter G for T_E from 1800 to 2100°K	57
52	Passive Mode Power at 2000°K	57
53	Passive Mode Power at 2100°K	58
54	Power Density from Porous Tungsten Emitter as Function of T_{Cs}	59
55	Power Density from Porous Tungsten Emitter as Function of d and T_W	59
56	Electron Saturation Current at Low Emitter and Cesium Temperatures.	59
57	Comparison of Theory and Experiment for Electron Currents at 1600°K	60
58	Comparison of Theory and Experiment at 1800°K.	62
59	Comparison of Theory and Experiment at 1900°K.	63
60	Comparison of Theory and Experiment at 2000°K.	64
61	Comparison of Theory and Experiment at 2100°K.	65
62	Passive Mode Characteristics at 1800 and 1900°K for d = 0.3 mm.	66
63	Passive Mode Characteristics at 2000 and 2100°K for d = 0.3 mm.	66
64	Emitter Temperature Distribution at 2000°K	68
65	Emitter Temperature Distribution at 2100°K	69
66	Comparison of I-V Characteristics from Porous and Foil Capillary Emitters.	69
67	Ion Current as Function of T_C for T_E = 1600°K and T_{Cs} = 473°K	71
68	Ion Current as Function of T_C for T_E = 1800°K and T_{Cs} = 473°K	71
69	Ion Current as Function of T_C for T_E = 1400°K and T_{Cs} = 523°K	72
70	Ion Current as Function of T_C for T_E = 1800°K and T_{Cs} = 573°K	72
71	Ion Current Summary Plot.	73

<u>Figure</u>	<u>Title</u>	<u>Page</u>
72	Pertinent Surface Areas in the Collector Volume.	75
73	Reverse Current as Function of T_E	76
74	Variation in Ion Current with Spacing for Constant T_C and Equilibrium T_C	76
75	Ion Current at 1900°K	77
76	Ion Current as Function of $1/T_C$ for $T_E = 1600^\circ K$ and $T_{Cs} = 473^\circ K$	78
77	Ion Current as Function of $1/T_C$ for $T_E = 1800^\circ K$ and $T_{Cs} = 473^\circ K$	78
78	Ion Current as Function of $1/T_C$ for $T_E = 1400^\circ K$ and $T_{Cs} = 523^\circ K$	79
79	Ion Current as Function of $1/T_C$ for $T_E = 1800^\circ K$ and $T_{Cs} = 573^\circ K$	79
80	Variation of I-V Characteristics with T_C for $T_{Cs} = 473^\circ K$	81
81	Variation of I-V Characteristics with T_C for $T_{Cs} = 673^\circ K$	81
82	Circuit for Oscillation Study	82
83	Oscillation Data for High Resistance Load	83
84	Oscillation Data for Low Resistance Load	84
85	Peak Current-Voltage Points from Oscillation Data	85
86	Typical I-V Characteristics	87
87	Spectra Observed in Each Mode of Operation	88
88	Test Arrangement for Converter 4	90
89	Comparison of Measured Work Function to Houston-Nottingham Values.	91
90	Current-Voltage Characteristics for Electron- and Ion-Rich Conditions	92
91	Effect of Spacing in the Ion-Rich Condition	93
92	Effect of Spacing in the Electron-Rich Condition (Sheet 1 of 2)	94
	(Sheet 2 of 2)	95
93	Comparison of Theory and Experiment at $T_{Cs} = 473^\circ K$ —Plane Emitter	97
94	Dimensions of the Slotted Emitter and Two Other RCA Designs	98
95	Picture of Converter 5	98
96	Current-Voltage Characteristic for 1400/423.	99
97	Current-Voltage Characteristic for 1600/423.	101
98	Current-Voltage Characteristic for 1600/473.	102
99	Current-Voltage Characteristic for 1600/523.	103
100	Current-Voltage Characteristic for 1500/473.	104
101	Comparison of Theory and Experiment at $T_{Cs} = 398^\circ K$ —Slotted Emitter	105
102	Comparison of Theory and Experiment at $T_{Cs} = 423^\circ K$ —Slotted Emitter	105
103	Comparison of Theory and Experiment at $T_{Cs} = 448^\circ K$ —Slotted Emitter	106
104	Comparison of Theory and Experiment at $T_{Cs} = 473^\circ K$ —Slotted Emitter	106

<u>Figure</u>	<u>Title</u>	<u>Page</u>
105	Comparison of Theory and Experiment at $T_{Cs} = 498^{\circ}\text{K}$ —Slotted Emitter	107
106	Comparison of Theory and Experiment at $T_{Cs} = 523^{\circ}\text{K}$ —Slotted Emitter	107
107	Comparison of Theory and Experiment at $T_{Cs} = 548^{\circ}\text{K}$ —Slotted Emitter	108
108	Comparison of Theory and Experiment at 490°K on Converter 6	110
109	Comparison of Theory and Experiment at 523°K on Converter 6	110
110	Dimensions of Typical Emitter	111
111	Several Emitter Samples	112
112	Sample Ceramic-Metal Seals	112
113	Sapphire-Niobium Seal Samples	113
114	Assembly Including Several Ceramic-Metal Seals	114
115	Corrosion Test Furnace	115
116	Corrosion Test Container	115
117	Corrosion Test Container for Ceramic-Metal Seals	116
118	Tungsten Vapor Deposition Apparatus	119
119	Tungsten Vapor Deposition Schematic	119
120	Integrating Specimen Holder for Cylindrical Samples Using High-Speed Motor	121
121	Integrating Specimen Holder Positioned for the Analysis of Flat Specimens	121
122	Integrating Specimen Holder for Cylindrical Samples Using a Low-Speed Motor	122
123	Experimental Setup for Analysis of Cylindrical Specimens	122
124	Tungsten Deposited at 650°C at a Mixture Ratio of 6:1 (250X)	126
125	Deposit in Figure 124 After Heat Treatment at 2300°K for Two Hours (250X)	127
126	Tungsten Deposited at 650°C at a Mixture Ratio of 30:1 (250X)	127
127	Deposit in Figure 126 After Heat Treatment at 2300°K for Two Hours (250X)	128
128	Tungsten Deposited at 750°C at a Mixture Ratio of 60:1 (250X)	128
129	Deposit in Figure 128 After Heat Treatment at 2300°K for Two Hours (250X)	129
130	Free-Standing Tungsten Structures Produced by Vapor Deposition (1X) . . .	129
131	Tungsten Tubing Before and After Joining by Vapor Deposition (3X)	130
132	Tungsten Resistance Furnace Capable of Operating in Vacuum or Inert Gas to 4500°F	132
133	Microstructure of CPS and Rolled Tungsten Plate Parallel to Rolling Direction (250X)	135

<u>Figure</u>	<u>Title</u>	<u>Page</u>
134	Sintered Microstructure of CPS Tungsten Bar (250X)	135
135	Microstructure of Arc-Cast and Extruded Tungsten Bar Parallel to Rolling Direction (250X)	136
136	Microstructure of CPS and Rolled Tungsten Bar Parallel to Rolling Direction (75X).	136
137	As-Cast Microstructure of Arc-Cast Tungsten Plate (10X)	137
138	As-Cast Microstructure of Arc-Cast 85W-15 Mo Plate (250X)	137
139	Microstructure of Rolled W-2% ThO ₂ Bar Parallel to the Rolling Direction (250X)	138
140	Microstructure of Type 218 Doped Tungsten Bar Parallel to the Rolling Direction (250X)	138
141	Low Voltage Electron Beam Welding Facility.	139
142	Sketch Showing Three Types of Sheath Conditions	158
143	Comparison of Tube Functioning as (1) an Ion or Electron Emitter and (2) an Emitter of Both Ions and Electrons— i.e., a Plasma Generator	159
144	Pressure, Density, and Potential Quantities as a Function of Capillary Length	164
145	Density Functions for Three Emitter Temperatures at a Constant Cesium Temperature of 473°K	165
146	Sketch Depicting Extraction of Charged Particles from Tube	166
147	Arrangement of Electrode-Probe Monocapillary System.	169
148	Photograph of Electrode-Probe Monocapillary System.	169
149	Example of I_c (-V) Characteristic Measured with the Electrode-Probe Monocapillary System.	170
150	Comparison of Curves Showing the Density of the Electron Current Against the Reciprocal of the Temperature.	171
151	Comparison of Curves Showing the Density of the Electron-Current Against the Reciprocal of the Temperature	171
152	Theoretical and Experimental Comparison of Electron Current Densities Measured with the Electrode-Probe Monocapillary System.	173
153	Theoretical and Experimental Comparison of Ion-Current Densities Measured with Electrode-Probe and Ion-Extraction Electrode Monocapillaries.	174
154	Sketch of the Electron Extraction Monocapillary	175
155	Example of Characteristic of Extracted Electron Current (I_c) Against Accelerating Potential (V_{acc}) Measured with the Electron Extraction Monocapillary	177

<u>Figure</u>	<u>Title</u>	<u>Page</u>
156	Theoretical and Experimental Comparison of Electron Current Measured with the Electron-Gun Extraction Monocapillary System.	177
157	Arrangement of Ion Extraction Monocapillary System	178
158	Example of Characteristic of Extracted Ion-Current (I_+) Against Accelerating Potential (V_{acc}) Measured with the Ion Extraction Monocapillary System.	178
159	Magnified Diagram of the Multicapillary Emitter and Collector	179
160	Microphotograph of a Multicapillary Emitter	179
161	Design Concept of Multicapillary Emitter Converter	180
162	Photograph of Experimental Multicapillary Emitter Converter Setup	181
163	I_c (V_c) Characteristic for Various Interelectrode Distances Measured with the Tantalum Multicapillary Emitter Converter	182
164	I_c (V_c) Characteristics. Comparison of a Tungsten Multicapillary Emitter Converter with a Sintered Porous Tungsten Emitter Converter	184
165	Preliminary Values of Measured Power Densities	185

LIST OF TABLES

<u>Table</u>	<u>Title</u>	<u>Page</u>
1	Pertinent Dimensions of Interelectrode Space for Computer Solution	9
2	Summary of Tests on Monocapillary Devices	49
3	Summary of Tests on Multicapillary Converters	52
4	Analysis of I-V Characteristics	67
5	Electron-Ion Ratios from Converter G	74
6	Summary of Corrosion Tests	116
7	Relative Intensities of Randomly Oriented Specimens	123
8	Deposition Parameters and Results of Evaluation of Tungsten Vapor Deposits	125
9	Materials Being Evaluated.	131
10	Results of X-Ray Analysis.	134

LIST OF SYMBOLS

<u>Symbol</u>	<u>Definition</u>
d	Distance
e	Charge on electron
f	Fractional ionization
I_0	Saturation current
I_+	Random ion current
I_-	Random electron current
I_w	Saturation current for tungsten surface
J	Current density
k	Boltzmann constant
K	Net cesium flow through capillaries
m	Mass of cesium atom
m_+	Mass of cesium ion
n	Incremental volume
N	Cesium atom number density at temperature T_E
N_+	Cesium ion number density
N_{Cs}	Cesium atom number density at temperature T_{Cs}
P	Power
T_{Cs}	Cesium temperature
T_C	Collector temperature
\bar{v}	Average kinetic velocity
V	Voltage
V_i	Ionization potential
V_T	Voltage equivalent of temperature (kT/e)
T_E	Emitter temperature
W	Probability factor
λ	Mean free path
ν	Arrival rate at capillary entrance
ϕ_E	Work function of emittance
ϕ_o	Plasma potential

I. INTRODUCTION

The material contained herein summarizes the theoretical and experimental results obtained on the investigation of a capillary emitter serving as a dual source of ions and electrons in a thermionic converter.

The theory of the capillary emitter is reviewed, and a theoretical model is described in which a thermal plasma is formed within the capillary. The model has been extended to include the effect of wall area. A discussion of the complete development of the theory from basic principles is contained in the appendix. Also, it is shown that there are potential advantages for thermionic conversion when electrons and ions are extracted from a capillary with ion-rich sheaths.

Experimental data are summarized from monocapillary and multicapillary devices. Good agreement is shown between the data and the plasma model theory. Experimental data are also reported on an excess area emitter designed with dimensions similar to the capillary-type emitter. However, in this cavity emitter concept there is no requirement to circulate cesium. This concept is shown to have potential advantages for practical thermionic converters.

Recent developments are reported in thermionic technology. Of considerable interest are the results relating the preferred crystal orientation of tungsten vapor-deposited surfaces to the deposition parameters.

Some conclusions are given in regard to the feasibility and practicality of using a capillary emitter in a thermionic converter. Finally, suggestions for future work are presented based on the results obtained from this project.

II. CONCLUSIONS

Based on results of work accomplished on this project, the following conclusions are stated.

1. Concerning the feasibility and practicality of using a capillary emitter as a dual source of ions and electrons in a thermionic converter:
 - A random current theory was formulated and verified by experimental results to demonstrate the feasibility of the capillary emitter.
 - Power densities in the temperature range from 1400 to 1800°K were competitive with, but not superior to, converters with the simpler cesiated planar surface emitter; hence, the concept is not practical in this operating range.
 - Power densities (5 to 15 watts/cm²) in the temperature range from 1800 to 2100°K, as measured on a 0.32-cm² area, were competitive with conventional converters and demonstrated three potential advantages over the conventional approach--wider electrode spacings (0.25 to 1.0 mm), higher converter voltages (1.25 to 1.50 volts), and lower cesium pressure to ease fabrication (10^{-2} to 3×10^{-1} mm Hg).
 - Experimental results indicated that the requirement for circulating cesium might not be important in operation of the capillary emitter.
 - Mechanical design problems, and possible difficulty in circulating the cesium in a zero-g environment, appear to make the capillary emitter concept impractical for application, particularly with a nuclear heat source.

In summary, the feasibility of the capillary concept was demonstrated, but the practicality of a circulating cesium system does not appear worthy of further development.

2. Concerning the feasibility and practicality of using a cavity emitter as a dual source of ions and electrons in a thermionic converter:
 - Experimental results in the temperature range from 1400 to 1700°K, as measured on a 3.14-cm² area, indicate that the cavity emitter follows the random current theory; therefore, the feasibility of the concept has been demonstrated.
 - Further experimental data are needed in the temperature range from 1700 to 2100°K before the concept can definitely be considered practical. However, the attendant advantages of wide spacing, high voltage, and low cesium pressure are inherent in the concept. No circulating cesium system is required and fabrication problems are no more difficult than with the conventional converter.
 - Practical methods have been developed for fabrication of cavity emitters.
3. The vapor deposition process does produce selectively oriented crystal surfaces. The type and degree of orientation depend on the deposition parameters.

4. From a spectroscopic study of the cesium plasma in a thermionic converter it was shown that:

- It is possible to make spectroscopic measurements in the power-producing region of a thermionic converter.
- Line broadening can be used to determine electron density in the arc mode.
- Line intensity ratios can be used to determine electron temperature in the arc mode.
- In the arc mode the deviation from a Maxwellian distribution is not detectable within the limit of measurement error using various line pairs to determine electron temperature.

III. THEORY OF THE CAPILLARY EMITTER

STATEMENT OF PROBLEM

In the capillary emitter concept it was proposed to have cesium from a high temperature reservoir flow through a refractory capillary structure of regular geometry. The cesium pressure at the exit of the capillaries is maintained at a low value by a low temperature sink reservoir. Actually, two separate problems require solution in order to predict the thermionic performance of such an emitter:

1. What is the pressure distribution across the capillary, and cesium coverage along the capillary, as a function of emitter temperature, capillary geometry, high temperature reservoir temperature (cesium vapor pressure at the capillary entrance), and electrode spacing?
2. What is the current density and work function of the capillary emitter as a function of emitter temperature, capillary geometry, reservoir temperature, and electrode spacing?

Solutions to the problems of flow and emission are discussed under separate headings in the following. Since the solution of the emission problem depends on the solution of the flow problem, the flow solution is discussed first.

FLOW SOLUTION

Mass transfer by diffusion through small tubes has been studied theoretically and experimentally for at least fifty years. M. Knudsen published his flow equation in 1909. * The only mechanism of mass transfer considered in this treatment is collision with the tube wall and subsequent evaporation from the wall. The Knudsen equation is:

$$G = \frac{\pi}{2mkT_E} a^3 \frac{\Delta P}{\Delta L} \quad (1)$$

where

T_E = temperature of capillary (°K)

a = radius of capillary

ΔP = pressure drop across capillary

ΔL = length of capillary

From this equation it can be seen that the pressure is a linearly decreasing function with distance along the capillary.

*Superscripts refer to references in Section VIII.

The Knudsen solution is valid if, at some point along the capillary, the mass transport is only through the volume of the section---the so-called volume flow. There are cases where the molecules or atoms striking the wall are adsorbed and the migrate a finite distance along the surface before being desorbed. This is the so-called surface flow. I. M. Dykman was the first to publish the exact equation including this phenomenon.² The equation is as follows:

$$-D\sigma_0 \left(\frac{d^2\theta}{dx^2} \right) = U + B - \nu(\theta) \quad (2)$$

where

$$U = 1/2 a \int_0^L \nu(\theta) \left(1 - \left| x' - x \right| \left[(x' - x)^2 + 6a^2 \right] \left[(x' - x)^2 + 4a^2 \right]^{3/2} \right) dx \quad (2a)$$

and

$$B = K/2a \left[(x^2 + 2a^2)/(x^2 + 4a^2)^{1/2} - x \right] \quad (2b)$$

where

D = diffusion constant

σ_0 = surface coverage of monolayer (3.56×10^{14} atoms/cm², as given by Langmuir)

θ = fractional surface coverage

$\nu(\theta)$ = rate of evaporation from the surface

K = total number of particles entering the capillary per square centimeter per second

Figure 1 shows the pertinent geometry.

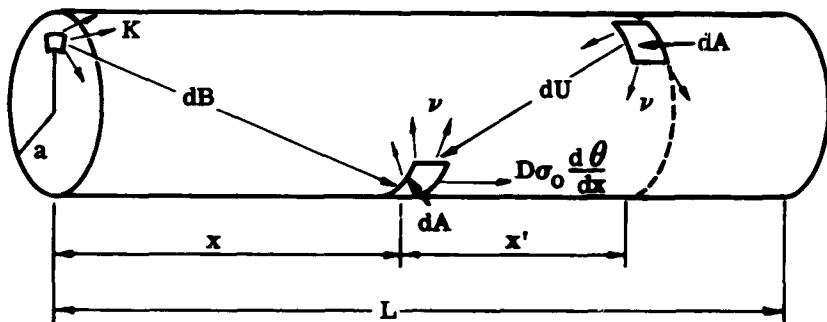


Figure 1. Capillary Geometry

In comparing the equations due to Knudsen and Dykman, it has been shown that the surface flow becomes comparable to volume flow where the capillary diameter is small compared to the surface diffusion length.³ Three other more recent papers on flow through porous refractory materials were studied as background for this problem.^{4,5,6}

Solutions of Dykman Equation

Using Langmuir's expressions for D and $\nu(\theta)$, and the value of K as given by kinetic theory, it is possible to attempt the solution of the Dykman equation.⁷ Three approaches were attempted:⁸

1. Iteration on θ
2. Iteration on ν
3. Solution of the integral equation

In summary, the iteration on θ was never completely successful because numerical errors were additive. The iteration on ν , which avoided some of the sources of error present in the θ calculation, was successfully completed—for the geometries being considered for the capillary emitter, the solution indicated that a linear pressure drop across the capillary was a good approximation. In the other approach the integro-differential equation was transformed by means of the inverse Green's function into a general inhomogeneous Fredholm integral¹ equation. In this way it was possible to use a numerical approach without iteration—the equation is replaced by n simultaneous linear equations in n unknowns. A solution of the no-surface-diffusion form of Equation (2) was obtained (D = 0) for $L/a \leq 10$. A linear variation of ν with x was found. Some attempts were made to solve the equation with various boundary conditions. The solution did not seem to be sensitive to the boundary conditions, but was again limited to small values of L/a .

Predicted Flow Through Multicapillary Emitter

Based on the results of solutions of the Dykman equation, and references that indicated that surface diffusion length is small compared to the capillary radii contemplated for experimental evaluation in this project, it was decided to assume a linear pressure drop along the capillary.

To estimate the pressure distribution throughout the experimental multicapillary electrode configuration to be studied, flow continuity equations were applied to the system. Figure 2 is an enlarged view of the multicapillary electrode geometry. Cesium flows up through a capillary structure of 320 capillaries, then radially outward in the interelectrode space, and finally discharges in a large volume surrounded by cool walls.

A numerical approach was selected. The multicapillary was divided into eight annular rings as shown in Figure 3, part (a). This division also defined eight cylindrical areas in the interelectrode space as shown in Figure 3, part (b). The primed areas vary depending on the interelectrode spacing.

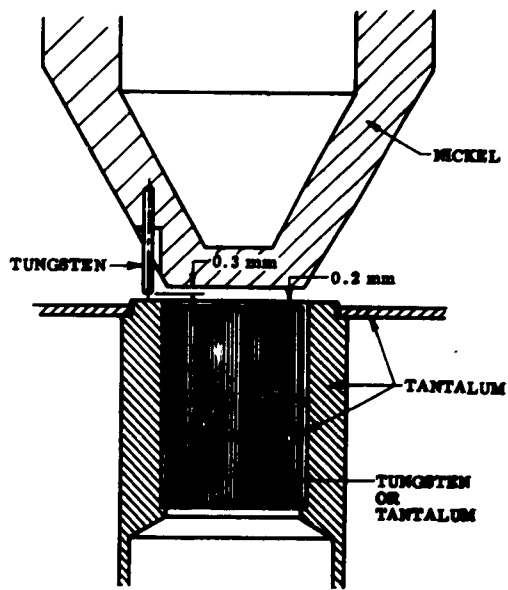


Figure 2. Enlarged View of Experimental Multicapillary Geometry

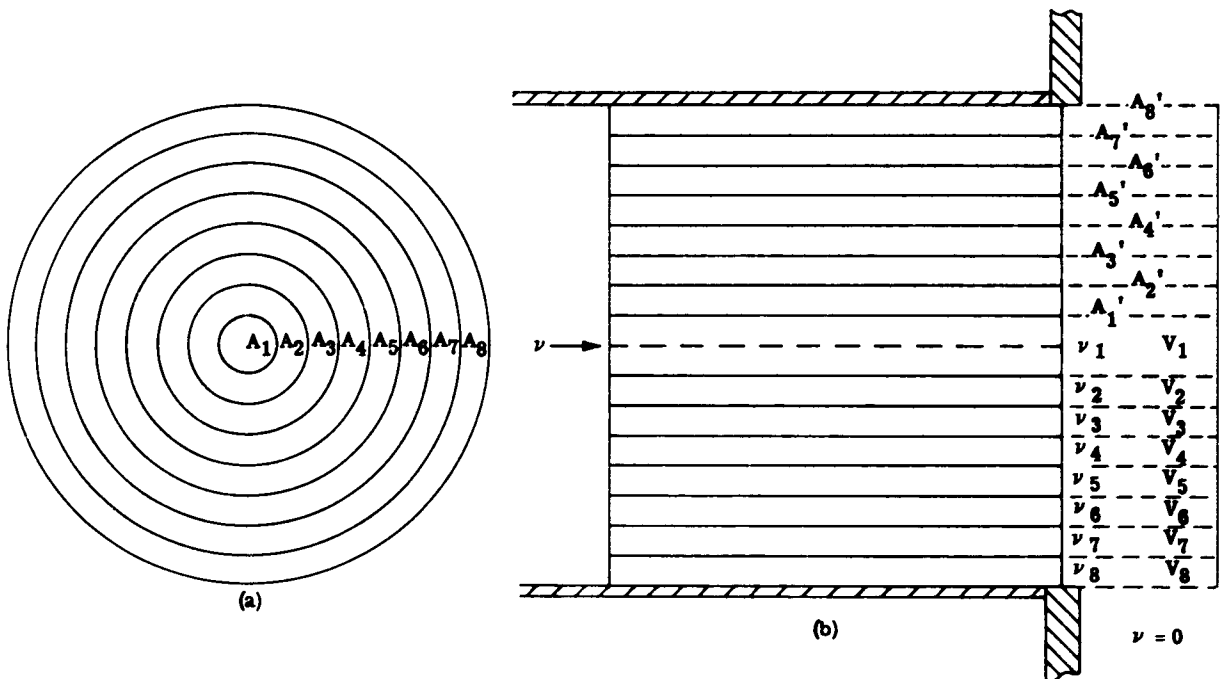


Figure 3. Increments for Numerical Solution

Table 1 summarizes the pertinent dimensions for various spacings. The solution was formulated by applying the requirement for flow continuity to each of the incremental volumes in the interelectrode space---these are identified as V_1 to V_8 in Figure 3, part (b). Flow through the capillaries was assumed to be given by the Knudsen equation in a more general form due to P. Clausing.⁹ Thus, the net flow into any volume is given by

$$K_n \text{ (in)} = W \times A_n (\nu - \nu_n) \quad (3)$$

where

$$W = 8/3 a/L$$

ν = arrival rate at capillary entrance

Of course, the arrival rate at the capillary entrance is defined by cesium reservoir temperature. The net flow out of any volume is:

$$K_n \text{ (out)} = A_n (\nu_n - \nu_{n+1}) \quad (4)$$

It is assumed that $\nu = 0$ in the region surrounding the interelectrode volume.

TABLE 1
Pertinent Dimensions of Interelectrode Space for Computer Solution

Capillary Area	Area ($\text{cm}^2 \times 10^3$)	Number of Capillaries	Spacing (mm)					
			Cylindrical Area	0.3 ($\text{cm}^2 \times 10^{-3}$)	0.5 ($\text{cm}^2 \times 10^{-3}$)	0.8 ($\text{cm}^2 \times 10^{-3}$)	1.4 ($\text{cm}^2 \times 10^{-3}$)	2.0 ($\text{cm}^2 \times 10^{-3}$)
A_1	5	5	A'_1	7.5	12.5	20	35	50
A_2	15	15	A'_2	15	25	40	70	100
A_3	25	25	A'_3	22.5	37.5	60	105	150
A_4	35	35	A'_4	30	50	80	140	200
A_5	45	45	A'_5	37.5	62.5	100	175	250
A_6	55	55	A'_6	45	75	120	210	300
A_7	65	65	A'_7	52.5	87.5	140	245	350
A_8	75	75	A'_8	20	60	120	240	360
Total	0.32 cm^2	320						

An analog computer was used to obtain a solution of the problem. In the computer, the difference between Equations (3) and (4) was made the input to an electronic integrator. Figure 4 gives the principle of solution in analog computer form. A solution is obtained when the inputs to all integrators are zero. The spacing is varied by changing the scale factors on all quantities involving primed areas.

Results of the solution are given in Figure 5---the arrival rate at a given station is expressed as a fraction of the arrival rate at the inlet to the capillaries. The arrival rate, ν , may be taken as approximately proportional to the pressure, disregarding the effect of temperature. Several conclusions are evident from the results.

1. There is a radial pressure gradient within the interelectrode space---the amount is dependent on the electrode spacing.

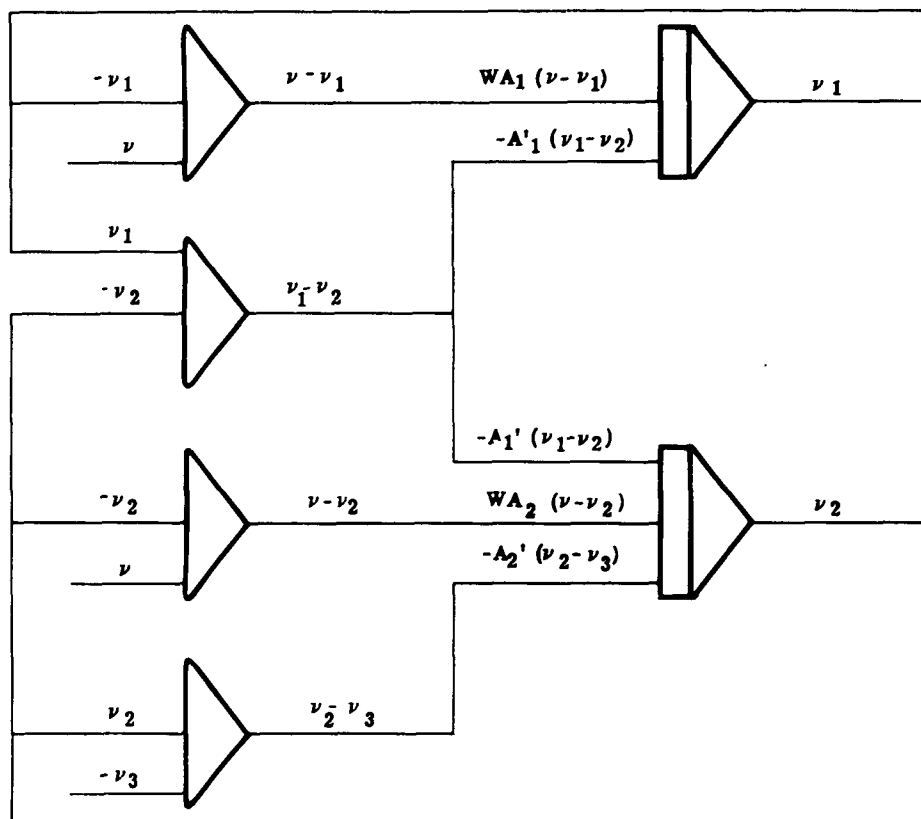


Figure 4. Principle of Analog Solution

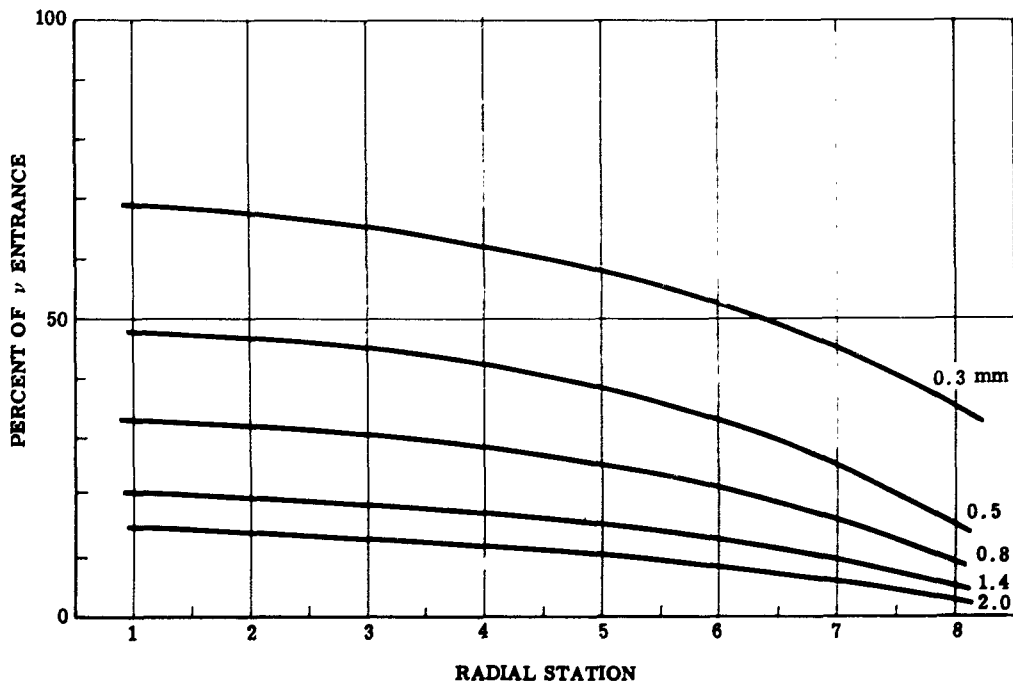


Figure 5. Results of Numerical Solution

2. As a result of the gradient, more cesium flows through the capillaries near the periphery of the emitter surface than near the center.
3. The average pressure in the interelectrode space may be as high as 55% or as low as 10% of the inlet pressure.
4. There is no electrode spacing at which the flow conductance represented by the interelectrode space is negligible.

Although this is a discussion of flow theory, it is appropriate to include at this point the comparison between the theory and experiment. Flow through the test electrode structure could be measured by observing the rise of cesium in the glass section of the cesium loop with the lower section cooled (Figure 6). Figure 7 shows the experimental results for three spacing values. The experimental data are compared with theory in Figure 8. The agreement is quite good.

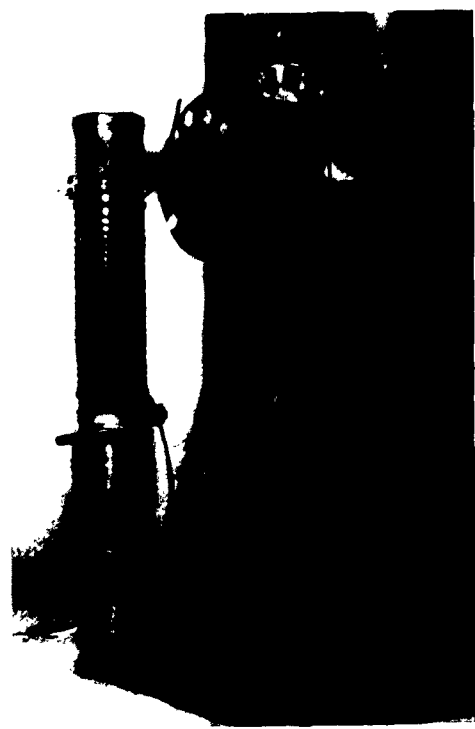


Figure 6. Cesium Flow Loop

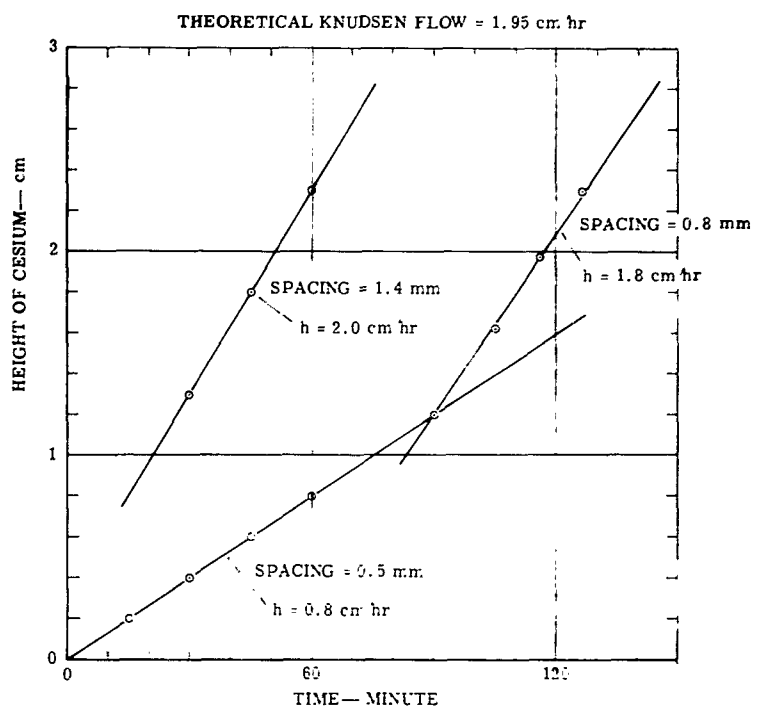


Figure 7. Cesium Flow Data

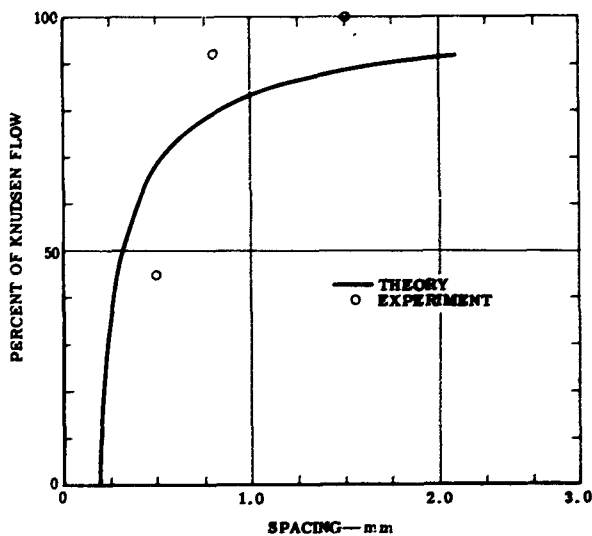


Figure 8. Comparison Between Theory and Experiment for Cesium Flow Through Multicapillary Emitter

EMISSION SOLUTION

The first approach used to predict the electron and ion emission from a capillary was as follows:

1. Assume a linear pressure drop across the capillary.
2. Determine the surface coverage fraction, θ , as a function of distance along the capillary using the Nottingham curves.¹⁰

The electron current was computed by summation from all areas where the ion emission was equal to or greater than 1 to 500 electrons. For the condition where the complete capillary surface was electron-space-charge-limited, the electron current was computed using the cross section area of the capillary at the exit. Comparison between the theory and experimental data from a monocapillary emitter yielded poor agreement.

Sheath Potential Model

The relatively crude model previously described was refined to include the effect of sheaths along the capillary wall. The sheath potential model is described in detail in Reference 11. It was shown that, based on a calculation of the localized plasma potential from ion and electron emissions, a large potential gradient could exist along the capillary under some conditions

of emitter temperature and cesium pressure gradient. Estimates were made of the electron current for two different cases. In the first case the potential distribution was approximated by a linear variation as shown in Figure 9. Then, the electron emission was calculated by summing the local emission over the total area of the capillary wall area. A comparison of theory and experiment for the molybdenum capillary is shown in Figure 10. It is noted that the theoretical results are higher than the experimental data.

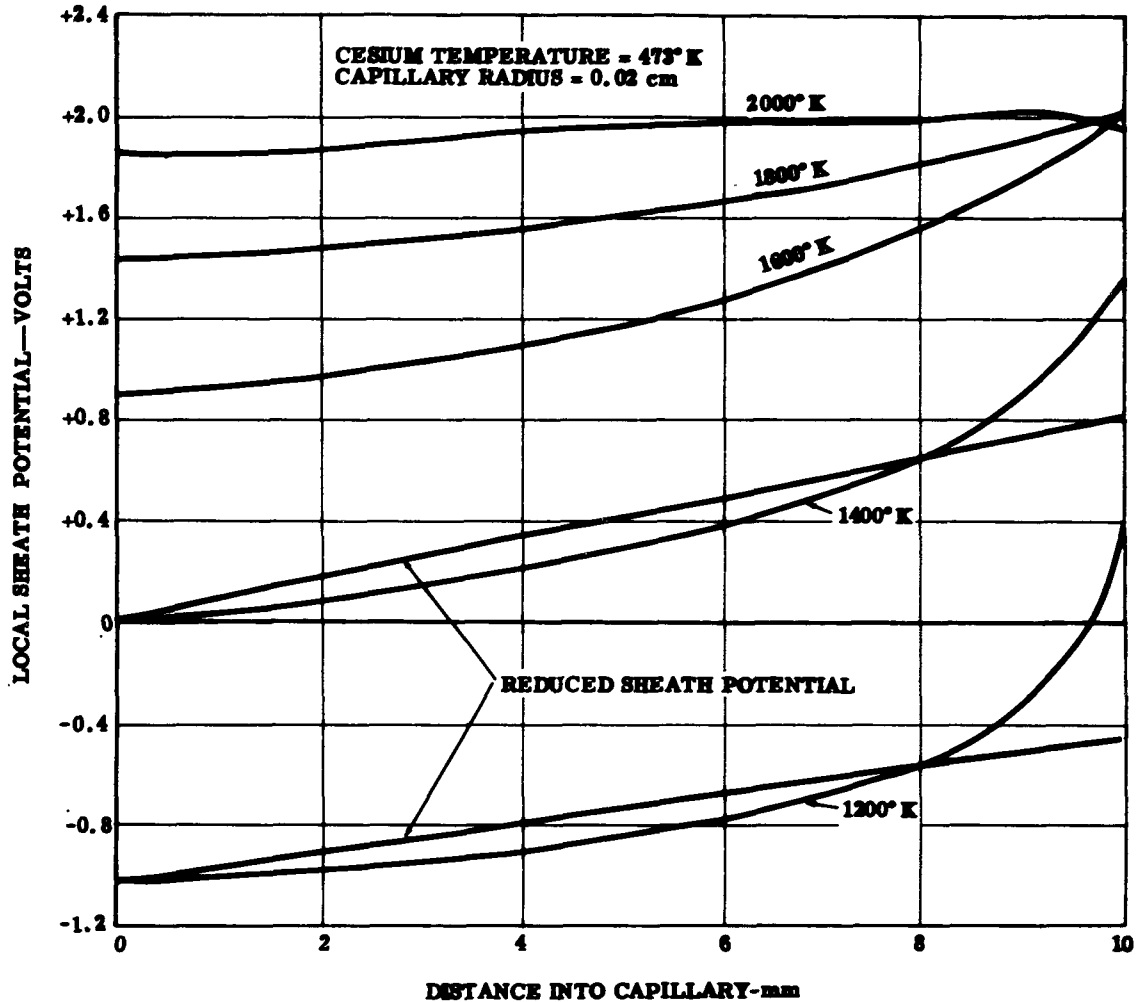


Figure 9. Local Sheath Potentials in the Capillary

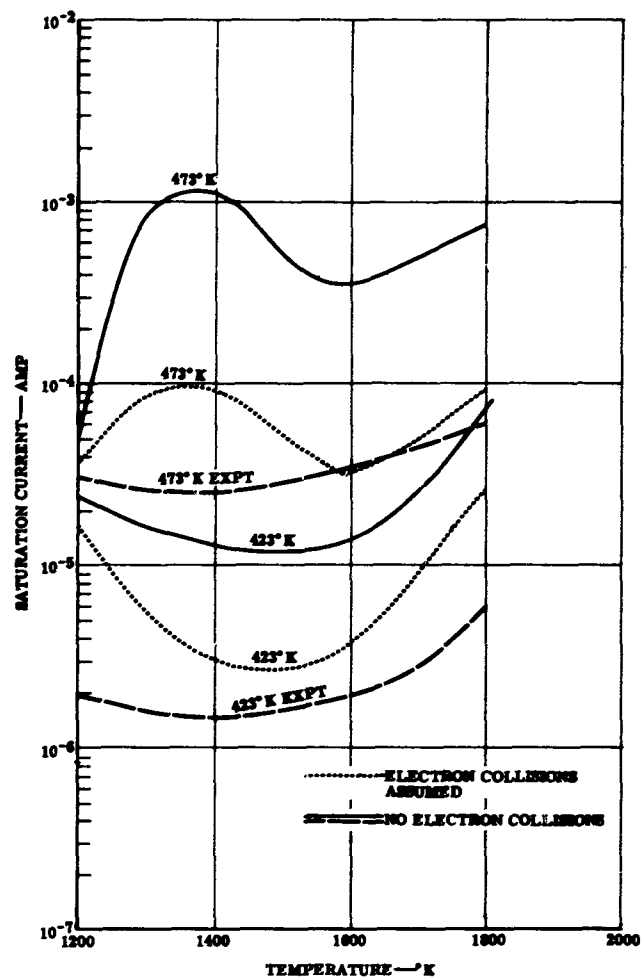


Figure 10. Comparison Sheath Model Theory with Experimental Monocapillary Data

In the second case, a reduced linear potential variation was assumed. In addition, it was assumed that only the electron current from the capillary wall area down to a depth of three times the mean free path of the atom (proportional to electron mean free path) contributed to the saturation current. For this case the agreement between theory and experiment is better, as shown in Figure 10. The improvement in agreement could be interpreted to mean that the electron collisions deep inside the capillary are effective in preventing contributions to the capillary drift current.

Random Current Model

References 12 and 13 describe a model of the capillary which grew out of the study of the sheath potential model. In this model the electron and ion currents are assumed to come from a plasma cross-sectional area at the exit of the capillary, as shown in Figure 11. Reference 12 describes the procedure for calculating the random electron current from the plasma:

$$I_{-}(p) = \frac{e\bar{v} A_p N_e(L)}{4} \quad (5)$$

where

- e = charge on the electron
- \bar{v} = electron velocity = $(8k T_e / \pi m_e)^{1/2}$
- T_e = electron temperature
- m_e = mass of electron
- A_p = cross-sectional area of plasma
- $N_e(L)$ = electron density at capillary exit

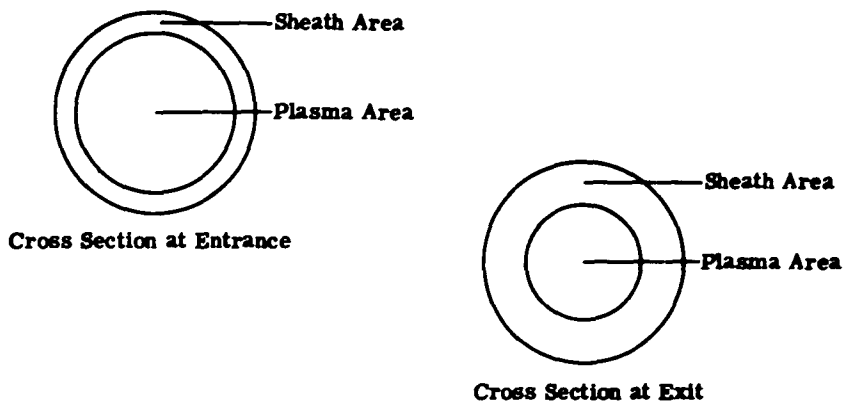
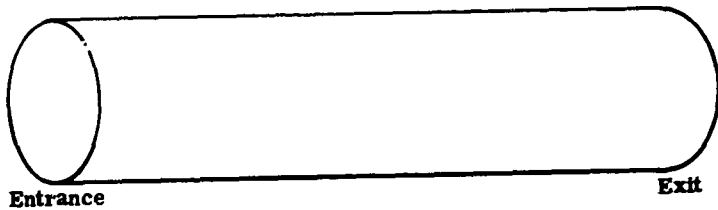


Figure 11. Geometry for Random Current Model

Electron current from the sheath area was calculated from:

$$I_{-}(s) = \frac{e\bar{V}}{4} N_e(r) dA_s \quad (6)$$

where

dA_s = incremental area of sheath

$N_e(r)$ = electron density as function of radius sheath

From Equation (5), assuming the electron temperature equal to the capillary temperature, it was found that the current predicted at 1200°K from a monocapillary was two orders of magnitude greater than observed. However, at 1800°K there was reasonable agreement between theory and experiment. From Equation (6), using Langmuir's equations for charge density within the sheath, the calculated currents were much lower than observed for low temperature monocapillary data. One curious result was observed--namely, if the random current was calculated based on the area of the sheath at the entrance rather than the exit, the results agreed very well with experimental data for all emitter and cesium temperatures.

Isothermal Diode Theory

A recent report by W. B. Nottingham describes the random current model and, consequently, was applied to the capillary emitter.¹⁰ As previously discussed, the theory is based on Equation (5). The problem solved may be stated as follows:

- Given an enclosure with walls at temperature T_E and filled with cesium at a density, N , what is the plasma potential, ϕ_0 , and what is the sheath condition at the wall?

Nottingham calls the enclosure an isothermal diode--Figure 12 is a sketch of an isothermal diode. The solution procedure is as follows:

1. Compute N_+ (ion density), knowing N and T_E by applying the Saha equation,

$$N_+ = \left[\frac{(2\pi mkT_E)^{3/2}}{h^3} N \exp \left(-\frac{V_i}{V_T} \right) \right]^{1/2} (1 - f)^{1/2} \quad (7)$$

2. Compute the random ion current density,

$$I_+ = \frac{N_+ e\bar{V}}{4} \quad (8)$$

3. The random electron current is

$$I_- = 500 I_+ \quad (9)$$

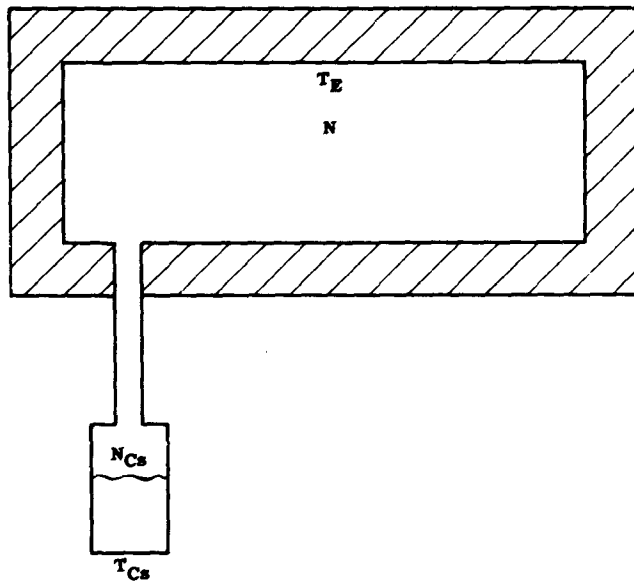


Figure 12. Isothermal Diode

4. The plasma potential, ϕ_0 , relative to the Fermi level of the surrounding conductor, is given by the work function at T_E which would yield a saturation current of I_- as given by Equation (9). This is given by the Richardson equation,

$$I_- = \frac{4 \pi m k^2 e}{h^3} T_E^2 \exp\left(-\frac{\phi_0}{V_T}\right) \quad (10)$$

5. Combining Equations (7) through (10), an expression is obtained for ϕ_0 , knowing T_E and N ,

$$\phi_0 = V_T \left[25.31 + 3/4 \ln T_E + \frac{V_i}{2V_T} - 1/2 \ln N + 1/2 \ln (1-f)^{-1} \right] \quad (11)$$

6. By assuming equal arrival rates throughout the system, the relationship between N and N_{Cs} is given by

$$\frac{N}{N_{Cs}} = \left(\frac{T_{Cs}}{T_E}\right)^{1/2} \quad (12)$$

With this procedure the plasma potential, ϕ_0 , may be calculated for a T_E and T_{Cs} , since N_{Cs} is given by the vapor pressure equation. The plasma potential as a function of T_E and T_{Cs} is shown in Figure 13, which is reproduced from Reference 10.

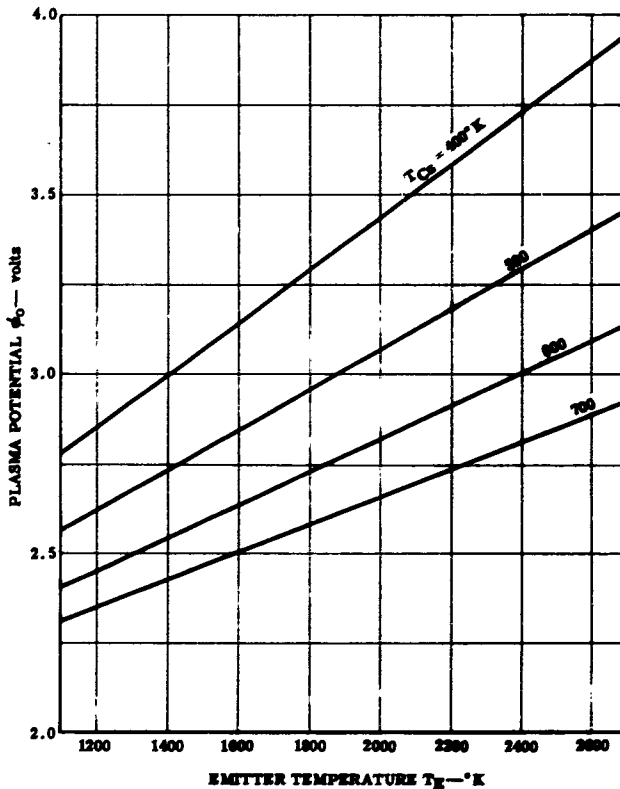


Figure 13. Plasma Potential as a Function of T_E and T_{Cs}

To complete the model of the isothermal diode, it is necessary to determine the sheath condition at the wall. For a given N and T_E , the atom arrival rate at the wall is known. If the wall material is specified, then the work function, ϕ_1 , is known from the experimental data of J. M. Houston and the extrapolations due to Nottingham.^{10,14} If ϕ_1 is greater than ϕ_0 , then a positive sheath exists. Conversely, if ϕ_1 is less than ϕ_0 , a negative sheath exists. Figure 14 shows these two conditions.

How is the isothermal diode theory applied to the capillary emitter? As a first approximation, the capillary emitter may be regarded as an isothermal diode with the special characteristics of having densities, atom, and plasma, which vary with position along the wall. This is illustrated in Figure 15. Thus, in order to predict the ion and electron emission from the capillary, it is necessary to know only the emitter temperature, T_E , and the plasma density, N_+ or N_- , at the capillary exit.

Using such an approach to calculate the random electron current, the resultant values can be compared with saturation currents from a cesiated surface as given by Reference 10.

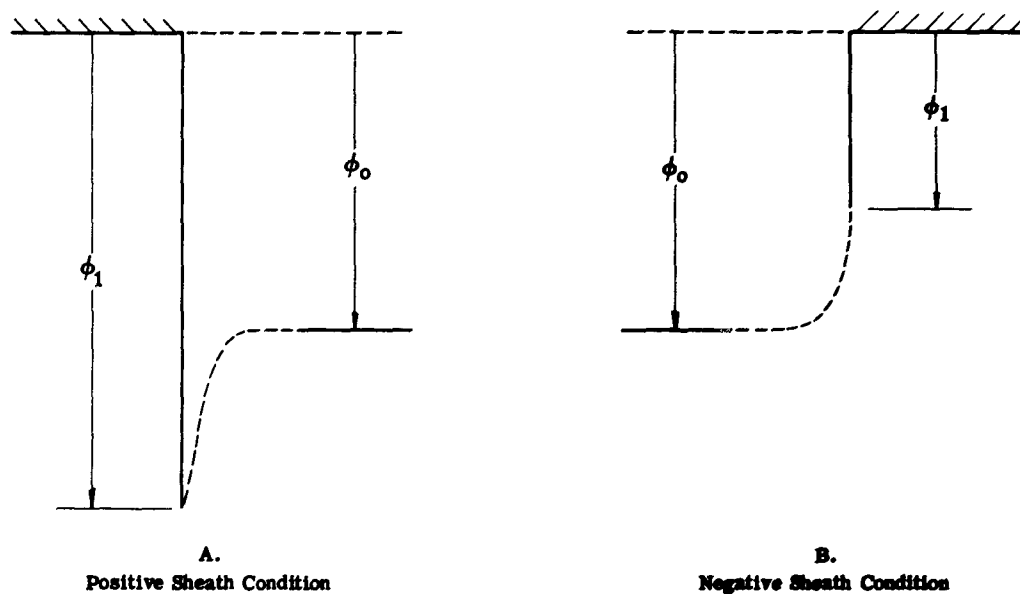


Figure 14. Sheath Conditions in Isothermal Diode

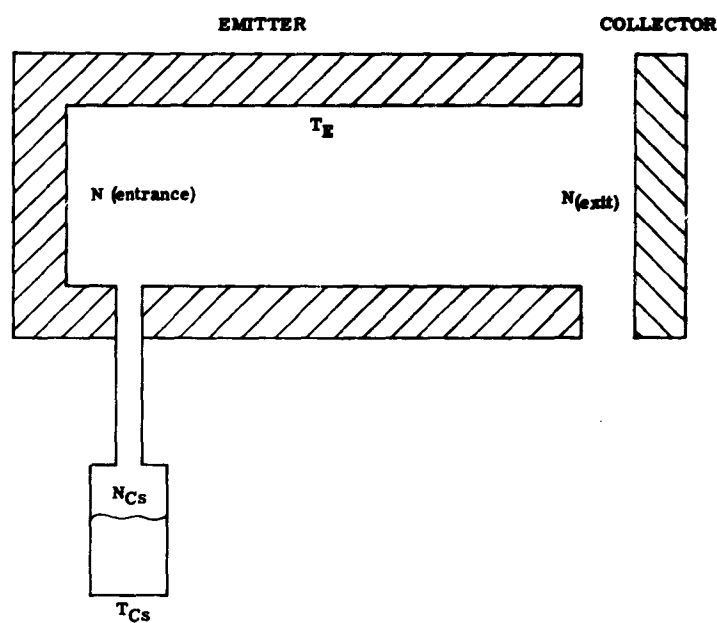


Figure 15. Capillary Emitter as Isothermal Diode

Figures 16. through 19 show the comparison with tungsten and tantalum for temperatures of 1600, 1800, 2000, and 2200°K, respectively. Values of random current are shown for full density and one-tenth density. It can be seen that, for a given T_E , the random current is greater than the saturation current from a cesiated surface up to a certain T_{Cs} ; above this value the saturation current is greater. As T_E increases, the crossover T_{Cs} value increases. Random current values of practical interest occur above 1800°K. For example, from Figure 18, for $T_E = 2000^{\circ}\text{K}$ and $T_{Cs} = 525^{\circ}\text{K}$, the comparison for a density in equilibrium with the cesium vapor gives:

$$\text{Random current } I_R = 10.5 \text{ amp/cm}^2$$

$$\text{Saturation current } I_W = 0.162 \text{ amp/cm}^2$$

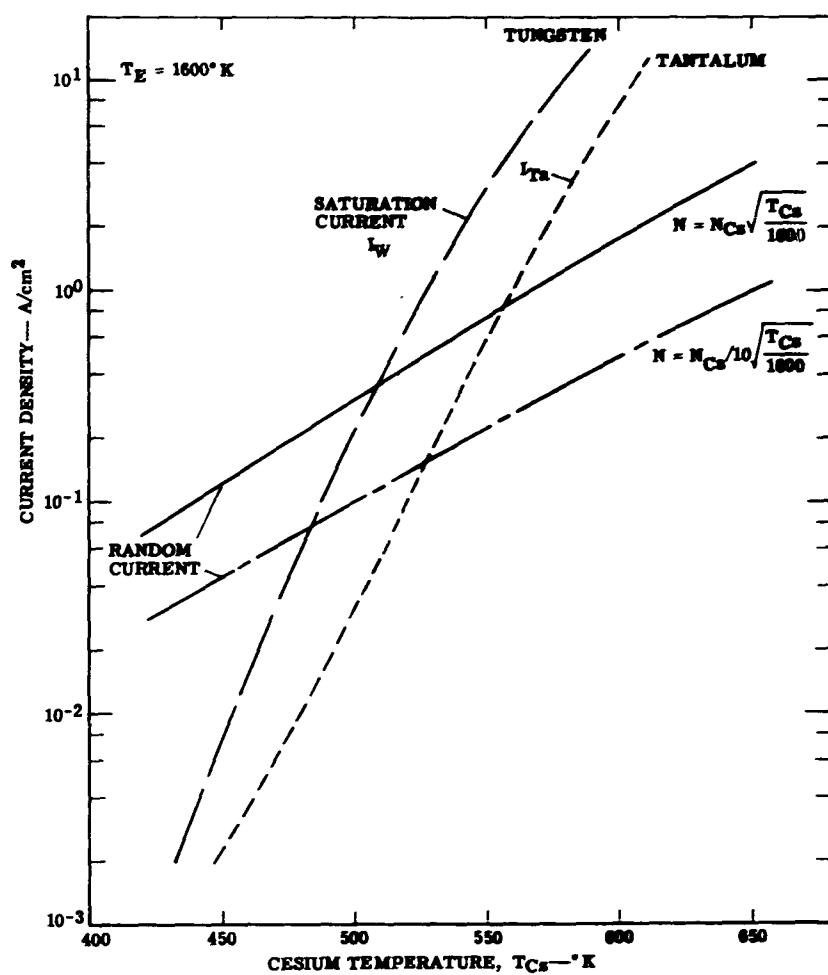


Figure 16. Comparison of Random Current to Saturation Current—1600°K

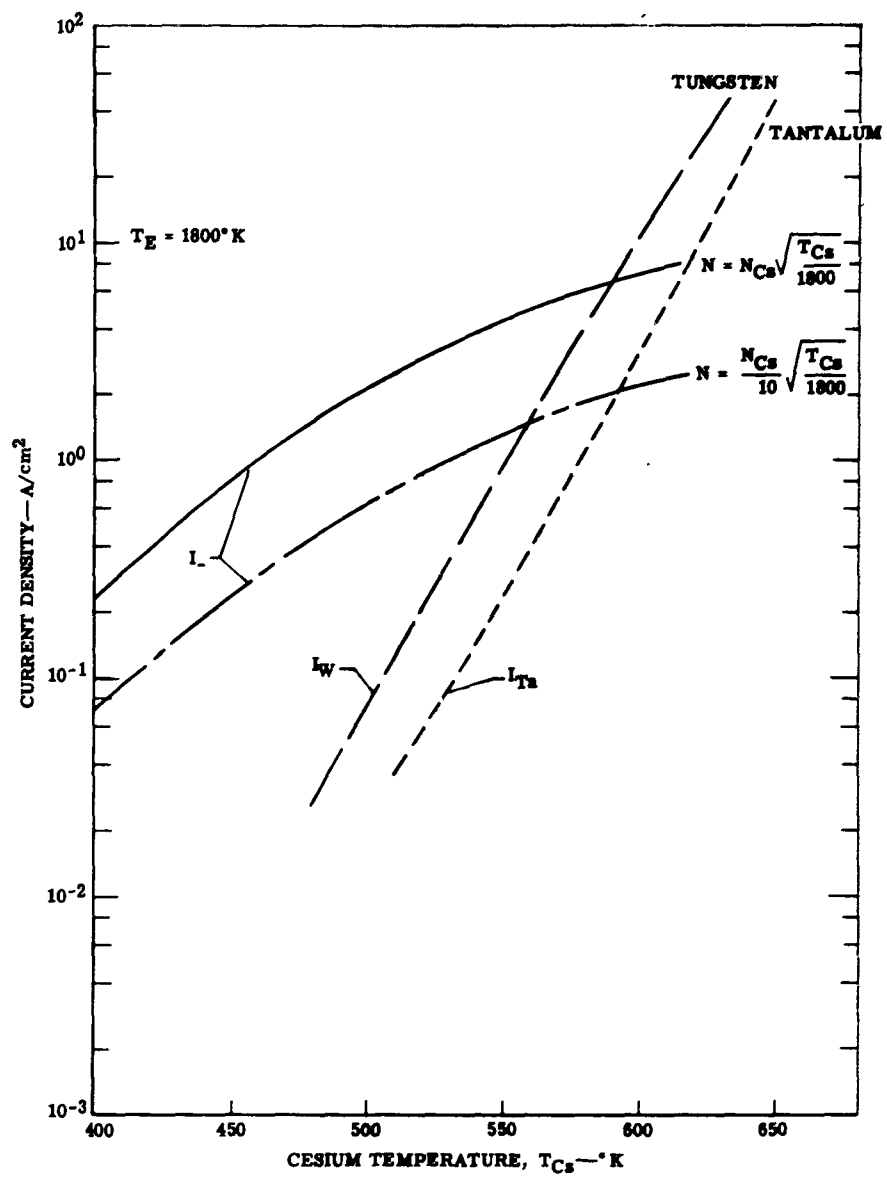


Figure 17. Comparison of Random Current to Saturation Current—1800°K

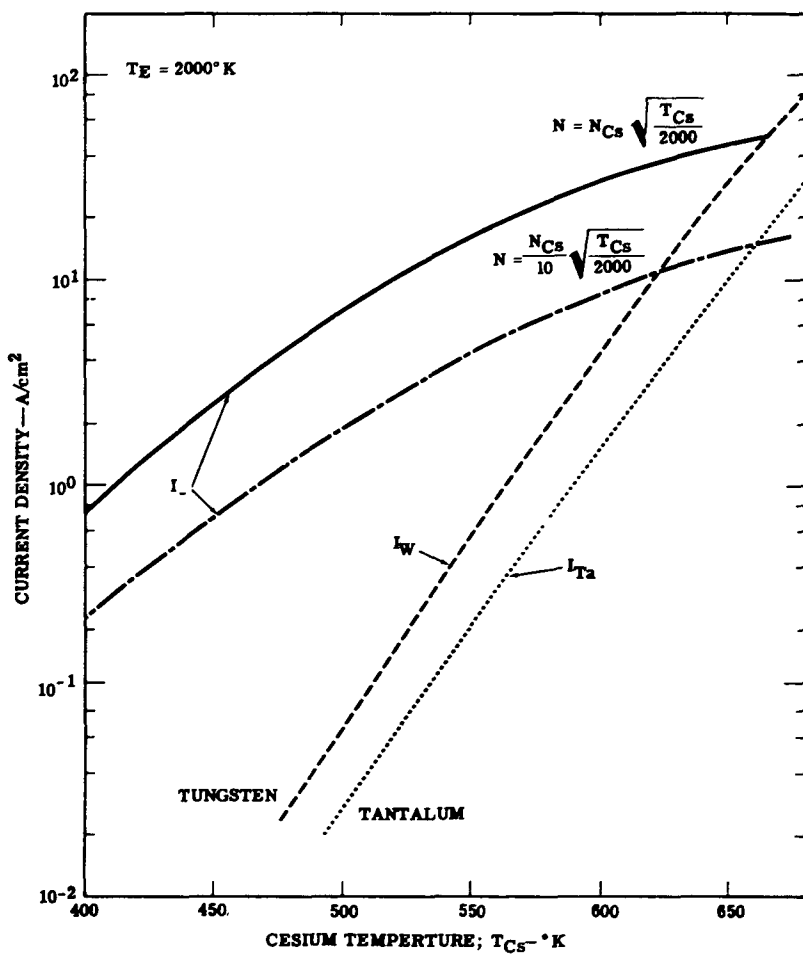


Figure 18. Comparison of Random Current to Saturation Current—2000°K

Work Function of Capillary

Prediction of the work function of the capillary emitter may be complicated by the interdependence of several parameters. Certainly, the amount of the pressure drop across the capillary—and the absolute values along the wall—are the primary factors. In turn, these values determine:

1. Nature and magnitude of the local sheath barrier
2. Ratio of mean free path to capillary diameter (importance of collision processes inside the capillary)

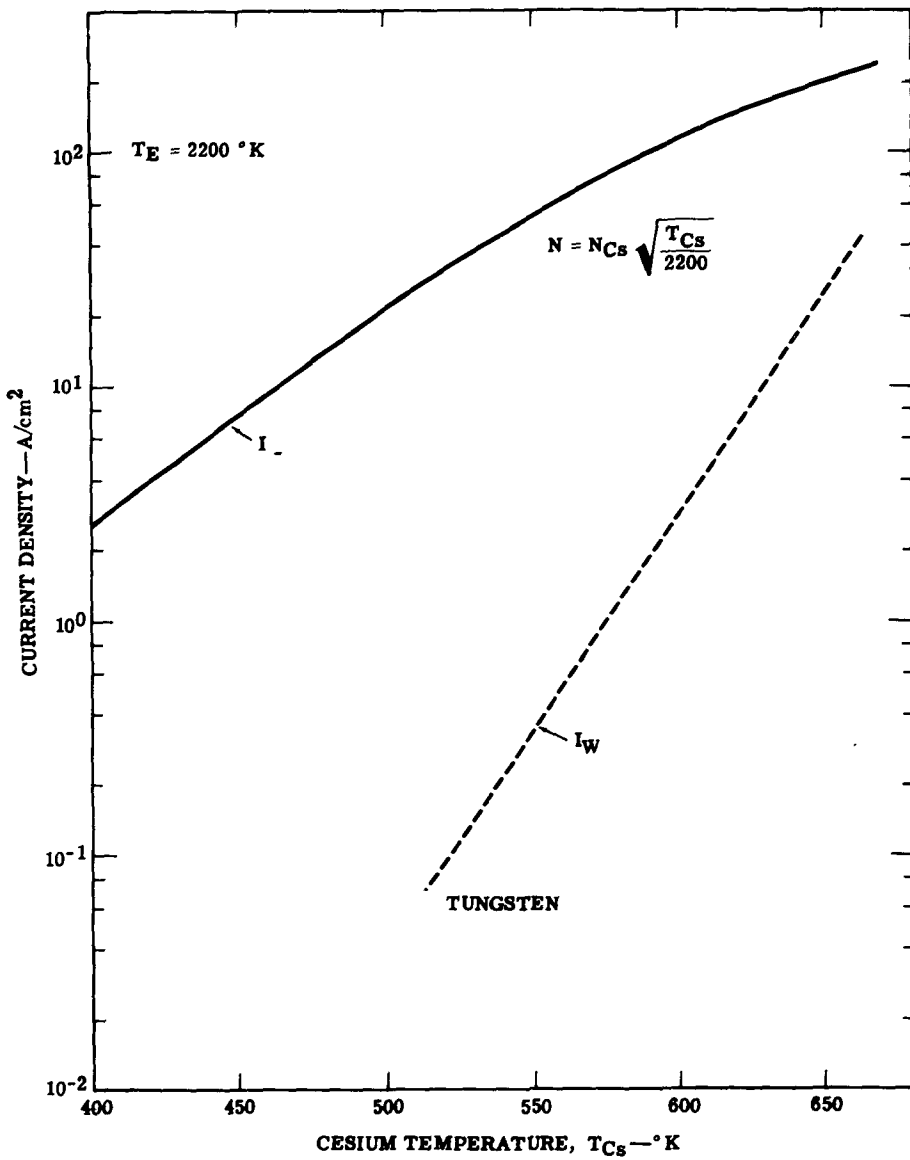


Figure 19. Comparison of Random Current to Saturation Current—2200°K

A recent paper by H. Huber and R. LeBihan gives the basic theory of the capillary emitter as summarized previously— included in this paper is a consideration of the sheath conditions which exist along the capillary.¹⁵ This paper is included as the appendix to this report—in Figure 144 of the appendix, the sheath conditions are shown for the specific conditions of $T_E = 2000^\circ\text{K}$ and $T_{Cs} = 473^\circ\text{K}$. In Figure 145 of the appendix, the three cases of electron-rich, neutral, and ion-rich sheaths are shown for a constant $T_{Cs} = 473^\circ\text{K}$ and emitter temperatures of 1000, 1400, and 2000°K, respectively.

As shown in Figure 143 of the appendix, various relationships between the surface and plasma densities exist, depending on the sheath conditions. For conversion, the case where a strong ion sheath exists along the capillary wall is of practical interest. In this case, J_- is greater than J_{-s} , where J_- is the random current and J_{-s} is the saturation current from the wall. Thus, in order to extract a current from the capillary which approaches the random current value, the total wall current must exceed the random current value. Stated in a different way, the current extracted from a capillary emitter can be no greater than the sum of the emission currents from the walls. For example, Figure 20 shows the random current for $T_{Cs} = 473^\circ\text{K}$ as a function of T_E . Various area ratios are shown; if the area ratio current is greater than the random current, then the random current should be measured. On the other hand, if the area ratio current is less than the random current, then the area ratio current should be measured.

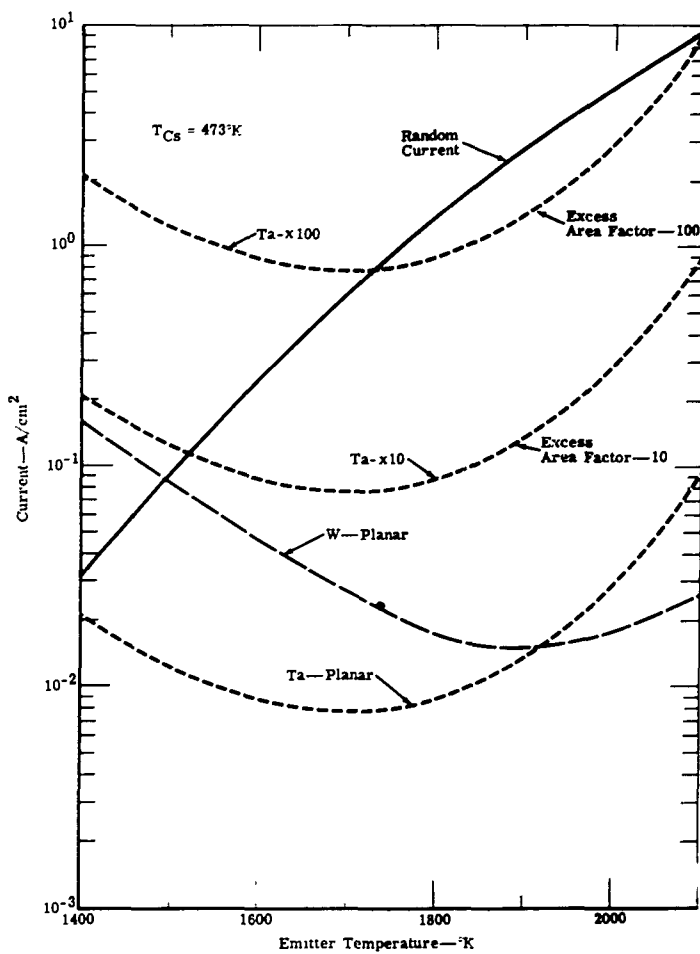


Figure 20. Random Current Model with Various Area Ratio Limits

In a paper by A. L. Eichenbaum and K. G. Hernqvist, a synthesized plasma is defined as one which is produced by the release of positively and negatively charged particles at boundary electrodes.¹⁶ However, as shown from the basic definitions in the appendix, this plasma is governed by the Saha equation. Reference 15 suggests that the mechanism for electron emission from a cylindrical cavity, as in the capillary emitter, is leakage along the axis, but no detailed explanation is given.

To determine the work function of the capillary, the energy of the electron leaving the capillary must be known. With a strong positive sheath at the wall surface, the electron is accelerated through the sheath into the capillary volume; in this process some of the potential energy represented by the surface work function is transformed into kinetic energy. However, this kinetic energy may still be reconverted to potential energy as the electron passes across to the collector, as shown in Figure 21. This appears reasonable because the mean free path is large compared to the capillary dimensions; also, the sheath thickness is small compared to the capillary radius (see Figure 144 in the appendix). Hence, it would appear that, ideally, the work function of a capillary emitter would be equal to the work function of the cesiated wall surface. For the case being considered, the surface work function change should not be very great along the capillary. For example, in Figure 144 of the appendix, the change is from 4.1 ev at the entrance to 4.3 ev at the exit.

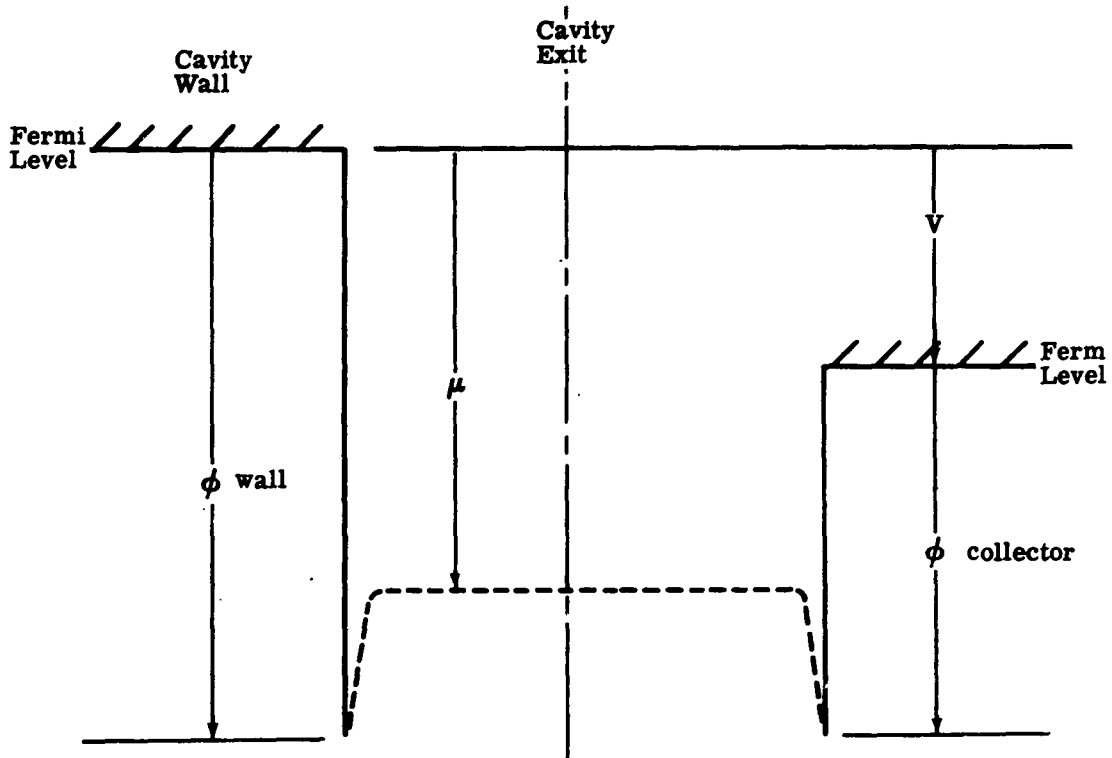


Figure 21. Potential Energy Diagram for Capillary Converter with a High T_E/T_{Cs} Ratio

IV. EXPERIMENTAL DEVICES

At the start of the program it was desired to determine the feasibility of the capillary concept. Therefore, it appeared reasonable to initially study a single capillary with accurately known geometry. A series of six monocapillary experimental devices was thus designed, fabricated, and tested. The experimental results showed improved emission over a conventional emitter. The results justified the realization of a multicapillary device. Nine multicapillary converters (identified as A through I) were designed, fabricated, and tested. The experimental results showed improved performance at wide spacings (Section V). The experimental results from the multicapillary led to the conception of six supplementary converters (1 through 6). The purpose of the supplementary converters was to study the performance of a cavity emitter as compared to a conventional emitter.

MONOCAPILLARY

The monocapillary experimental diode was used to study the feasibility of the capillary concept for thermionic emission. The single capillary was used for ease of fabrication and because it has a well defined geometry. Initially it was designed to be a sealed ceramic-metal device. However, after construction of three devices which failed, a bell jar device was constructed and tested.

Of the six monocapillary diodes fabricated, extensive test data were obtained on two. Diodes 5 and 6 were both operated over 100 hr. The capillary for diode 5 was tantalum and for diode 6 molybdenum.

The design and cause of failure for these diodes are briefly reviewed. Detailed information is presented in Reference 8.

Design

Since no detailed theory was available during the design activity to guide the selection of the capillary diameter, the diameter was chosen based on the current predicted by the Knudsen flow equation. To accurately measure ion current (tens of microamperes) as predicted by the Knudsen equation, the capillary diameter should be 0.4 mm. Thus, the following capillary geometry was selected:

- Diameter—0.4 mm
- Length—10.0 mm

A tantalum capillary (ID of 0.4 mm) was selected for the first device.

In designing the test device, a major concern was the measurement of ion and electron currents and neutral cesium flow. The design selected was a collector of the same diameter as the capillary. A guard ring was located at the collector to eliminate the influence of ion or electron emission from the capillary support. Electron and ion emission from the capillary could be measured. Neutral flow was determined as predicted by the Knudsen flow. Figure 22 is a sketch of the monocapillary. This design was of complete metal-ceramic construction. Figure 23 is an assembly layout of the first diode.

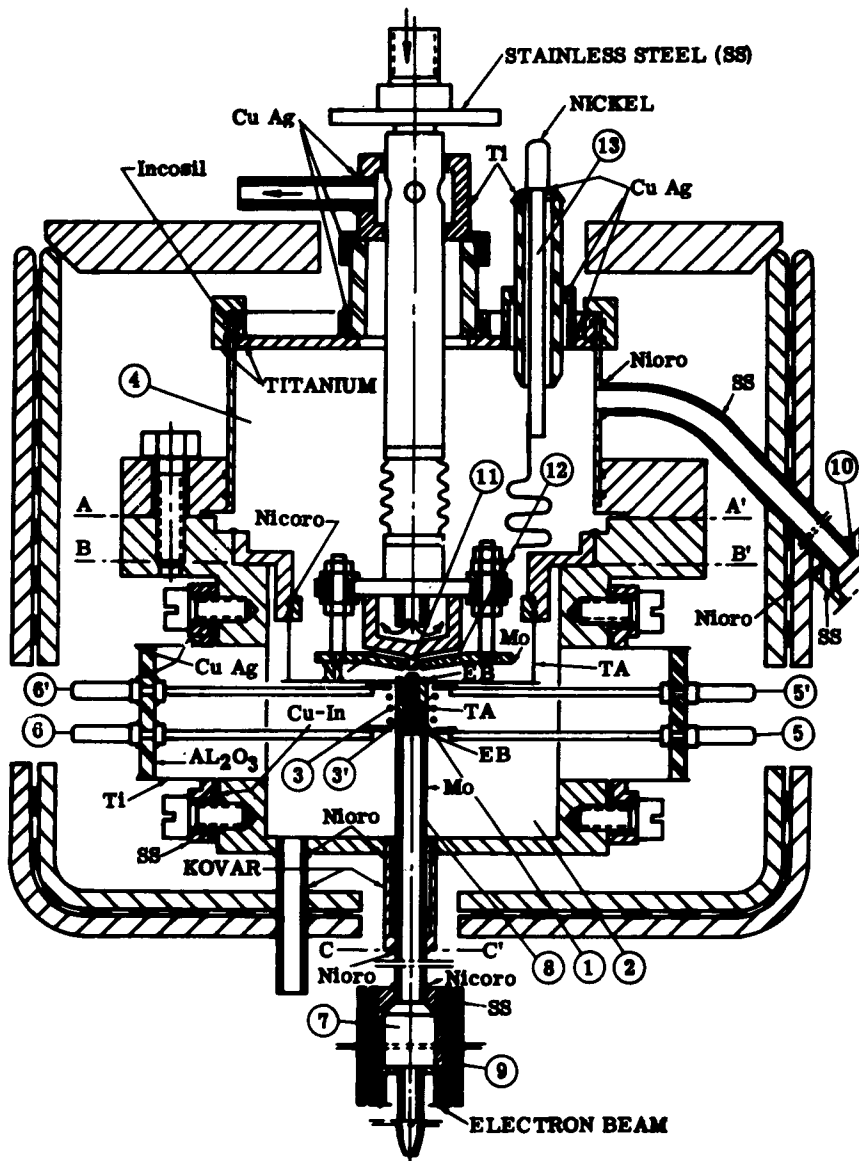


Figure 22. Sketch of Monocapillary

Component Development

Capillary Emitter

Initial tests on heating the capillary tubing by electron beam bombardment showed that the capillary became distorted and the temperature was not uniform. The structure was redesigned with a tantalum tube inserted into a large-diameter molybdenum cylinder.

Figure 24 shows the final heater design. The variation in temperature along the capillary was within the limit of error of the optical pyrometer ($\pm 5^{\circ}\text{K}$). A dimensional sketch of the capillary structure is shown in Figure 25.

Collector Assembly

The collector was nickel and the guard ring molybdenum. A detailed sketch of the collector structure is shown in Figure 26. The spacing between the collector and the capillary is adjustable from 0 to 1.0 mm. A heater and cooling duct are included to control the collector temperature.

Operation and Failure Analysis

Diode 1

Leaks appeared along the lead-in tube to the capillary and the capillary structure itself after several heating cycles. The cause for the leaks was that the standard sintered molybdenum contained gas pockets aligned in the melting zone of the electron beam weld. Vacuum tightness could not be maintained at high temperature.

Diode 2

This diode was fabricated before the failure analysis of Diode 1 was completed. The cause of failure was the same as for Diode 1. A metallurgical study was made to determine the welding characteristics of molybdenum in the following states: sintered, arc-melted, and arc-melted with 0.5% titanium added. Microphotographs of argon-arc and electron bombardment welds for arc-melted molybdenum showed no gas pockets. However, the grain growth was very pronounced. With titanium added as an oxidizing agent, grain growth was suppressed.

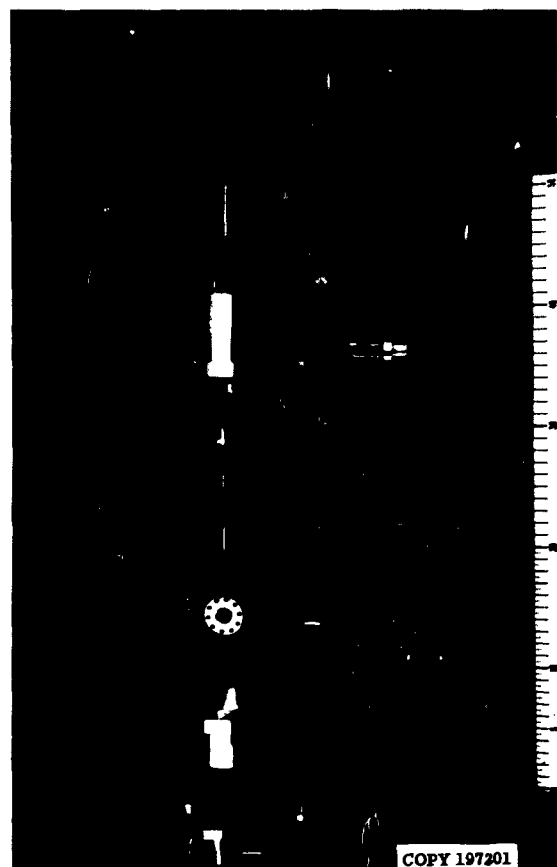


Figure 23. Assembled Layout of First Diode

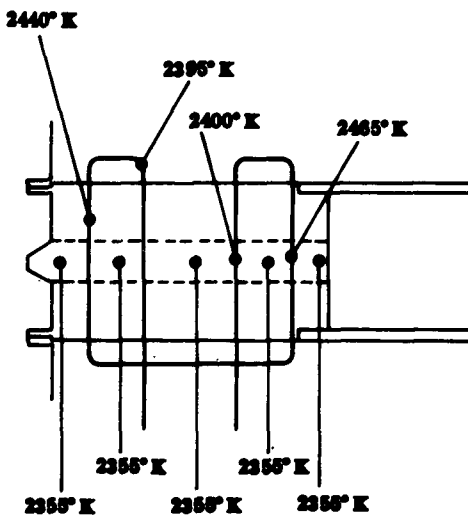


Figure 24. Final Heater Design

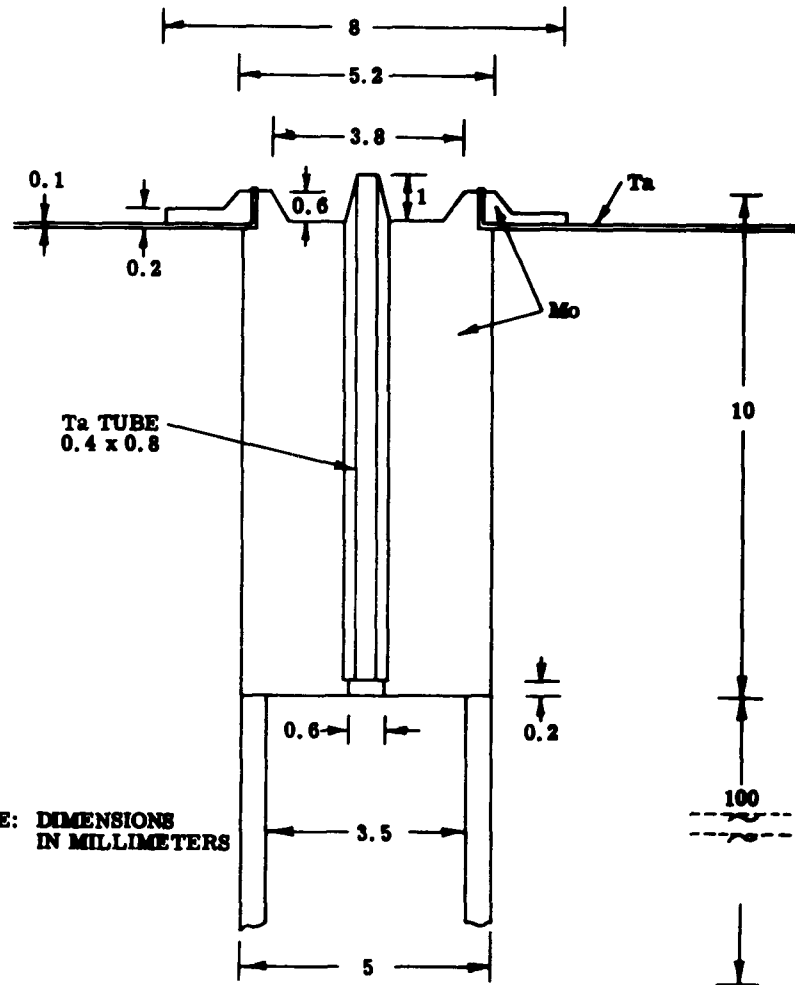


Figure 25. Enlarged Sketch of Capillary Structure

Diode 3

During final sealing of the cesium reservoir by electron bombardment, the cesium capsule opened and the cesium filled the bell jar. At this point it was decided to modify the design. Instead of attempting to fabricate a sealed diode, it was decided to put the diode in a bell jar. With this approach, emission data could be obtained even with a leak in the diode structure. A sketch of the bell jar diode is shown in Figure 27.

Diode 4

After about 8 hr of operation, this diode failed. When the diode was opened, it was found that a deposit on the collector had plugged the capillary. A spectrographic analysis showed the deposit to be mostly Au with some Ta and Sn. The testing was done at T_E greater than 2100°K with T_{Cs} from 473 to 603°K. It appeared that the microbrazing joining the cesium reservoir to the lead-in tube had been attacked by cesium.

The capillary and lead-in tube were made from a single piece of vacuum arc-melted molybdenum. No leaks appeared in the structure.

Diode 5

This diode operated for approximately 100 hr. Test data were obtained over a range of T_E from 1000 to 2100°K with T_{Cs} from 300 to 650°K. The capillary and lead-in tube were made from a single piece of tantalum. There was no evidence of a deposit on the collector as had been observed with Diode 4.

Diode 6

This diode had a capillary support and lead-in structure made from a single piece of vacuum arc-melted molybdenum with 0.5% titanium and 0.1% zirconium added. The molybdenum capillary had the same dimensions as the tantalum capillary (ID of 0.4 mm and length of 10 mm). Over 100 hr of test data were obtained before opening for inspection. Careful examination of the parts revealed no deleterious effects.

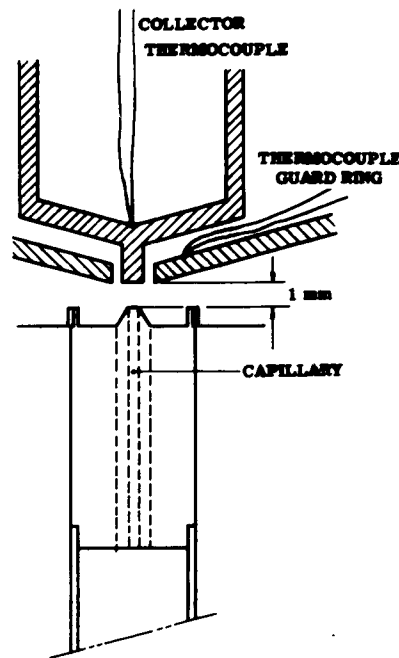


Figure 26. Capillary Emitter, Guard Ring, and Collector Arrangement

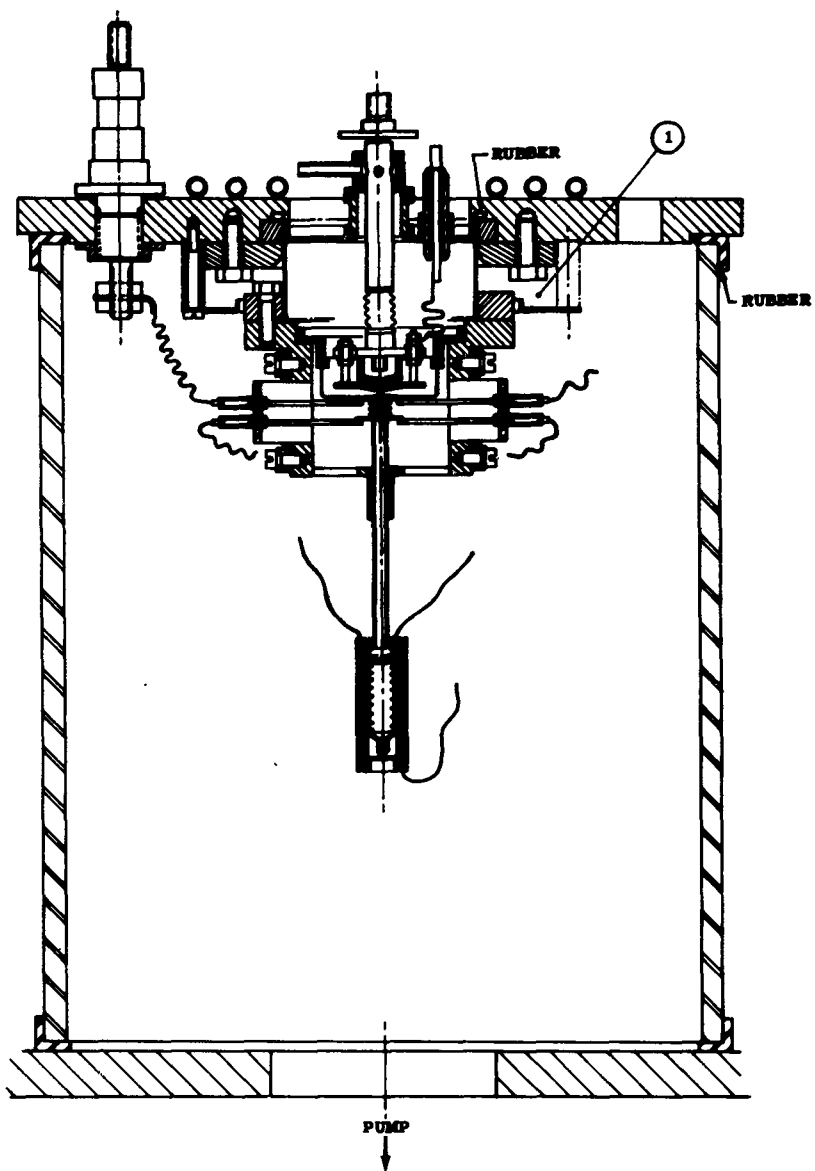


Figure 27. Sketch of Bell Jar Arrangement

MULTICAPILLARY

The experimental data obtained from the tantalum monocapillary indicated an increase of a factor of 10 in current density over a plane tantalum surface. Also, there was a marked decrease in sensitivity to interelectrode spacing as compared to a conventional device. The test results were sufficiently promising to warrant the design and fabrication of a multicapillary device.

A series of nine multicapillary converters was built and tested. A detailed description of the converters is presented in Reference 11, 12, 13, and 17. Over 930 hr of test data were obtained from these converters. In particular, over 540 hr of testing was accomplished on Converters C and G. Converter C had a tantalum emitter and Converter G a tungsten emitter. During activation, one of the filaments for bombardment heating failed in Converter C which limited the maximum emitter temperature to 1750°K. However, extensive data were obtained on Converter G up to temperatures of 2100°K. A brief summary of the objectives and design approach follows. Converter H is not discussed because it was used only for temperature studies.

Converter A

The design and fabrication of this converter are described in Reference 11. The emitter was made by stacking alternately corrugated and flat 16-micron thick tantalum foils as shown in Figure 28. The emitter diameter is 6.2 mm, the front surface area 0.3 cm^2 , and the length 1 cm. There were 317 capillaries, each with an equivalent circular diameter of 0.35 mm.

The spacing between the emitter and collector was fixed at 1.0 mm. During operation the spacing was observed to be changing. After 35 hr of operation the emitter shorted to the collector.

The capillary design for this converter seemed satisfactory.

Converter B

The basic design for Converter B was the same as for A with the exception of providing for adjustable spacing between the emitter and collector. The spacing was adjustable between 0.5 and 2.0 mm. A tungsten shorting pin mounted in the collector provided a stop at 0.5 mm. The design of the electrode arrangement is shown in Figure 2. A view of the emitter and collector surfaces is shown in Figure 29. The shorting pin is missing.

In Converter B there were 288 capillaries with a front surface area of 0.302 cm^2 .

The converter failed after 8 hr of operation. The glass-to-kovar seal between the converter and vacuum system failed with the emitter heated.

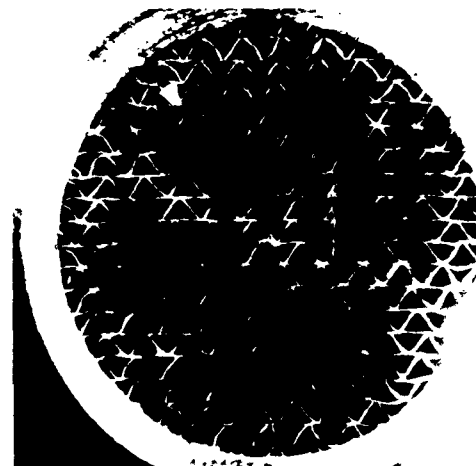


Figure 28. Multicapillary Emitter Structure



Figure 29. Photographs of Emitter on Collector Surface

Converters C and E

The stress between the glass-to-kovar seals was eliminated by inserting metal bellows. The basic design for C was the same as for B. A sketch of Converter C is shown in Figure 30. A tantalum membrane separates the electrode chamber with the cesium from the electron bombardment heating chamber. The capillary side wall was heated by electron beam bombardment. Various filament geometries were studied to obtain a uniform temperature distribution across the capillary exit. The final design with the resultant temperature distribution is shown in Figure 31.

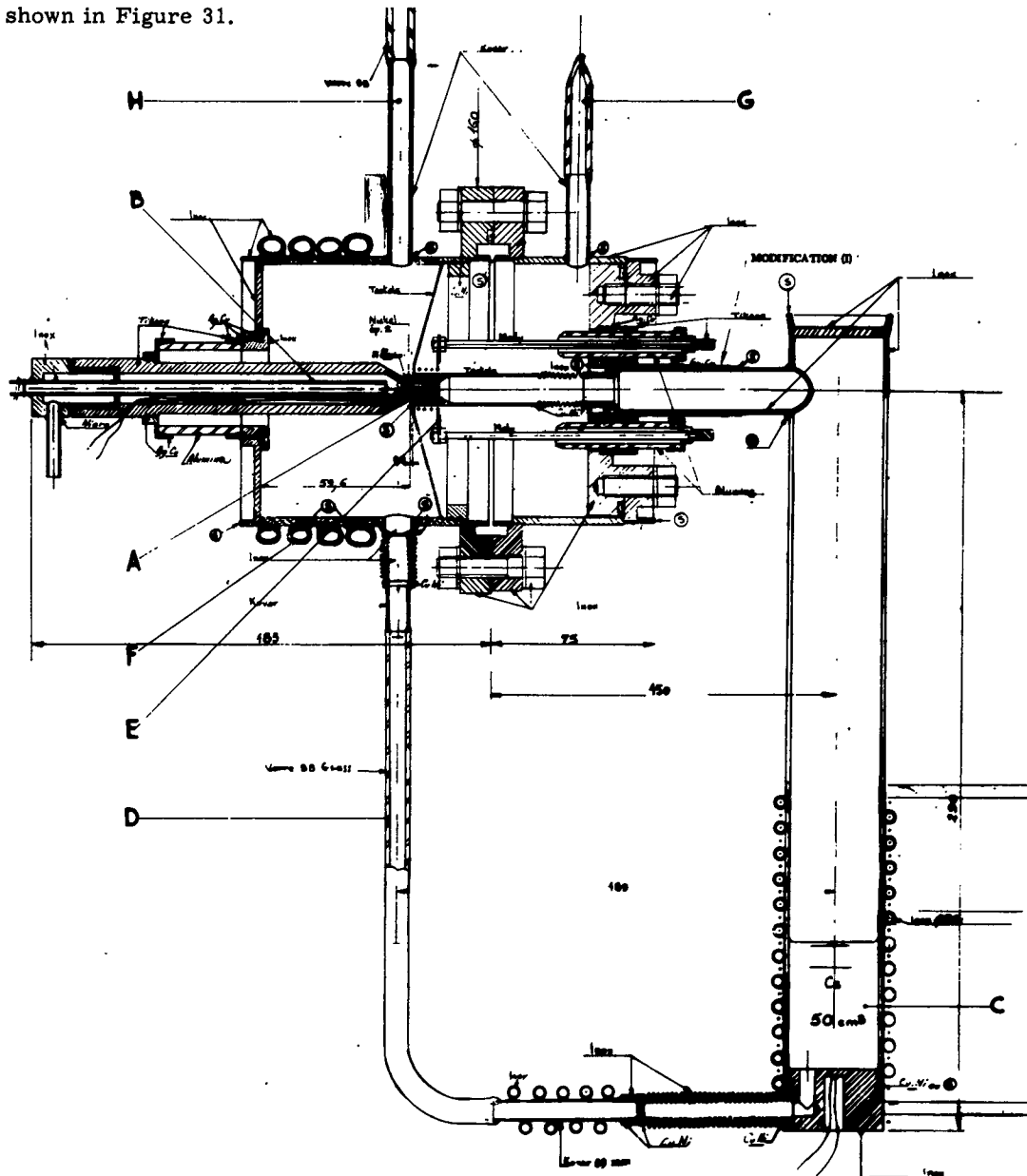


Figure 30. Layout Diagram of Converter C

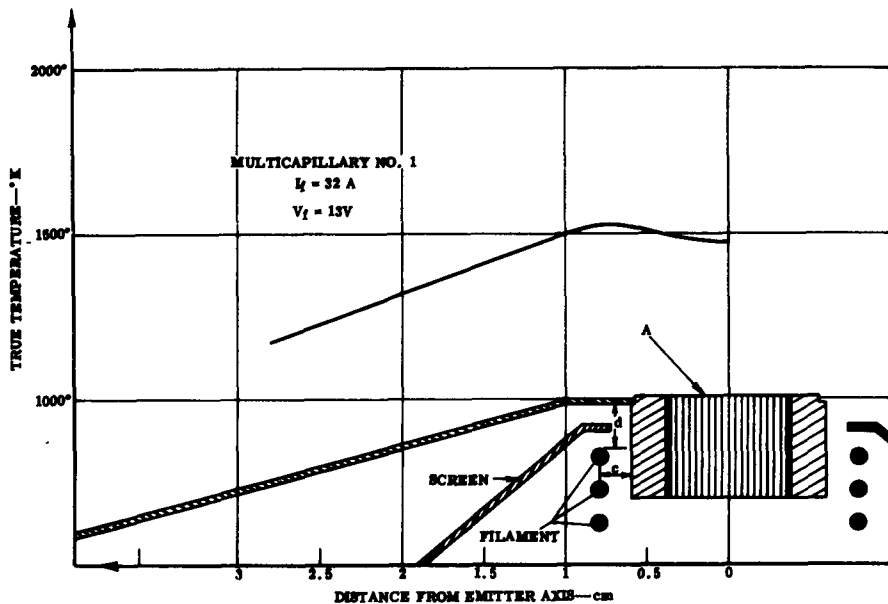


Figure 31. Temperature Distribution with Final Heating Design

During the activation of Converter C, one of the two filaments supplying bombardment current shorted to the emitter. The emitter had to be heated with one filament, resulting in a temperature gradient across the capillary exit. The capillary structure could be viewed through a sapphire window at an angle of approximately 80 degrees. The temperature was measured with an optical pyrometer. The true temperature was determined by assuming the emissivity of tantalum ($\epsilon_\lambda = 0.43$) and a 2% correction for the sapphire window. A careful emitter temperature study was made with a special test structure to determine the effect of heating with one filament. A tantalum emitter structure was modified by inserting a Pt/Pt-10% Rh thermocouple in the center capillary and three gold wires and two nickel wires in capillaries near the center. The melting points of the gold and nickel-tantalum eutectic wires were used to calibrate the thermocouples. The results of this study are summarized as follows.

- The true temperature may be obtained by correcting the brightness temperature for an emissivity $\epsilon_\lambda = 0.95$ and adding 2% for absorption through the sapphire window.
- The temperature gradient from the center to the edge of the emitter surface may be 70 to 160°C, depending on the absolute temperature.

Converter C was operated for 240 hr and extensive data were obtained at emitter temperatures up to 1750°K. The converter failed when the filament became shorted to the emitter.

Converter E was exactly the same as Converter C in design. The converter was tested for 80 hr. Early leaks in the membrane allowed cesium in the bombardment chamber and limited the emitter temperature to 1700°K. The converter failed due to an open filament.

Converters D and F

Because of the difficulty with Converter E due to a membrane leak, Converters D and F were designed with one chamber. The tantalum membrane was eliminated. It was anticipated that the wall temperature of the converter could be maintained low enough to keep the cesium pressure low. However, during operation the data obtained were questionable. The chamber pressure was too high. Figure 32 shows a layout diagram of Converter D.

Converter G

The basic design of Converter G was similar to that of Converter C with the exception that the emitter was of tungsten. Over 300 hr of test data were obtained. Extensive data were taken up to temperatures of 2100°K. The emitter area was 0.32 cm².

The tube failed when the tantalum tube joining the capillary was melted, fusing closed the capillary entrance. It appears that a small leak developed in the electron beam weld resulting in an arc discharge. Parts from Converter G are shown in Figure 33. In the close-up of the capillary shown in Figure 34, the capillary structure appears to be in good condition.

Converter I

This converter was conceived to evaluate the dispenser type of capillary emitter. Figure 35 shows a sketch of the emitter and mounting structure. A tungsten disk (2 mm thick) with a porosity of 23% was used. Test data were obtained up to 1600°K with cesium temperatures to 673°K.

SUPPLEMENTARY CONVERTERS

Results obtained on the multicapillary test devices indicated that there might not be an advantage in circulating cesium through the emitter. In fact, the measurements made on the test devices with spacings less than 0.8 mm were actually evaluating a form of a hollow cathode emitter. A supplementary program was initiated to evaluate experimentally the hollow cathode concept. To accomplish this objective it was first necessary to design and fabricate a baseline planar geometry device. The base line devices (Converters 1 through 4) were used to evaluate the design concept. Converters 5 and 6 were similar in design to Converter 4 with the exception that a slotted hollow cathode emitter was used.

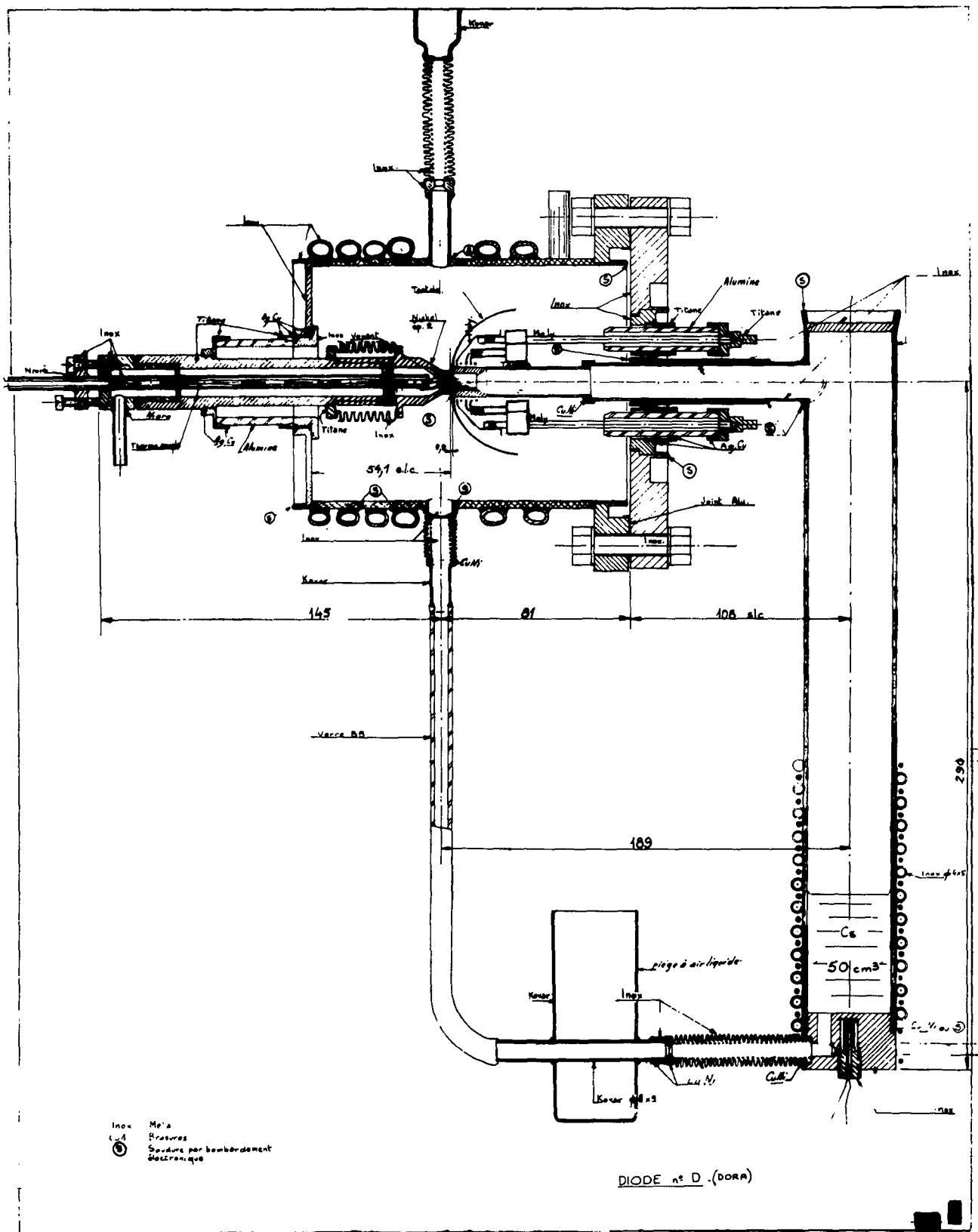
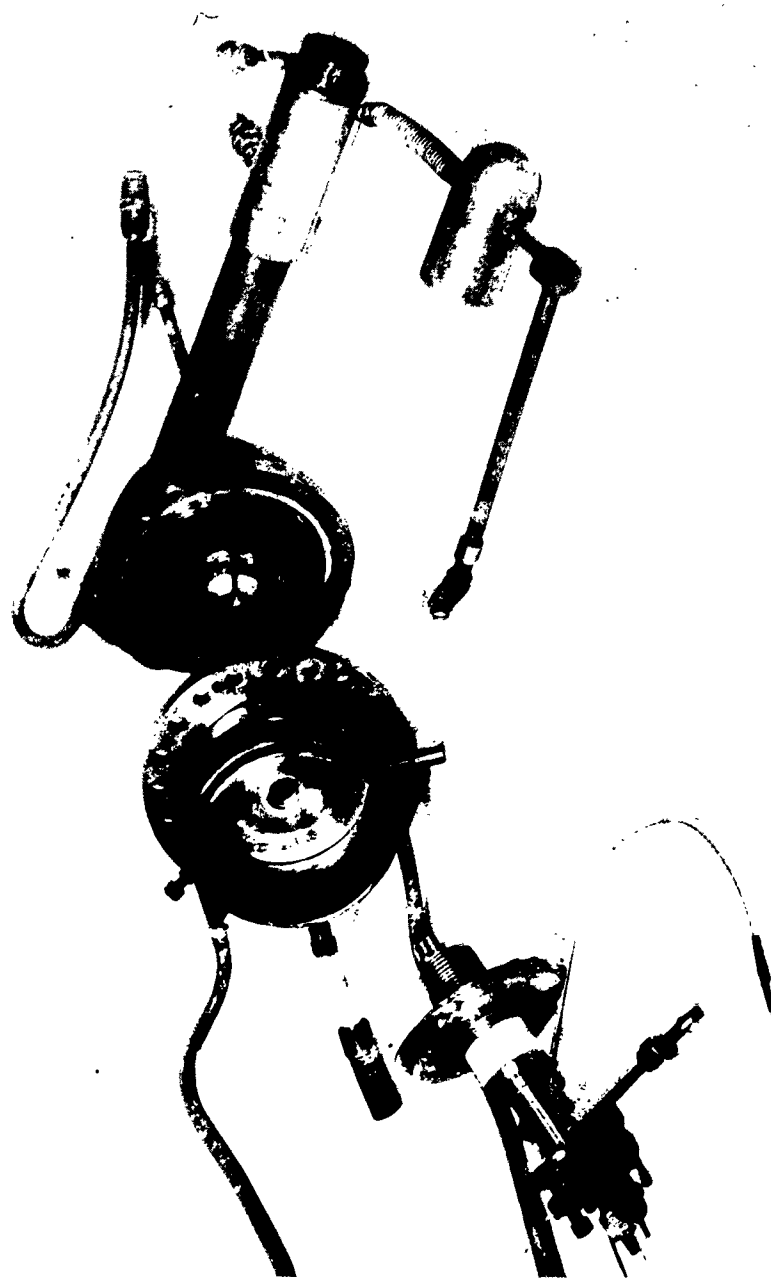


Figure 32. Layout Diagram of Converter D

Figure 33. Parts from Converter G



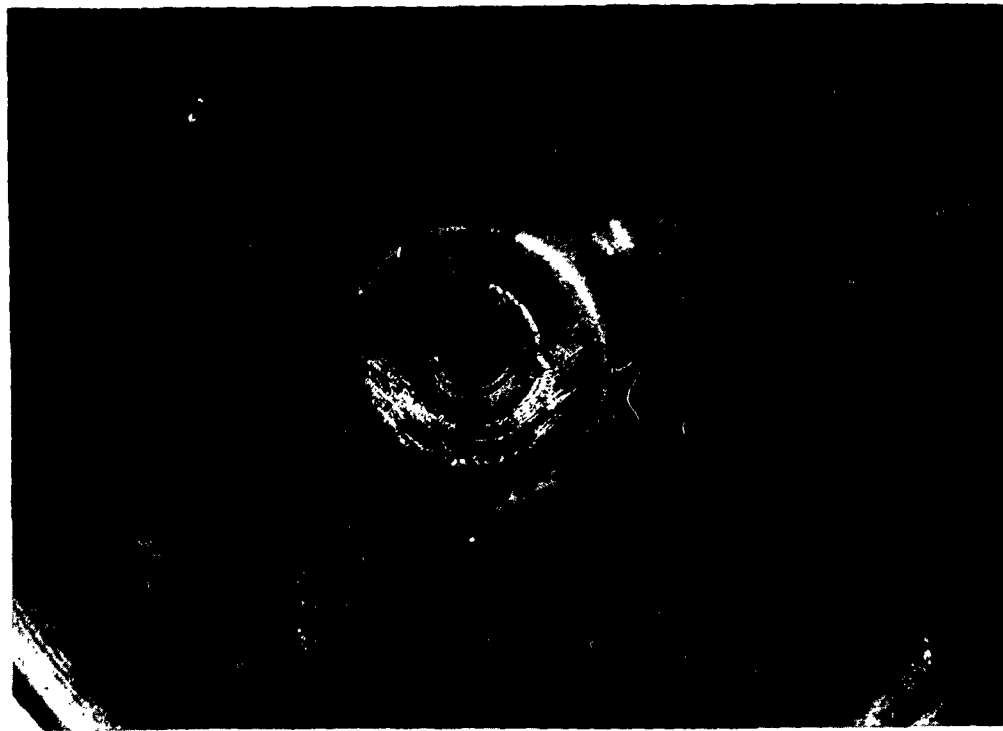


Figure 34. Emitter Surface of Converter G

Converters 1 and 2

Converter 1 was designed and fabricated for the primary purpose of exposing the general mechanical and thermal problems associated with a relatively large planar geometry converter. A sketch of the device is shown in Figure 36, and a picture is shown in Figure 37. The concentric cup geometry was selected since this geometry is commonly used for solar heated devices. Initially, considerable data were taken at 1800°K. Then, the converter was used to obtain a set of data for comparison with Converter G with the same T_E/T_{Cs} combinations. After over 200 hr of testing, the converter was still operable even though Ag-Cu brazes were used.

Converter 2 was designed to investigate the mechanical and thermal problems involved when the inverted cup design is introduced (Figure 38). This device was operated for 80 hr when a seal failure occurred. The failure was traced to an excessive temperature at the emitter base caused by the method of bombardment heating used. This problem has been eliminated in subsequent designs.

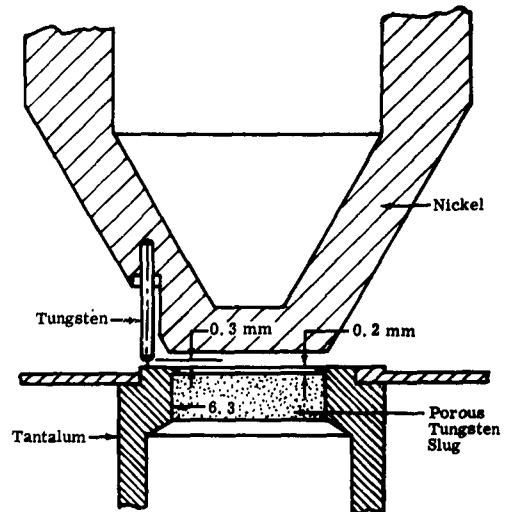


Figure 35. Sketch of Converter I

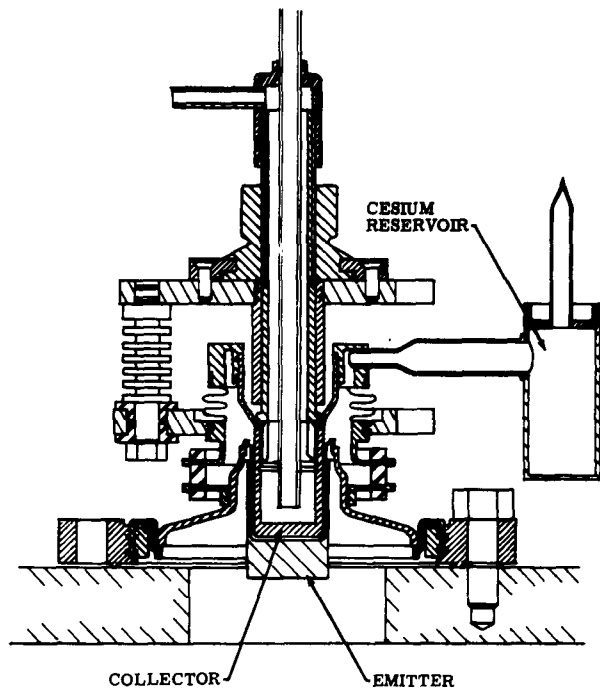


Figure 36. Sketch of Converter 1

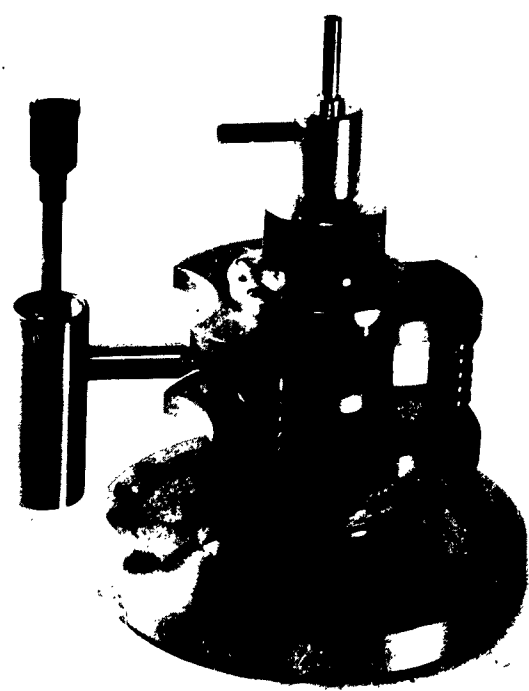


Figure 37. Picture of Converter 1

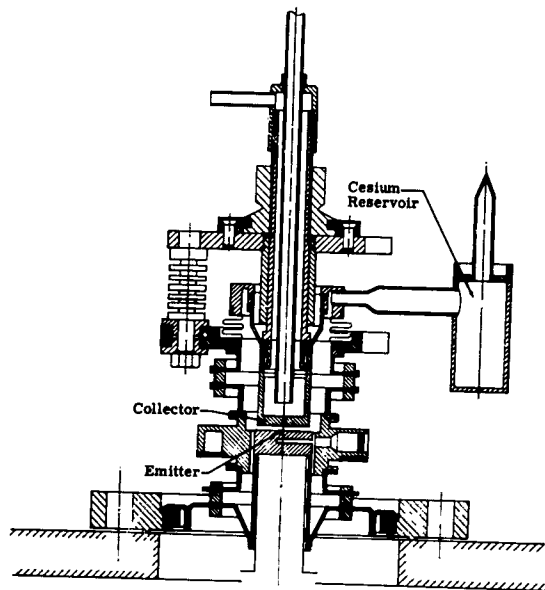


Figure 38. Sketch of Converter 2

Converters 3 and 4

Converters 3 and 4 were conceived as baseline devices. The objective was to establish a design which would give valid data for a conventional planar geometry. The results from these converters could then be used for comparison to the experimental results from a cavity emitter of the same basic design. Thus, a sound experimental basis was provided for evaluation of the hollow cathode emitter.

Design

A sketch of Converters 3 and 4 is shown in Figure 39. Tantalum was used for the emitter and molybdenum for the collector in Converter 3. Molybdenum was used for both the emitter and collector in Converter 4. A guard ring structure was included to eliminate side emission from the emitter. The guard ring is insulated from the emitter and collector. This arrangement is sufficient for measuring electron saturation currents accurately over the desired operating range. However, it is not sufficient for measuring ion currents accurately when an ion-rich condition exists at the emitter surface. For an ion-rich condition, a large accelerating potential must be applied to the collector to eliminate space charge effects. To measure ion currents accurately it is necessary to have a double guard ring with three insulators similar to the design of the NASA diode as reported by Breitwieser.²⁰ For purposes of comparison of a conventional device to the hollow cathode, the primary interest is in measurements of electron saturation current. Therefore, the design of Converters 3 and 4 is satisfactory. This statement is made on the basis of the experimental results. The data from Converter 4 were analyzed by comparison of the measured work function, at different emitter and cesium temperatures, to the work function predicted for molybdenum from Nottingham's extrapolation of Houston's data.²¹ The results were in good agreement.

According to the theory, the hollow cathode emitter geometry is potentially useful in the temperature range from 1800 to 2200°K, not in the range from 1400 to 1800°K. In the fabrication of converters 3 through 6, a Ag-Cu braze was used. This limited the emitter temperature to a maximum of 1700°K. If results were encouraging at these low temperatures, further study in devices with Cu-Ni brazes would be justified. To obtain valid experimental data, the temperature distribution across the face of the emitter should not vary over 10°C. Various gun geometries and arrangements were studied for maintaining a uniform surface temperature. The temperature distribution over the emitter surface and along the support wall is shown in Figure 40. To measure the emitter temperature, blackbody holes were drilled at different locations in the emitter structure (Figure 41). In addition, Pt/Pt + 10% Rh and IC thermocouples were located along the wall structure. The distance between the emitter and the cathode of the gun was optimized at 16 mm. This distance provided for the optimum beam dispersion to heat the emitter uniformly. A radiation shield was included on the inside of the emitter structure but isolated from the emitter. The temperature was observed across the front surface of the emitter and at the blackbody cavities on the sides and back of the emitter. Agreement was obtained within 10°C with an optical pyrometer.

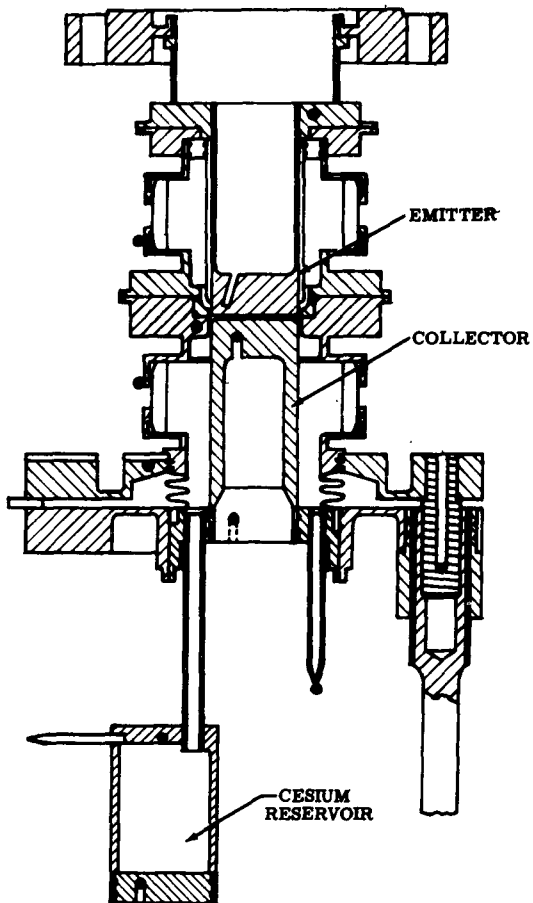


Figure 39. Sketch of Converters 3 and 4

The spacing between the emitter and collector was controlled by three differential screws which engaged to one common gear. Each tooth on the common gear corresponds to 4 microns. The spacing can be adjusted between 0.3 and 2.0 mm.

Summary on Converter 3

Converter 3 was beneficial in evaluating design concepts for a baseline converter. These included EB gun design, spacing adjustment, temperature distribution, and general design parameters. The experimental results from Converter 3 were questionable. During the activation two accidents occurred. A leak developed during bakeout and a leak developed in the EB welding of the stainless steel tubing. The leak during bakeout with the emitter heated may have resulted in oxidation of the emitter surface. The leak was fixed and bakeout repeated. The EB weld was done inside a bell jar. The pressure in the bell jar was about 1×10^{-5} torr. This means that the pressure inside the diode was 1×10^{-5} torr. The measured saturation currents were too high as might be expected if the emitter was oxidized.

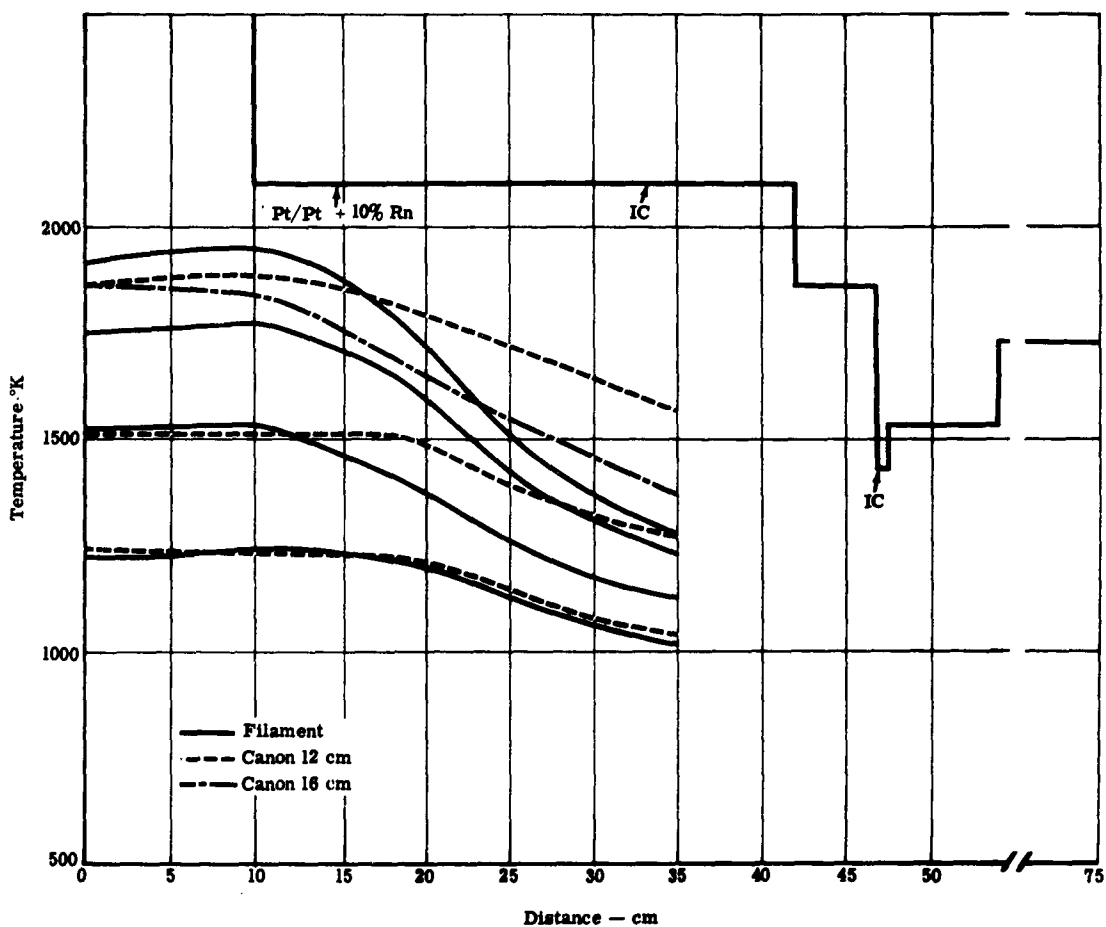


Figure 40. Temperature Distribution Along Emitter Structure

Summary on Converter 4

There were no accidents during the activation of Converter 4. This device had a molybdenum emitter and collector. The emitter area was 3.14 cm^2 .

The converter has been tested for 60 hr to date. The experimental results show that the measured work function is in good agreement with the expected work function for molybdenum as obtained from Houston's data.²¹ Thus, the results show that this device fits the expected results for a planar geometry in a cesiated atmosphere and can be used for comparison with the cavity emitter.

Converters 5 and 6

The design for Converters 5 and 6 is the same as for Converter 4 with the exception of the emitters, which are hollow cathode, cavity-type emitters. The objective is to evaluate the cavity emitter concept.

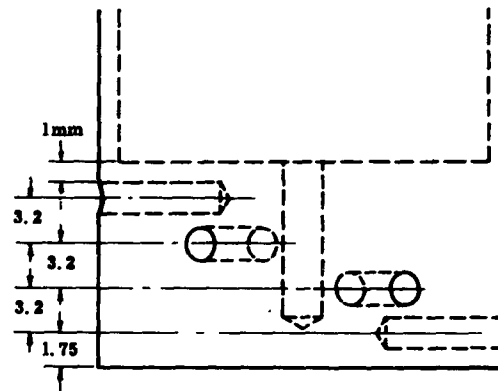
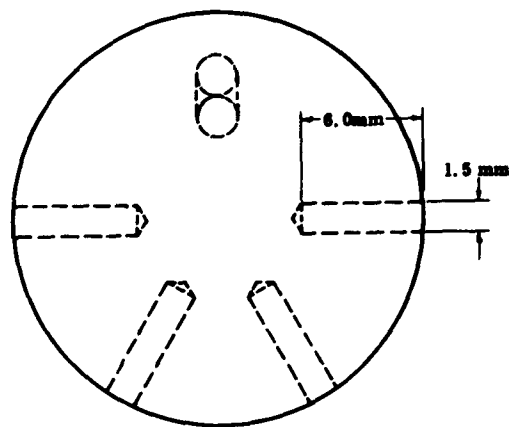


Figure 41. Sketch Showing Blackbody Holes for Temperature Study

A picture of the emitter being studied is shown in Figure 42. The material is tantalum.



Figure 42. Picture of Excess Area Emitter

V. TESTING AND ANALYSES OF RESULTS

SUMMARY OF TESTING

Monocapillary

Several monocapillary devices were tested with varying degrees of success.⁸ Table 2 summarizes the pertinent information. The test circuit used is shown in Figure 43. Data were taken from an ammeter and voltmeter, point by point, and plotted to determine the current-voltage characteristic curve.

TABLE 2 Summary of Tests on Monocapillary Devices				
<u>Test Starting Date</u>	<u>Device No.</u>	<u>Duration of Test (hr)</u>	<u>Emitter Material</u>	<u>Comments</u>
22 Oct 61	2	10	Ta	Operated with water-cooled electron bombardment section; leaks made the data unreliable; sealed tube design
8 Nov 61	4	8	Ta	Operated satisfactorily until capillary closed due to gold build-up on collector; bell jar design
17 Nov 61	5	100	Ta	Satisfactory operation
5 Jan 62	6	100	Mo	Satisfactory operation

Multicapillary

Several multicapillary converters were tested. Table 3 summarizes the pertinent information. The converter measurement circuit is shown in Figure 44. The test arrangement for Converter C is shown in Figure 45. Details of the testing procedure are given in References 12, 13, and 17.

ANALYSES OF RESULTS

Monocapillary

Experimental data were taken for various combinations of T_E , T_{Cs} , and d . A typical data curve is shown in Figure 46. The open circuit voltage was taken as the reference point for measurement of electron and ion currents. As seen in Figure 46, the ion current was determined at -3 volts and the electron current at +3 volts from the reference point.

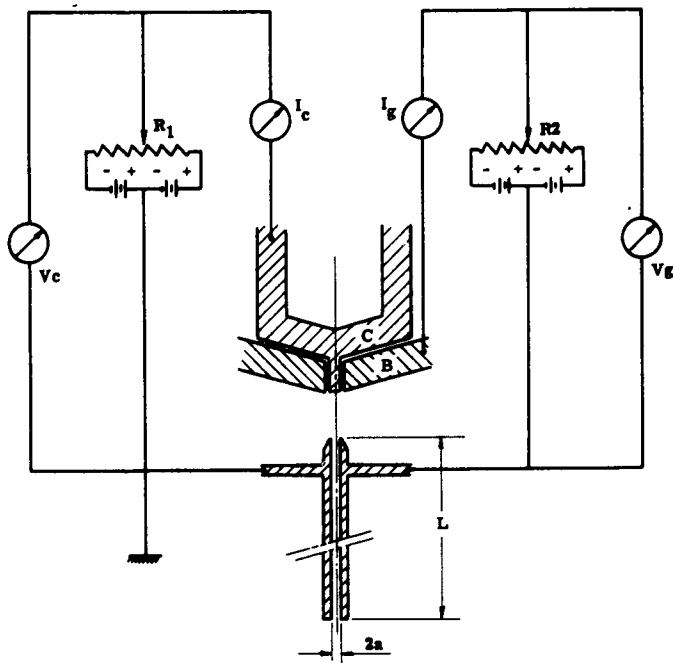


Figure 43. Test Circuit for Monocapillary Measurements

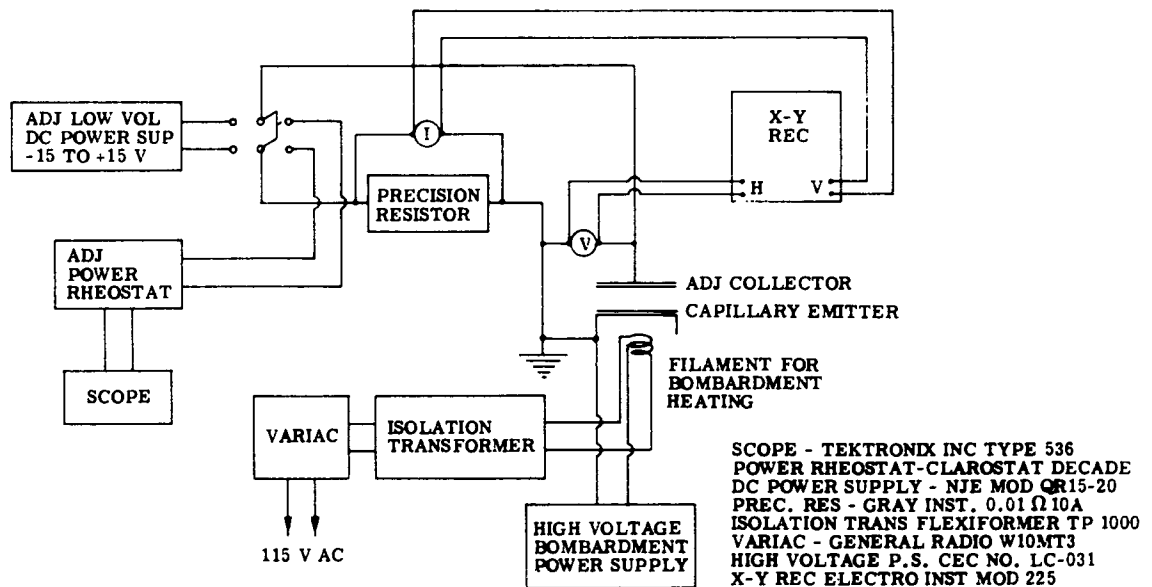


Figure 44. Test Circuit for Multicapillary Measurements



Figure 45. Test Arrangement for Converter C

The monocapillary geometry presents some serious difficulties with respect to accurate measurement of emission currents because the currents are quite small and the capillary cross-sectional area is small compared to the surrounding areas. An enlarged (100X scale) drawing of the emitter-collector geometry of the capillary is shown in Figure 47. Note that the frustum area is more than 10 times greater than the capillary cross section.

Electron and ion currents were compared with various models of the monocapillary with limited success. Since the random current model was not formulated until several months after completion of the monocapillary testing, no attempt has been made to compare the data with this model. Generally, the data from the monocapillary devices were somewhat inconsistent and difficult to organize in a completely coherent manner. Details are given in Reference 8.

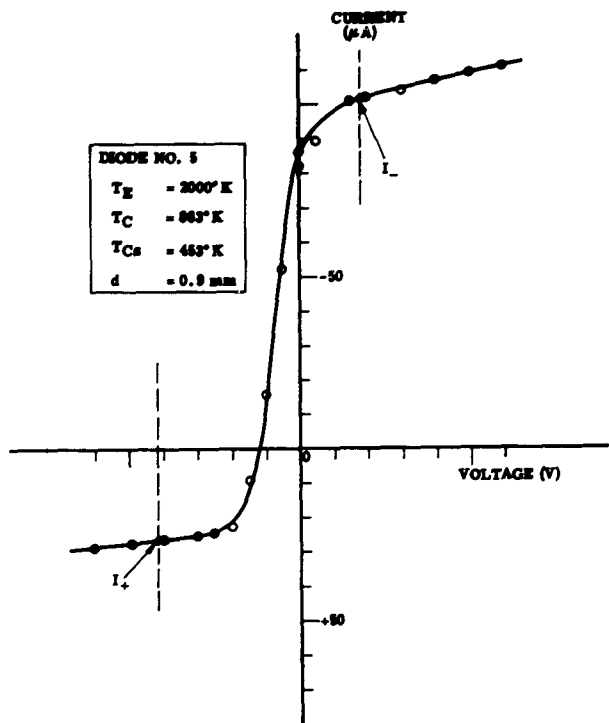


Figure 46. Typical I-V Curve from Monocapillary Device

TABLE 3
Summary of Tests on Multicapillary Converters

Test Starting Date	Converter	Duration (hr)	Emitter Material	Comments
25 May 62	A	35	Ta	Data taken at 1800°K with small amount at 2000°K. Failure due to emitter short to collector.
16 June 62	B	8	Ta	Data taken at 1800°K for cesium temperatures of 623 and 653°K. Failure in connections to vacuum system.
30 Sept 62	C	240	Ta	Extensive data taken up to 1750°K. Failure due to filament short.
14 Dec 62	D	30	W	Open chamber design. Failure due to high pressure in chamber.
6 Dec 62	E	80	Ta	Data taken up to 1700°K. Failure due to open filament.
8 Oct 62	F	137	W	Open chamber design. Data questionable because of high chamber pressure.
1 Mar 63	G	300	W	Extensive data taken up to 2100°K. Failure due to leak in capillary support tube.
1 Oct 63	H		Ta	Not a complete converter--emitter structure for temperature study.
1 May 63	I	100	Porous W	Data taken up to 1600°K and 673°K cesium temperature.
Total		930 hr		

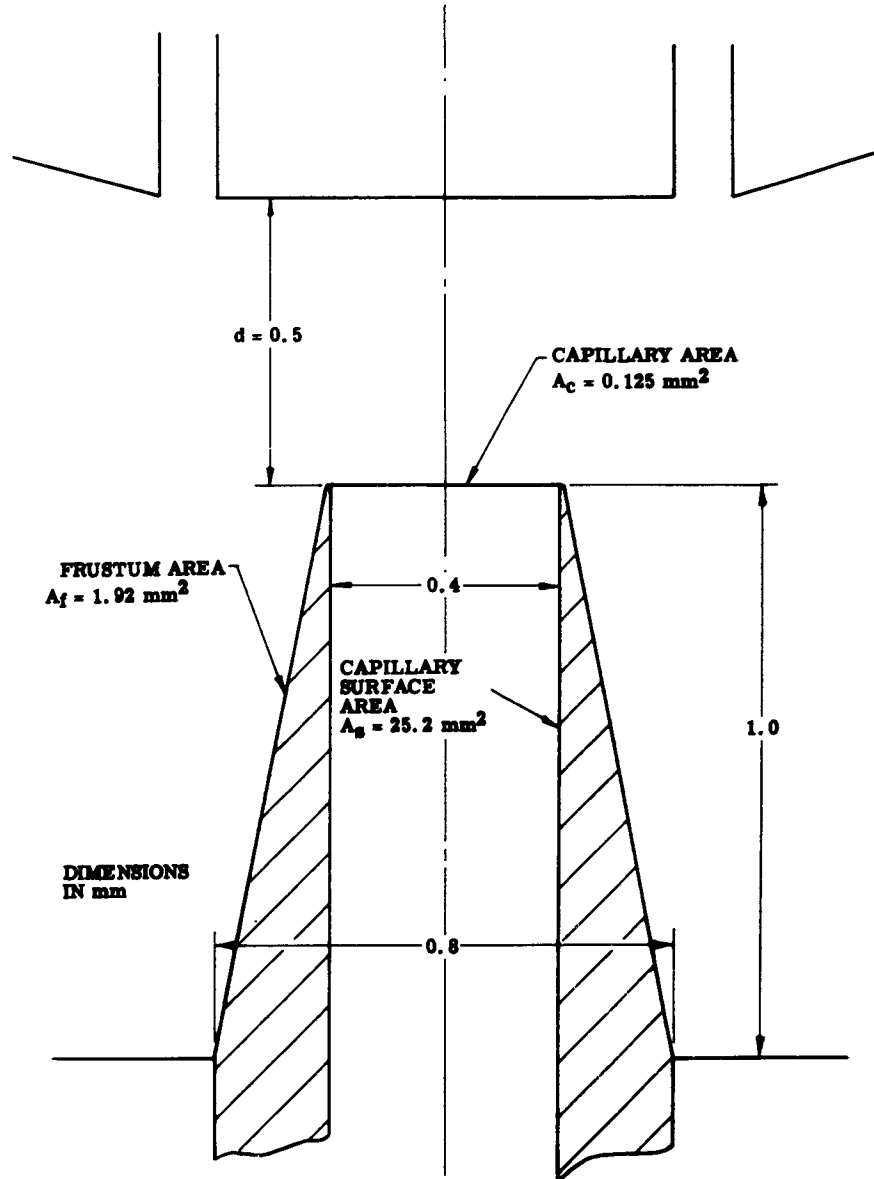


Figure 47. Pertinent Areas in the Monocapillary Geometry

However, the text data indicated that under certain conditions of T_E and T_{Cs} , the electron emission measured from the monocapillary was much greater than predicted from the equivalent cesiated planar surface. Figure 48 shows the results for tantalum. The results for molybdenum were not as good.

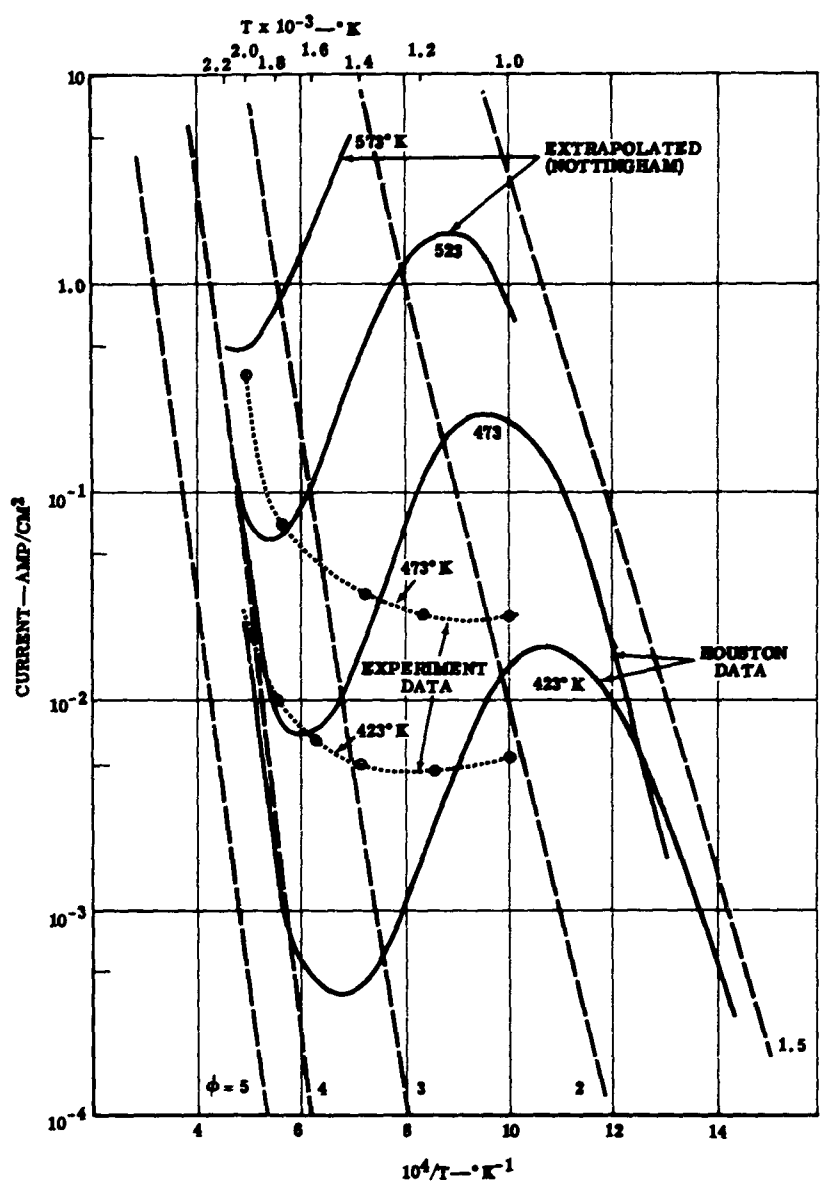


Figure 48. Comparison of the Monocapillary Data with the Houston Data for Tantalum

Multicapillary

The multicapillary converter offered a better opportunity to measure accurately the electron and ion currents from a capillary emitter because there were now approximately 320 capillaries instead of just one as in the monocapillary device. Data were taken for the following ranges of parameters:

- T_E —1400 to 2100°K
- T_{Cs} —423 to 673°K
- d —0.3 to 2.0 mm

Several types of data were taken. First, of most immediate interest and practical importance, were the measurements of maximum power. Second, electron current measurements were compared with the random current theory. Third, ion current measurements were made to compare with theories of the capillary—the effect of collector temperature on ion current was of particular interest. Fourth, high frequency oscillations were observed and studied because such data can give qualitative information on the type of emitter sheath and the nature of the potential distribution within the interelectrode space. Finally, spectroscopic techniques were used to study operation of the converter in several modes of operation.

Maximum Power

Detailed results of the maximum power measurements on Converters C and G are given in References 13 and 17—the emitter area is 0.32 cm^2 . Figure 49 shows the results from Converter C for the range from 1400 to 1800°K. Figure 50 shows the results from Converter G for the range from 1400 to 1800°K. The power density values agreed with those reported by other investigators. The following observations were made concerning the maximum power in the temperature range from 1400 to 1800°K.

- Occurred in the arc mode
- Quite sensitive to electrode spacing
- Existence of optimum cesium temperature at spacings of 0.3 (minimum spacing) and 0.5 mm

The discussion of the flow solution in Section III on the theory of the capillary gives an explanation for the performance reported here. At close spacings in the converter, the pressure in the interelectrode space approaches the cesium reservoir pressure. When the pressure in the interelectrode space is high enough to sustain the arc mode, the converter has a performance similar to that of a planar converter.

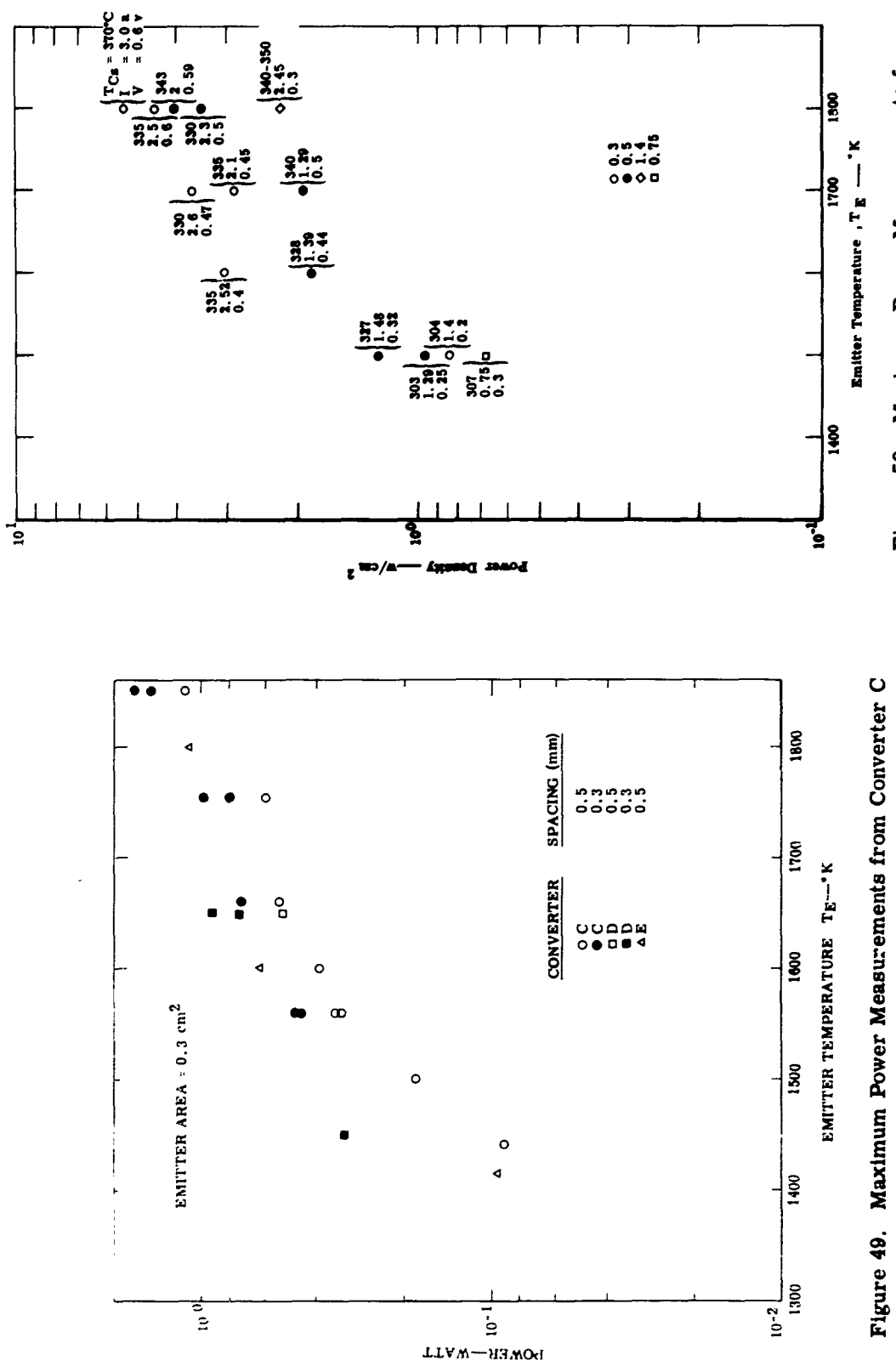


Figure 49. Maximum Power Measurements from Converter C

Figure 50. Maximum Power Measurements from Converter G for T_F from 1400 to 1800°K

It was suggested in Reference 13 that, based on the random current model, power measurements should be made at higher emitter temperatures. Converter G was operated at 1900, 2000, and 2100°K in accordance with this suggestion. Figure 51 shows the maximum power at a 0.3-mm spacing as a function of cesium temperature. Power in the passive mode is plotted below 290°C, while above 290°C the power in the arc mode is shown. At the lower emitter temperatures of 1800 and 1900°K, the power in the arc mode is much higher than in the passive mode. However, at 2000°K there is not much difference between the two regions of operation. Figures 52 and 53 show the variation in passive mode power with T_{Cs} and d for emitter temperatures of 2000 and 2100°K. Some specific values are given as follows:

<u>T_E (°K)</u>	<u>T_{Cs} (°K)</u>	<u>d (mm)</u>	<u>V (v)</u>	<u>J (a/cm²)</u>	<u>P (w/cm²)</u>
2000	523	0.3	1.25	7.5	9.35
2000	523	1.0	1.50	4.4	6.6
2100	523	0.3	1.25	11.25	14.1
2100	523	1.0	1.50	6.7	10.0

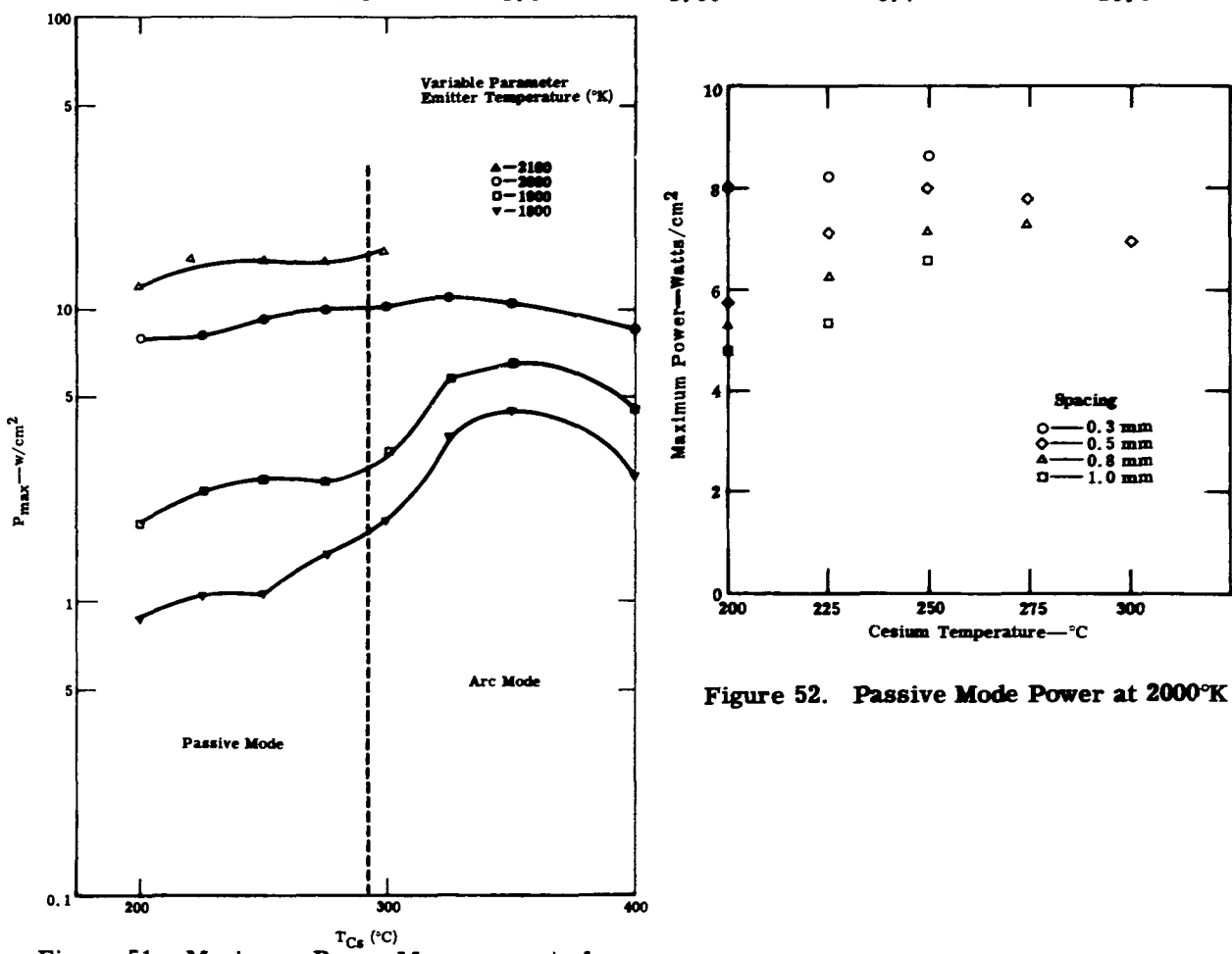


Figure 51. Maximum Power Measurements from Converter G for T_E from 1800 to 2100°K

Figure 52. Passive Mode Power at 2000°K

The multicapillary converter operating at the higher emitter temperatures of 2000 and 2100°K has several features which would contribute to the reliability and utility of a practical device---these are:

- Comparatively wide electrode spacing
- Low cesium pressure to reduce the possibility of ceramic-metal seal failure
- High converter voltage to ease the problems of generator design and improve the efficiency of the power conditioning process

It was also suggested in Reference 13 that a dispenser form of the multicapillary appeared worthy of further investigation. As described in Section IV, a porous tungsten-type emitter was assembled in Converter I. The converter was studied in the temperature range from 1400 to 1600°K. Figure 54 shows the power density as a function of T_{Cs} for the conditions noted. The performance was not high enough for practical interest. The temperature denoted as T_w in Figure 54 is the temperature of the chamber wall surrounding the collector structure. It was found that the power output increased greatly if the wall temperature was increased. Figure 55 shows the power density as a function of spacing and wall temperature. The highest power density recorded was 1.64 watts/cm²---this was not an optimized value.

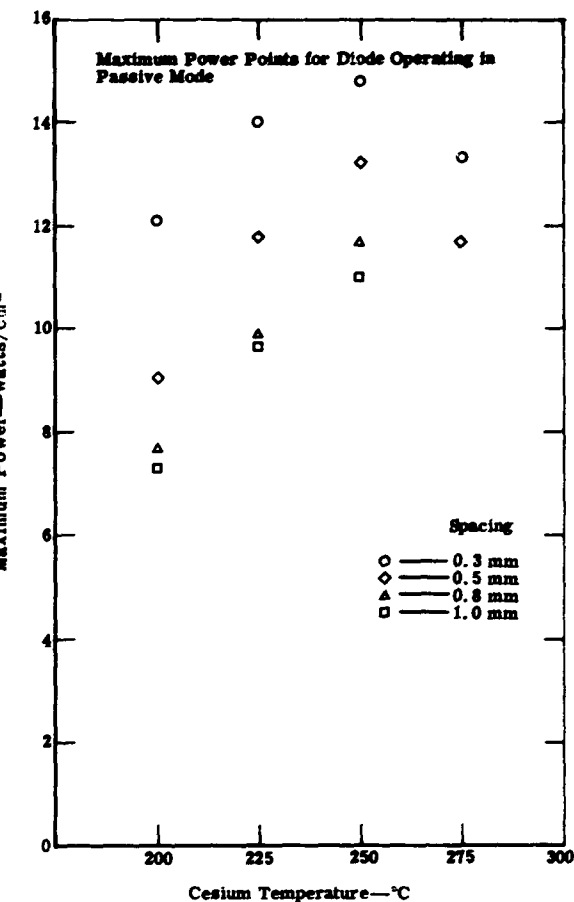


Figure 53. Passive Mode Power at 2100°K

Electron Current Measurements Compared to Theory

Electron saturation currents in the passive mode were compared with the theory based on a random current model. A comparison was first made on the Converter C data over the emitter temperature range from 1400 to 1800°K. Measurements were possible only at cesium temperatures below the optimum value for maximum power because at higher pressure the arc mode was present. Figure 56 shows a typical result at $T_E = 1755°K$ and $T_{Cs} = 473°K$. The maximum power for this case is 0.375 watt/cm². Calculating the maximum power to be expected from a converter with a cesiated planar tantalum surface under these conditions, the power density from the multicapillary converter is about 30 times greater. A detailed comparison of this type is found in Reference 13.

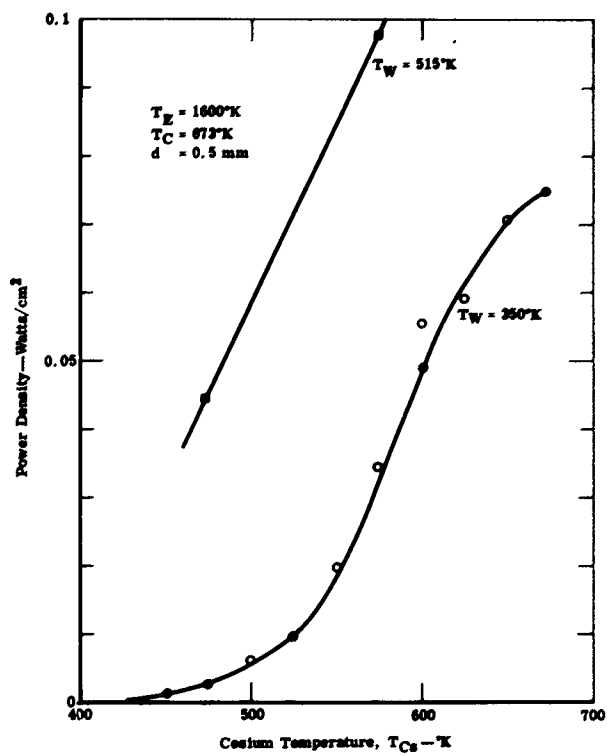


Figure 54. Power Density from Porous Tungsten Emitter as Function of T_{Cs}

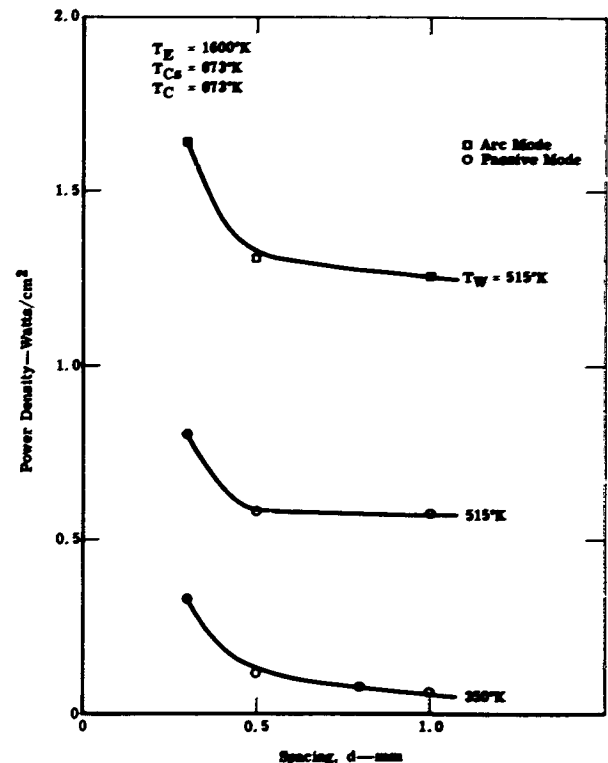


Figure 55. Power Density from Porous Tungsten Emitter as Function of d and T_W

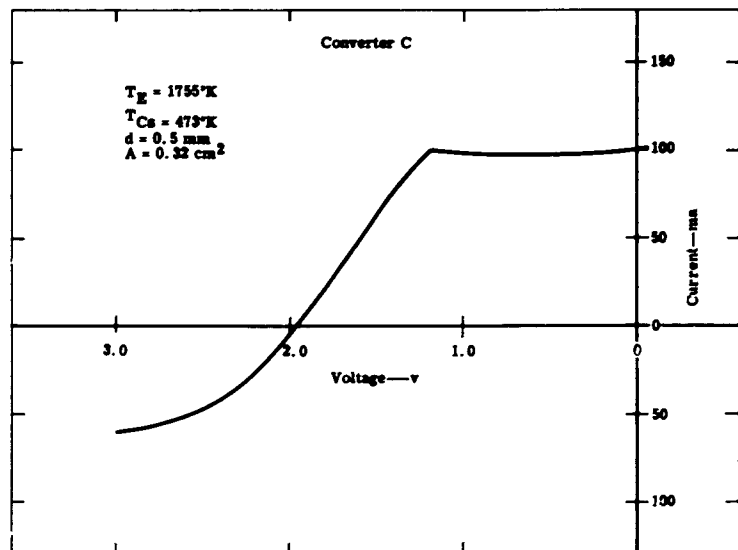


Figure 56. Electron Saturation Current at Low Emitter and Cesium Temperatures

The saturation currents from the multicapillary converter were then compared with the random current model. For example, Figure 57 shows some data at, or near, 1600°K. The agreement with theory was quite good if the pressure drop across the capillary was included.

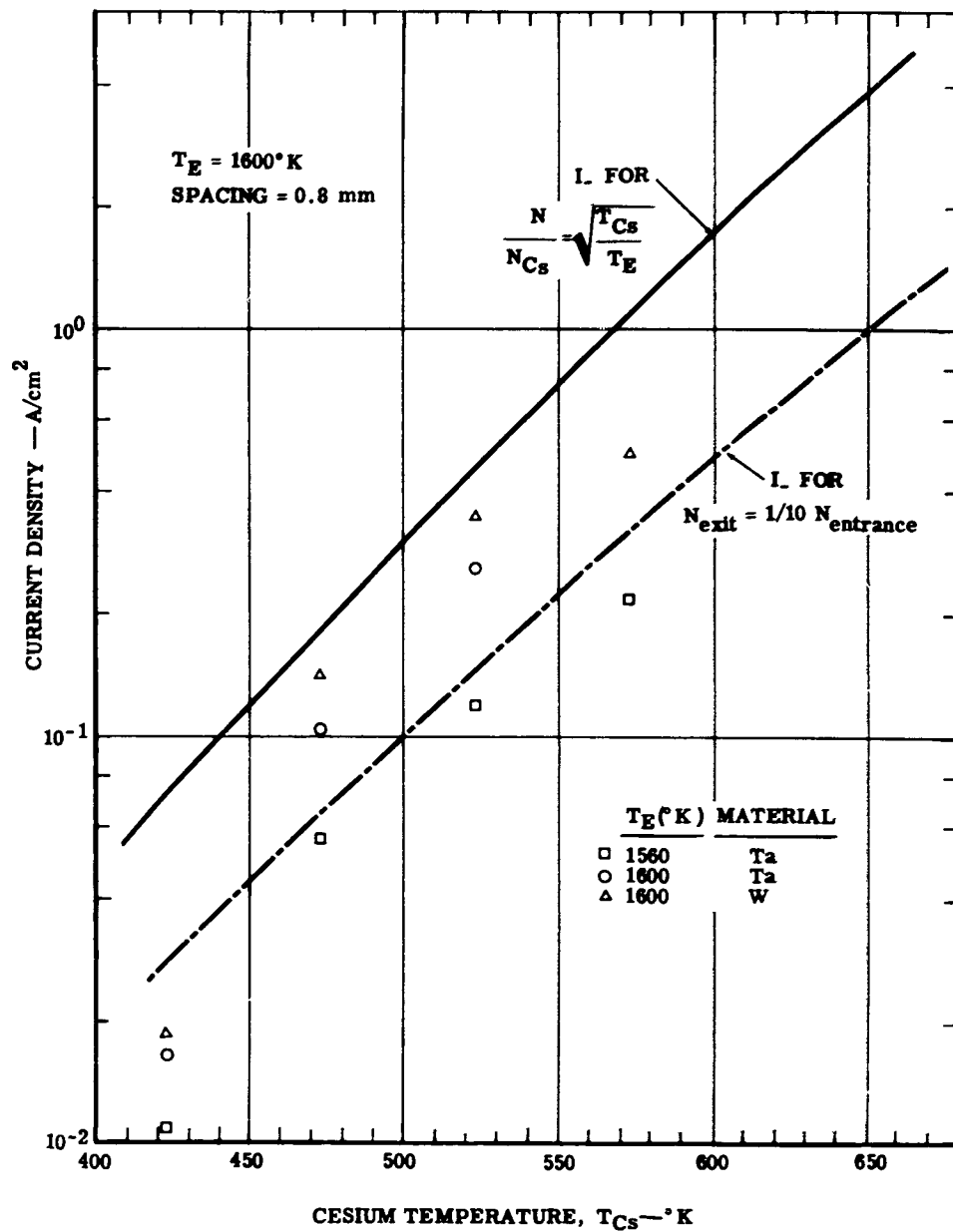


Figure 57. Comparison of Theory and Experiment for Electron Currents at 1600°K

While the power densities obtained at low emitter and cesium temperatures were too low for practical application, the experimental results did indicate that operation of the emitter at temperatures above 1800°K should yield power densities in the 5- to 15-w/cm² range. Therefore, on the last converter tested, Converter G, the temperature range from 1800 to 2100°K was investigated. Power density results as reported in the previous subsection verified the predictions of the theory. Figures 58 through 61 compare the saturation electron currents with the random current theory. In general, the correlation between theory and experiment is good. However, a more detailed study shows that there are two trends in the data which are not explained by the random current theory. First, there is no reason to expect that, at constant d, the density ratio should increase as T_{Cs} increases. And second, for a given d and T_{Cs} , the density should not change greatly as T_E increases. For example, at $T_{Cs} = 473^{\circ}\text{K}$ and d = 0.5 mm, the ratio is about 1/8 for $T_E = 1800^{\circ}\text{K}$, and 1/3.5 for $T_E = 2100^{\circ}\text{K}$. The trend of the data as a function of T_{Cs} suggests that space charge effects may be limiting the current. In the case of the behavior as a function of T_E , one possibility would be that other ionization processes besides thermal are becoming important.

Current-voltage curves for 1800, 1900, 2000, and 2100°K were analyzed to estimate the capillary work function and to check the area ratio limit. Figures 62 and 63 show the passive mode characteristics for d = 0.3 mm and $T_{Cs} = 473^{\circ}\text{K}$. At this close spacing, the pressure drop across the capillaries is a minimum, and, as a consequence, the operation should approximate a cavity-type emitter. The collector temperature was 673°K for these curves.

As seen in the figures, the contact potential was estimated by the intercept method. Although there is no clear Boltzmann region, a line with a slope approximating the emitter temperature was fit to the points. The following values were determined.

<u>T_E (°K)</u>	<u>Contact Potential (v)</u>
1800	1.82
1900	1.90
2000	2.03
2100	2.07

The following calculation procedure was used to determine the random and wall currents:

1. Compute the experimental current from one capillary, assuming that the emitter consists of 320 capillaries.
2. For the given T_E and T_{Cs} , obtain the work function of the capillary wall.
3. Assume that the work function obtained in 2 is present over the total capillary wall. This is tantamount to assuming that there is no pressure drop across the capillary. Compute the saturation Richardson current.

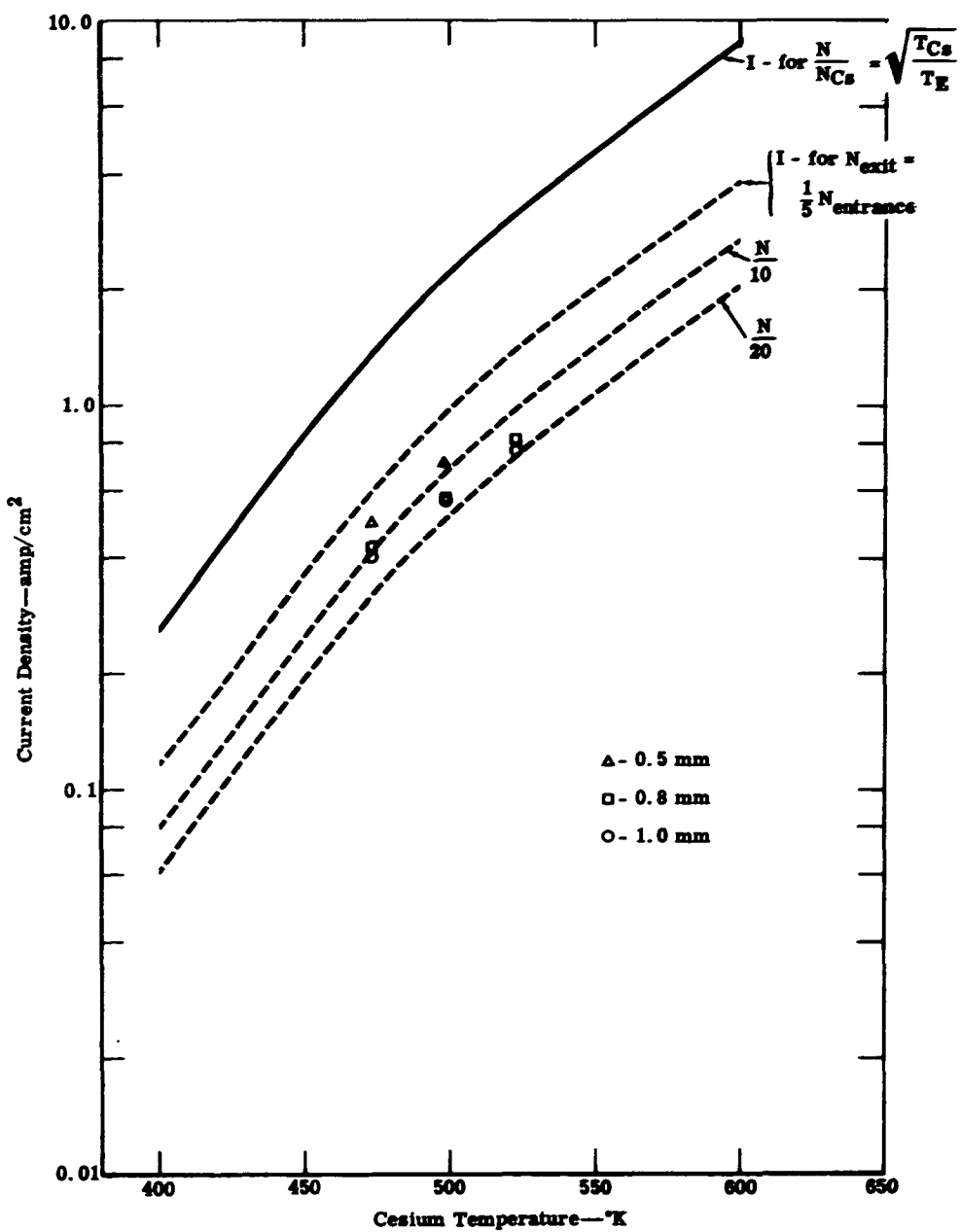


Figure 58. Comparison of Theory and Experiment at 1800°K

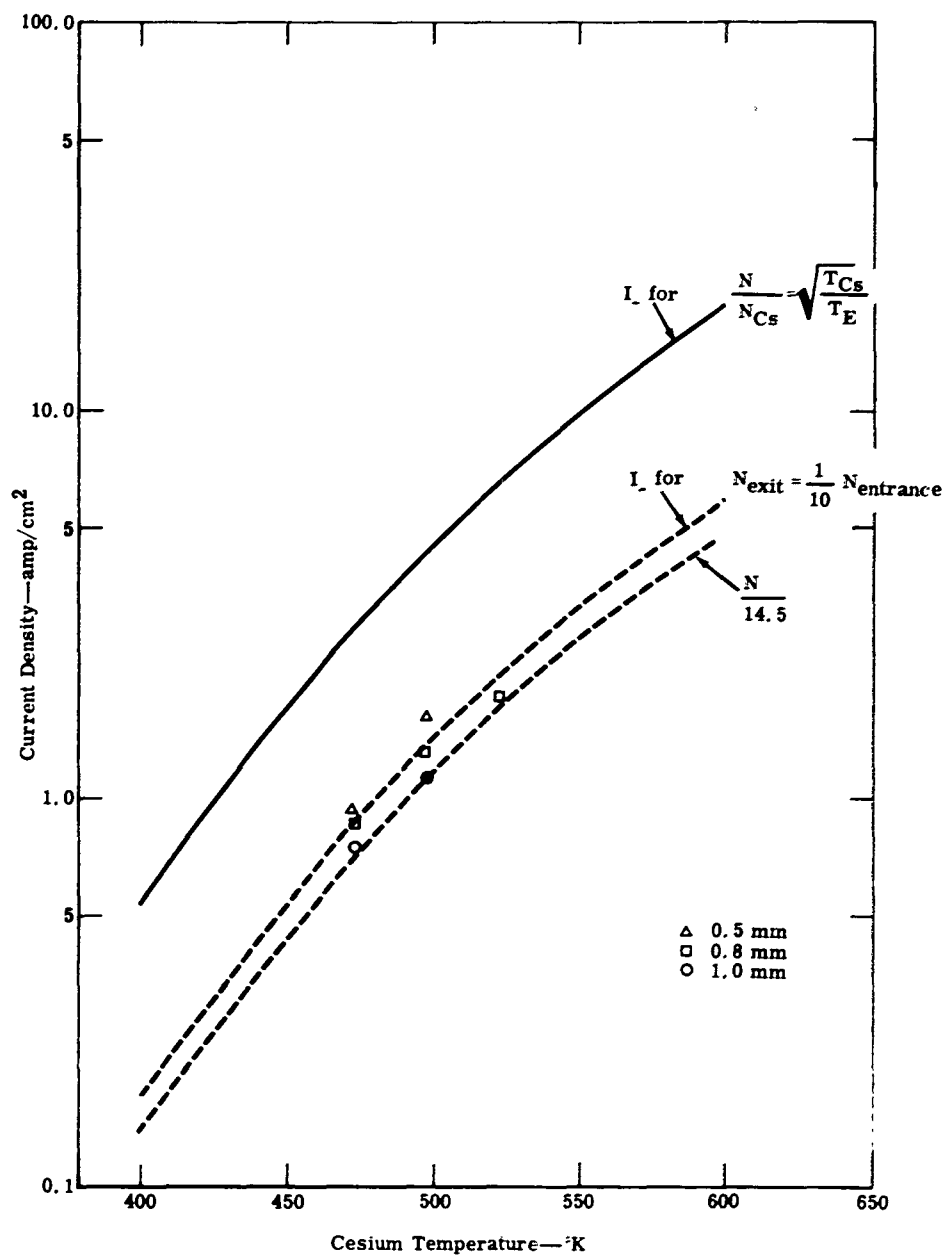


Figure 59. Comparison of Theory and Experiment at 1900°K

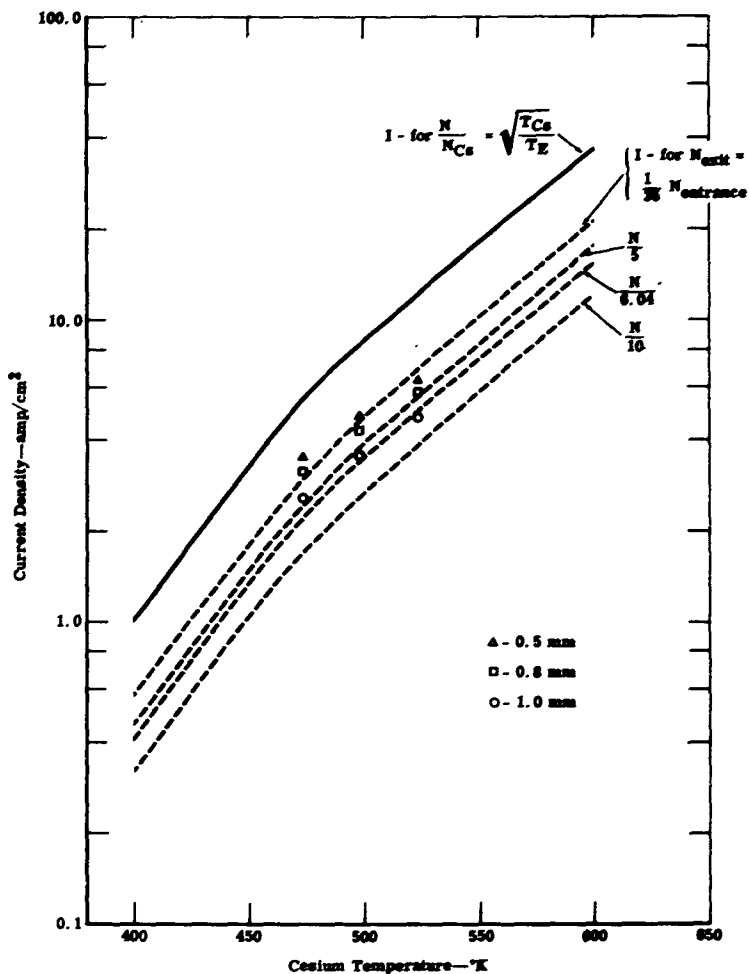


Figure 60. Comparison of Theory and Experiment at 2000°K

4. Calculate the current that would be emitted by a single capillary if the total inside wall emitted the saturation current computed in 3—area of the capillary wall is 0.11 cm^2 .
5. Determine the plasma potential.
6. Calculate the emission current from the capillary with a capillary cross-sectional area of $0.96 \times 10^{-3} \text{ cm}^2$.
7. Compare the results of 4 and 6 with 1.

Table 4 summarizes the results.

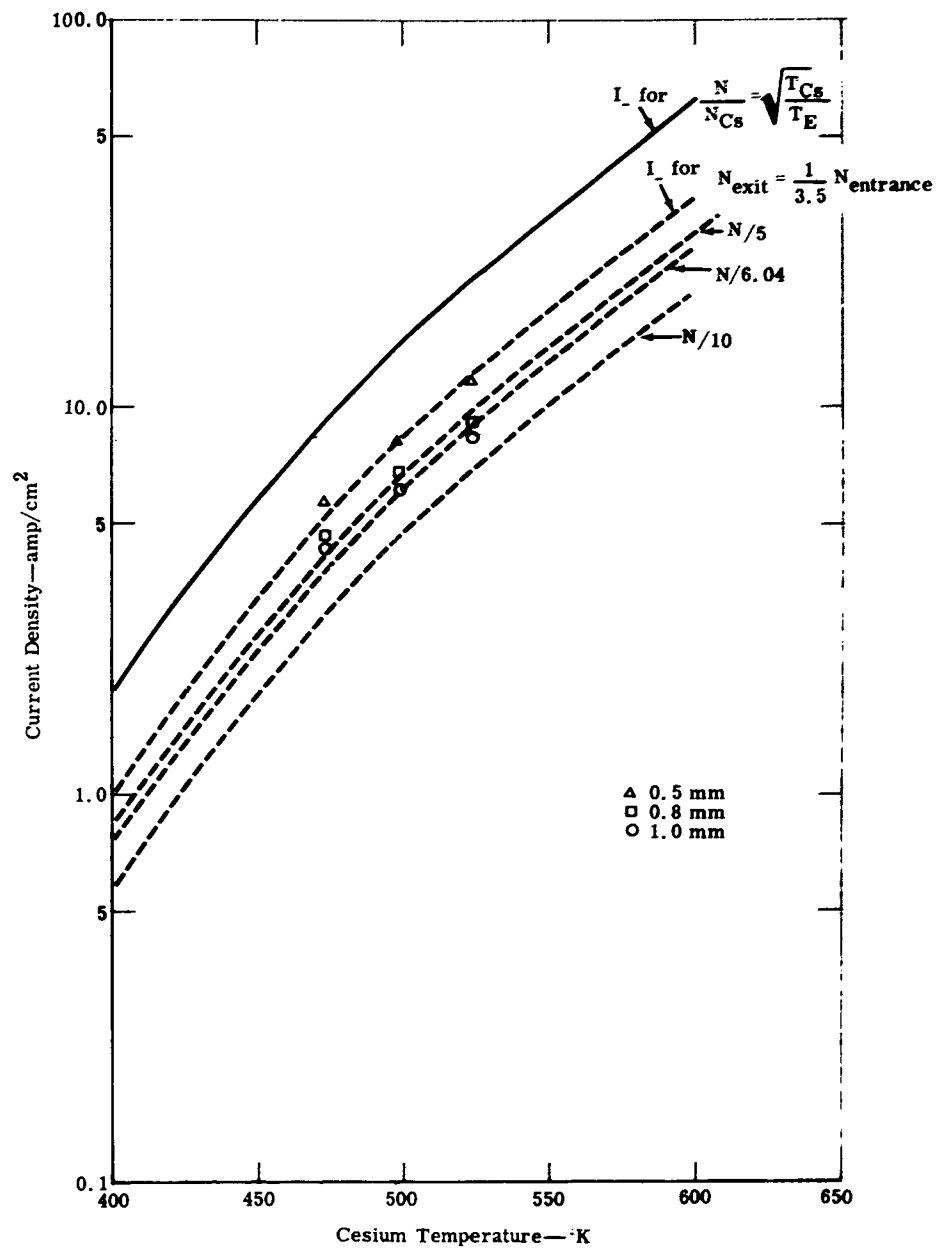


Figure 61. Comparison of Theory and Experiment at 2100°K

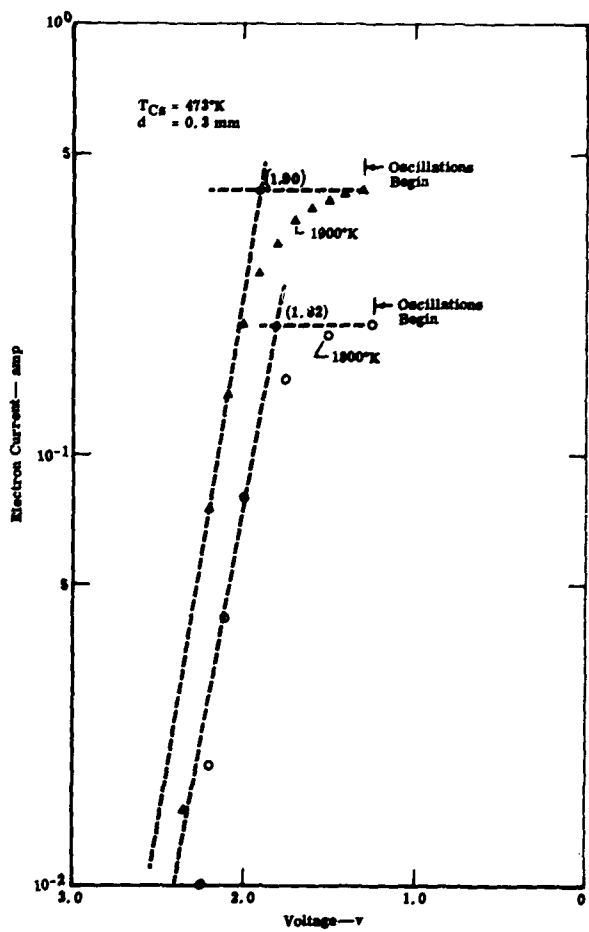


Figure 62. Passive Mode Characteristics at 1800 and 1900°K for $d = 0.3$ mm

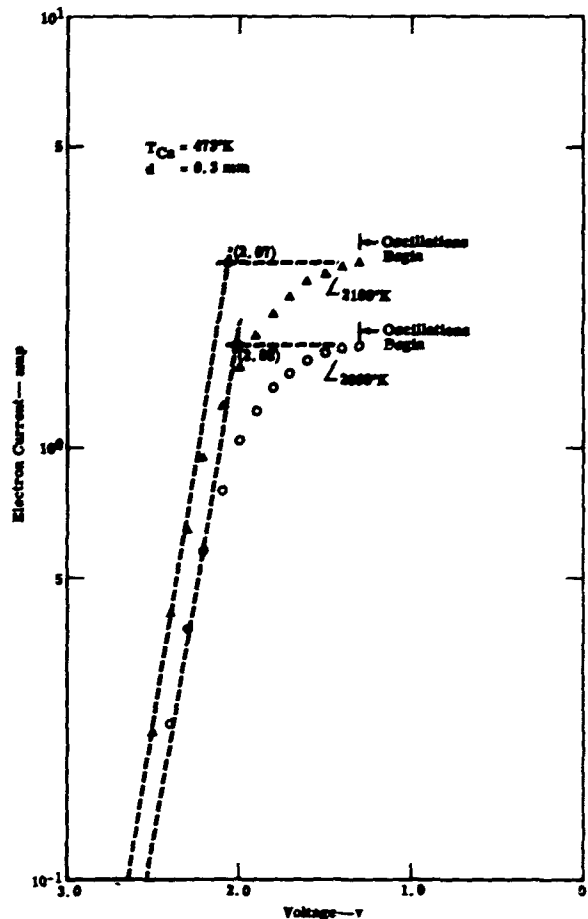


Figure 63. Passive Mode Characteristics at 2000 and 2100°K for $d = 0.3$ mm

TABLE 4
Analysis of I-V Characteristics

T_E (°K)	T_{Cs} (°K)	d (mm)	Experimental Current (a)		Current per Capillary (μ a)	
1800	473	0.3	0.20		625	
1900	473	0.3	0.42		1310	
2000	473	0.3	1.75		5470	
2100	473	0.3	2.80		8450	
		Total				
		Richardson Current (ma/cm ²)	Wall Current (μ a)	Plasma Potential (v)	Plasma Current (ma/cm ²)	Random Current (μ a)
3.7	17.0	1870	3.02	1500	1440	
3.9	19.5	2150	3.09	2300	2210	
4.1	21.5	2360	3.15	6000	5750	
4.3	24.0	2640	3.22	10000	9600	

From the results given in Table 4, the following conclusions are indicated:

1. There is good agreement between the theoretical random current and experimental currents.
2. If a collector work function of 1.9 volts is assumed, the contact potential is in better agreement with experimental values when the wall work function is used rather than the plasma potential.
3. The experimental currents exceed the total wall current for 2000 and 2100°K.

In Section III, it was shown that the total wall current represents a theoretical upper limit for the current which can be extracted from a single capillary. Since the observed currents at 2000 and 2100°K are higher than the total wall values, some effect outside theory must be present. Three possible explanations were considered. First, the emitter temperature was actually higher than measured. This did not seem to be a reasonable explanation because an extensive temperature study was made on the emitter as reported in Reference 13. Also the input bombardment power at the higher temperatures followed along a smooth continuous extension from the lower temperatures. Second, it is possible that emission from the structure surrounding the emitter is contributing to the measured current because there are no guard

rings. Figures 64 and 65 show the pertinent areas surrounding the emitter with temperature gradients as reported in Reference 11. Saturation electron currents from each area are indicated. Also noted on the figures are the measured saturation currents as a function of d for a cesium temperature of 473°K. It is assumed that the cesium pressure above these surfaces is so low that the cesium coverage is zero. As can be seen, the current contributed by the surrounding areas is small compared to the measured values. Further, it is difficult to explain the large change in current with a small change in spacing as being due to extraneous emission currents. Finally, a third possibility is Schottky enhancement of the emission from the capillary wall. Reference 10 shows that a factor of 1.75 is reasonable for these ratios of T_E/T_{Cs} . Patched work function effects could easily increase this to a factor of 2 to 4. V. C. Wilson and J. Lawrence report a factor of 11 with an applied voltage of 1.1 volts.¹⁸

Electron currents from the porous tungsten emitter were much lower than from the stacked foil tungsten emitter for the same operating conditions. In Figure 66, the current-voltage characteristics are compared for $T_E = 1600^{\circ}\text{K}$. As can be seen when the T_{Cs} values were equal, the short circuit electron current from the stacked foil was about 40 times greater.

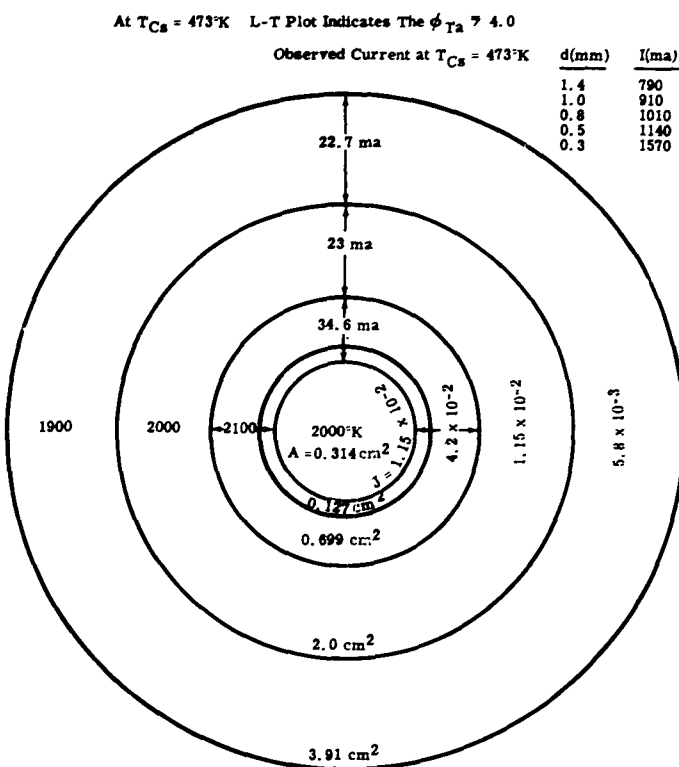


Figure 64. Emitter Temperature Distribution at 2000°K

At $T_{Cs} = 473$ K L-T Plot Indicates $\phi_{Ta} = 4.1$
Observed Current at $T_{Cs} = 473$ K

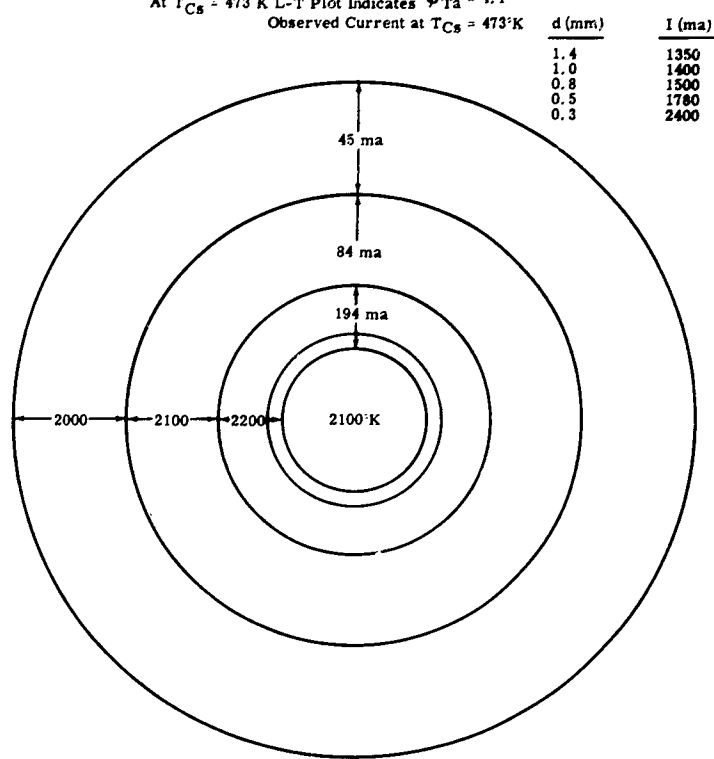


Figure 65. Emitter Temperature Distribution at 2100°K

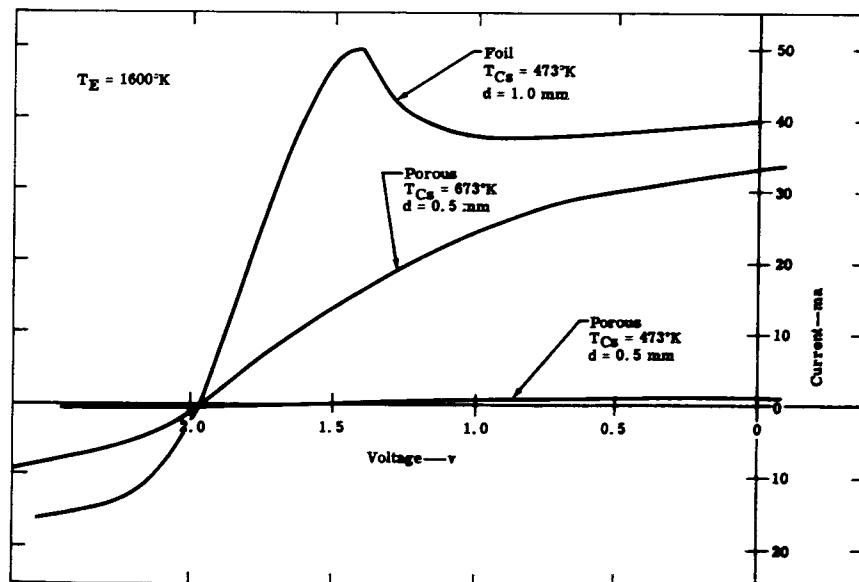


Figure 66. Comparison of I-V Characteristics from Porous and Foil Capillary Emitters

The cesium temperature had to be increased to 673°K in order to make the porous emitter current equal to the stacked foil current. Of course, this is to be expected because the cesium flow rate through the porous matrix is much lower than through the stacked foil. Experiments on ionizers have shown that a stacked wire configuration is 10 times more permeable to nitrogen than an average porous tungsten matrix.¹⁸

Ion Current Measurements

In References 13 and 17 experimental results were reported concerning the effect of collector temperature, T_C , on the current-voltage characteristic. It was found that, as the collector temperature was reduced, the following changes occurred:

1. Ion current decreased rapidly and then leveled off at 373°K.
2. Interelectrode pressure decreased as evidenced by the disappearance of the arc mode in certain cases.
3. Open circuit voltage reached a peak value at 473°K.
4. Passive mode electron current remained essentially constant.
5. At the lowest T_C value, 323 to 373°K, the electron and ion currents were sensitive to spacing.

Typical results of ion current measurements on Converter G are shown in Figures 67 through 70. Figure 71 is a summary plot comparing theory with the currents measured at the lowest T_C value. Shown on the summary plot are the ion currents as predicted by the random current model; the theoretical calculation assumes the cesium density at the capillary exit to be 1/20 of the entrance density, a result predicted by the Knudsen flow equation. Under these conditions the cesium flowing out of the emitter condenses directly on the collector; therefore, the interelectrode pressure should be negligible compared to the entrance pressure. As seen from the summary plot, the ion currents measured are much higher than predicted by the random current model.

Electron-ion ratios were computed for the data described—Table 5 summarizes the results. Saturation electron currents were difficult to determine because, in most cases, there were high frequency oscillations present. The electron current was estimated from the I-V characteristic, ignoring the effect of the oscillations. Ion current measurements at the cesium temperature of 573°K were difficult because cesium buildup on the collector was quite rapid. Within these uncertainties, the electron-ion ratios fell between 50 and 150.

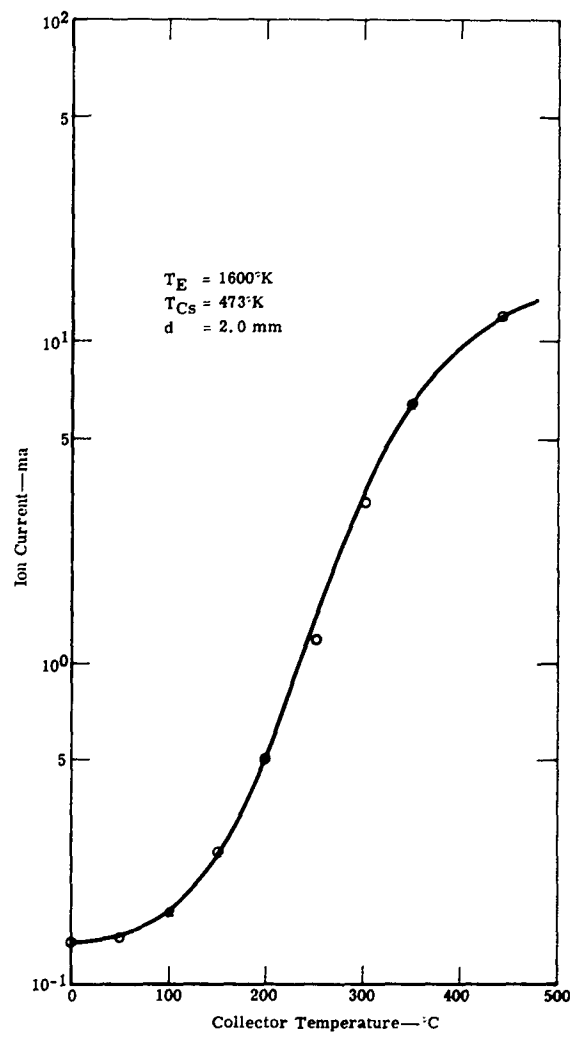


Figure 67. Ion Current as Function of T_C for $T_E = 1600^{\circ}\text{K}$ and $T_{\text{Cs}} = 473^{\circ}\text{K}$

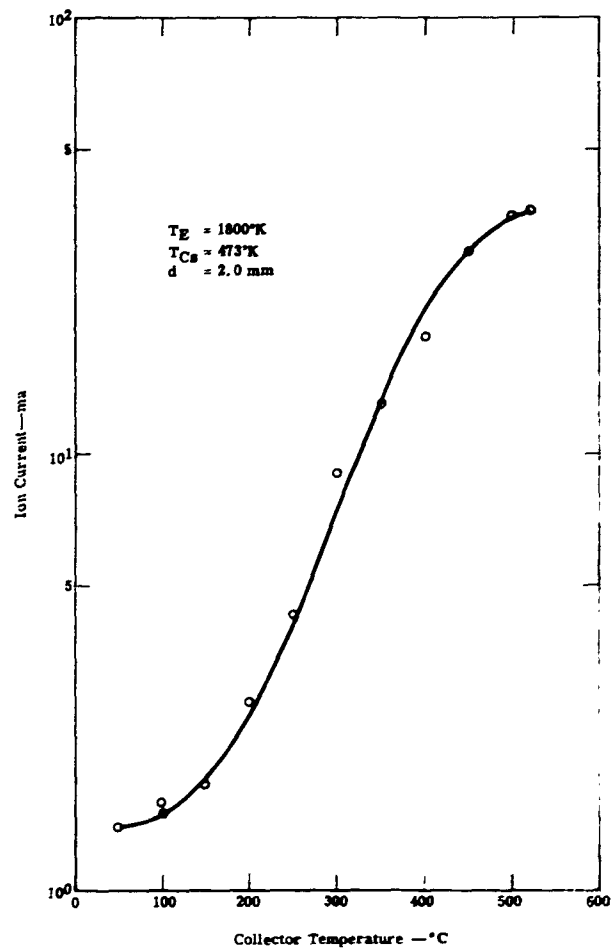


Figure 68. Ion Current as Function of T_C for $T_E = 1800^{\circ}\text{K}$ and $T_{\text{Cs}} = 473^{\circ}\text{K}$

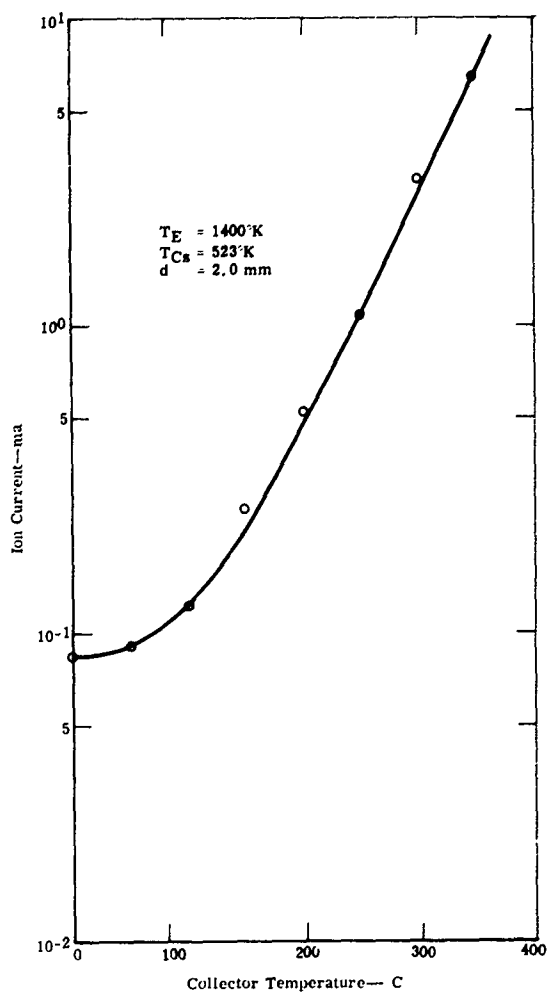


Figure 69. Ion Current as Function of T_C for $T_E = 1400^\circ\text{K}$ and $T_{Cs} = 523^\circ\text{K}$

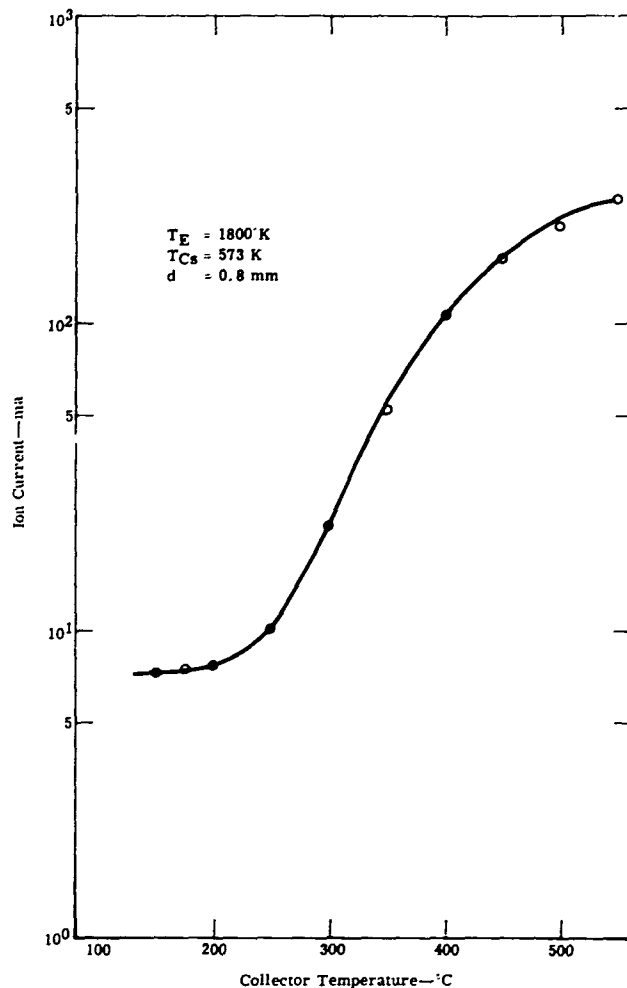


Figure 70. Ion Current as Function of T_C for $T_E = 1800^\circ\text{K}$ and $T_{Cs} = 573^\circ\text{K}$

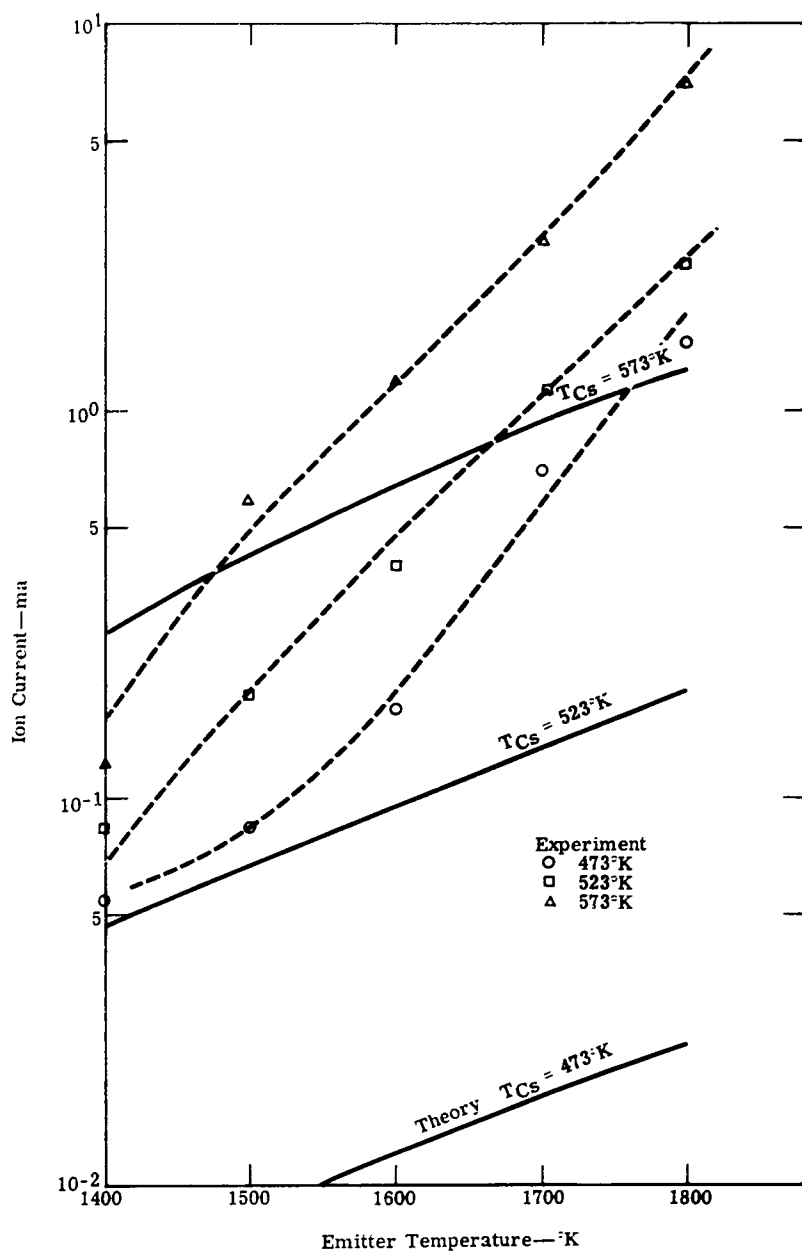


Figure 71. Ion Current Summary Plot

TABLE 5 Electron-Ion Ratios from Converter G				
<u>T_E (°K)</u>	<u>T_{Cs} (°K)</u>	<u>I_- (ma)</u>	<u>I_+ (ma)</u>	<u>I_-/I_+</u>
1400	473	2.3	0.048	48
1600	473	20.0	0.128	156
1700	473	105	0.71	148
1800	473	250	1.52	164
1400	523	6	0.082	73
1500	523	25	0.182	137
1600	523	55	0.52	96
1700	523	110	1.1	100
1800	523	250	3.4	73.5
1400	573	12	0.1	120
1500	573	38	0.7	54
1600	573	120	1.2	100
1700	573	300	2.7	111
1800	573	375	7.0	53.5

The source of the observed ion currents was a matter of considerable conjecture during the project. Four possible sources were considered:

1. Thermionic electrons from the collector
2. Photoelectrons from the collector
3. Some type of discharge which creates the ions by volume processes
4. Ions generated at the emitter surface

Considering each of these in more detail, the pertinent surface areas in the collector volume chamber are shown in Figure 72. Current density as a function of work function is given as follows for $T_C = 700^\circ\text{K}$.

<u>Work Function</u>	<u>Current Density (ma/cm²)</u>
1.7	0.27
1.6	0.175
1.5	0.9
1.4	4.8
1.3	25.5

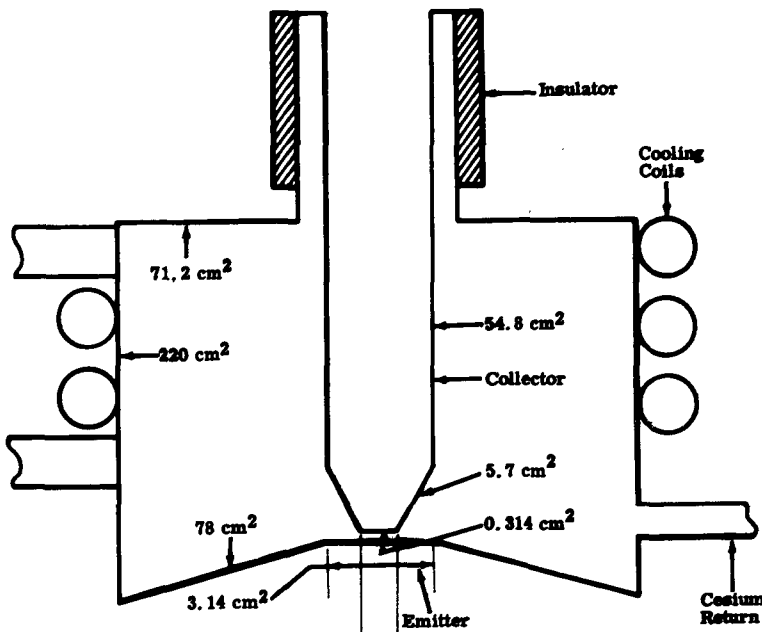


Figure 72. Pertinent Surface Areas in the Collector Volume

Referring to Figure 67, a typical value of 11 ma was observed at a $T_C = 700^\circ\text{K}$. A work function of 1.3 would be required on the collector surface (0.314-cm^2 area) to explain the observed current (see Figure 72). If all of the collector area including the trapezoidal section were emitting, a work function of slightly less than 1.5 volts would be necessary. Other data were obtained which did not support the premise that the current is electrons from the collector. Figure 73 shows the reverse current for two T_C values, 603 and 638°K , as a function T_E for a $T_{\text{Cs}} = 473^\circ\text{K}$ and $d = 2.0\text{ mm}$. As seen from the graph, the ion current increases rapidly as T_E increases. Since T_C is constant, the reverse current should remain constant if due to electrons from the collector. Finally, no investigator has reported conclusive evidence that a work function as low as even 1.5 volts has been obtained in a cesium thermionic converter.

Photoelectric currents from cesium-covered surfaces are difficult to predict since the yield factor is not well known. Dr. L. R. Kollar of National Research Corporation has made an estimate of the photoelectric current from a Cs-O-W surface as reported in Reference 17. He concluded that the photoelectric current for 1800°K tungsten radiation would be 0.16 ma/cm^2 , a value negligible in comparison to the reverse currents measured.

It is difficult to understand what type of discharge could be producing ions by volume processes. All discharges or arc phenomena observed on the multicapillary converter, and reported by

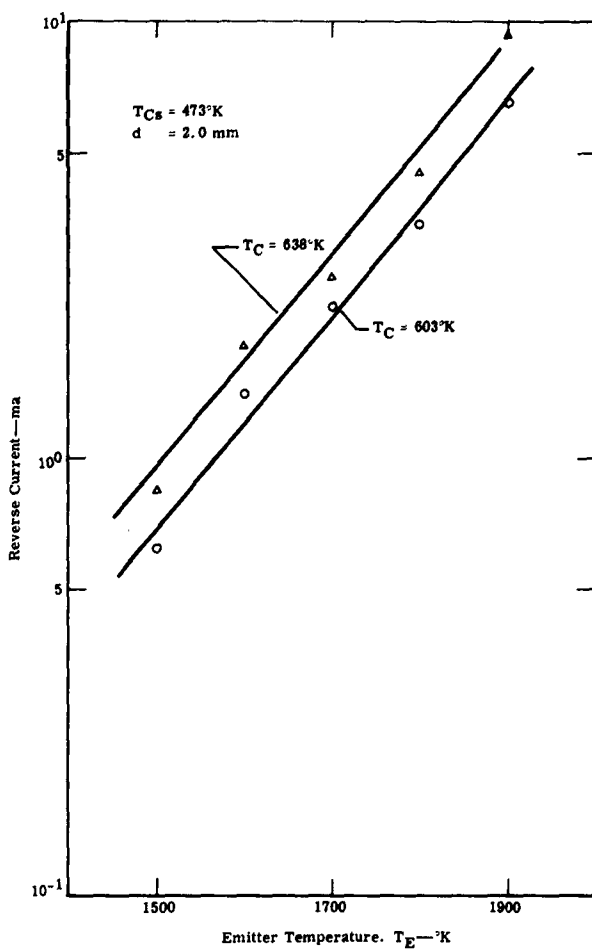


Figure 73. Reverse Current as Function of T_E

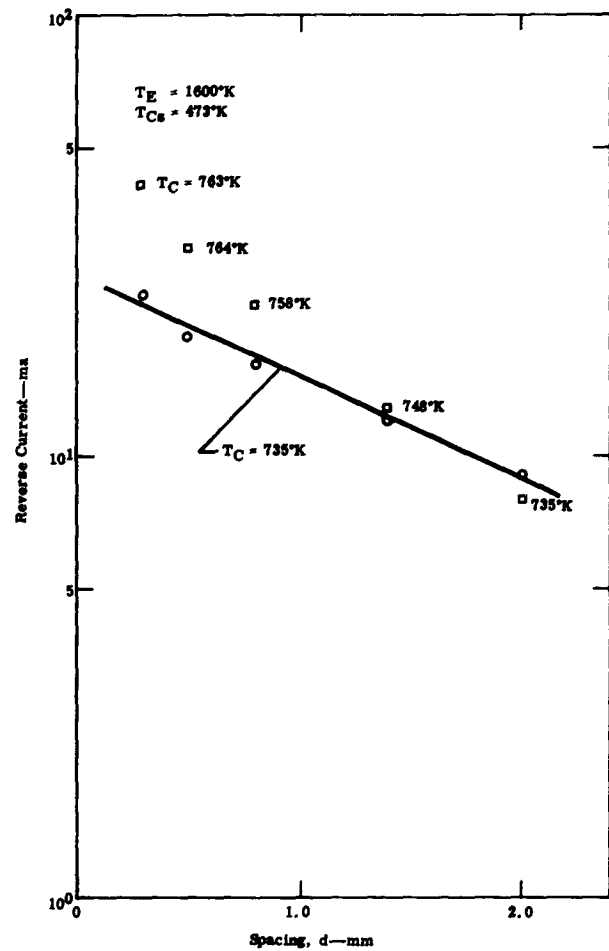


Figure 74. Variation in Ion Current with Spacing for Constant T_C and Equilibrium T_E

other investigators, are characterized by a sharp rise in current as the voltage is increased, or a discontinuity in the I-V curve. Reverse current was measured to 15 volts negative without a sharp rise or discontinuity in the ion current curve.

Finally, the ion current could be due to ions generated on the emitter surface. Two additional experiments were performed to illustrate the nature of reverse current. In Figure 74, the current variation is shown as a function of spacing. In one run the collector temperature was maintained constant--the current increased from 9 ma at 2.0 mm to 23 ma at 0.3 mm. This could be interpreted as due to an increase in the interelectrode pressure. In a second run the collector was permitted to seek an equilibrium temperature--as the spacing was decreased

the T_C increased. In this case, at 2.0 mm the current was 8 ma while at 0.3 mm the current was 42 ma. This could be interpreted to be the cumulative effect of pressure and temperature. In Figure 75, the emitter was raised to 1900°K so that the collector equilibrium temperature was 953°K. Upon reducing T_C , the ion current actually increased, reaching a broad peak around 773°K and finally decreasing as in Figures 67, 68, 69, and 70.

From an analysis of the data it appears that cesium atoms evaporating from the collector surface are responsible for the observed results. These atoms impinge on the hot emitter surface and become the source of ion current—this reflux of cesium also creates a back pressure in the interelectrode space. Although the general characteristics observed in the data can be explained by this model, the data reported in Figure 75 do not appear to support this view. If the ion current were due to atom evaporation, it should saturate at some higher value of T_C . In addition, if the current were due to atom evaporation from a collector coated with several layers of cesium, then the logarithm of current as a function of reciprocal temperature should give the heat of evaporation of cesium (0.79 electron volt/gm atom). The data from Figures 67 to 70 are plotted in this form in Figures 76 to 79. In no case is a value of 0.79 obtained—the values vary from 0.28 to 0.55.

Although there is evidence to support the contention that ions are being generated on the emitter front surface, the extremely low electron-ion ratios at high collector temperatures preclude the possibility of the ions being generated on the active emitter surface. For example, in Figure 67, the ion current at $T_C = 710^\circ\text{K}$ is 12 ma. The saturation electron current for this case is, from Table 5, 20 ma. If the emitter surface were ion rich, the observed ion current could not flow because of space charge effects. If the emitter surface were electron rich, the electron current should be much higher. Under the circumstances it is concluded that the ions are being produced on the surfaces

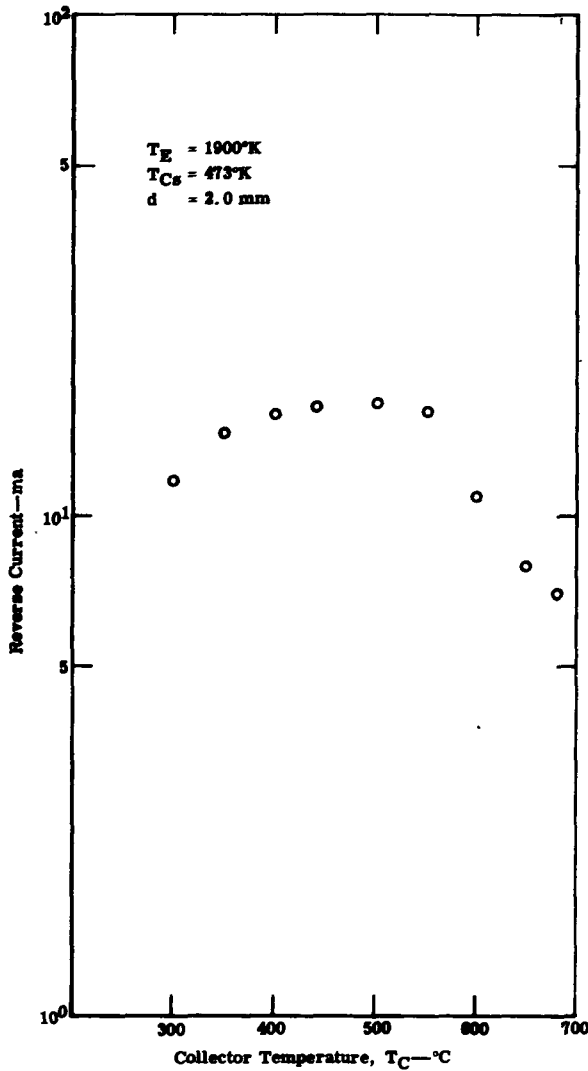


Figure 75. Ion Current at 1900°K

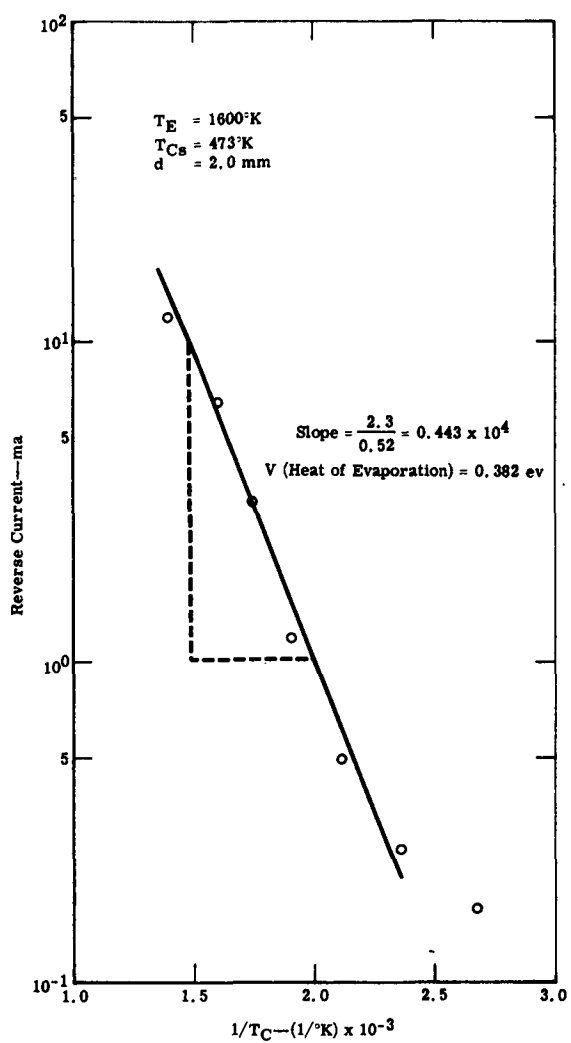


Figure 76. Ion Current as Function of $1/T_C$ for $T_E = 1600^\circ\text{K}$ and $T_{Cs} = 473^\circ\text{K}$

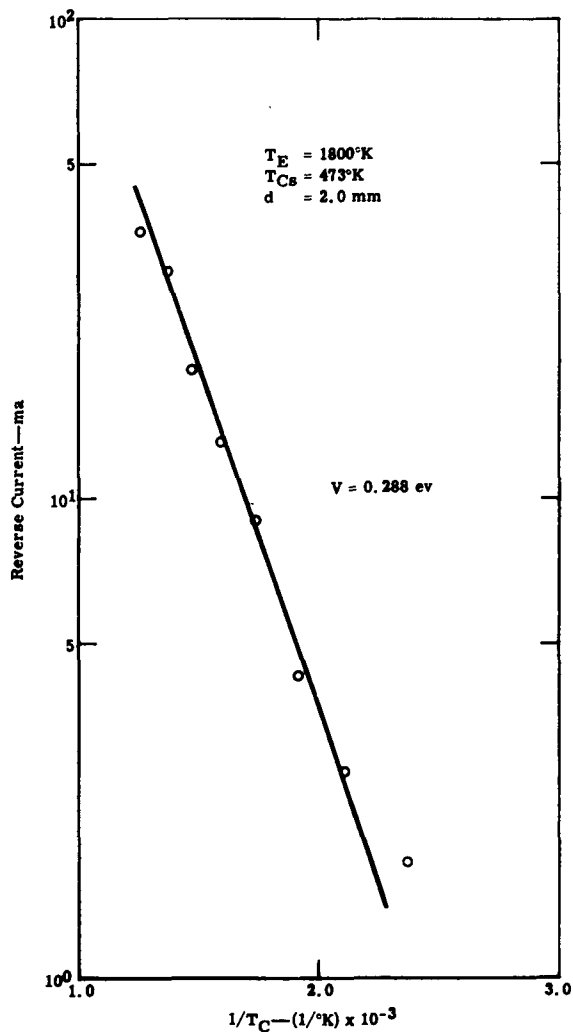


Figure 77. Ion Current as Function of $1/T_C$ for $T_E = 1800^\circ\text{K}$ and $T_{Cs} = 473^\circ\text{K}$

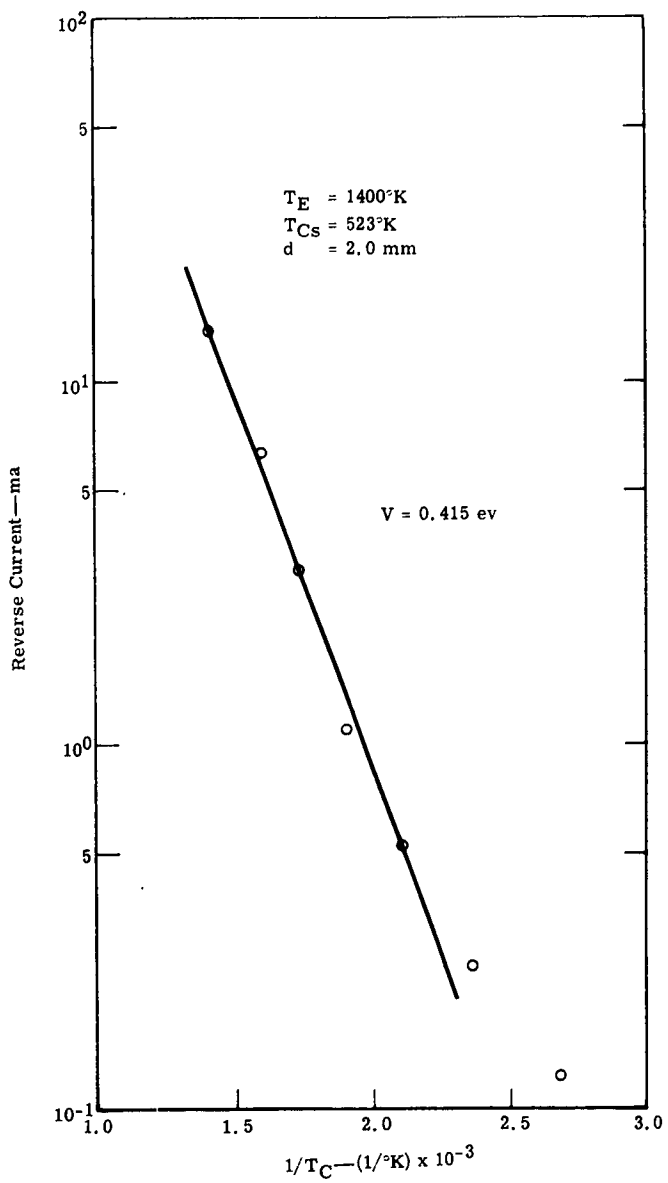


Figure 78. Ion Current as Function of
 $1/T_C$ for $T_E = 1400^\circ\text{K}$ and $T_{Cs} = 523^\circ\text{K}$

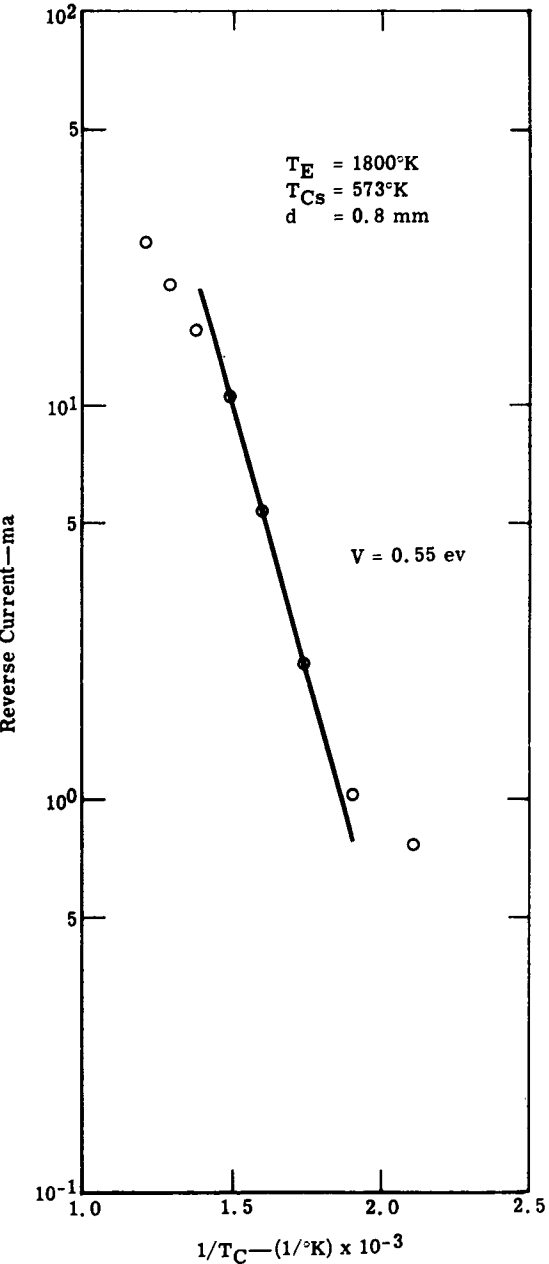


Figure 79. Ion Current as Function of
 $1/T_C$ for $T_E = 1800^\circ\text{K}$ and $T_{Cs} = 573^\circ\text{K}$

surrounding the active emitter surface. However, even in this case it is difficult to explain the large ion currents because the surfaces surrounding the emitter should be ion rich, and therefore, ion space charge limited as far as ion flow to the collector is concerned.

As the collector temperature is reduced, the electron-ion ratio increases. As shown in Table 5, values between 50 and 150 are finally obtained. Since the electrode geometry is not ideal for accurate measurements of this type, the experimental values are interpreted to indicate that the ratio is actually near 500. The nature and magnitude of the sheath at the active emitter surface can only be estimated from the data. In Reference 21 it is reported that the ignited mode and high frequency oscillations are predominant in a slightly ion-rich to slightly electron-rich condition. Since these characteristics are observed in the multicapillary data, it is concluded that the capillary emitter surface has little or no sheath.

Voltage-current curves as a function of T_C were obtained on Converter I (porous tungsten emitter) to supplement and, possibly, clarify the results from the ordered capillary structures. Figures 80 and 81 show how the I-V characteristics varied with T_C for two different T_{Cs} values. In comparison with previous data, the principal difference was in the electron currents. For example, the electron current from the porous emitter, for $T_{Cs} = 673^\circ\text{K}$, decreased as T_C was reduced. This behavior was never observed with the ordered structure. From the figures it is seen that the electron-ion ratios follow the trend of the other data--namely, the ratio increases as T_C decreases. The very low ratios at high T_C are again observed.

The difference in electron current behavior as a function of T_C for the porous surface may be explained by the effect of cesium coverage. As the T_C value decreases, previous data indicates that the interelectrode pressure decreases. In Figure 80, the electron emission decreases very little because the pressure is already so low that little or no surface coverage exists. On the other hand, in Figure 81, the electron emission decreases quite drastically because the initial surface coverage was relatively high.

In summary, several conclusions have been drawn from the collector temperature study; they are as follows:

1. The capillary emitter operates with little or no sheath at the surface.
2. The high reverse currents observed at high T_C values appear to be ions produced on the hot surfaces surrounding the active emitter surface.
3. The reverse current at the lowest T_C value is a measure of the ions produced within the capillary cavities. These currents are higher than predicted by the random current model.

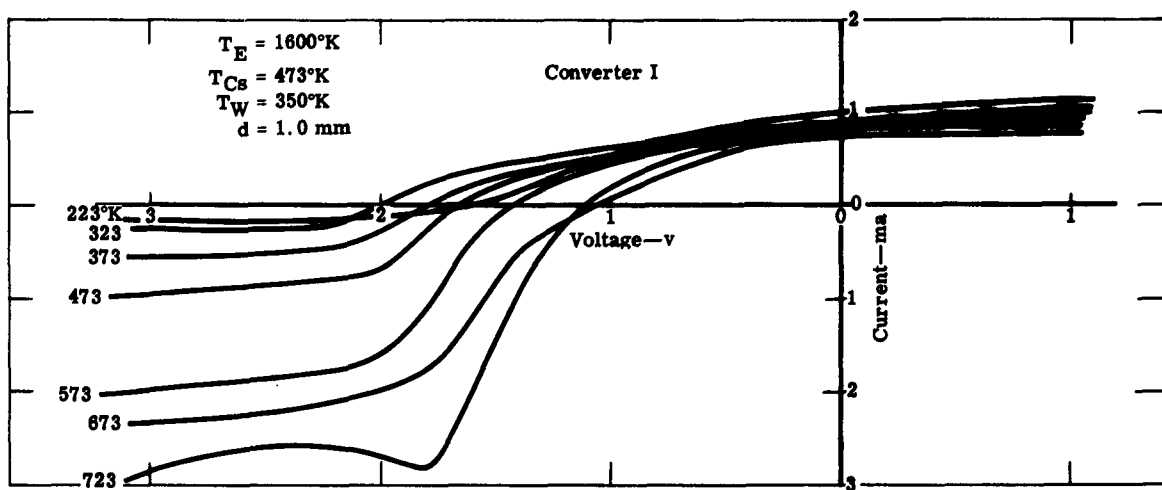


Figure 80. Variation of I-V Characteristic with T_C for $T_{Cs} = 473^\circ\text{K}$

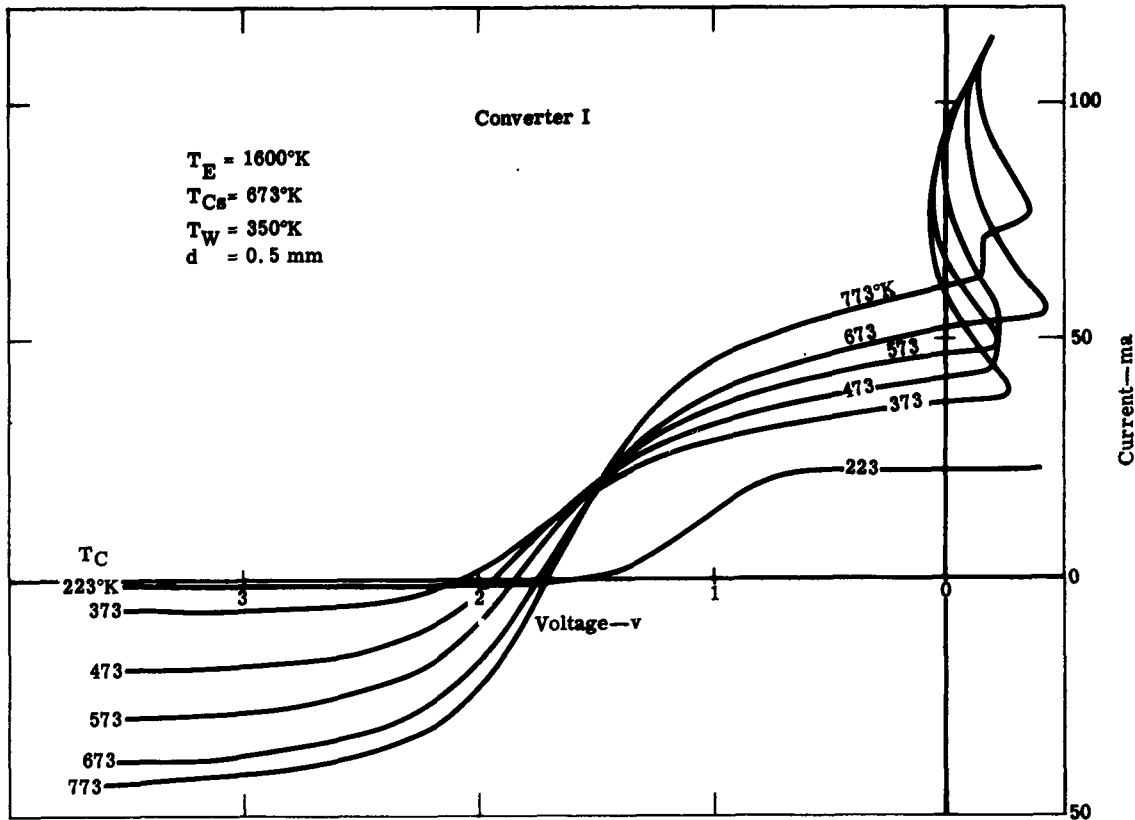


Figure 81. Variation of I-V Characteristic with T_C for $T_{Cs} = 673^\circ\text{K}$

High Frequency Oscillations

High frequency oscillations were observed for several operating conditions. Considerable difficulty was experienced in recording the oscillations because external circuit inductance produced large inductive pulses when the converter current changed abruptly. From a study of the wave form, it appeared that the current, under certain conditions, dropped instantaneously toward zero. This was the source of the large inductance pulses.

After considerable investigation, the circuit shown in Figure 82 gave the best results. Two 18-in. lengths of wire twisted together to reduce the inductance gave a short circuit resistance of 0.020 ohm. Figures 83 and 84 show a set of oscillograms taken at $T_E = 1800^\circ\text{K}$ and $T_{Cs} = 473^\circ\text{K}$ on Converter G. Note how the inductive pulse increases as the load resistance is reduced toward short circuit.

The peak negative voltage was recorded for a series of load values. The peak current was then computed, and the resultant voltage-current points were plotted for comparison with the I-V characteristic recorded on the x-y recorder. The result is shown in Figure 85. It appears that the converter operates periodically in the arc mode.

Further detailed study of the oscillations as a function of T_E , T_{Cs} , T_C , and d were planned on Converter G, but failure of the converter prevented this from being accomplished. It may be stated that oscillations were observed over a range of emitter temperatures from 1400 to

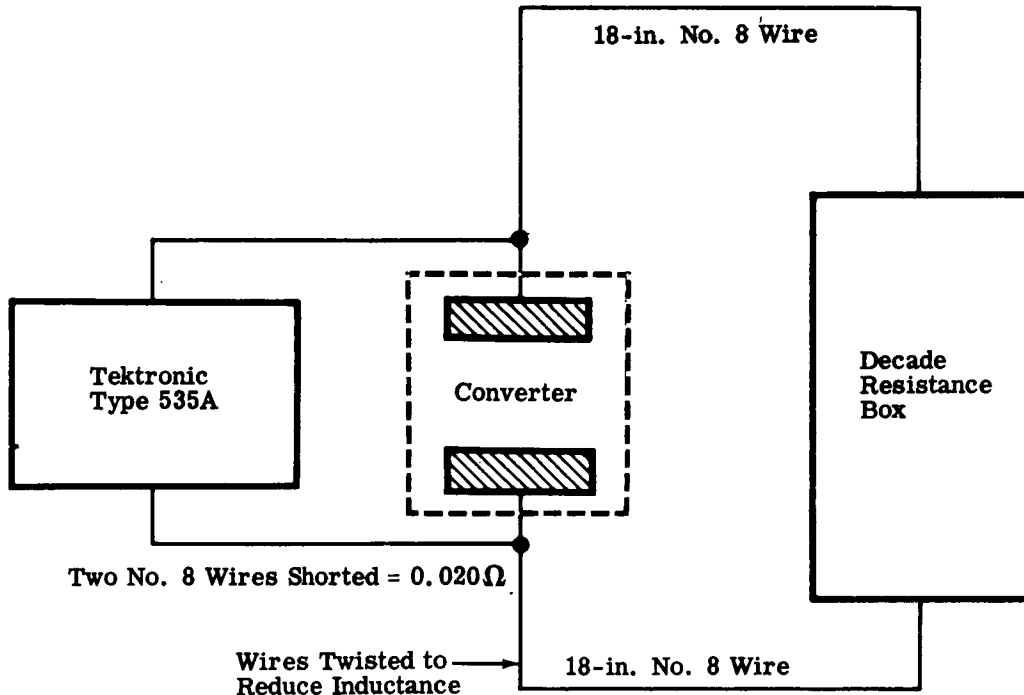


Figure 82. Circuit for Oscillation Study



Figure 83. Oscillation Data for High Resistance Load

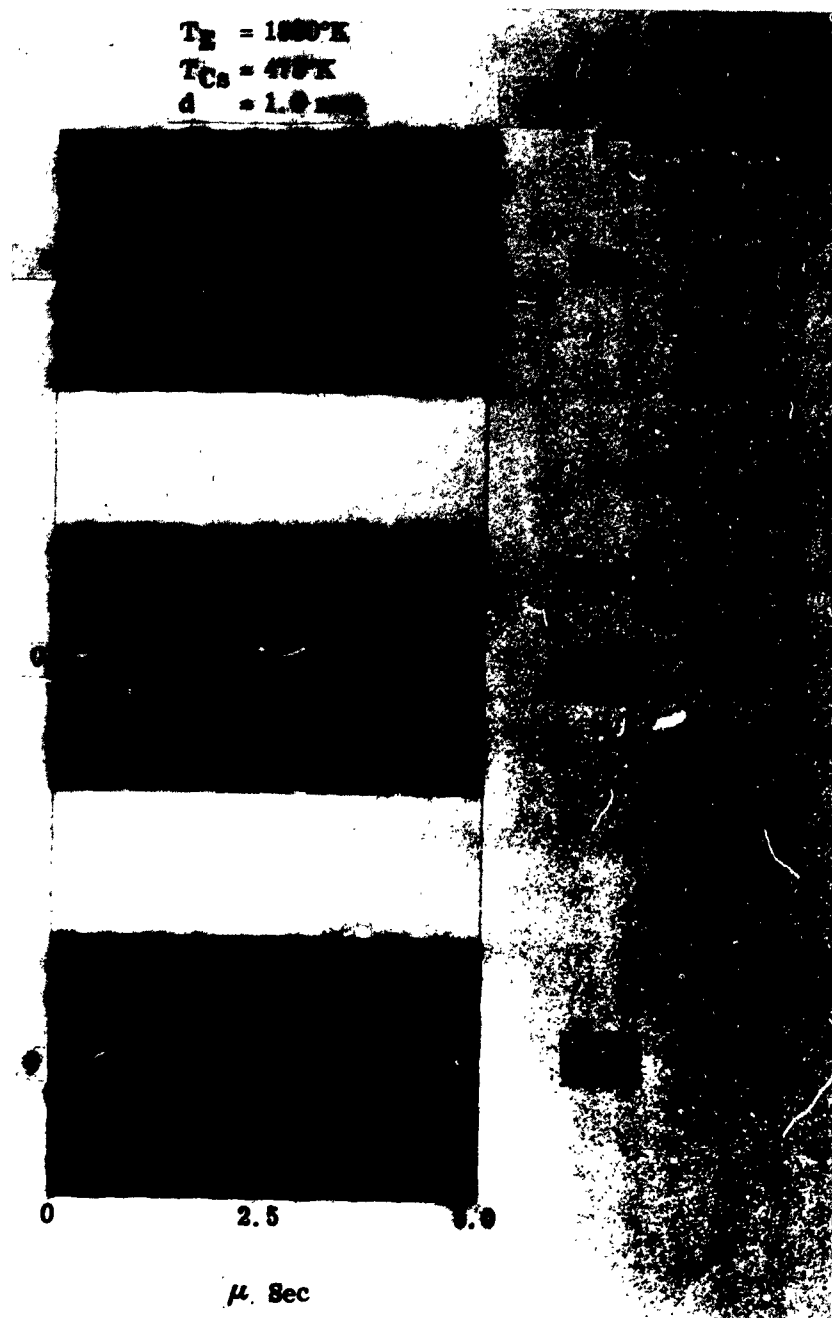


Figure 84. Oscillation Data for Low Resistance Load

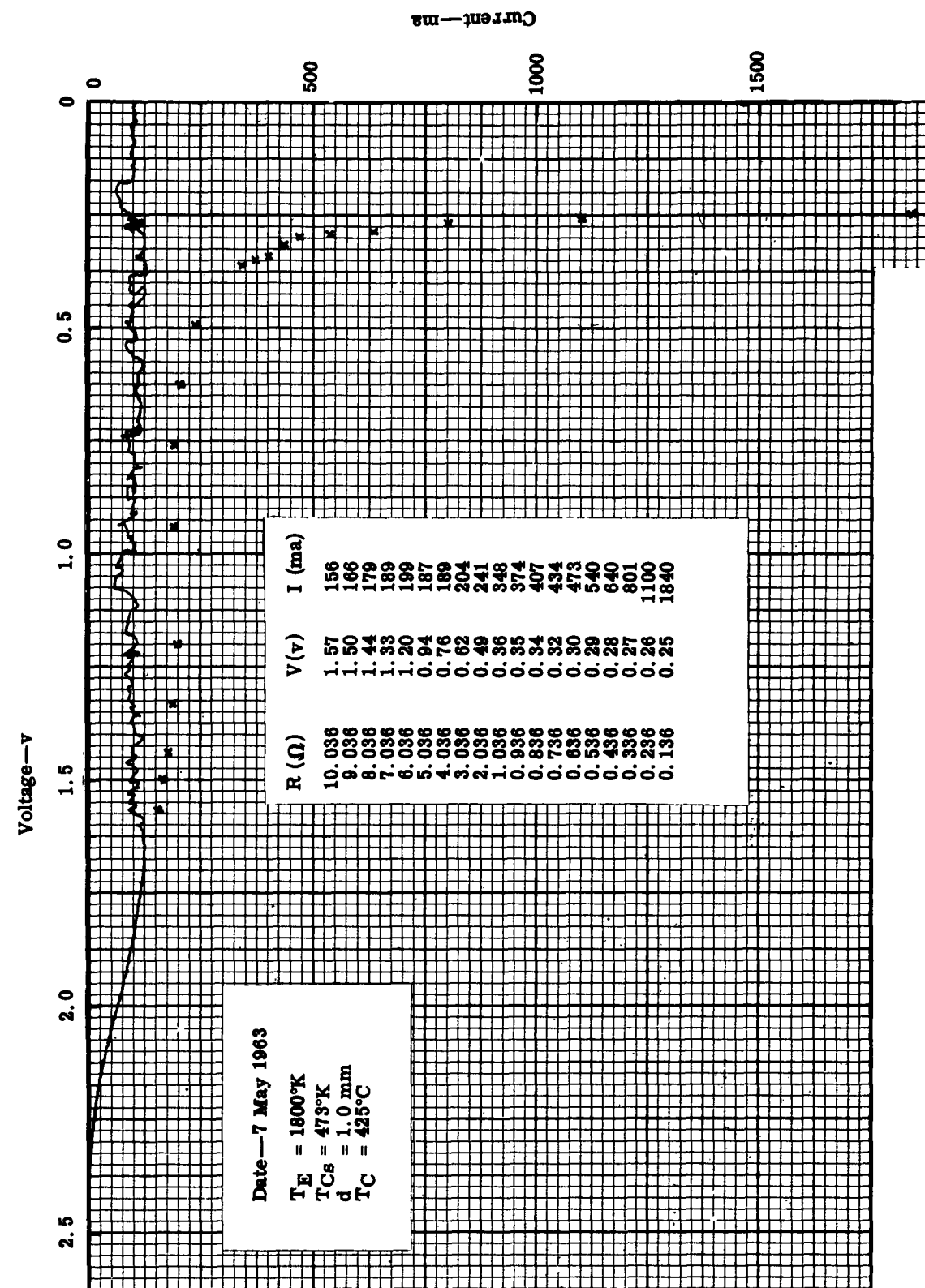


Figure 85. Peak Current-Voltage Points from Oscillation Data

2100°K, and up to 573°K cesium temperature at 1500°K emitter temperature. Generally, the higher the emitter temperature, the lower the cesium temperature at which the oscillations disappeared.

Spectrographic Study

A spectrographic study was conducted to determine if it was possible to obtain useful information on the converter operating in the power generating region. There were two major questions concerning the application of the measurement technique:

1. Would the line intensity be sufficient to evaluate the spectrum?
2. Would the plasma be in such a state of nonequilibrium that the spectra could not be interpreted with existing theory?

A detailed description of the measurement technique and complete discussion of the results are given in Reference 17. For purposes of this report, a summary of the results is presented.

A typical voltage-current characteristic is shown in Figure 86. Four different modes of operation can be observed: passive, oscillating, ignited, and arc. Spectra were obtained in each mode of operation; typical spectra are shown in Figure 87. These spectra were obtained by forming an enlarged image of the interelectrode space in the plane of the entrance slit of the spectrograph. The slit was parallel to the electrodes and midway between them. In this way, direct blackbody radiation from the emitter was avoided.

The passive mode spectrum is shown in part A of Figure 87. The continuous radiation consisted mainly of blackbody radiation from the emitter which was reflected by the walls into the light path. By using an extremely narrow entrance slit, the reflected radiation was suppressed and the cesium resonance lines could be seen as in part B of Figure 87. However, even at extremely long exposure times no other cesium lines were observed—including the spectral regions which were not overshadowed by the blackbody radiation. From this result it was concluded that there are no electrons with energies high enough to populate significantly the energy levels above the first excited state. Or, if they exist, they do not collide with cesium atoms.

As the converter went from the passive mode into the oscillating mode, additional spectrum lines were observed as shown in part C of Figure 87. The plasma oscillation frequency was in the 0.5-mc range. There are two possible explanations for the observation:

1. The energy of the electrons was increased by the oscillations.
2. The electrons already had higher energies but did not collide.

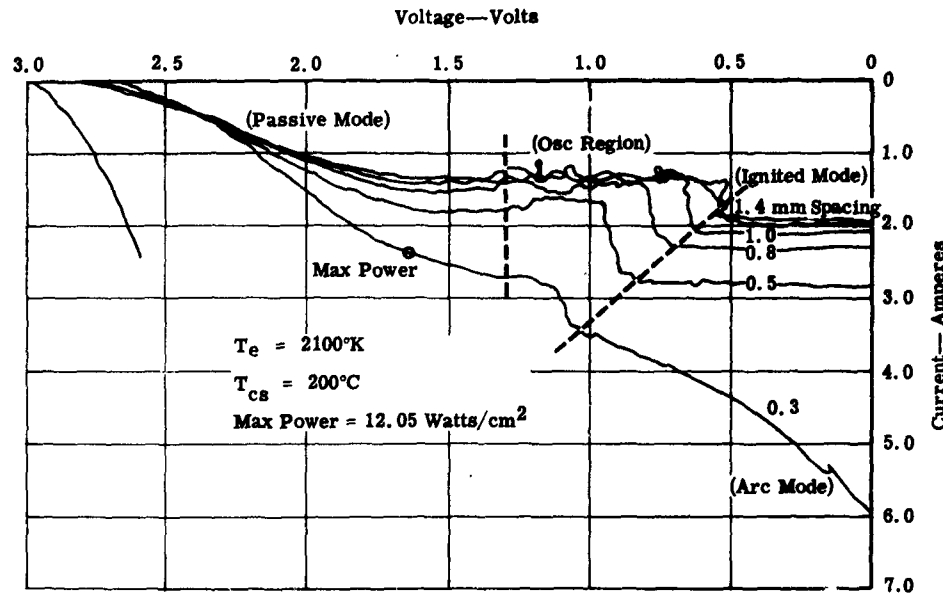


Figure 86. Typical I-V Characteristic

If the latter is true, then the effect of the oscillations is to randomize the velocity distribution through the increased number of collisions.

A typical spectrum in the arc mode is shown in part D of Figure 87. The radiation intensity was much higher than in the other modes. In addition, rubidium and potassium lines were observed.

Using cesium lines 6288, 6250, 6472, and 6432 Å, the electron density was estimated by line broadening measurements. A value of 2×10^{14} electrons/cm³ was obtained for the arc mode.

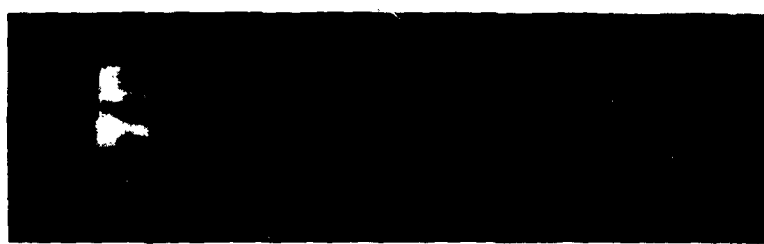
The electron temperature in the arc mode was determined by measurements of intensity ratios of lines originating from higher energy levels. Results for several line combinations are as follows:

Line Pairs (Å)	Electron Temperature (°K)	Line Pairs (Å)	Electron Temperature (°K)
$\frac{8761}{6212}$	4250	$\frac{6010}{4555}$	4290
$\frac{7609}{6212}$	4000	$\frac{7609}{6010}$	3800
$\frac{6212}{4555}$	4700	$\frac{8761}{6010}$	4000

The values agree to within $\pm 10\%$.



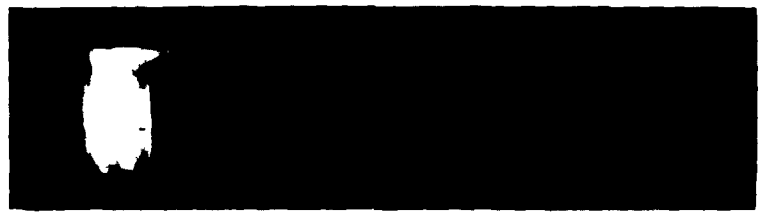
A



B



C



D

Figure 87. Spectra Observed in Each Mode of Operation

The spectra in the ignited mode showed a lower intensity than in the arc mode. The radial intensity distribution of the radiation in the ignited mode gave a bell shaped curve while the arc mode showed striations. The presence of striations could be explained by a constriction of the discharge and a change of position with time.

It has been concluded from this study that:

1. It is possible to make spectroscopic measurements in the power generating region of a thermionic converter.
2. Line broadening can be used to determine electron density in the arc mode.
3. Line intensity ratios can be used to determine electron temperature in the arc mode.
4. In the arc mode the deviation from a Maxwellian distribution is not detectable within the limit of measurement error using various line pairs to determine electron temperature.

Supplementary Converters

Converter 3

As reported in Section IV, two accidents occurred during activation of the converter. From the data it appears that the tantalum emitter absorbed oxygen. The measured saturation currents were considerably above the values measured by Houston and extrapolated by Nottingham.¹⁰ It was concluded that results from this device could not be used as a base line for comparison with slotted cavity emitter data. Testing was suspended after 40 hr.

Converter 4

Converter 4 was prepared for test without an accident. Testing began at Allison on 29 July 1963. This converter had a molybdenum planar emitter rather than a tantalum emitter as in Converter 3.

Test Arrangement

The experimental test arrangement is shown in Figure 88. The current-voltage characteristic curves were plotted on an x-y plotter over the range from -15 to +10 volts. A transistorized d-c power supply in series with a 6-volt battery provided the necessary voltage range. The converter voltage was measured directly across the emitter and collector to eliminate lead losses. The current was determined by measuring the voltage across a precision resistor in series with the converter.



Figure 88. Test Arrangement for Converter 4

Work Function Measurements

Since the primary objective of this converter was to serve as a base line for evaluation of the slotted cavity emitter, it was decided to follow the experimental procedure as used by Breitwieser.²⁰ In this approach, current-voltage characteristics were obtained in the temperature range from 1300 to 1650°K with emitter sheath conditions varying from electron to ion rich by control of the cesium temperature. Spacing data provided helpful information as to the converter operating modes.

The effective emitter work function was determined from the measured electron saturation current at a very close spacing (4 to 8 microns). At this close spacing, space charge effects are minimized. Figure 89 shows a comparison of the measured work function to the value given by Houston-Nottingham.¹⁰ The emitter temperature was varied from 1300 to 1650°K for cesium temperatures of 473 and 523°K. As can be seen, the measured values compare favorably with Houston-Nottingham values.

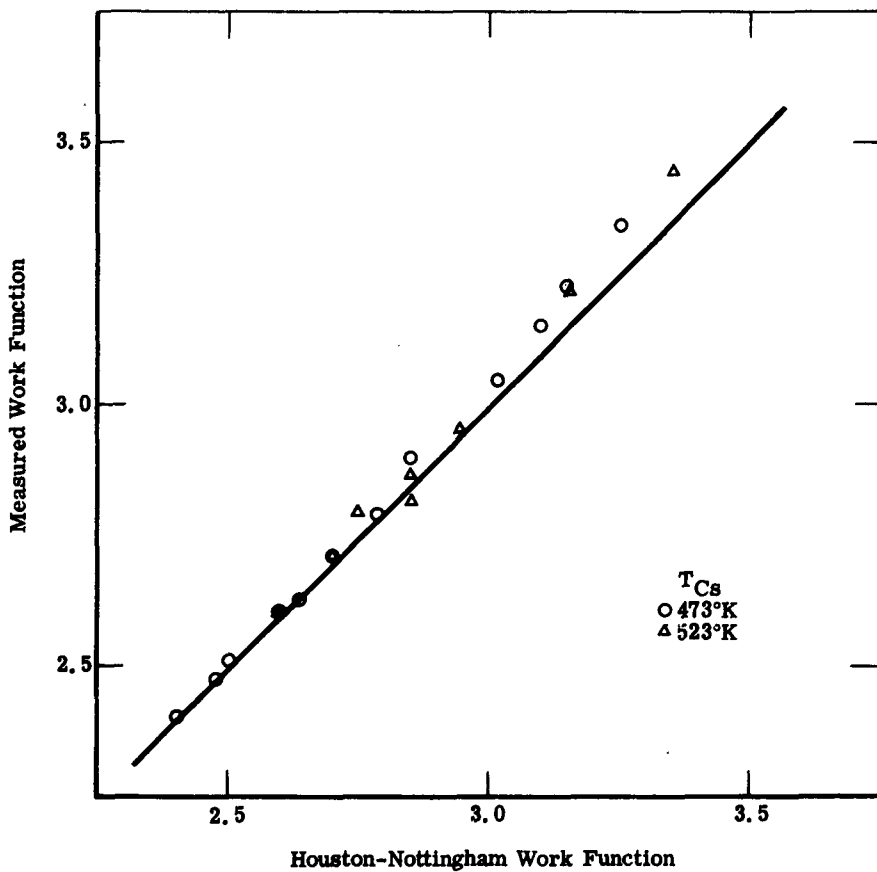


Figure 89. Comparison of Measured Work Function to Houston-Nottingham Values

In the electron-rich condition, the electron current is space charge limited in the power generating region. To determine accurately the saturation current, a Schottky plot is required with an accelerating field at the emitter of up to 30,000 volts/cm. However, when an ion sheath exists at the emitter surface, the electron current is not space charge limited. Thus, the saturation current can be measured at zero voltage on the I-V curve. The transition from an electron-rich to an ion-rich condition is quite apparent in Figure 90. For these data the cesium temperature was held constant at 473°K, and the emitter varied from 1329 to 1579°K. From 1329°K to the zero field condition at 1400°K, the emitter is operating electron rich. Above 1400°K, the emitter is ion rich. All data were taken at the 4- to 8-micron spacing. The increasing work function with increasing emitter temperature as given by Houston-Nottingham is clearly evident in this region.

In the ion-rich region, the current does not change appreciably with spacing until the plasma losses take effect. This is shown in Figure 91. Conversely, in the electron-rich condition, the electron current is quite sensitive to spacing (see Figure 92, sheets 1 and 2).

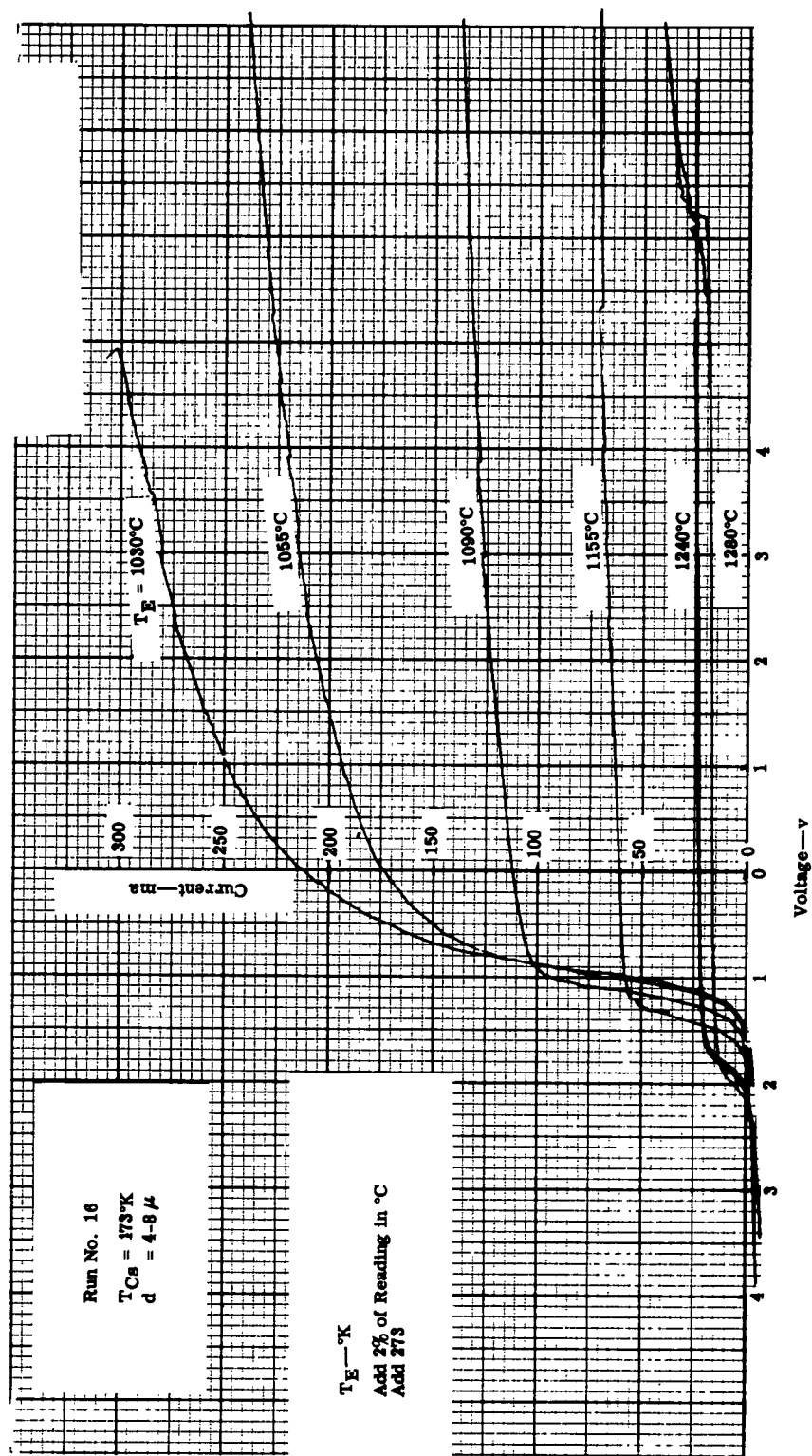


Figure 90. Current-Voltage Characteristics for Electron- and Ion- Rich Conditions

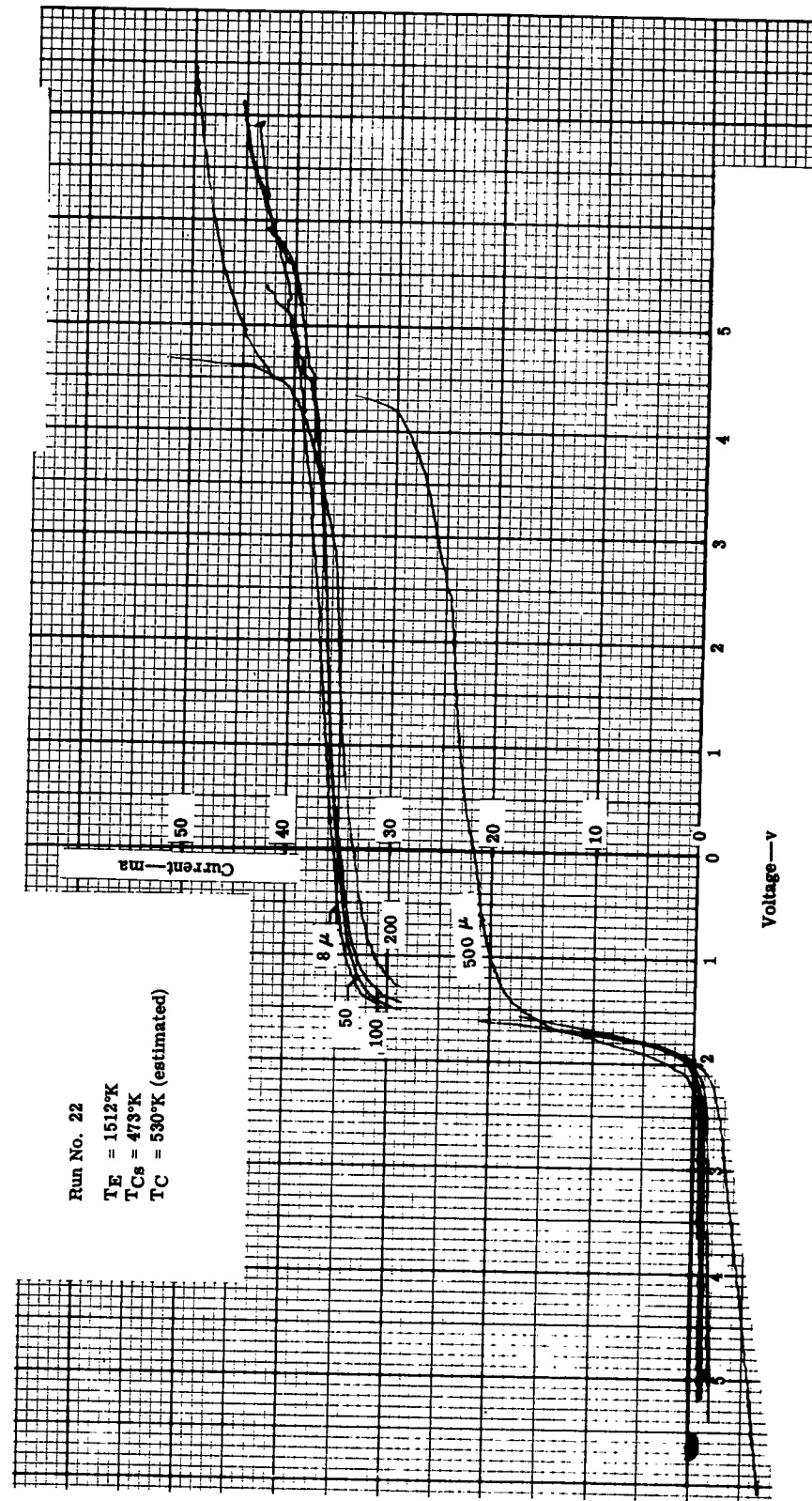


Figure 91. Effect of Spacing in the Ion-Rich Condition

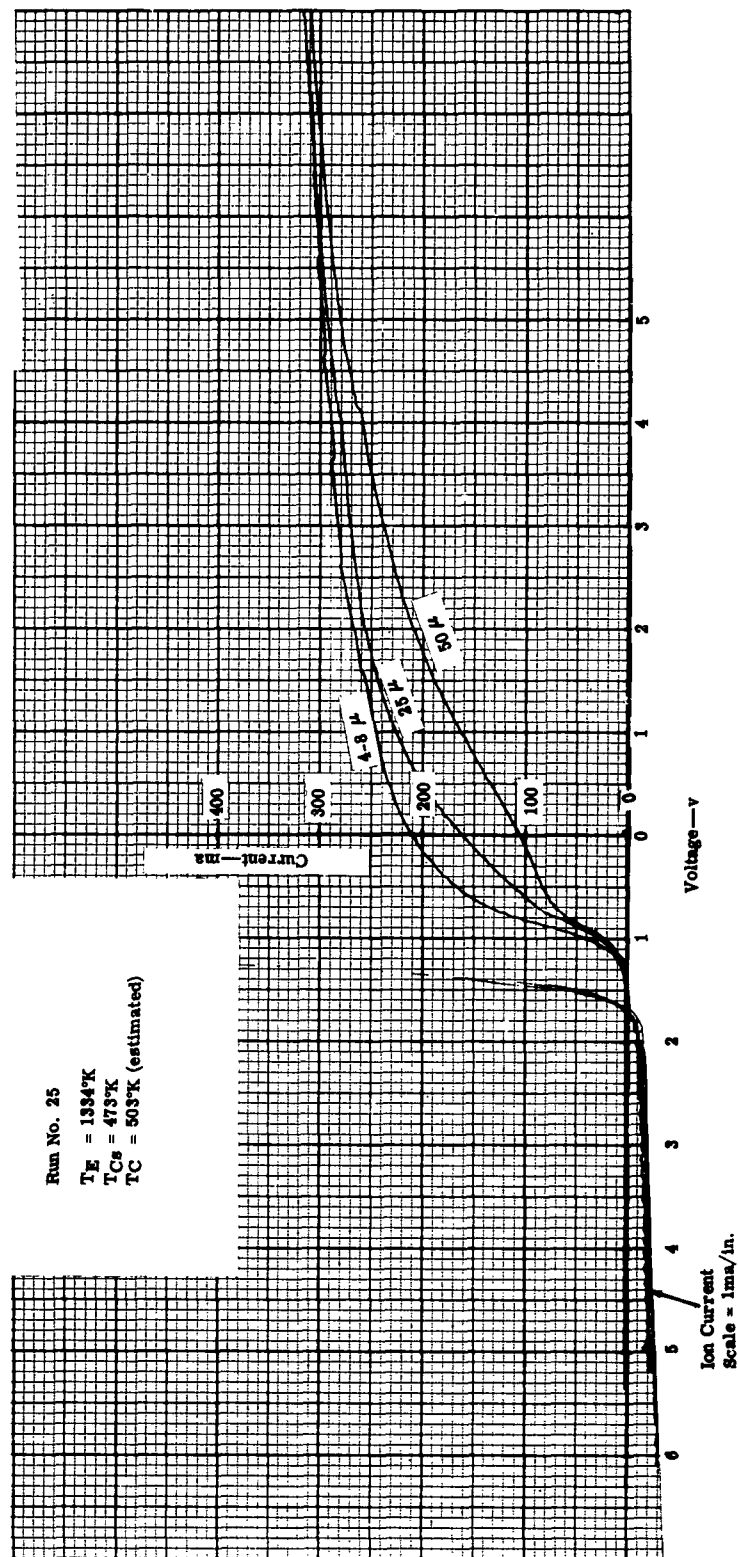


Figure 92. Effect of Spacing in the Electron-Rich Condition (Sheet 1 of 2)

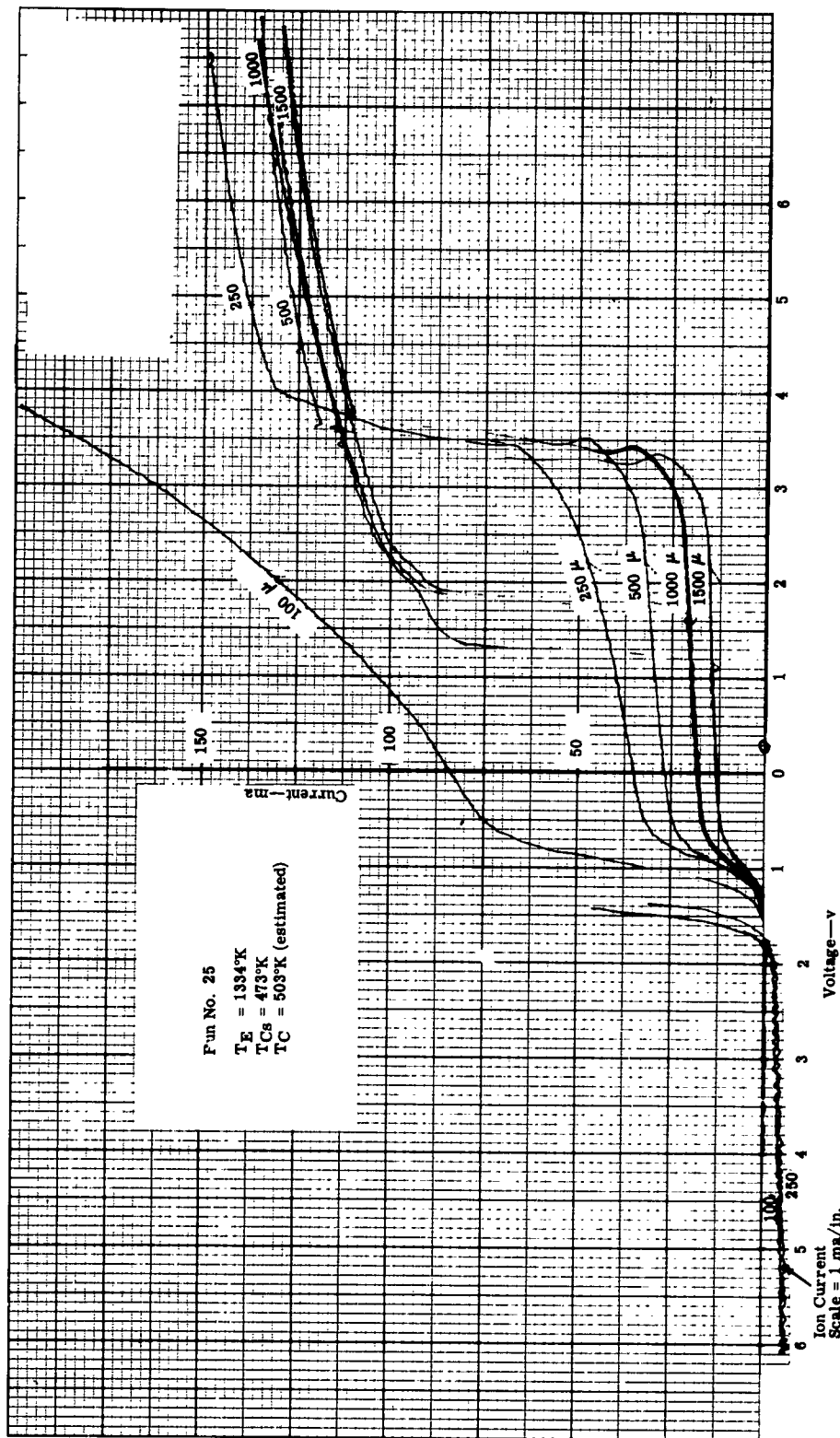


Figure 92. (Sheet 2 of 2)

It is useful for later comparison with slotted emitter data to plot the variation of saturation electron current density with values predicted by theory. For lack of a more elegant method, it was decided to use the short circuit current as a measure of the saturation current. In an ion-rich condition, such as Figure 91, this is a reasonable measure of the saturation current. On the other hand, in the electron-rich case, as in Figure 92, the short circuit current may be in error due to space charge effects. Figure 93 shows the results for $T_{Cs} = 473^{\circ}\text{K}$. The theoretical zero field temperature is also shown. There is great sensitivity to spacing below 1400°K and reduced sensitivity above this temperature, as shown in Figures 91 and 92.

Summary

Converter 4 was operated for 60 hr. The work function measurements agreed well with other published data on molybdenum. The general current-voltage characteristics were in agreement with those reported by Breitwieser in Reference 20. The test results indicated that the converter design concept was appropriate for "base line" converter measurements.

Converter 5

As reported in Section IV, Converters 5 and 6 had the same design as Converters 3 and 4 (see Figure 39). However, in these devices the planar emitter was replaced by a slotted geometry with the dimensions as shown in part A of Figure 94. In both converters the material was tantalum. In Figure 94, large-scale drawings are also shown of two excess area geometries studied by RCA.²² The saw-tooth design did not greatly improve performance; the box design was suspended in favor of the saw-tooth design. As may be seen from the large-scale drawings, the slotted emitter has a much different geometry than the RCA designs. Also, the theory of operation is quite different from the "cross current" theory proposed by RCA. Figure 95 shows Converter 5 before testing started at Allison on 12 August 1963. At the date of writing, the converter has operated 140 hr and is still in good condition.

Typical I-V Characteristics

The test arrangement for this converter was the same as described for Converter 4. Extensive data were taken over the following ranges:

- T_E —1400 to 1700°K
- T_{Cs} —398 to 548°K
- d —6 to 500 microns

Figure 96 shows the data at 1400/423. The curves suggest that an electron-rich condition exists at the emitter surface even though the local surface of the slot operates ion rich according to the Nottingham plot.¹⁰

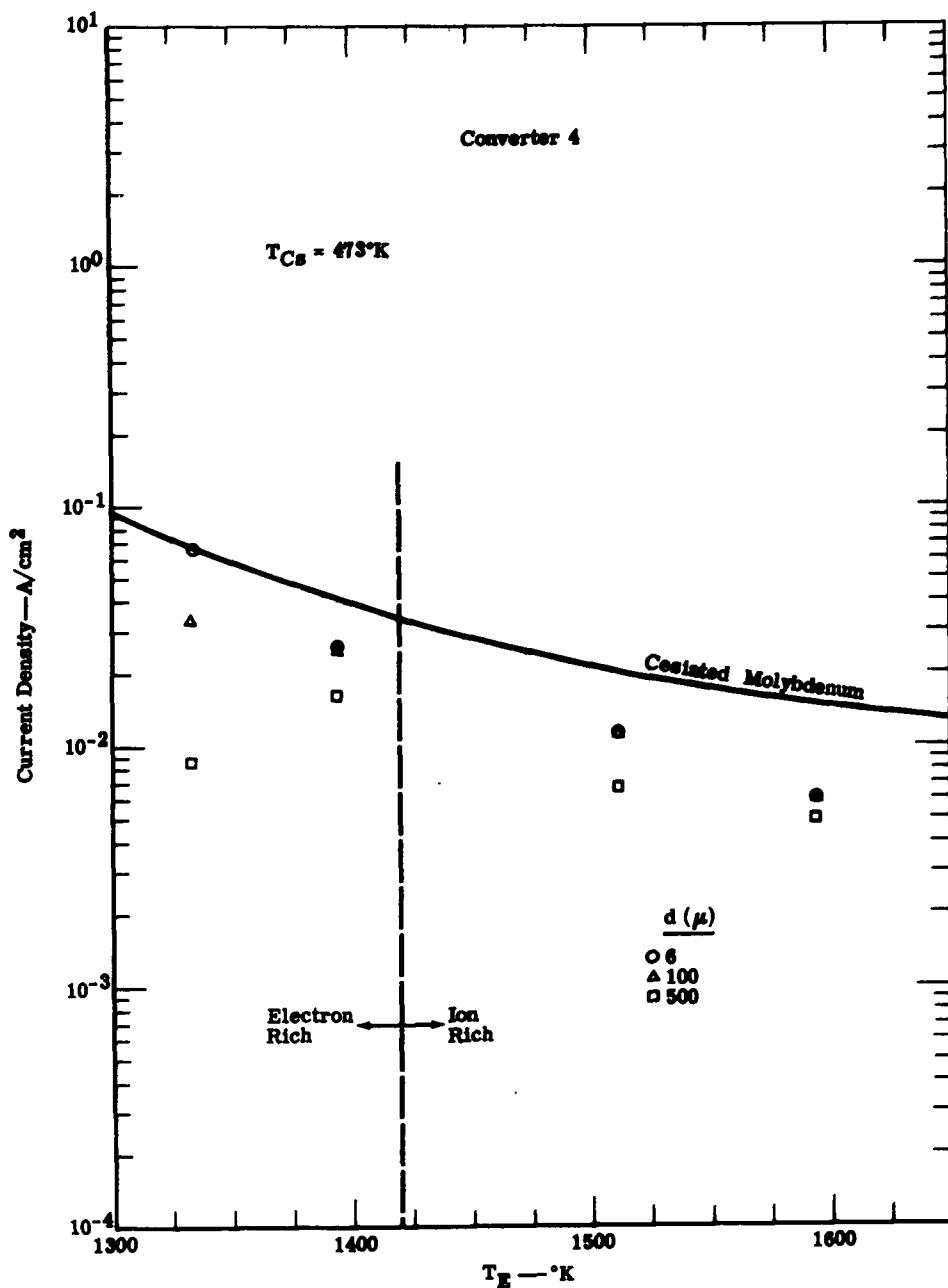


Figure 93. Comparison of Theory and Experiment at $T_{Cs} = 473^{\circ}\text{K}$ —Plane Emitter

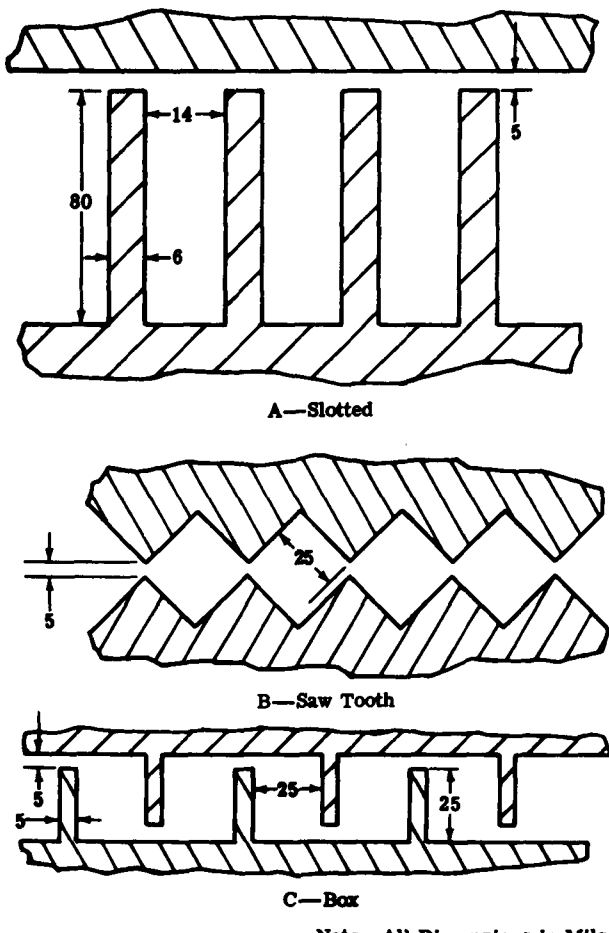


Figure 94. Dimensions of the Slotted Emitter and Two Other RCA Designs



Figure 95. Picture of Converter 5

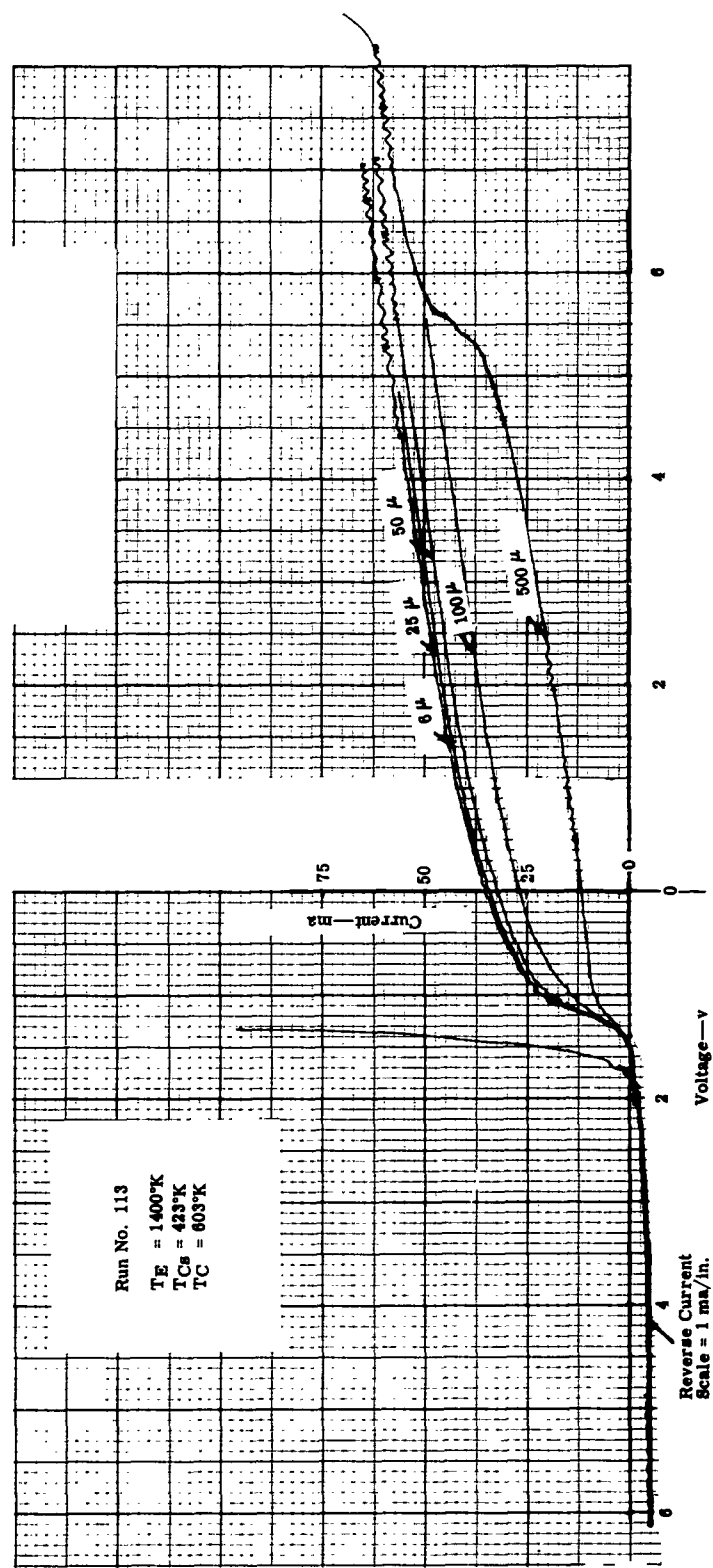


Figure 96. Current-Voltage Characteristic for 1400/423

If the emitter temperature is increased as in Figure 97, the converter characteristics shift to an extremely ion-rich condition. The reverse currents in Figure 97 are not ion currents, since later measurements showed these currents were due to electron emission from the collector. As the cesium temperature is raised at constant T_E as in Figures 98 and 99, then the electron current increases and the characteristics shift toward the electron-rich form. However, according to Reference 10, the zero field temperature for 1600/473 is 1375°K; therefore, the data in Figure 98 should show strong ion-rich characteristics. Even in Figure 99, the data should tend toward ion-rich behavior since the zero field temperature is 1500°K. Again, in Figures 98 and 99, the reverse currents shown are not a true measure of the ion current because the collector temperature was too high.

As further evidence to demonstrate the change in operating conditions between a plane surface and the slotted emitter surface, the data shown in Figure 100 were compared with converter 5 data of Figure 91 with approximately the same T_E/T_{Cs} ratio. Several differences are apparent.

1. Electron currents are much higher in Converter 5 even though the emitter is tantalum rather than molybdenum.
2. Converter 5 data are much more sensitive to spacing.
3. In Converter 5 the I-V curves at close spacing do not exhibit a "saturation" characteristic.

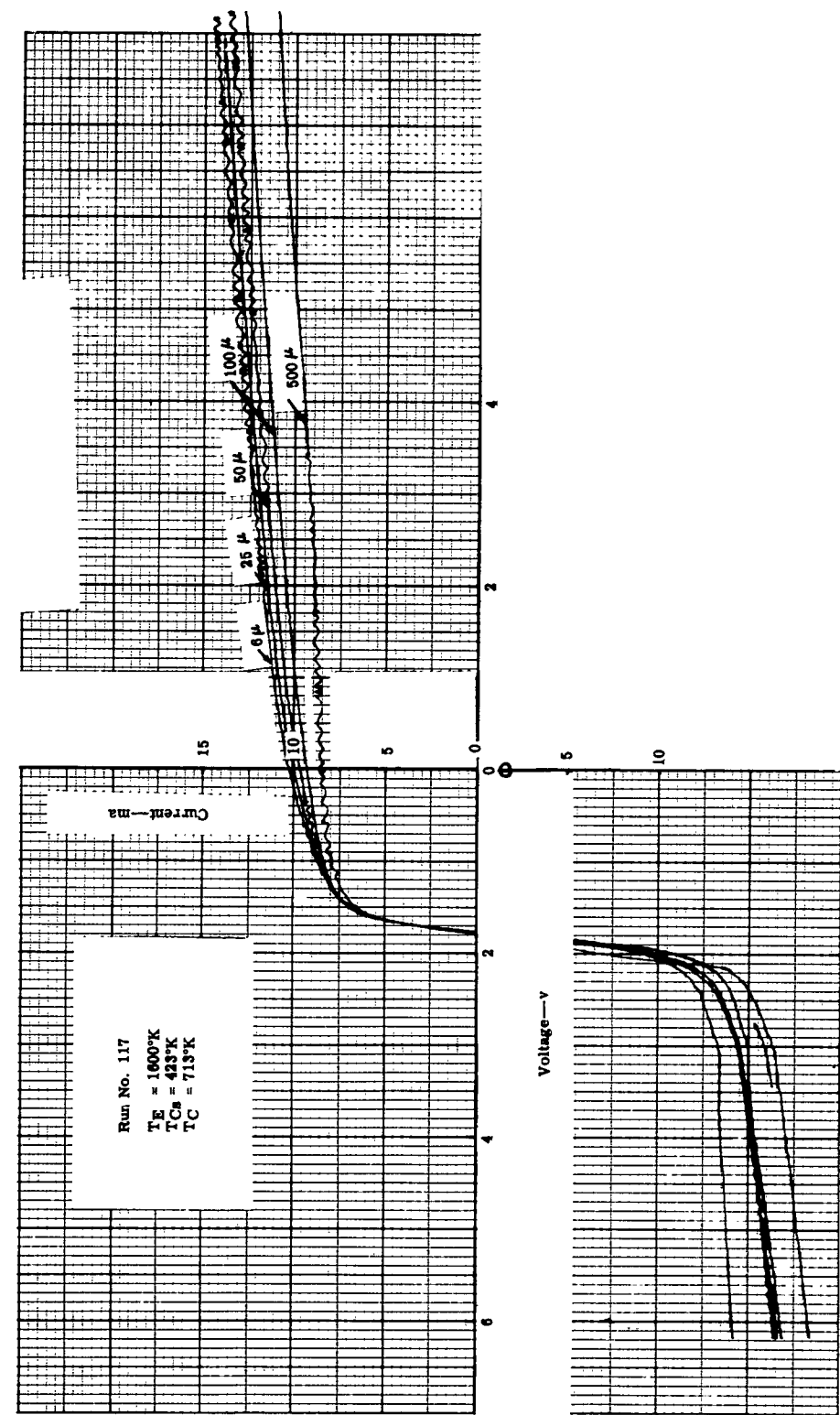
All of these differences substantiate the contention that for the same T_E/T_{Cs} ratio, the slotted emitter operates much more electron rich than predicted by Langmuir-Saha theory.

Comparison with Random Current Theory

As discussed in Section III, the random current theory should apply to the slotted emitter with the limitation that the random current cannot exceed the wall current. In the case of the emitter under study, the excess area factor is 8.9. Figures 101 through 107 compare the electron currents at short circuit with the predicted random current and the excess area current. Several observations are noted:

1. At wide spacing (50 to 500 μ) the data follow the random current model unless limited by the excess area factor.
2. At close spacing (6 μ) the data tend to follow the random current model unless limited by the random current model.
3. At every T_{Cs} the sensitivity to spacing decreases as T_E increases.

Figure 97. Current-Voltage Characteristic for 1600/423



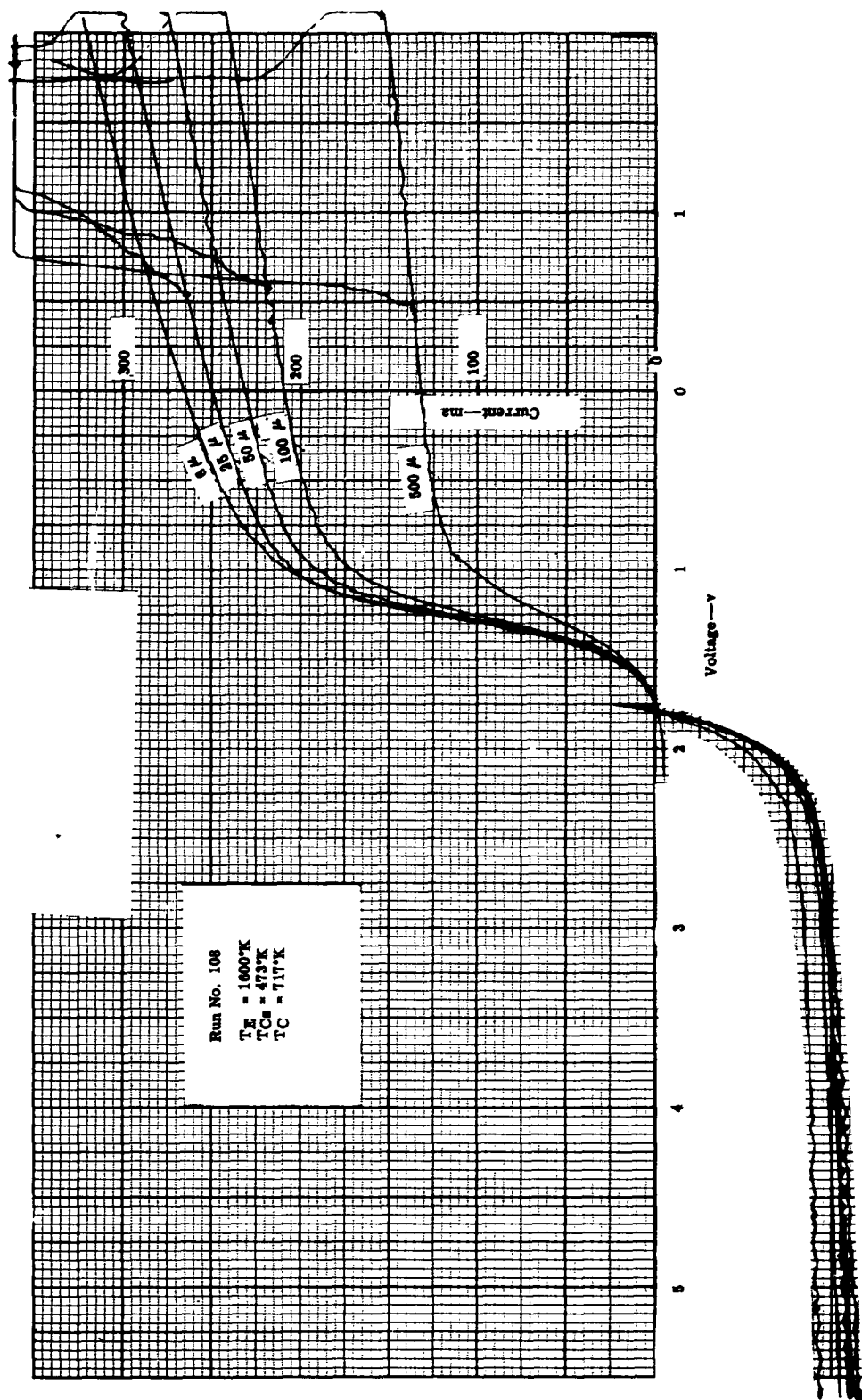


Figure 98. Current-Voltage Characteristic for 1600/473

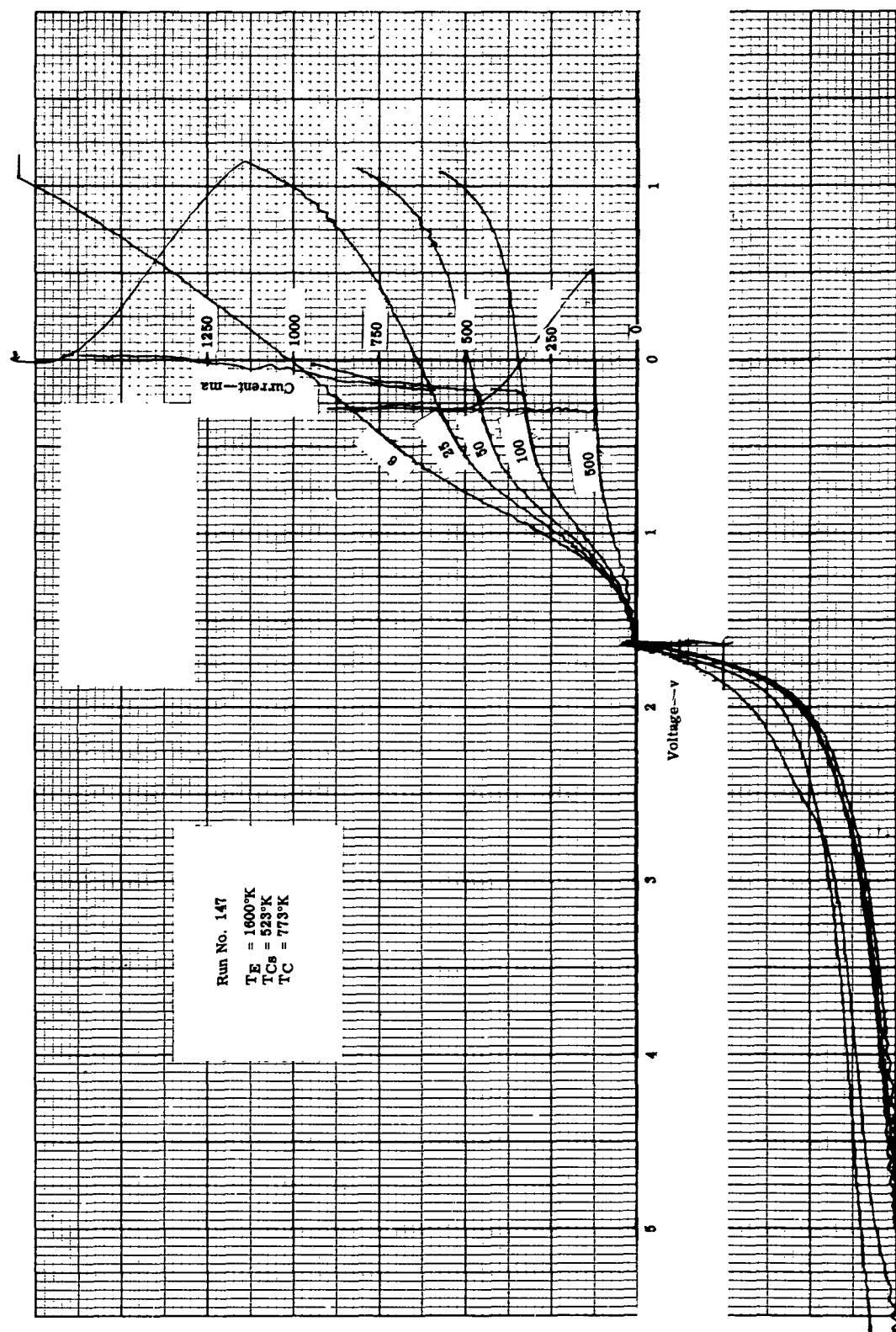


Figure 99. Current-Voltage Characteristic for 1600/523

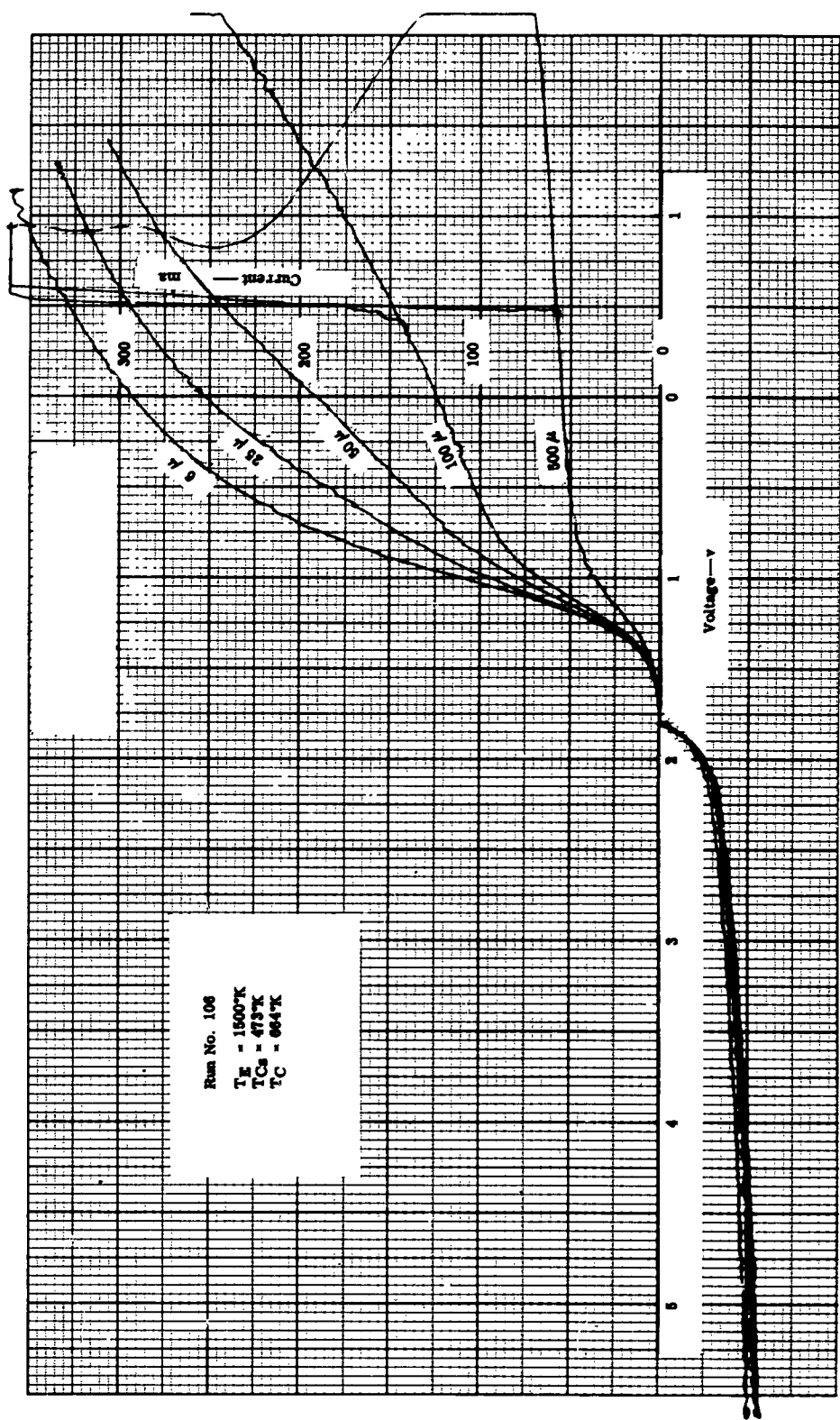


Figure 100. Current-Voltage Characteristic for 1500/473

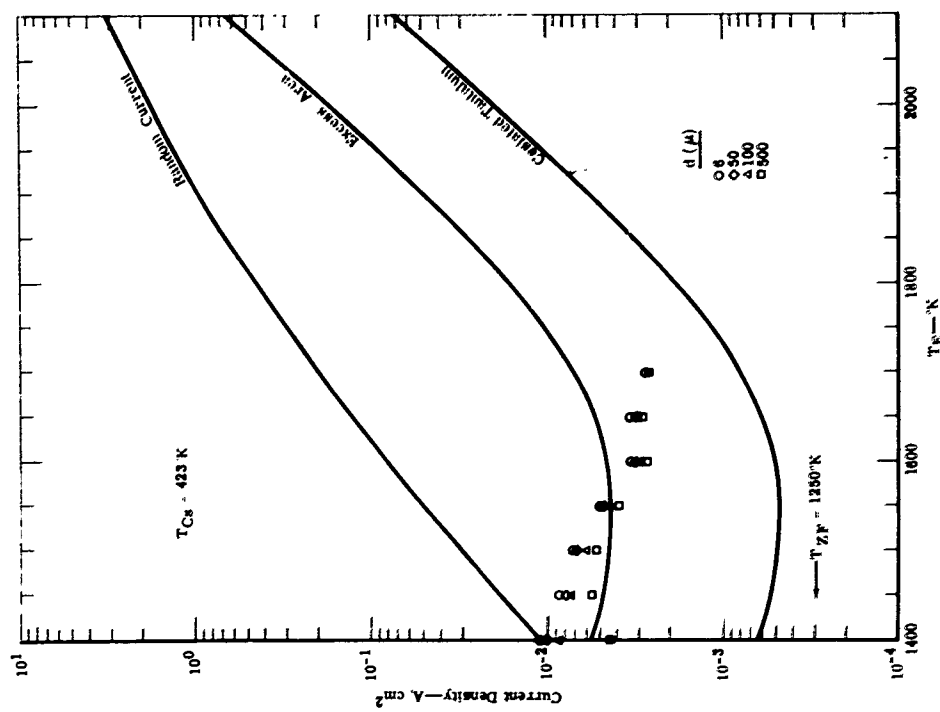


Figure 102. Comparison of Theory and Experiment
at $T_{Cs} = 423^{\circ}\text{K}$ — Slotted Emitter

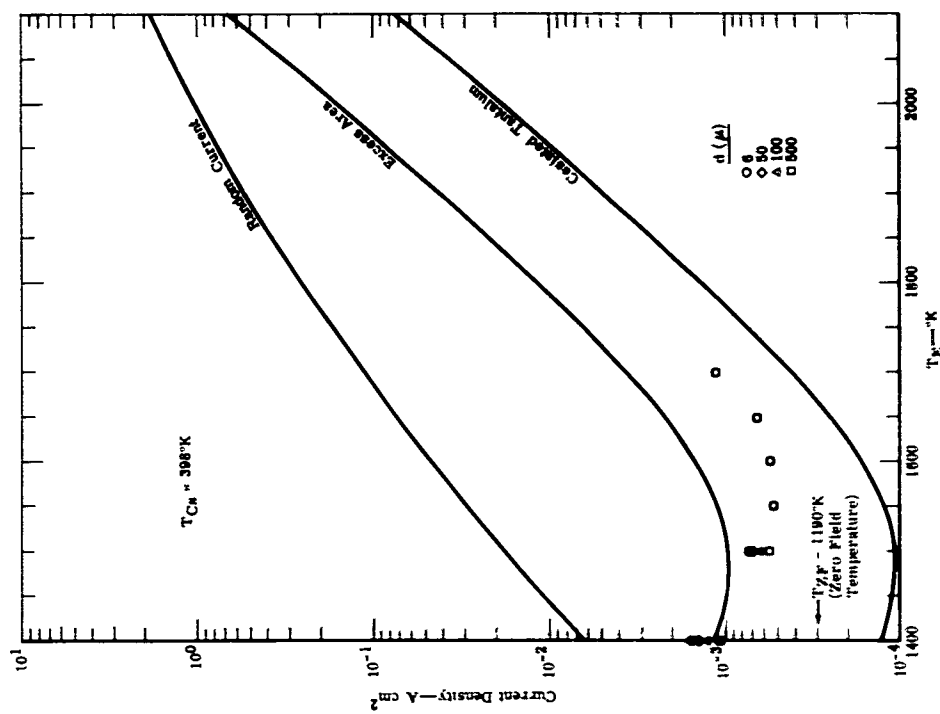


Figure 101. Comparison of Theory and Experiment
at $T_{Cs} = 398^{\circ}\text{K}$ — Slotted Emitter

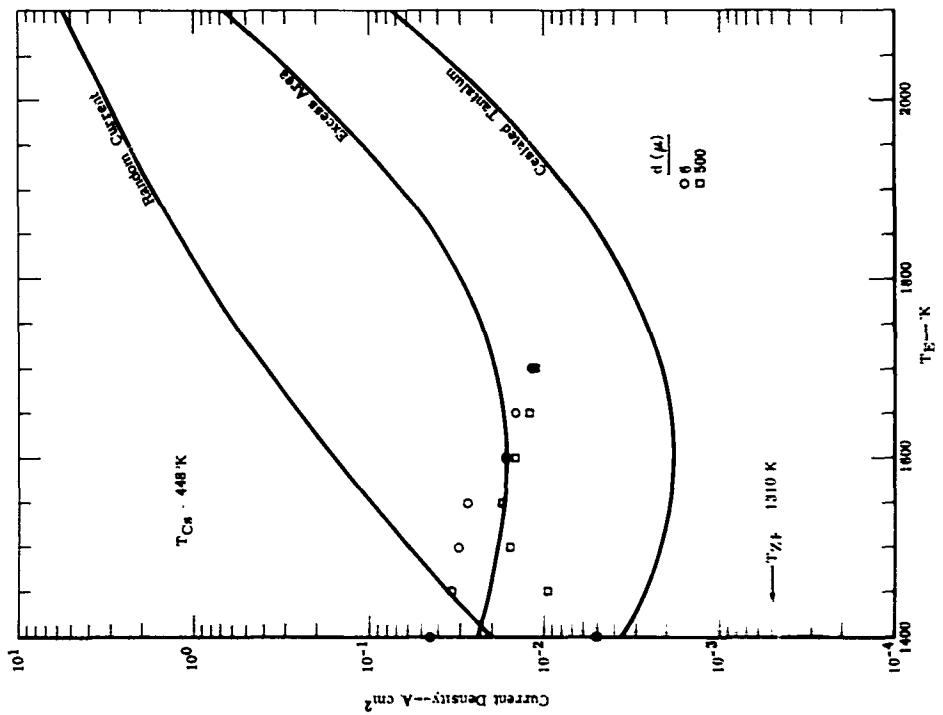


Figure 103. Comparison of Theory and Experiment
at $T_{Cs} = 448^{\circ}\text{K}$ — Slotted Emitter

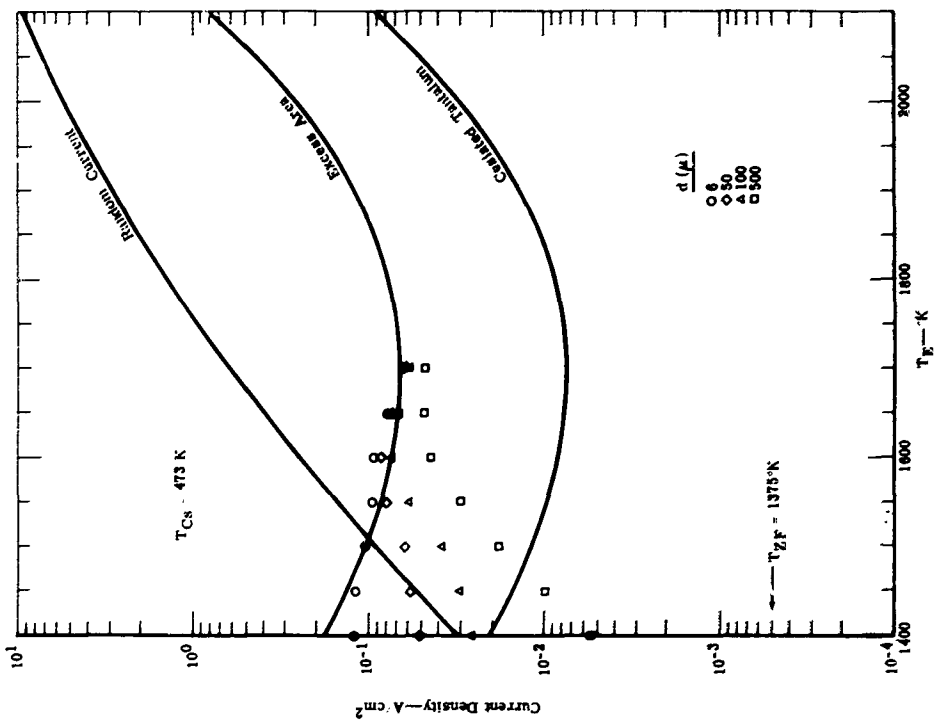


Figure 104. Comparison of Theory and Experiment
at $T_{Cs} = 473^{\circ}\text{K}$ — Slotted Emitter

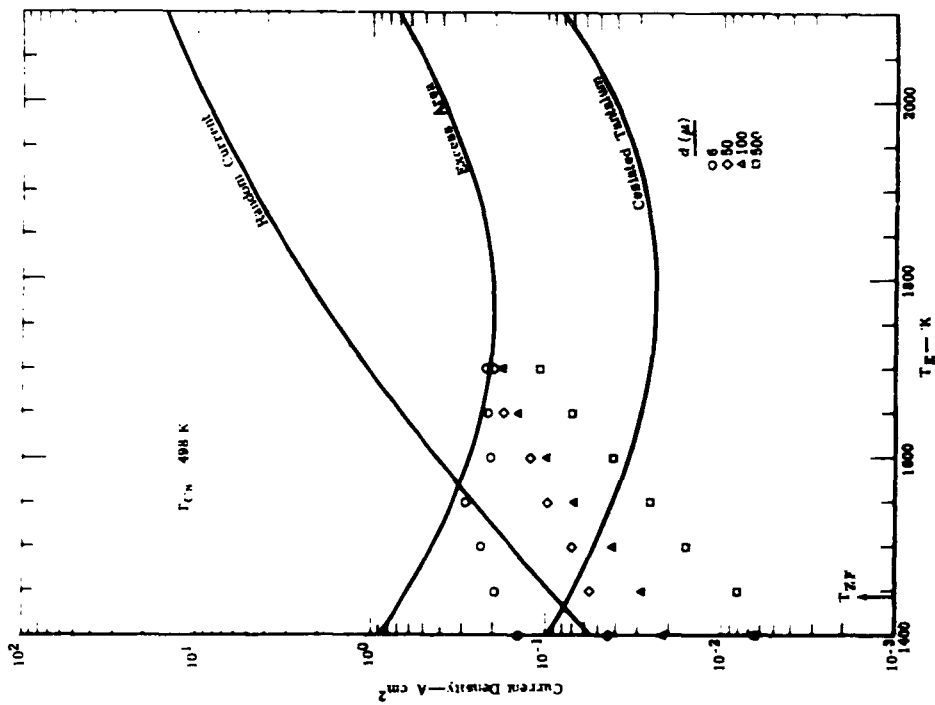


Figure 105. Comparison of Theory and Experiment at $T_{CS} = 498^{\circ}\text{K}$ —Slotted Emitter

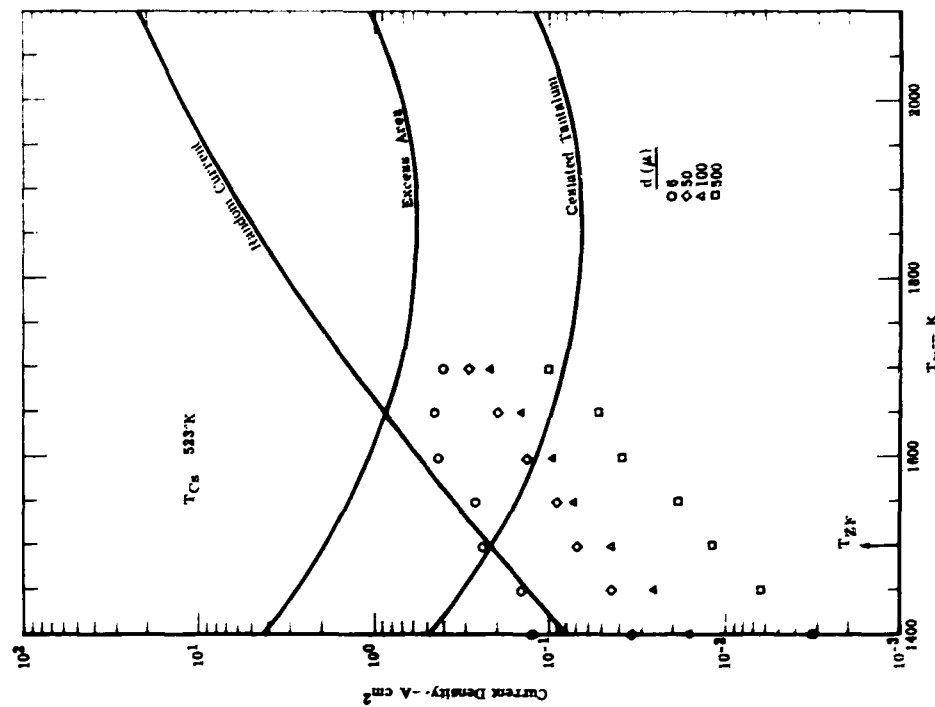


Figure 106. Comparison of Theory and Experiment at $T_{CS} = 523^{\circ}\text{K}$ —Slotted Emitter

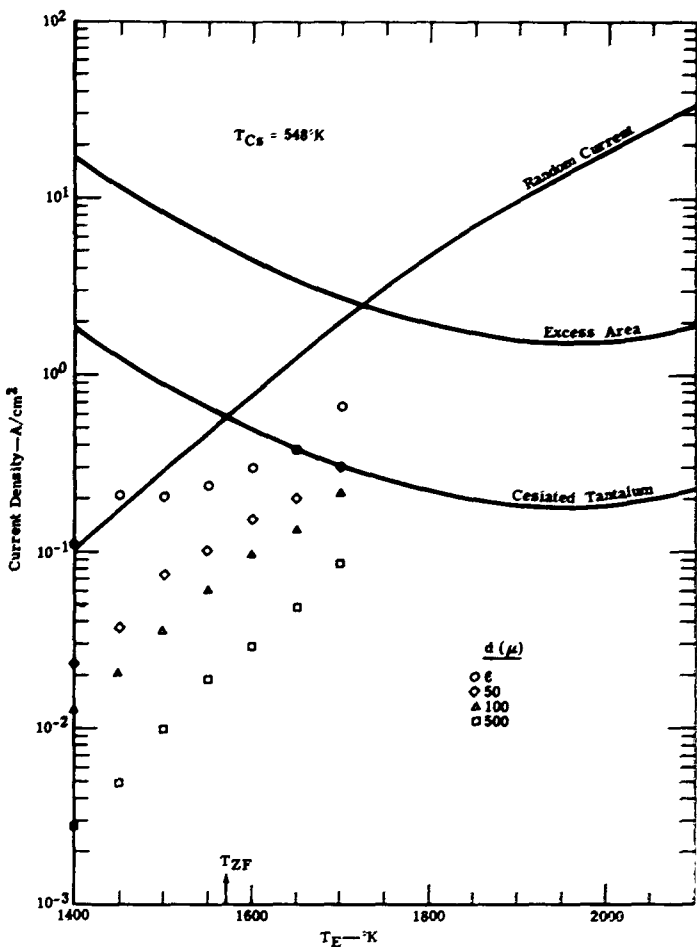


Figure 107. Comparison of Theory and Experiment
at $T_{Cs} = 548^{\circ}\text{K}$ —Slotted Emitter

Comparing these data with similar data on the plane molybdenum surface (see figure 93), electron space charge effects are evident at temperatures above the theoretical zero field temperature. Specifically, Figures 105, 106, and 107 clearly show this feature.

More data are required to establish in detail the differences between the slotted-type emitter and a planar surface. In particular, it would be desirable to measure the ion currents, and compare the data with the random current theory and the Langmuir-Saha current (possibly an excess area factor). Also, more detailed data from a planar device are required to define more exact differences in the current-voltage characteristics. However, based on the results reported here, several conclusions are evident:

1. Electron currents from a cavity emitter follow the trend predicted by the random electron current theory when not limited by the excess area factor.

2. Under the conditions shown desirable by the theory--i.e., strongly ion rich conditions along the cavity wall--the advantages of high voltage, wide electrode spacing, and low cesium pressure are obtained.
3. It is feasible to extract the excess current from a cavity emitter with an excess area of 8.9.

Converter 6

Testing was started on Converter 6 at CSF on 24 July 1963. Extensive data were obtained on this converter over the ranges:

- T_E --1300 to 1700°K
- T_{Cs} --423 to 573°K
- d --50 to 1000 microns

The results agree with those obtained on Converter 5. For example, Figures 108 and 109 compare the experimental currents at 490°K and 523°K--these results are similar to those shown in Figures 105 and 106. Testing is continuing on this device.

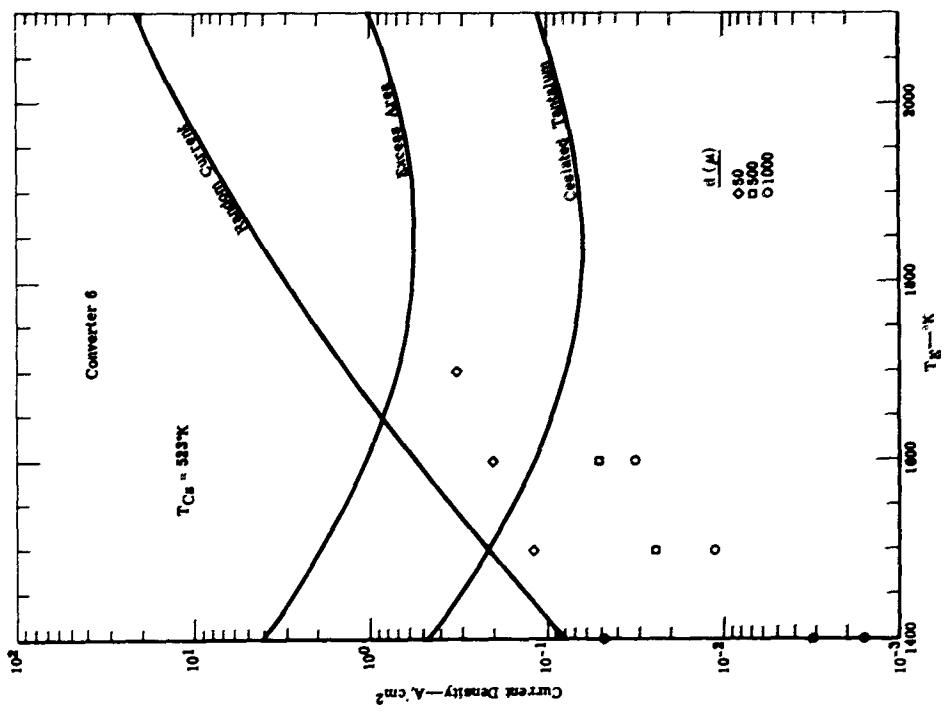


Figure 109. Comparison of Theory and Experiment at 523°K on Converter 6

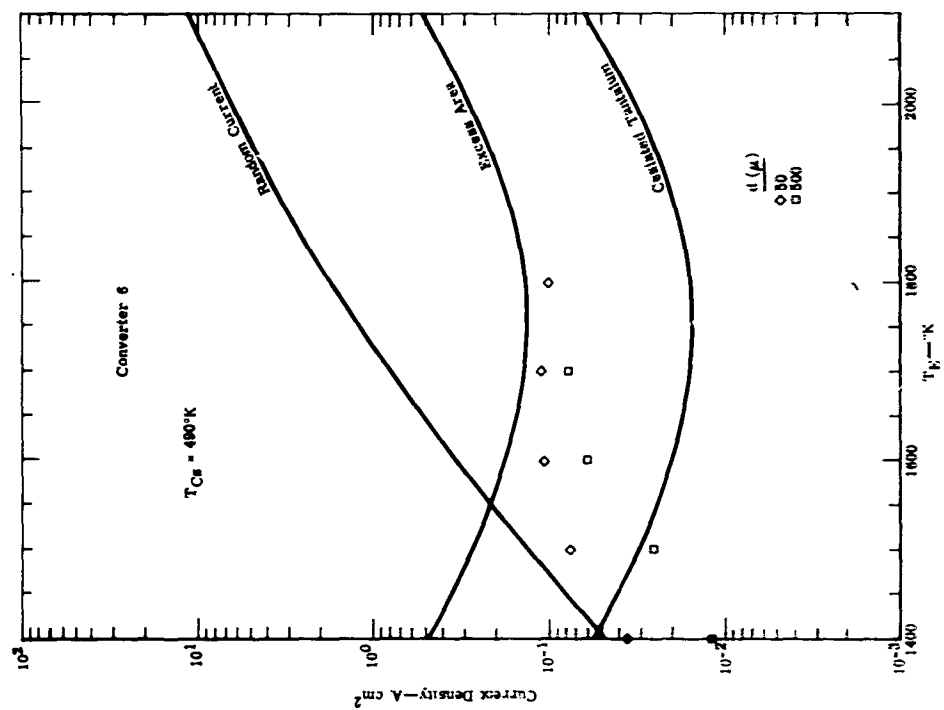


Figure 108. Comparison of Theory and Experiment at 490°K on Converter 6

VI. TECHNOLOGY FOR THERMIONIC CONVERTERS

MACHINING AND JOINING

Machining Emitters

Problems of fabricating emitter structures with planar geometry for experimental devices were studied. Typical emitter dimensions are shown in Figure 110. Considerable difficulty was encountered initially in attempting to machine the part on a lathe. Frequently leaks were found in the support envelope. A summary of the results is given in the following tabulation.

<u>Number of Pieces</u>	<u>Material</u>	<u>Wall Thickness (mm)</u>	<u>Number of Pieces Without Leaks</u>
2	Mo-Climax	0.2	0
12	Ta-Heracus	0.2	6
1	Ta-NRC	0.25	1
2	Ta-NRC	0.5	0
1	Ta-W-NRC	0.2	0

Thus, only seven out of 18 pieces were vacuum tight.

Based on the machining problems encountered, a roll extrusion process was investigated. Tooling has been designed and tested. Tantalum emitters of 0.2-mm wall thickness are now being made with no difficulty. In fact, a tantalum tube of 2-cm diameter, 60-mm length, and 0.075-mm wall thickness has been fabricated and was found to be vacuum tight.

Welding Emitters

Both tantalum and molybdenum disks have been successfully EB welded to a tantalum sleeve. The structures were leak tight after 20 cycles to 2000°K. A single crystal tungsten disk was successfully EB welded to a tantalum sleeve. However, a crack developed in the weld zone on the second cycle to 2000°K. Figure 111 shows several emitter samples including a roll-extruded tantalum structure.

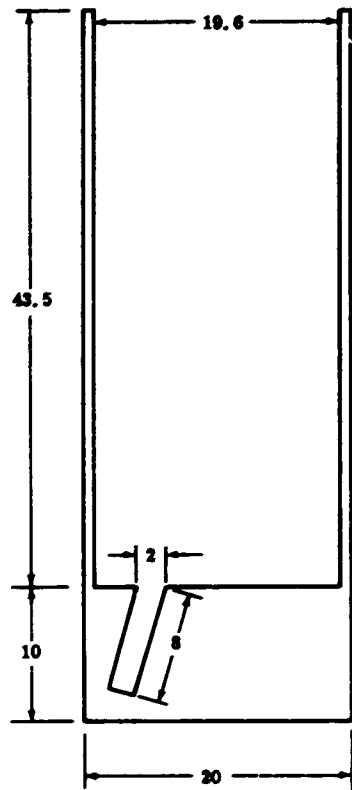


Figure 110. Dimensions of Typical Emitter

SEAL DEVELOPMENT

A ceramic-metal seal of Alucer 99 to niobium using a Ti/Ni braze filler has been developed. The first tests were made on a sample with dimensions as shown in Figure 112. The brazing temperature was 1050°C--brazing was done in a vacuum. Six samples were prepared and evaluated by thermal cycling in an argon atmosphere. The following temperature-time schedule was employed:

- Heat from 300 to 700°C in 15 min
- Stabilize for 60 min at 700°C
- Cool from 700 to 300°C in 15 min

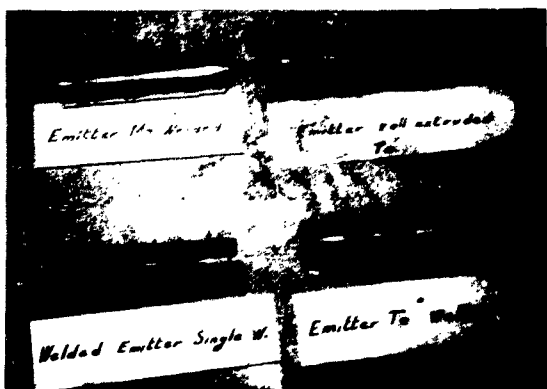


Figure 111. Several Emitter Samples

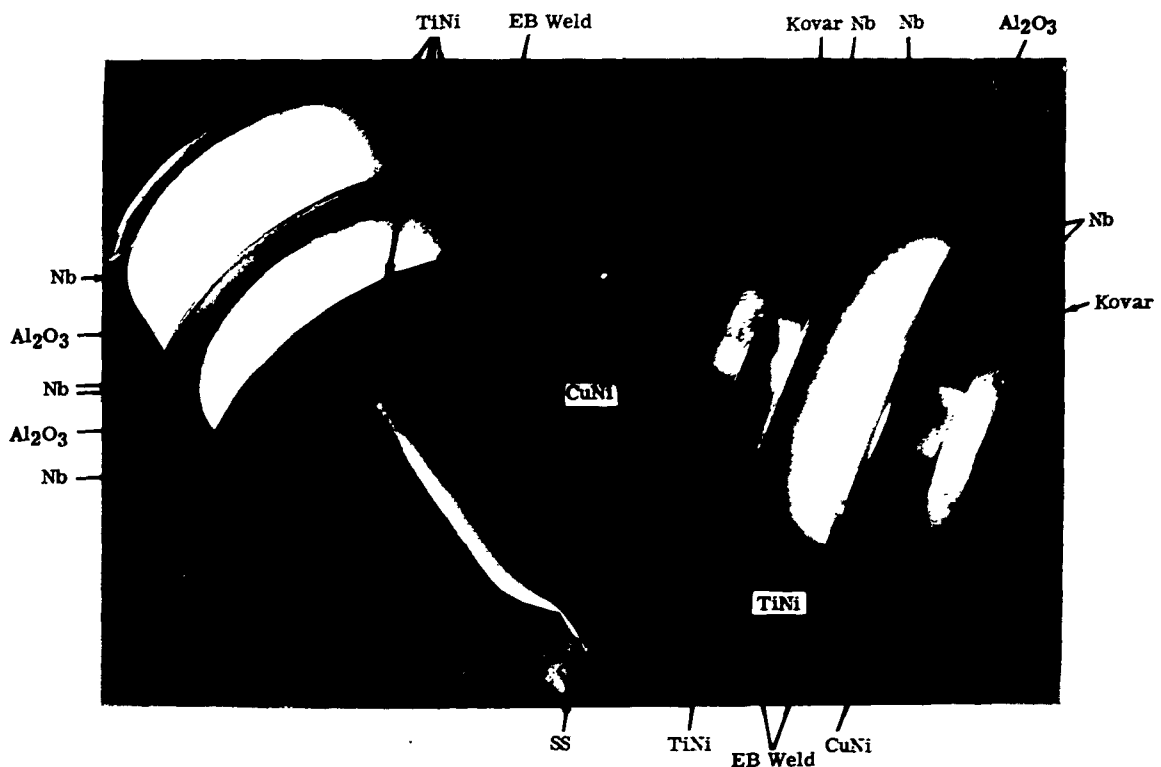


Figure 112. Sample Ceramic-Metal Seals

After 36 cycles, all samples were vacuum tight. Other samples were prepared for cesium corrosion evaluation.

A seal between niobium and sapphire was investigated since it was desired to have windows in some research devices, especially for spectroscopic studies. Several samples have been prepared successfully using a Ti/Ni braze alloy (Figure 113). One sample remained vacuum tight after six cycles to 700°C.

Techniques have also been developed for making several brazes on one assembly—for example, Figure 114 shows an assembly including sapphire- and alumina-to-niobium seals.

CESIUM CORROSION

Cesium corrosion tests have been conducted using the furnace shown in Figure 115. Specimens are placed in the test container shown in Figure 116. The cesium temperature can be controlled by adjusting the length of the tube which protrudes below the furnace base. Other test containers, as shown in Figure 117, are used to evaluate ceramic-metal seals. Test conducted during this project have been at 600°C for 500 hr with a cesium pressure of 10 mm Hg. Table 6 summarizes the corrosion test results. Stainless steel, copper, nickel, and titanium appear satisfactory for devices up to 600°C. The Alucer 99 alumina needs further



Figure 113. Sapphire-Niobium Seal Samples

tests since the first sample failed completely while the second test indicated little attack. It is possible that there was a leak in the first test container. It appears that ceramic-metal seals which depend upon a metallized layer of lithium molybdate are not feasible.

Tests have been completed on several bonded structures, but the results are not complete at this time. Structures tested include:

- Alucer 99 with Ag-Cu braze
- Stainless to stainless with Cu-Ni braze
- Stainless to Ti with Ag-Cu braze
- Alucer 99-Nb with Ti-Ni braze
- Alucer 99-Nb with V braze
- Metallized Alucer 99-Nb with Cu-Ni braze
- Metallized Alucer 99-Nb with Nicrobrazee
- Stainless to stainless with Nicrobrazee
- Nb to stainless with Nicrobrazee

Preliminary analysis shows that the Alucer 99 to Nb with Ti-Ni successfully passed the 500-hr test.



Figure 114. Assembly Including Several Ceramic-Metal Seals

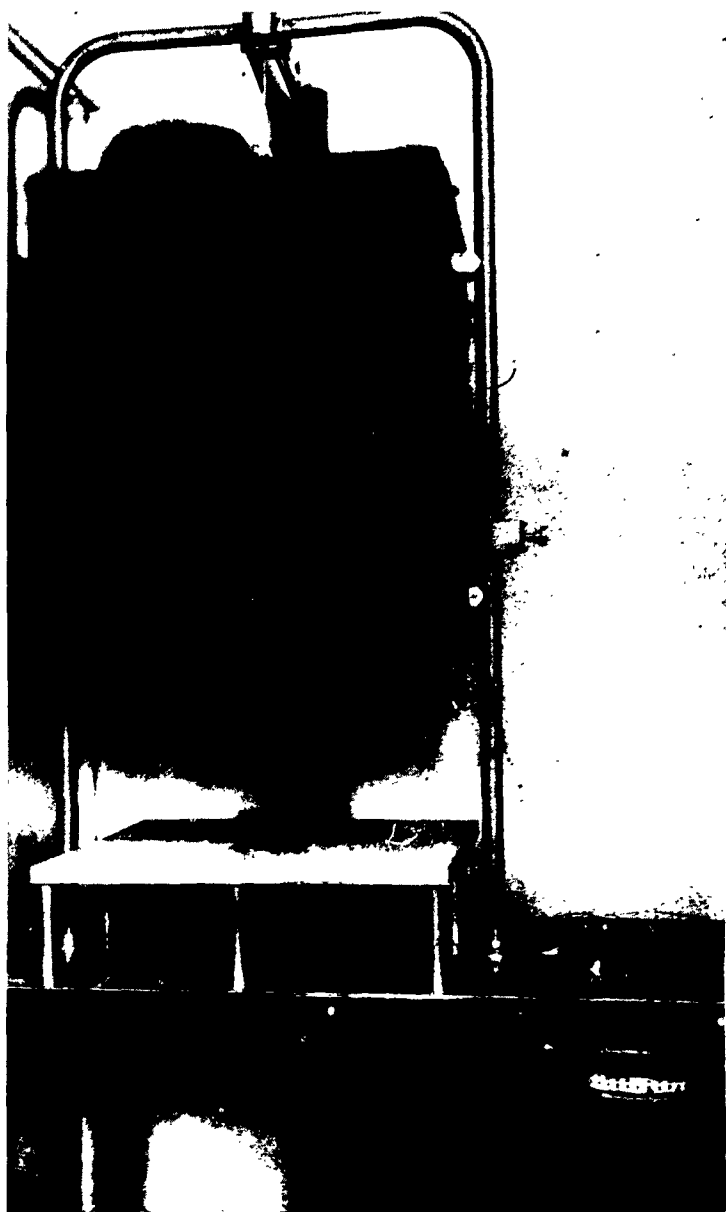


Figure 115. Corrosion Test Furnace

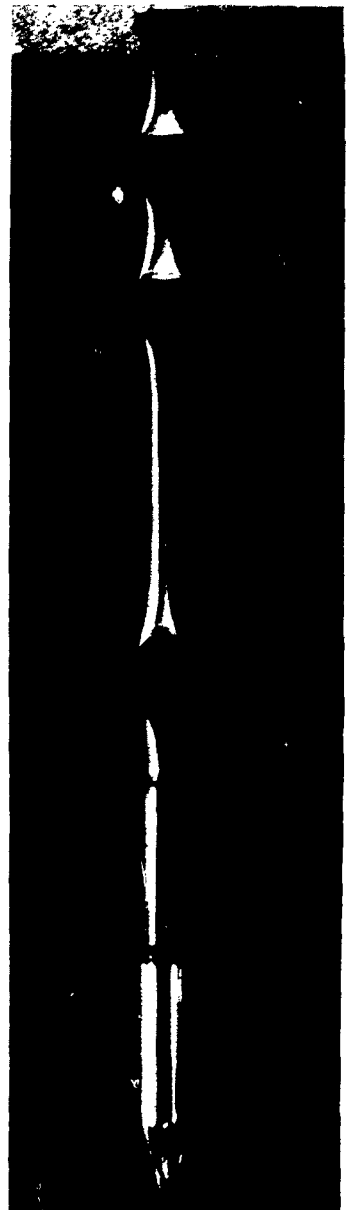


Figure 116.
Corrosion Test Container



Figure 117. Corrosion Test Container for Ceramic-Metal Seals

TABLE 6
Summary of Corrosion Tests

Material	Weight of Sample (mg)		Weight Change (mg/cm ²)	Results of Micro- photographic Examination
	Before	After		
Nickel—Polished	840.20	840.20	0	No visible attack
—Not Polished	972.75	973	+0.25	
Copper—Polished	1888.60	1888.65	+0.024	Visible attack on surface layer
—Not Polished	2169.50	2169.65	+0.07	
Stainless				
Steel—Polished	1588.15	1588.65	+0.24	No visible attack
—Not Polished	2250.90	2251.35	+0.7	
Titanium—Polished	708.75	709	+0.13	No visible attack
—Not Polished	1115.90	1116.3	+0.21	
Alucer 99				
(No. 1)—Polished	992.65	1076.60	+136.92	Complete destruction
—Not Polished	992.60	1187.50		
Wesgo				
AL300—Polished	862.65	865.40	+1.1	Vitreous phase attack in sample
—Not Polished	935.80	938.00	+0.88	
Coors				
AD96—Polished	911.60	913.65	+0.82	Vitreous phase attack
—Not Polished	913.70	916.50	+1.1	
Alucer 99*				
(No. 2)—Polished	591.30	591.25		Vitreous phase in bond
—Not Polished	903.20	904.00		
Ba-Sr-Ca**—No. 1334	261.75	258.50		Visible attack
—No. 3704	286.40	291.90		

* Metallized with lithium molybdate

** Oxide cathode

CHEMICAL VAPOR DEPOSITION OF TUNGSTEN

The progress of an investigation of the chemical vapor deposition of tungsten by the hydrogen reduction of tungsten hexafluoride is presented in this subsection. The objectives of the investigation were:

1. To conduct a comprehensive study of the process to determine if the properties and the crystal orientation can be predicted and controlled by controlling the reaction variables
2. To develop techniques for depositing tungsten, both as free standing structures and as coatings on refractory metals, for use in thermionic converters
3. To develop techniques for joining refractory metals by vapor deposition as an alternate to welding

The first experience with this process at Allison was in 1960 when an investigation was conducted to determine the feasibility of applying tungsten liners to graphite rocket nozzles by vapor deposition.²³ Two subscale nozzles, which had a surface area of approximately 25 in.², were successfully plated with 40 mils of tungsten. Although the application was shown to be feasible, the advancement of more attractive methods of producing nozzle liners precluded the use of vapor deposition and no further work was done with the process at that time.

In 1962 interest in chemical vapor deposition was revived because of potential application in thermionics. An agreement was formulated with San Fernando Laboratories in Pacoima, California (a company active commercially in the field of chemical vapor deposition), to investigate the potential of vapor deposited refractory metals in the field of energy conversion. Results were attractive and it was concluded that Allison should expand its capabilities in vapor deposition.

Late in 1962, per agreement, two visits were made to San Fernando Laboratories for consultation on techniques and the design of apparatus. In early 1963, the Allison Materials Research Laboratory constructed apparatus and initiated the present project.

The investigation is presently 60% completed. It has been shown that vapor deposits have a preferred orientation, and that the degree and type of orientation can, to a certain extent, be controlled by the plating conditions. Two of the three principal orientations have been produced parallel to the surface—the (100) and the (111) planes. As yet, the (110) plane has not been controlled. All deposits have a columnar structure as plated but recrystallize more or less completely to an equiaxed structure when heated to 2300°K. This is believed to be due to stresses in the deposits. The (100) orientation is retained through recrystallization without loss in magnitude, but the (111) orientation suffers a considerable loss. Free standing structures have been produced as thin as 3 mils and have been found to be vacuum tight. Coatings

have been applied to tungsten but have not been evaluated. Two sections of tungsten tubing formed by vapor deposition have been joined by vapor deposition. The joint was vacuum tight.

Process Development

Description of Apparatus

A photograph of the apparatus is shown in Figure 118 and a diagram is shown in Figure 119. The deposition chamber is constructed of Inconel and has a Plexiglas window for viewing. Rubber O-rings are used to seal the window and to seal the flange to the base plate. The substrate is positioned on a spindle which is rotated at 20 rpm through an O-ring seal and a Teflon bearing in the base plate. Heat is supplied by a 7.5-kw, 150-400-kc induction unit. Temperature is controlled by a thermocouple which is run through the spindle and placed against the inside wall of the substrate. Rotation of the thermocouple is provided by mercury slip rings. The reactants are mixed and brought into the chamber through a common line and are delivered to the specimen through a slotted aluminum oxide jet which runs the full length of the specimen approximately 1/4 in. from the surface. Hydrogen flow is regulated by Manostat predictability flowmeters and can be varied from 5 to 6000 cc/min. The tungsten hexafluoride flow is controlled by a Hastings-Raydist mass flowmeter that has a range of 0 to 200 cc/min. Pressure is maintained and spent gases are removed by a water ejector vacuum pump, which also serves as an efficient exhaust scrubber. The pressure is regulated by throttling the water to the pump and by bleeding nitrogen into the exhaust line.

Effects of Variables and Experimental Approach

The factors which are the most likely to influence the properties and orientation of chemical vapor deposits are pressure, temperature, mixture ratio, flow rate, and substrate. To determine the effects of these variables in a reasonable number of tests, the program was divided into groups of experiments. Each group was designed to study the effects of two or three variables.

In the first group the pressure was fixed at 0.3 atm, wrought copper was chosen as the substrate, and the mass flow rate of WF_6 was fixed at 0.025 gm/cm²/min. The total gas flow, of course, varies considerably with mixture ratio but it was considered more meaningful to maintain a constant quantity of available tungsten. Deposits were made at three different molar ratios of hydrogen-to-tungsten hexafluoride—6:1, 30:1, and 60:1—which amounts to two times, 10 times and 20 times stoichiometric hydrogen. A number of specimens were prepared at each mixture ratio over a range of temperatures. The deposits were then evaluated. The results showed that the most marked effects of the variables were reflected in the orientation (Table 8). At the lower mixture ratios, 6:1 and 30:1, a (100) preferred orientation resulted, and at the 60:1 ratio the preferred orientation was (111). The most highly oriented (100) deposits were produced at the lowest temperatures while intermediate temperatures were best for the (111) orientation.

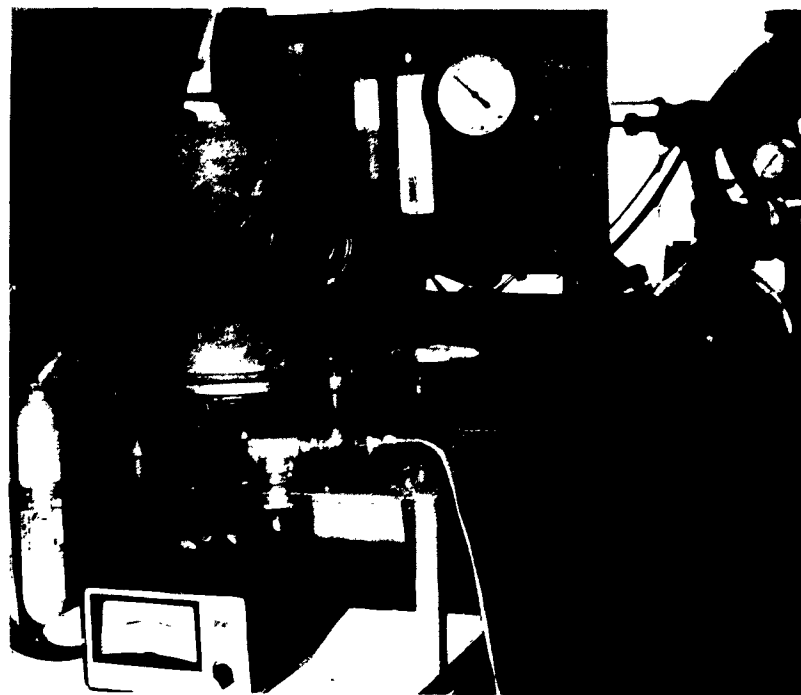


Figure 118. Tungsten Vapor Deposition Apparatus

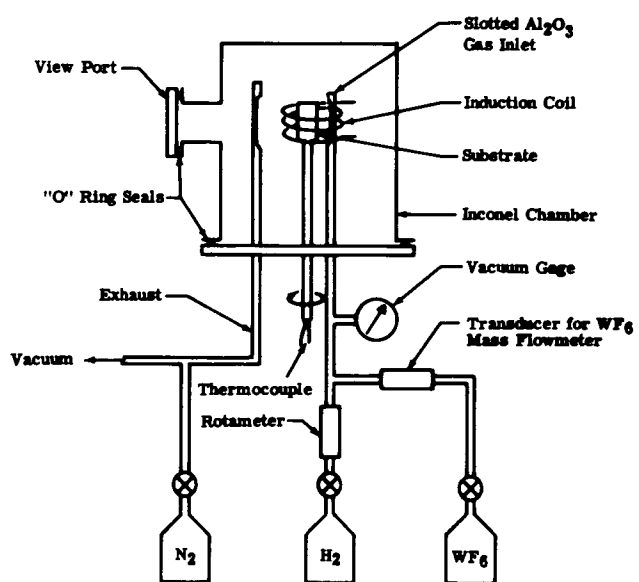


Figure 119. Tungsten Vapor Deposition Schematic

To determine the effects of flow rate, additional specimens were then prepared at each ratio at the temperature at which orientation was highest at one half and twice the mass of WF₆. The results were the same. Thus, it could be concluded that at 0.3 atm, temperature and mixture ratio are the orientation determining parameters. A similar group of deposits was prepared at 0.8 atm using the same procedure but has not been sufficiently evaluated to draw conclusions.

A third group is planned at 0.1 atm. There have been no indications as yet that the (110) orientation can be controlled, but further attempts will be made. Since mixture ratio seems to be the most important controlling factor, deposits should be made at extremely high ratios. The effects of substrate are being determined in a separate group. Deposits have been made on copper, graphite, and electroplated nickel. No change in orientation has been noted, but there have been indications that the magnitude of preferred orientation may be enhanced by the choice of substrate. Additional work is planned in this area.

Evaluation of Deposits

Deposits were evaluated by hardness, metallographic examination, and X-ray diffraction analysis. Since in actual application emitter deposits will be exposed to very high temperatures, examinations were made both as plated and after exposure to 2300°K for 2 hr.

Crystal Orientation

All preferred orientation studies in this program were conducted on a General Electric XRD-3 diffractometer. A special diffractometer sample holder was built to accommodate either cylindrical or flat specimens. To allow integration of the specimen surface, rotational motions were incorporated into the holder. Cylindrical specimens are rotated about the cylinder axis and flat specimens are rotated about the axis normal to the surface being analyzed. The specimen is rotated at a speed of approximately 120 rpm by a Universal motor coupled to the specimen holder by a flexible cable drive. A 1/2-rpm synchronous motor can also be used to rotate the specimen at a slower rate, thus allowing a complete pole concentration mapping of cylindrical surfaces. Photographs of the specimen holder are shown in Figures 120, 121, and 122.

A copper anode X-ray tube in conjunction with a nickel filter provides the CuK_α radiation for the analysis. A 0.4° incident beam slit is used to give a narrow beam at the sample, minimizing the curvature effects of the cylindrical surface of the specimens. The sample is positioned so that the cylinder axis is perpendicular to the plane of the incident and reflected X-ray beams, and both the incident and reflected beams make equal angles with the tangent to the cylinder surface (Figure 123). This ensures that only planes parallel to the surface are in a position for diffraction to occur. The specimen is then rotated about the cylinder axis and the intensity of the diffracting planes is recorded on a strip chart recorder as a function of twice the Bragg angle, θ .

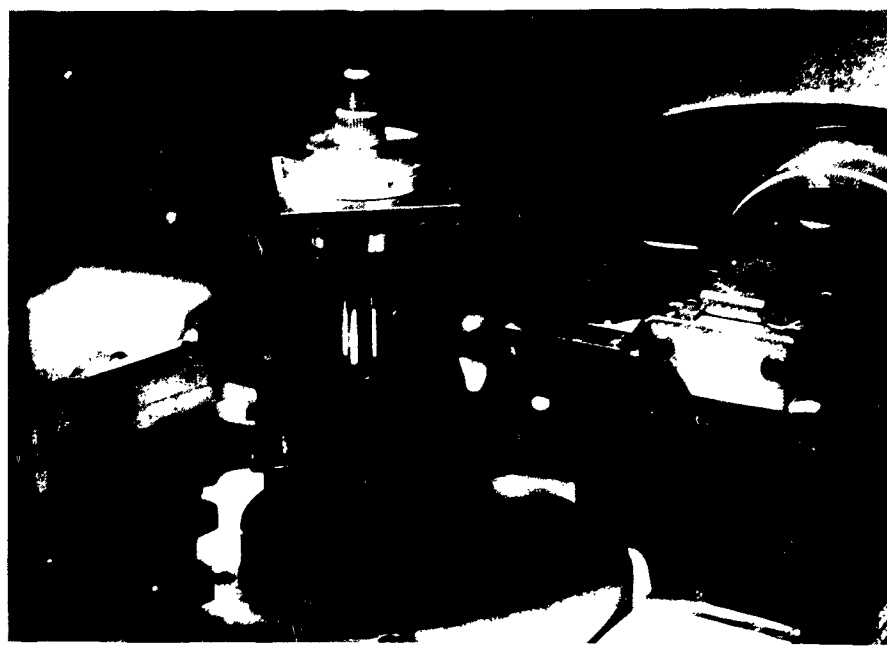


Figure 120. Integrating Specimen Holder for Cylindrical Samples Using High-Speed Motor

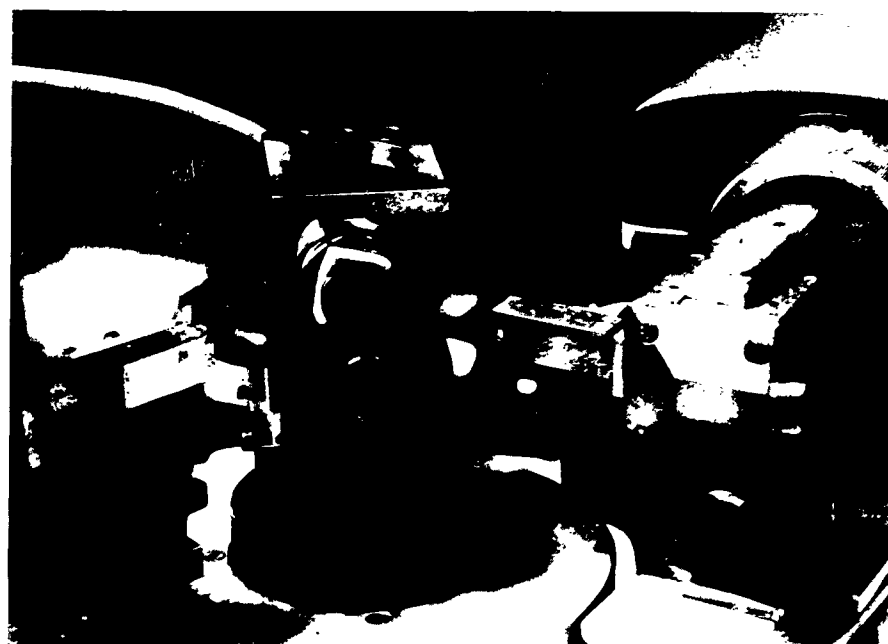


Figure 121. Integrating Specimen Holder Positioned for the Analysis of Flat Specimens



Figure 122. Integrating Specimen Holder for Cylindrical Samples
Using a Low-Speed Motor

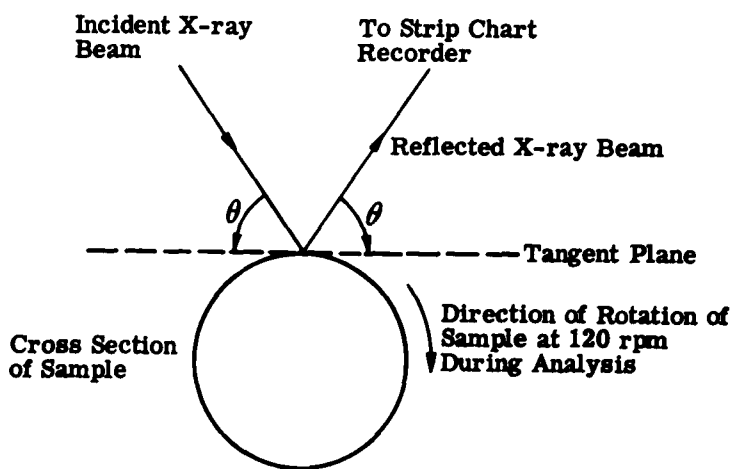


Figure 123. Experimental Setup for Analysis of Cylindrical Specimens

In practice, the reflected intensity is recorded for each diffraction peak by scanning over four degrees in 2θ , at a rate of two degrees per minute on the spectrogoniometer, starting two degrees ahead of where the peak occurs. In the case of the (110) planes where the diffraction peak occurs at 40.3° , a record of the scan from 38.0° to 42.0° would be made.

A randomly oriented standard specimen of the same configuration as the vapor-deposited tungsten samples has been prepared by mixing tungsten powder, Duco cement, and acetone and air spraying this mixture (minimum thickness of 0.005 in.) onto the OD surface of a piece of 0.75-in. diameter copper tubing. The relative intensities obtained on this standard specimen are compared with the ASTM Pattern²⁴ in Table 7 which shows the excellent agreement obtained.

TABLE 7
Relative Intensities of Randomly Oriented Specimens

Crystal Plane (hkl)	Tungsten Powder Sprayed on 3/4-in. dia Copper Cylinder	ASTM
110	100	100
200	16	15
211	29	23
220	8	8
310	11	11
222	4	4
321	17	18

After a record has been made of the reflected intensities of the eight diffracting planes of tungsten, measurements are made on the strip chart by scaling the height of each diffraction peak above background level. The intensity value for each diffraction peak is then compared to the intensity value of the same peak in the standard random sample. This number, $I_{\text{Unknown}}/I_{\text{Standard}}$, for each diffraction peak is then proportional to the concentration of the particular crystallographic plane parallel to the specimen surface. If the assumption is made that the peak height is a direct measure of the concentration of the crystal planes and that all other effects* are absent or insignificant, then this number, $I_{\text{Unknown}}/I_{\text{Standard}}$, may be used as a factor expressing the concentration of a given plane in the unknown specimen compared to the sample plane in the random sample. The factor 25X then would mean that the concentration

*The other effects referred to are peak height reducing factors, such as grain size, stress, surface finish, absorption change due to alloy elements, and ordering in tungsten alloy systems.

of a given crystal plane in the unknown was 25 times the concentration of the same crystal plane in the standard random sample. A summary of the orientation data compiled on vapor-deposited tungsten is given in Table 8.

The question has been raised as to whether it is possible to determine the percentage of the surface area that has a given crystal plane oriented parallel to that surface. The first problem associated with this type of determination is that X-rays penetrate the specimen material to a finite depth (a function of the Bragg angle, θ , and the linear absorption coefficient, μ) and the reflected intensity is representative of a volume of material and not the surface alone. If the orientation did not vary with depth, the orientation of the irradiated volume would be representative of the surface orientation. However, it is not possible to know the variation of orientation with depth without destroying the sample. If the assumption is made that there is no change in orientation with depth, there are still other complications that arise. This makes such an analysis, practically speaking, impossible unless very broad assumptions are made.

One of the primary complications is that the intensity of a perfectly oriented surface (i.e., 100% of a given surface having the same orientation) must be established. The only way that this could be practically realized is to determine the reflected intensity from a specified set of crystal planes of an oriented single crystal of the same material as the unknown specimen. This would require the utilization of a number of large single crystals of tungsten, each properly oriented with a different family of crystal planes parallel to a flat face of the crystal. In the case where CuK_α radiation is used, and there are six families of diffracting planes, this would require a minimum of six large oriented tungsten single crystals. The single crystals would have to be large because the beam slit used on the vapor-deposited tungsten specimens, which by necessity irradiates an area 0.5 in. high, must also be used on the single crystal. This is necessary due to the reflected intensity being a function of the irradiated area.

Assuming that six single crystals of the required orientation were readily available, another significant problem is encountered. Two single crystals of the same orientation will not have exactly the same reflected intensity. This is due to the presence of imperfections and impurities in the tungsten as well as effects known as primary and secondary extinction.^{25, 26} Further, the reflected intensity of a polycrystalline material that is perfectly oriented in one of its surfaces would be far different from the reflected intensity of a single crystal. It should be evident from the foregoing that an accurate determination of the percentage of a surface containing a given crystal plane parallel to that surface is not feasible.

A random sample, on the other hand, is an ideal type of standard specimen. By definition, a random sample is the same no matter which direction or surface is examined. Further, extinction effects are absent when the particle size of the powder used to make the random sample is correctly chosen. While the use of random sample standards will not allow the concentration of a given plane to be expressed as a percentage of the irradiated surface, it will allow the concentration to be assigned a numerical value that is directly proportional to the concentration of planes in the irradiated volume parallel to the sample surface. A random sample is also easy to prepare and only one standard is required.

Microhardness

Hardness determinations were made on a Durimet microhardness tester and are reported as diamond pyramid hardness numbers (DPH). Results are shown in Table 8. The as-plated hardnesses were about equal at all deposition temperatures in the 6:1 and 30:1 ratios but were about 100 points higher at the lower ratio. At the 60:1 ratio, deposits were extremely hard at the lowest temperature, 883 DPH, but decreased to 435 at higher temperature. The differences in hardness are believed to be related to differences in inherent stresses. After heat treatment, all deposits were approximately 385 DPH.

TABLE 8
Deposition Parameters and Results of Evaluation of Tungsten Vapor Deposits

Pressure (atm)	Molar Ratio H ₂ :WF ₆	Deposition Temp (°C)	Mass Flow WF ₆ (gm/cm ² /min)	Orientation I _X /I ₀						Deposition Efficiency (%)	Hardness (DPH)		
				(100)		(111)		(110)			As Plated	Heat Treated	As Plated
0.3	6	650	0.025	28	21						78	600	391
0.3	6	650	0.012		6						50		
0.3	6	650	0.050	22							26		
0.3	6	700	0.025	9	12						52	575	410
0.3	6	750	0.025	4	3						67	612	388
0.3	6	800	0.025	4	5						58	612	388
0.3	30	600	0.025	50	53						57	500	385
0.3	30	650	0.025	54	57						57	475	385
0.3	30	650	0.013	5							47		
0.3	30	650	0.033	18							22		
0.3	30	700	0.025	20	25						61	485	383
0.3	30	750	0.025	12	12						63	480	383
0.3	60	600	0.011			19	7				35	883	383
0.3	60	750	0.013			93	3				36	435	383
0.3	60	750	0.025			131					16		
0.3	60	850	0.007			32					38		

Microstructure

Metallographic examination showed that all of the deposits had a columnar structure, and revealed no major differences resulting from changes in deposition conditions. Structures illustrative of deposits formed at each of the three mixture ratios are shown in Figures 124, 126, and 128. All of the deposits recrystallized when exposed to 2300°K for two hours. Recrystallization probably results from stresses in the deposits. Structures after heat treatment are shown in Figures 125, 127, and 129.

Free-Standing Structures

Free-standing structures have been made by two different techniques. In one the tungsten is deposited on a mandrel material which bonds to the tungsten and is subsequently removed chemically. This technique has the advantage that machining operations can be performed on

thin structures before removing the mandrel. The disadvantages are that a new mandrel must be made for each part, and stresses imposed by thermal expansion mismatch between the mandrel and the tungsten often result in cracking on cooldown from the plating temperature. In the second method, deposition is done on a material which does not bond to the tungsten and is self-releasing on cooldown. This technique permits the reuse of the mandrel, but machining operations are difficult. Examples of structures that have been made are shown in Figure 130. The permeability of a vapor-deposited tungsten thimble (1/2-in. height \times 1/4-in. ID \times 0.003-in. wall thickness) was determined and found to be less than 2×10^{-10} cc/sec helium at a vacuum of 0.05 μ Hg.

Joining Development

Two sections of 3/4-in. diameter tungsten tubing which were formed by vapor deposition were successfully joined by vapor deposition. The joint was checked for porosity on a helium leak detector, and the leak rate was less than 2×10^{-10} cc/sec at 0.05 μ Hg. The tubing before and after joining is shown in Figure 131.

Coatings Development

Vapor-deposited coatings have been applied to cold pressed and sintered tungsten but have not been evaluated.



Figure 124. Tungsten Deposited at 650°C at a Mixture Ratio of 6:1 (250X)



Figure 125. Deposit in Figure 124 After Heat Treatment at 2300°K for Two Hours (250X)



Figure 126. Tungsten Deposited at 650°C at a Mixture Ratio of 30:1 (250X)

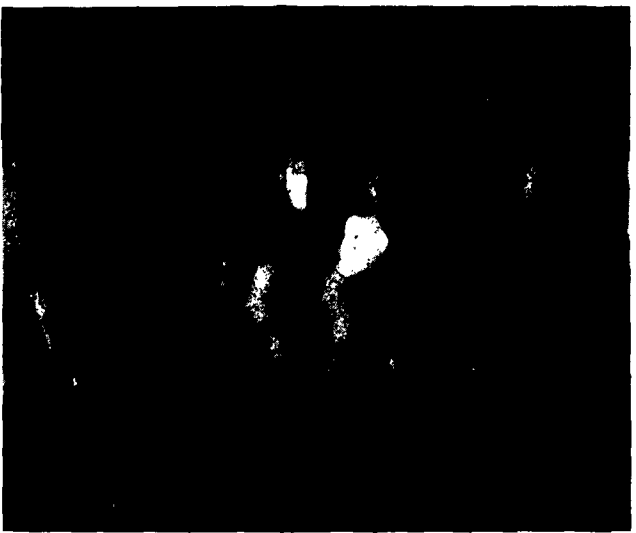


Figure 127. Deposit in Figure 126 After Heat Treatment at 2300°K for Two Hours (250X)



Figure 128. Tungsten Deposited at 750°C at a Mixture Ratio of 60:1 (250X)



Figure 129. Deposit in Figure 128 After Heat Treatment at 2300°K for Two Hours (250X)

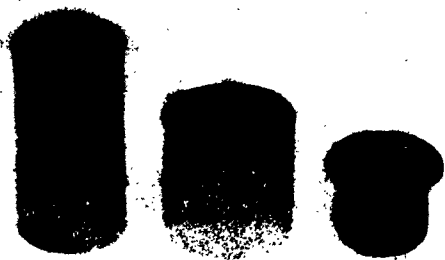


Figure 130. Free-Standing Tungsten Structures Produced by Vapor Deposition (1X)

RECRYSTALLIZATION CHARACTERISTICS OF REFRACtORY METAL THERMIONIC Emitter MATERIALS

The optimum operating temperatures of thermionic emitters are generally above the recrystallization temperatures for all of the refractory metals of interest as emitter materials. Consequently, it is expected that microstructural changes will occur during outgassing and operation of the thermionic device. Recrystallization and grain growth will occur as a result of wrought structures produced by material processing and/or cathode fabrication. These effects may also alter crystallographic orientations derived by material fabrication processes. Emission, being a surface property, may be affected by crystallographic changes in the emitter

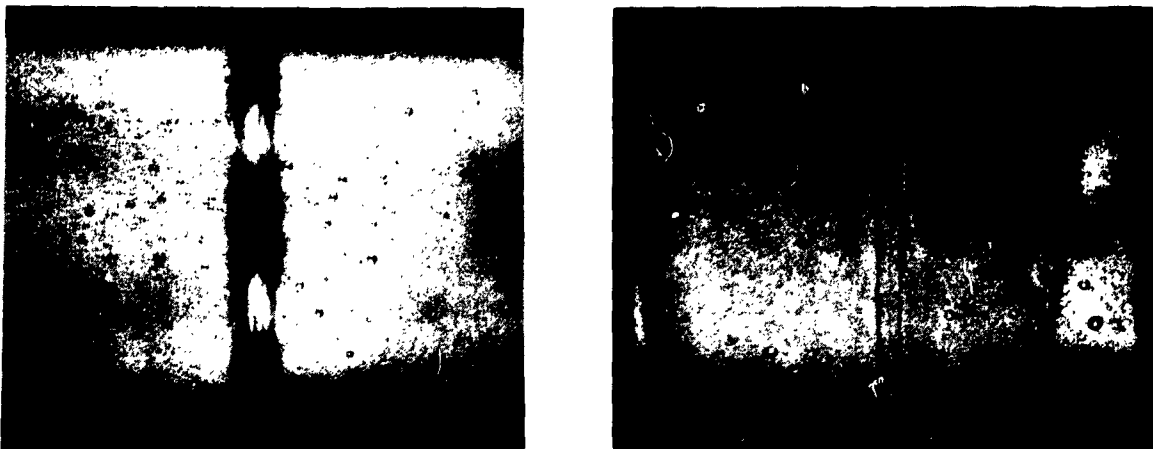


Figure 131. Tungsten Tubing Before and After Joining by Vapor Deposition (3X)

material. Consequently, the effect of operating temperature on grain size and crystallography will be important criteria in the selection of emitter materials for extended operation. Furthermore, these data will provide information concerning the possibilities of improving emission properties by controlling the microstructure of the emitter material.

The objective of the materials program at Allison is (1) to study the microstructural changes which occur in proposed materials at the emitter operating temperature, and (2) to fabricate test cathodes with known microstructures for emission measurements. These data will provide some basis for correlation of microstructure with emission characteristics of the emitter material.

This program has not progressed sufficiently to permit any general conclusions with regard to the objectives of the program. Progress to date has been concerned with the development of metallographic and electropolishing techniques for the various alloys in the program. Electro-polishing techniques for tungsten and tantalum base alloys have been developed which produce adequate surfaces, but smooth electropolished surfaces are difficult to produce on rhenium base alloys. Current metallographic polishing is adequate for tungsten base alloys, but additional development will be required for tantalum and rhenium base alloys.

X-ray diffraction analysis of electropolished surfaces on tungsten base materials indicates that wrought structures show a tendency for (110) orientations in a plane perpendicular to the working direction. This effect is in agreement with other observations of orientation in wrought structures of the body centered refractory metals. Mechanical polishing through 400 grit paper tends to randomize the surface structure. No data are currently available on the effect of recrystallization on the observed orientations.

Experimental Approach

Materials

The materials selected for evaluation in this program are listed in Table 9. Selection was basically designed to include variations in initial alloy fabrication, work history, and alloy additions in tungsten, tantalum, and rhenium base alloys. Material selection was also based on the availability of the material in shapes amenable to emitter fabrication.

TABLE 9
Materials Being Evaluated

<u>Material</u>	<u>Method of Fabrication</u>	<u>Form</u>
Tungsten Base		
W	Arc-cast	3-in. dia ingot
W	Arc-cast + extruded + recrystallized	1-in. dia bar
W	CPS*	1.4-in. dia bar
W	CPS + rolled	0.250-in. plate
W	CPS + rolled	1-in. dia bar
W-2% ThO ₂	CPS + rolled	0.5-1.0-in. dia bar
W-Type 218 (doped)	CPS + rolled	1-in. dia bar
75W-25Re	CPS	1-in. dia bar
Tantalum Base		
Ta	EB melted + rolled + annealed	0.750-in. dia bar
Ta	EB melted + rolled + annealed	0.250-in. plate
90 Ta-10W	EB melted	4-in. ingot
90 Ta-10W	EB melted + rolled + annealed	0.125-in. plate
Rhenium Base		
Re	CPS	1-in. dia bar
Re	CPS + rolled	0.250-in. plate
Re	CPS + rolled	0.050-in. sheet
Coatings		
W on W	Vacuum evaporation	0.002-in. coating
W on W	Plasma-arc sprayed	0.030-in. coating
W on W	Electroplated	0.002-in. coating
Ta on Ta	Electroplated	0.002-in. coating

*Cold-pressed sintered

Experimental Procedure

In addition to the variables resulting from material fabrication processes, alloying, and material condition, the program will also investigate the effects of environment and processing on the recrystallization characteristics and surface orientations. These variables include:

- Temperature—2000, 2300°K
- Time—2, 18 hr
- Surface treatment—electropolished, mechanically polished

Elevated temperature exposure will be accomplished in the tungsten resistance furnace shown in Figure 132. This furnace is capable of operating to 2700°K in vacuum to 0.01 μ Hg. Test samples will be heat treated in vacuums in the range of 0.01-0.1 mm Hg absolute.

The exposure temperatures were selected to provide some data on the effect of both outgassing treatment and emitter operation on the grain growth of the materials. Test samples will be heated for 2000 and 2200°K, which are the operating and outgassing temperatures, respectively, for periods of 2 and 18 hr. The 2- and 18-hr heat treatments will be obtained on a single sample of each material. After the initial 2-hr exposure, the sample will be removed for X-ray analysis and metallographic sectioning and then will be heated for the remaining period. These exposure periods are intended to provide information on the rate of grain growth as a



Figure 132. Tungsten Resistance Furnace Capable of Operating in Vacuum or Inert Gas to 4500°F

function of time within practical limits. Furthermore, the rate of grain growth should decrease with time; consequently, the value of very long exposure periods is questionable in this program.

The surface treatments will be investigated to ascertain the effects of surface stress on the orientation of the recrystallized structures. These will include essentially stress free electro-polished surfaces and a stressed surface produced by grinding and polishing through 400 mesh paper.

Material Evaluation Methods

Evaluation of the effects of the program variables on the structure of the selected materials will attempt to determine recrystallization grain growth and changes in surface orientations. The methods employed will include:

- Metallographic examination
- X-ray diffraction analysis
- Chemical analysis for trace impurities
- Electron microscopy

Ultimately, the materials will be fabricated into cathodes for emission measurements to correlate the effect of microstructure with emission characteristics.

The results of X-ray diffraction analysis of as-received tungsten base alloys are listed in Table 10. Observed orientations are described as the ratio of the diffraction peak height of the test sample to that of a random sample for the particular plane of interest. The diffraction method employed is essentially the same as that reported previously for the analysis of crystallographic orientations in vapor deposited coatings.

The results of metallographic examination of tungsten base alloys as fabricated are shown in Figures 133 through 140. Some anomalies are noted, particularly in the rolled microstructure of Figure 136, which does not appear to be representative of a rolled material. Some difficulty has resulted from attempts to obtain complete fabrication history for some of the vendor materials. Efforts to obtain these data are continuing, since the complete fabrication history is essential for interpretation of observed microstructures.

Emitter Fabrication

Test emitters will be fabricated by machining and/or joining the emitter surface to tantalum tubing. Materials in bar form will be machined into emitter shapes. Sheet and plate materials will be EB welded, brazed with columbium or molybdenum, or joined by tungsten vapor deposition.

TABLE 10
Results of X-Ray Analysis

Sample	Shape	Plane of Analysis	Surface Condition*	Observed Orientation** (hkl)					
				(100)	(110)	(111)	(211)	(310)	(321)
W	CPS bar	Cross section	E						
			M						
W	Cast bar	Cross section	E						2X
			M						Nearly random
W	CPS + rolled plate	Perpendicular to roll direction	E	2X	3X				3X
			M						Nearly random
W	CPS + rolled bar	Cross-section	E		3X				
			M		3X				
W	Cast + extruded + recrystallized bar	Cross section	E	5X	8X				
			M	2X	3X				
W + 2% ThO ₂	CPS + rolled bar	Cross section	E		8X				2X
			M						Nearly random
W (doped) Type 218	CPS + rolled bar	Cross section	E			7X	2X		
			M						Nearly random
85 W-15Mo	Arc-cast	Surface	E				Nearly random		
			M				Nearly random		

*Surfaces are electropolished (E) or mechanically polished (M) through 400 grit paper.

**Represents the ratio of diffraction peak heights to that of a random sample.

Preliminary investigation of joining by electron beam welding has been initiated in the welding facility shown in Figure 141. Adequate joints have been obtained for tantalum to tantalum welds, but attempts to join tantalum to tungsten have resulted in cracks in the tungsten materials. Efforts to improve tantalum to tungsten welds are continuing through modification of the preheating cycle and fixture design.

Feasibility studies on the brazing of tungsten to tantalum with columbium and molybdenum have been initiated, but no results are currently available.



Figure 133. Microstructure of CPS and Rolled Tungsten Plate Parallel to Rolling Direction (250X)

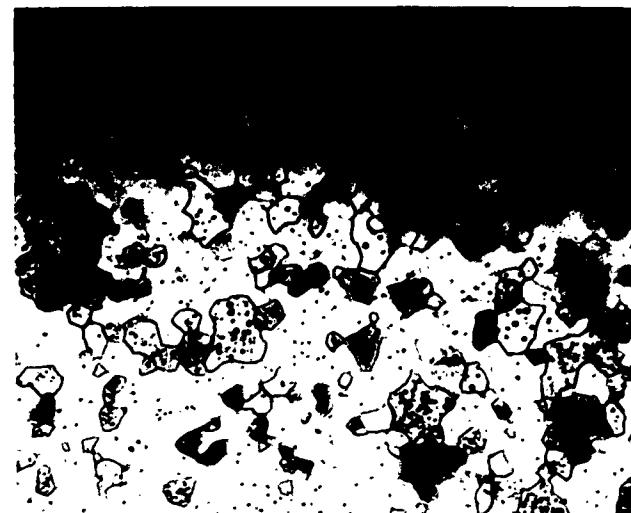


Figure 134. Sintered Microstructure of CPS Tungsten Bar (250X)



Figure 135. Microstructure of Arc-Cast and
Extruded Tungsten Bar Parallel to Rolling
Direction (250X)



Figure 136. Microstructure of CPS and Rolled
Tungsten Bar Parallel to Rolling Direction (75X)



Figure 137. As-Cast Microstructure of Arc-Cast Tungsten Plate (10X)



Figure 138. As-Cast Microstructure of Arc-Cast 85W-15Mo Plate (250X)

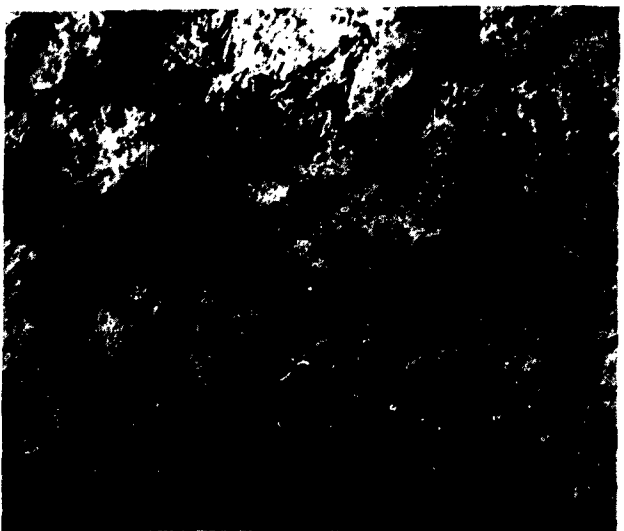


Figure 139. Microstructure of Rolled W-2% ThO₂
Bar Parallel to the Rolling Direction (250X)

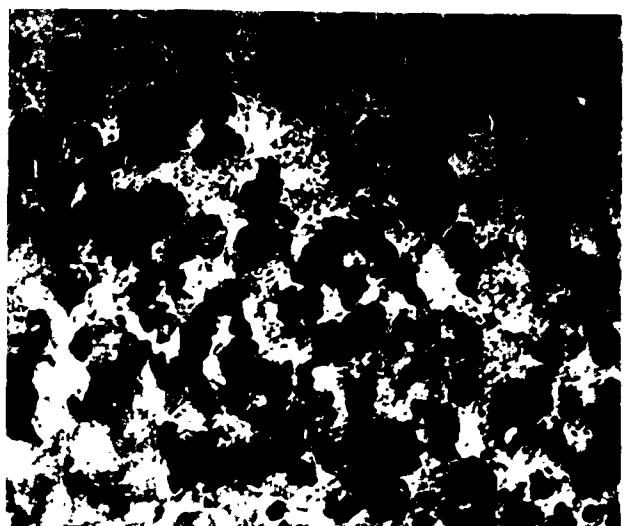


Figure 140. Microstructure of Type 218 Doped
Tungsten Bar Parallel to the Rolling Direction (250X)

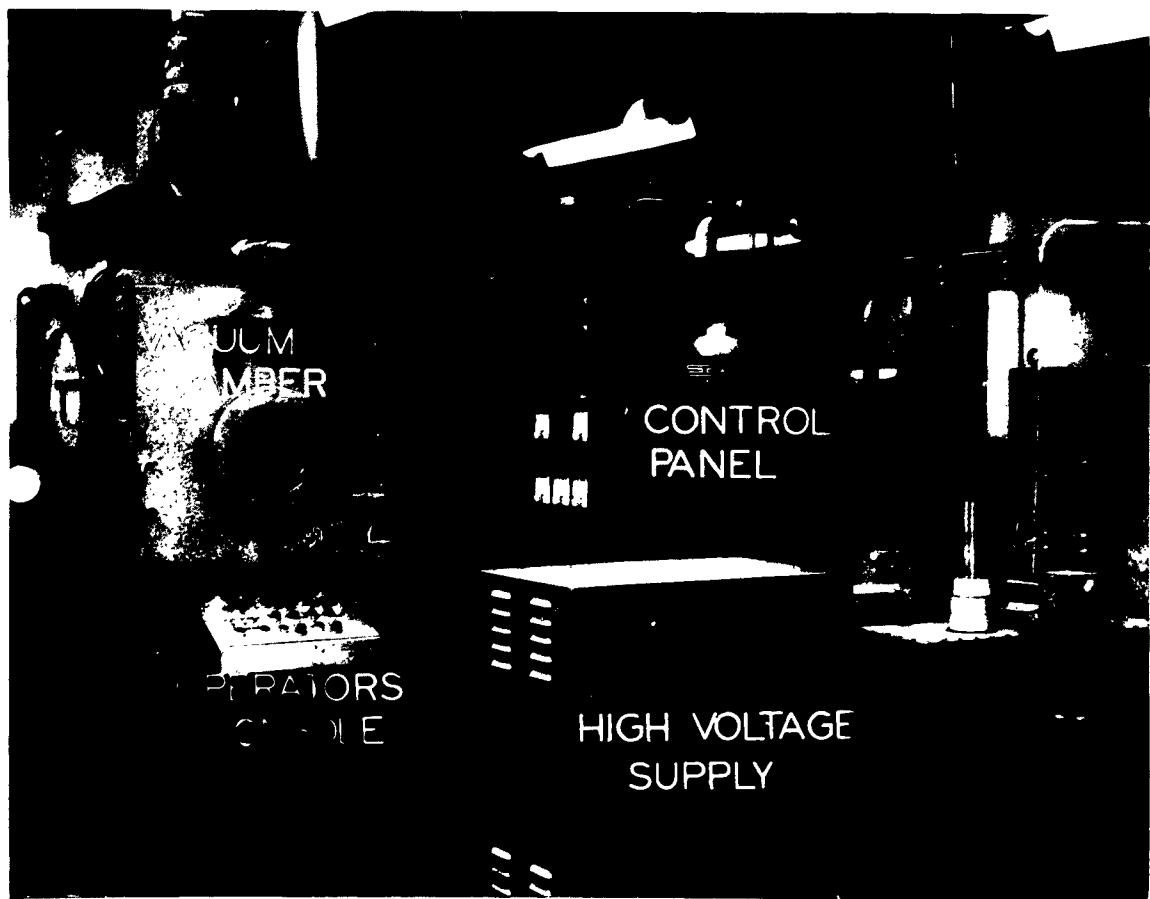


Figure 141. Low Voltage Electron Beam Welding Facility

VII. SUGGESTED FUTURE WORK

Theoretical and experimental results obtained during this investigation suggest research and development work which should be pursued in the future. Two areas appear particularly promising:

1. The development of a thermionic converter with a cavity emitter should continue. The investigation program should include:
 - Operation of the present slotted emitter in the temperature range from 1700 to 2100°K--the test device should have good guard ring geometry, variable spacing, windows for spectroscopic studies, and an insulator design to permit accurate measurement of ion currents.
 - Investigation of other materials, such as tungsten and rhenium, for the emitter material, and a determination of the optimum cavity geometry as influenced by system considerations, such as reactor core criticality, core diameter, and effects of burnup and fission gas release.
 - Design and test of an electrically heated cylindrical converter or converters with the optimum cavity emitter--the design should duplicate as closely as possible a practical nuclear heated fuel element design.
2. The investigation of vapor-deposited tungsten and rhenium surfaces as improved emitters in a thermionic converter. The program should include:
 - A flexible test device to permit accurate comparison of data from conventional and vapor deposited surfaces--the device should have variable spacing, large emitter area, windows for spectroscopic study, an insulator design to permit ion current measurements, and demountability for changing emitter surfaces.
 - Development of vapor deposition process to produce high uniformity of preferred crystal directions in tungsten and rhenium--metallurgical data should be correlated with the thermionic data.
 - On the basis of these results, the most promising surface should be incorporated into a cylindrical converter design and tested to demonstrate high performance. Then, life tests should proceed on several units to demonstrate repeatability and reliability.

VIII. REFERENCES

1. Knudsen, M. in Ann. Physik. Vol 28 (1909) p 75.
2. Dykman, I. M. in Radiotekhnika i Electronika. Vol 2 (1957) p 1525.
3. Sears, G. W. in Journal of Chemical Physics. Vol 22 (1954) p 1252.
4. Nazarian, G. M. and Shelton, H. ARS Paper No. 1386-60 (1960).
5. Zuccars, D., Speiser, R. C., and Teem, J. ARS Paper No. 1387-60 (1960).
6. Reynolds, T. W. and Kreps, L. W. NASA TN D-871 (1961).
7. Taylor, J. B. and Langmuir, I. in Physical Review, Vol 44, No. 6 (1933) p 423.
8. First Quarterly Technical Progress Report on Investigation of the Monocapillary Thermionic Emitter as a Dual Source of Ions and Electrons. Allison Division, General Motors Corporation. EDR 2617. Prepared on Contract No. AF33(616)-8299 (15 February 1962).
9. Clausing, P. in Ann. Physik, Vol 7 (1930) p 569.
10. Nottingham, W. B. Topical Report for the Thermionic Emitter Materials Research Program. Contract NONR-3563(00) (October 1962).
11. Second Quarterly Technical Progress Report on Investigation of the Monocapillary Thermionic Emitter as a Dual Source of Ions and Electrons. Allison Division, General Motors Corporation. EDR 2791. Prepared on Contract No. AF33(616)-8299 (15 May 1962).
12. Third Quarterly Technical Progress Report on Investigation of the Monocapillary Thermionic Emitter as a Dual Source of Ions and Electrons. Allison Division, General Motors Corporation. EDR 2978. Prepared on Contract No. AF33(616)-8299 (15 August 1962).
13. Fourth Quarterly Technical Progress Report on Investigation of the Monocapillary Thermionic Emitter as a Dual Source of Ions and Electrons. Allison Division, General Motors Corporation. EDR 2978. Prepared on Contract No. AF33(616)-8299 (15 February 1962).
14. Houston, J. M. in Proceedings of the Second Government-Industry Thermionic Round-table Discussions. PIC-ELE-TI 3/3 (1961).

15. Huber, H. and LeBihan, R. The Capillary Emitter of Cesium Ions: Application to Thermionic Converters. Presented at the Combustion and Propulsion Panel, AGARD-NATO, Athens, Greece, 15-17 July 1963.
16. Eichenbaum, A. L., and Hernqvist, K. G. in Journal of Applied Physics. Vol 32, No. 1 (1961).
17. Fifth Quarterly Technical Progress Report on Investigation of the Monocapillary Thermionic Emitter as a Dual Source of Ions and Electrons, Allison Division, General Motors Corporation. EDR 3390. Prepared on Contract No. AF33(616)-8299 (15 June 1963).
18. Wilson, V. C. and Lawrence, J. in Advanced Energy Conversion. Vol 2 (July-Sept. 1962).
19. Kuskevics, G. and Teem, J. M. Surface Ion Source Phenomena and Technology - Part I. Presented at the Combustion and Propulsion Panel, AGARD-NATO, Athens, Greece, 15-17 July 1963.
20. Breitwieser, R. "Cesium Diode Operation in Three Modes." Proceedings of the 23rd Annual MIT Conference on Physical Electronics. March 20-22 1963.
21. Nottingham, W. B. "Analysis of Typical Voltage-Current Curves." Proceedings of the Third Government-Industry Thermionic Roundtable Discussions. 6 and 7 December 1961.
22. The Development of an Auxiliary Electrode Thermionic Converter. Technical Documentary Report No. ASD-TRD-63-442, May 1963. Prepared under Contract No. AF33(657)-8005 by Radio Corporation of America, Electron Tube Division, Direct Energy Conversion Department, Lancaster, Pa.
23. Feasibility of Applying Tungsten Liners to Graphite Rocket Nozzles by Vapor Deposition. Allison Division, General Motors Corporation. Materials Research Laboratory Report No. 59 CD 7. (1960).
24. X-Ray Powder Data File. American Society for Testing Materials, ASTM Special Publication 48J (Sets 1-5 revised, 1960).
25. Klug, H. P. and Alexander, L. E. X-Ray Diffraction Procedures (1954) p 129.
26. Bunn, C. W. Chemical Crystallography (1946) pp 208-9.

A P P E N D I X

Cesium Ion Capillary Emitter: Application to Thermionic Converters

by

H. Huber and R. LeBihan
CSF, Orsay, France

Summary of a joint investigation by Allison Division, General Motors Corporation, Indianapolis, Indiana, and the Corpuscular Physics Research Center of the Compagnie générale de télégraphie Sans Fil (CSF), Paris, France.

The work was partially supported under Contract No. AF33(616)-8299 with the Aeronautical Systems Divisions, Air Force Systems Command, United States Air Force.

This appendix is a translation of a paper presented at the Combustion and Propulsion Panel, AGARD-NATO, 15-17 July 1963, Athens, Greece.

LIST OF SYMBOLS FOR APPENDIX

<u>Symbol</u>	<u>Definition</u>
A	Total flux of neutral particles issuing from the section at the input of a cylindrical tube and striking an element of the inner surface of this tube
B	Total flux of neutral particles issuing from the whole of the inner surface of a cylindrical tube and striking the element surface ds
D	Surface diffusion coefficient (migration)
$d_{E/C}$	Emitter-collector distance
f	Degree of ionization = $\frac{n+p}{n_g}$
h	Planck's constant
I	Electric current
I_c	Collector current
I_+	Ion current
I_-	Electron current
j	Electric current density
j_-	for electrons
j_+	for ions
j_s	on the inner surface
j_{lim}	Limit value in the cross section of a cylindrical tube emitting either electrons or ions
k	Boltzmann constant
L	Tube length
m	Particle mass
m_-	for electrons
m_+	for ions
n	Volume particle density = number of particles per cm^3
n_o	on the axis of a hollow tube
$n_{o, lim}$	maximum limit value of n_o
n_s	on the inner surface
n_-	for electrons
n_+	for ions
\bar{n}	mean geometric value
n_{tp}	for electrons and ions in the plasma
n_g	for any gas
n_{Cs}	for cesium vapor
n'_g	for gas before ionization
n'_{gs}	for gas before ionization, on the surface
P	Pressure of a neutral gas
q	Proton charge
r	Variable radius
R	Radius of a cylinder

<u>Symbol</u>	<u>Definition</u>
T	Absolute temperature
T_E	for emitter
T_{Cs}	for the cesium bath
T_w	for the wall
T_c	for the collector
V	Potential
V_G	grid potential
V_{acc}	accelerating potential
V_c	collector potential
V_i	ionization potential
V_w	wall potential
x	Variable distance
W	Power density
δ	Diffusion length = $(D\tau)^{1/2}$
ϵ_0	Vacuum dielectric constant
μ_p	Plasma potential with respect to Fermi level
ν	Density of particle flux in a 2π solid angle
ν_s	on the inner surface of the tube
γ	Flux density of neutrals entering the entrance section of the tube
ϕ	Extraction potential (work function)
ϕ_0	$= \mu_p$
ϕ_1	$< \mu_p$
ϕ_2	$> \mu_p$
σ	Density of neutral surface particles = number of particles per cm^2
τ	Mean lifetime of an absorbed neutral particle

INTRODUCTION

During the past few years attempts have been made to produce sources of electrons or ions with a high current density by using hollow structure geometries (cavities, cylinders, pores), either for application in electronic tubes (references 1 through 11)* or for ion propulsion (references 12 through 18). In what follows, a new structure will be described, a hollow structure in the form of capillary tubes as a dual source of electrons and ions; the conditions will be discussed for which these capillary tubes form a purely thermal plasma generator particularly useful for the extraction of electrical energy in a thermo-ionic converter.

First, the models are considered as a means toward understanding the phenomena of the double emission of electrons and ions as well as the transport phenomena. Results will then be given of experimental work undertaken to ascertain the validity of the models discussed and to consider possible applications of the capillary tube emitter, in particular for thermo-ionic conversion.

*See Bibliography at end of this appendix.

SUMMARY

The principle of the capillary emitter is developed as a dual source of electrons and cesium ions. Considering the distribution of charges inside an infinitely long cylinder which emits either electrons or ions, it is shown that such a cylinder can be usefully employed as a source of electrons or ions with a high current density only when the radius is sufficiently small. Even with such cylinders, the current density in the cross section is always less than that from the internal surface.

Conditions in the cylinder change when electron and positive ion emission occur simultaneously. A plasma is formed which may constitute a source of electrons with a greater current density than that of the surface of the cylinder. An ion sheath is present under certain conditions. The sheath can be obtained in the capillary emitter by passing a cesium gas through a refractory metal capillary tube heated to a high temperature (1500 to 2200°K). The pressure of the cesium vapor at the capillary entrance is chosen so that the number of ions generated exceeds the number of electrons. This leads to the formation of a high density plasma (10^{10} to 10^{14} particles/cm³) surrounded by an ion sheath. A sheath of electrons can also be obtained by proper choice of the cesium vapor pressure.

The data for this model are compared against the experimental measurements taken on three different structures:

- Monocapillary devices with an electrode-probe biased between -10 volts and + 6 volts
- Monocapillary devices with electrodes for the extraction of electrons or ions
- Multicapillary devices forming the emitter of thermionic converters

Experimental results in the form of current-voltage characteristics show satisfactory agreement with the models under consideration.

MODELS OF THE CAPILLARY EMITTER

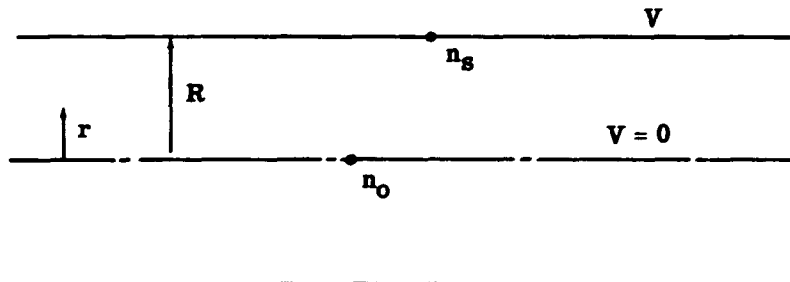
THE INFINITELY LONG TUBE EMITTING ELECTRONS OR IONS

In order to understand the operation with dual emission of electrons and ions inside a capillary tube, the emission of only one type of charged particle—either electrons or ions—shall first be considered.

Consider a tube of radius R and infinite length—i.e., sufficiently long to ignore the end effects on the space charge in the middle of the tube.

The tube is a material capable of emitting either electrons or ions; if it is raised to a sufficiently high temperature, each element of area on the internal surface becomes a source of charged particles capable of emitting a random flux, ν_s particles per cm^2 per second in the solid angle 2π . Equation (13) expresses the random flux in terms of its density, n_s , on the inner surface.

$$n_s = \nu_s \left(\frac{2\pi m}{k T} \right)^{1/2} \quad (13)$$



This density is the number of particles/ cm^3 , assuming the kinetic velocity of the particles to have a Maxwell distribution. The potential distribution and the distribution of particle density in a section of the tube are calculated using Boltzmann's theorem and the Poisson equation.*

Equation (14) gives the potential as a function of the radial distance, r , with respect to the potential on the tube axis ($V=0$); a positive or a negative potential sheath at the wall is obtained depending on the sign of the charge.

$$\frac{V}{V_0} = -2 \ln \left(1 - \frac{n_0 r^2 q^2}{8 \epsilon_0 k T} \right) \quad (14)$$

*Details of this calculation are found in Technical Note BN-214, H. H. Weymann, University of Maryland, July 1960.

Equation (15) expresses the temperature equivalent in volts.

$$\bar{V} = \frac{k T}{q} \quad (15)$$

Equation (16) gives the ratio of the values of the densities on the axis and on the inner surface of the tube; in this equation, $n_{o, \text{lim}}$ is the limit value which cannot be exceeded by the axial density, and for which the surface potential becomes infinitely high.

$$\frac{n_o}{n_s} = \left(1 - \frac{n_o}{n_{o, \text{lim}}} \right)^2 \quad (16)$$

Equation (17) gives the expression for this limit axial density as a function of the radius, R , of the tube and of temperature.

$$n_{o, \text{lim}} = \frac{8 \epsilon_0 \bar{V}}{R^2 q} \quad (17)$$

Equation (18) gives the mean density which is the geometric mean of the axial density and of the surface density.

$$\bar{n} = (n_o \times n_s)^{1/2} \quad (18)$$

Taking the surface density, n_s , as being determined by the emissive properties of the surface, it should be noted that the axial density, n_o , is always less than n_s ; hence, the mean density, \bar{n} , is always less than n_s . The mean density becomes substantially equal to n_s only if n_s is less than the limit value $n_{o, \text{lim}}$.

The question could be asked, what is the mean density when the surface density is equal to the limit axial density? This would give the density for a zero sheath potential at the wall.

$$\text{If } n_s = n_{o, \text{lim}} \quad (19)$$

$$\text{then } n_o = 0.382 n_{o, \text{lim}} \quad (20)$$

The result is given by Equation (21).

$$\bar{n} = 0.618 n_{o, \text{lim}} \quad (21)$$

Equation (22) gives the available density of the current of charged particles.

$$j_{\text{lim}} = 0.618 \left(\frac{k T}{2\pi m} \right)^{1/2} \frac{8 \epsilon_0 \bar{V}}{R^2} \quad (22)$$

It is found that this current density is inversely proportional to the radius R of the tube. Examples are given in the following (giving the orders of magnitude for $T = 2000^\circ\text{K}$):

R	$200\ \mu$	$2\ \mu$
\bar{n}_+	$10^9/\text{cm}^3$	$10^{13}/\text{cm}^3$
j_-	$10^{-3}\ \text{amp}/\text{cm}^2$	$10\ \text{amp}/\text{cm}^2$
$j_+(\text{Cs})$	$2 \times 10^{-6}\ \text{amp}/\text{cm}^2$	$20 \times 10^{-3}\ \text{amp}/\text{cm}^2$

If it is required to extract from a tube an electron current density of the order of $10\ \text{amp}/\text{cm}^2$, or of $20\ \text{milliamp}/\text{cm}^2$ of cesium ions, then a radius of about $2\ \mu$ would be required. A radius of $200\ \mu$ would give a current density 10,000 times less and be of little technical interest. This remark has already been made by Brodie and Niewold for the electron emission from a hollow cathode, as well as by Kotnik for the emission of cesium ions from a cylinder.^{11,12}

THE INFINITELY LONG TUBE WITH SIMULTANEOUS EMISSION OF ELECTRONS AND IONS

The Isothermal Cavity, the Infinitely Long Tube of Large Radius

Conditions change considerably when the tube surface emits both electrons and ions toward the inside of the tube because partial or complete space charge neutralization occurs. Thus, the limitation imposed on the tube radius when the tube emits only one type of charged particles is removed.

The problem can be rigorously solved, as in the preceding case, by applying the Poisson-Boltzmann equation for both types of charges. However, the problem can be more easily treated in a general way by applying Nottingham's theory of the isothermal diode.*²⁰ To this end, a large cavity will be considered—in particular, a tube of large diameter and sufficiently long to ensure that the ends play no part in the events occurring in the middle section of this tube. This tube will be filled with a readily ionizable gas, such as cesium, at $n'g\ \text{atoms}/\text{cm}^3$.

The Saha Equation

When the tube is raised to the temperature T , the gas is thermally dissociated into ions and electrons and, after a certain time, equilibrium is reached between the densities of neutrals, ions, and electrons, according to the equilibrium reaction:



$$n_g = n_{+p} = n_{-p}$$

*Here it is more the case of an isothermal cavity.

A plasma is thus formed ($n_{-p} = n_{+p}$). Equilibrium was calculated by Saha applying the law of action of mass of Guildberg and Waage, and calculating the equilibrium constant by thermodynamic statistics, Equation (23).

$$n_{\pm p}^2 = \left(\frac{2\pi m_e k T}{h^2} \right)^{3/2} \cdot n' g (1 - f) e^{-V_i/\bar{V}} \quad (23)$$

$$f = \frac{n_{\pm p}}{n' g} \quad \bar{V} = \frac{k T}{q}$$

It may be noted that:

- This equation describes a volume phenomenon in the state of thermal equilibrium, taking total account of all microphenomena existing between neutrals, ions, and electrons
- $n_{\pm p}$ depends only on the temperature, T, on the ionizing potential, V_i , and on the neutral density, n_g , expressed by the density of neutrals before dissociation $n' g$ and the degree of ionization defined by

$$f = \frac{n_{\pm p}}{n' g}$$

- There is no indication as to the influence of the nature of the surface on the composition of the plasma

Correlation Between the Charge Densities in the Plasma and the Charge Densities at the Surface

The density of ions and electrons in the plasma can be compared with that on the internal surface of the tube. With the work function of the surface having any value, a dual emission of electrons and ions exists on the surface. It is possible to calculate the densities of the electrons and ions close to the surface, where their kinetic velocities are purely thermal, by applying Equation (13).

The electron density at the surface, n_{-s} , can then be obtained by the Richardson-Dushman equation, Equation (24), and the density of the ions at the surface, n_{+s} , by the Saha-Langmuir equation, Equation (25).

$$n_{-s} = 2 \left(\frac{2\pi m_e k T}{h^2} \right)^{3/2} \cdot e^{-\phi/\bar{V}} \quad (24)$$

$$n_{+s} = \frac{n' g (1 - f)}{2} \cdot e^{-(V_i - \phi)/\bar{V}} \quad (25)$$

Comparing Equation (25) with Equation (24), it is found that the product of densities n_{-s} and n_{+s} at the surface is equal to the square of the charge density $n_{\pm p}$ in the plasma, Equation (26).

$$n_{\pm p} = (n_{-s} \times n_{+s})^{1/2} \quad (26)$$

This is an important relation which relates the plasma density with the emissive properties of the surface.* Three facts are brought out:

- The charge density, $n_{\pm p}$, in the plasma is the geometric mean between the electron and ion densities on the surface
- The electron density at the surface can be interchanged with the ion density at the surface without changing the plasma density
- There is a special case for which the electron density, n_{-s} , on the surface is equal to that of the ions, n_{+s} , on the surface; hence, equal to the charge density, $n_{\pm p}$, in the plasma, whatever the degree of ionization

The Plasma Potential

The case of equal electron and ion densities at the surface was chosen by Nottingham in order to define the plasma potential.²⁰ Note that the equality of the densities at the surface and in the plasma means that, at thermal equilibrium, the emissions of electrons and ions at the surface towards the plasma are respectively equal to the random flux of electrons and ions towards the surface—that is, not only does the presence of the surface not affect the composition of the plasma, but the plasma extends undisturbed up to the surface. To fulfill this condition, the extraction potential at the surface must have the particular value, ϕ_0 , equal to the potential, μ_p , of the plasma. This special value of the extraction potential can thus be taken as a measure of the plasma potential. It can be expressed in many ways as a function of the quantities T , V_i , $n'g$, f , $n_{\pm p}$. It is expressed by Equation (27) in terms of T and $n_{\pm p}$ as shown in Figure 142.

$$\phi_0 = \bar{V} \left[\ln 2 + \frac{3}{2} \ln \left(\frac{2\pi m_e k}{h^2} \right) - \ln n_{\pm p} + \frac{3}{2} \ln T \right] \quad (27)$$

Equation (27) shows that the plasma potential depends only on the temperature, T , and on the density, $n_{\pm p}$, of the charges in the plasma. That is to say, two plasmas at different degrees of ionization but with equal densities $n_{\pm p}$ have the same plasma potential.

*It follows that, in an isothermal enclosure, it is possible to calculate the charge density in the plasma—either by the Saha equation or by the density of the electrons and ions on the internal surface.

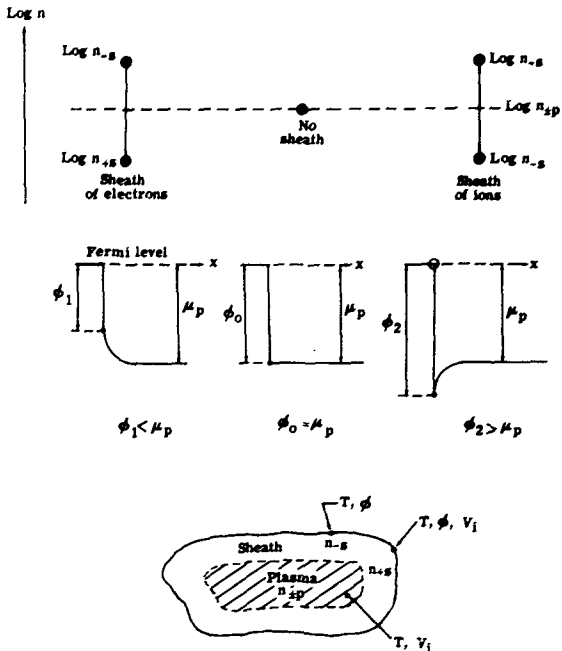


Figure 142. Sketch Showing Three Types of Sheath Conditions

The Electron and Ion Sheaths

Except for the special case where $\phi_0 = \mu_p$, a sheath is formed containing an excess of electrons (electron sheath) when ϕ_1 is less than μ_p , and an excess of ions (ion sheath) when ϕ_2 is greater than μ_p (Figure 142). The charge and potential distributions in the sheaths can be calculated by the Poisson-Boltzmann equation. An important magnitude is the thickness of the sheath which can be defined as the distance from the surface at which 97.5% of the total fall of potential occurs (after Nottingham²⁰). Calculations show that the thickness of the sheath is inversely proportional to the square root of the charge density $n_{\pm p}$ in the plasma. For example, it is 10 microns for a density of the order of $10^{12}/\text{cm}^3$. Thus, the plasma extends through an isothermal cavity, apart from the sheath; in the special case of the infinitely long tube of large radius, the radius can now be reduced to 200μ without losing much of the plasma section by the extension of the sheath.

JUXTAPOSITION OF CURRENT DENSITIES AVAILABLE IN THE CROSS SECTION OF THE INFINITELY LONG TUBE CONSTITUTING EITHER AN ELECTRON OR ION EMITTER OR A DUAL EMITTER OF ELECTRONS AND IONS

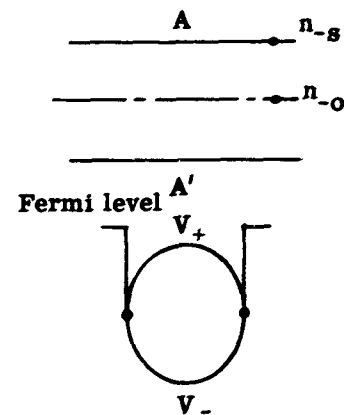
It is now possible to compare the current densities available in the cross section of an infinitely long tube with a radius of about 200μ when this tube is either an electron or an ion emitter, or an emitter of both electrons and ions; hence, a plasma generator. This comparison is shown in Figure 143.

Case 1.

$$j_- = -q(n_{-0} \times n_{-s})^{1/2} \left(\frac{kT}{2\pi m_-} \right)^{1/2} \quad (28 \text{ a})$$

$$j_+ = +q(n_{+0} \times n_{+s})^{1/2} \left(\frac{kT}{2\pi m_+} \right)^{1/2} \quad (28 \text{ b})$$

$$\begin{array}{l} n_{-0} < n_{-s} \\ n_{+0} < n_{+s} \end{array} \left. \begin{array}{l} \text{then} \\ \quad \quad \quad \end{array} \right. \begin{array}{l} j_- < j_{-s} \\ j_+ < j_{+s} \end{array}$$

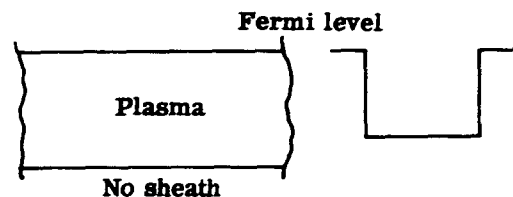


Case 2.

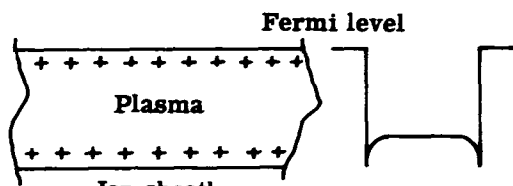
$$j_- = -q(n_{+s} \times n_{-s})^{1/2} \left(\frac{kT}{2\pi m_-} \right)^{1/2} \quad (29 \text{ a})$$

$$j_+ = +q(n_{+s} \times n_{-s})^{1/2} \left(\frac{kT}{2\pi m_+} \right)^{1/2} \quad (29 \text{ b})$$

$$\begin{array}{l} \text{If } n_{+s} = n_{-s} \\ \text{Then } j_- = j_{-s} \\ \quad \quad \quad j_+ = j_{+s} \end{array}$$



$$\begin{array}{l} \text{If } n_{+s} > n_{-s} \\ \text{Then } j_- > j_{-s} \\ \quad \quad \quad j_+ < j_{+s} \end{array}$$



$$\begin{array}{l} \text{If } n_{+s} < n_{-s} \\ \text{Then } j_- < j_{-s} \\ \quad \quad \quad j_+ > j_{+s} \end{array}$$

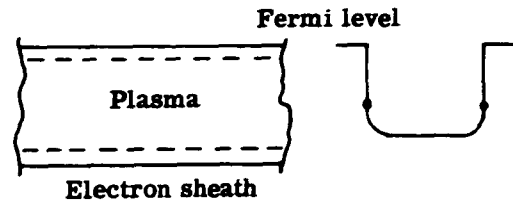


Figure 143. Comparison of Tube Functioning as (1) an Ion or Electron Emitter and (2) an Emitter of Both Ions and Electrons—i.e., a Plasma Generator

The first case, shown at the top of Figure 143, shows schematically the density distribution and the potential distribution. The available current densities j_- or j_+ , Equation (28), are given by the mean charge density, Equation (18). Since the densities at the tube axis (n_{-0} and n_{+0}) are always less than those at the surface (n_{-S} and n_{+S}), the available current density is always less than that at the surface; therefore, a metal surface with the same extraction potential and with the same surface area as the tube cross section would emit more current.

Such is not true when the tube is a plasma generator; this case is shown at the bottom of Figure 143. Three conditions are shown where the available current densities, j_- and j_+ , are given by Equations (29) and (26).

First Condition

Assume the densities of the electrons and ions emitted at the surface to be equal, corresponding to fluxes of emission of electrons and ions in the ratio of the square roots of the masses of the ion and of the electron. In this condition, the plasma completely fills the tube (there is no sheath), and the available current density in the cross section is the same as the current density at the inner surface of the tube.

This is already a considerable advantage over the first case, but a metal surface with the same surface area as the tube cross section would produce the same effect.

Second Condition

Assume the same plasma potential, but in a tube with a surface potential higher than the plasma potential; hence, an ion sheath surrounds the plasma. In this condition, the available electron current density is greater than the electron current density at the surface; conversely, the available ion current density is less than the density of the ion current at the surface.

This condition is, therefore, more favorable than the former one, in the sense that this plasma provides a greater source of electrons than the local tube surface.

Third Condition

Assume once again the same plasma potential, but in a tube with a surface potential less than the plasma potential; hence, an electron sheath surrounds the plasma.

This condition is the inverse of the second condition and is of less interest as a source of electrons since the available electron current density is less than the density of the electron current emitted by the surface. A metal surface with the same surface potential as the tube section would provide more electrons. The available ion current density is greater than the density of the ion current from the surface.

From these considerations, it can be noted that the most useful condition as a source of electrons exists when the tube is filled with a plasma surrounded by an ion sheath.

THE TUBE OF FINITE LENGTH WITH EMISSION OF ELECTRONS AND IONS

The Model of the Linear Decrease of Neutral Density Along the Tube

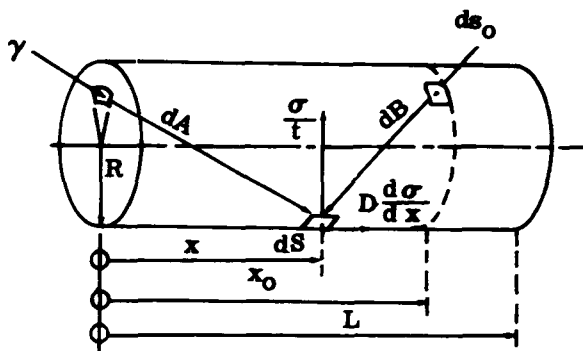
So far, an infinitely long tube has been assumed—i. e., the gradient of vapor pressure (cesium) is zero. In this case there is no clear transport of particles, either charges or neutrals. This is no longer true if the length of the tube is finite. The first problem to be considered is the flux of neutrals and the pressure variation of the neutrals.

To deal with the problem rigorously, two fluxes must be taken into consideration:

- The volume flux (volume diffusion)
- The surface flux (surface diffusion or migration)

The former depends on the gradient of the neutral density in the volume of the tube and may be a molecular flux (Knudsen flux), a viscous flux (Poiseuille flux), or a turbulent flux. In the capillary, the conditions for a molecular flux would exist when the mean free path of the neutrals is greater than the diameter of the capillary; consequently, in this case the only collisions suffered by the neutrals would be with the tube surface. For example, if the tube diameter were 400μ , this condition would exist at a pressure of 2.6×10^{-3} mm of mercury (corresponding to a cesium bath temperature of 400°K if the cesium vapor has this pressure at saturation). The second flux depends on the gradient of the surface density, σ .

The balance of the two neutral fluxes under steady conditions, at a specific point on the tube internal surface, leads to Dykman's integral-differential equation, Equation (30).



$$\frac{d}{dx} \left(D \frac{d\sigma}{dx} \right) + A + B - \frac{\sigma}{\tau} = 0 \quad (30)$$

$$A = \frac{\gamma}{2R} \left[\frac{x^2 + 2R^2}{\left[x^2 + 4R^2 \right]^{1/2}} - x \right] \quad (31)$$

$$B = \frac{1}{2R} \int_0^L \frac{\sigma(x_0)}{\tau} \left[1 - \frac{|x - x_0| \left[(x - x_0)^2 + 6R^2 \right]}{\left\{ (x - x_0)^2 + 4R^2 \right\}^{3/2}} \right] dx_0 \quad (32)$$

The first term in Equation (30) is the migration flux, the second is the part represented by neutrals directly from the section at the tube entrance, the third is the part represented by neutrals from the total inner surface of the tube, and the fourth is the loss of neutrals by evaporation.

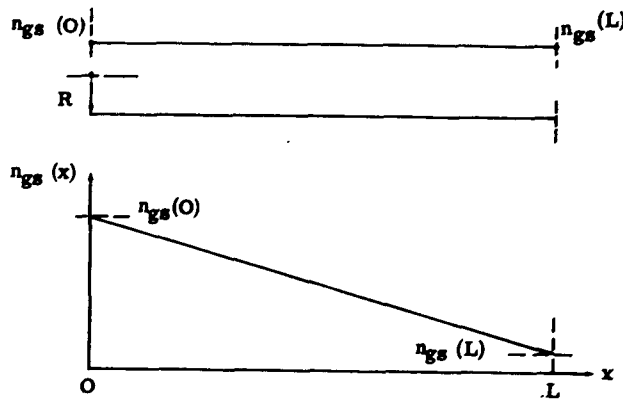
Two facts have been derived from the approximate solutions of Dykman's equation. The first is that two flux modes are dominant at the tube exit depending on the value of the ratio of the diffusion length, defined by $\delta = (Dr)^{1/2}$, to the diameter, $2R$ of the tube.

- Surface flux is dominant for very small radii (a few microns) with zero volume density gradient near the exit.
- Volume flux is dominant for relatively large radii (100 microns and more) with a negligible surface density gradient.

The first mode corresponds to cesium ionizers in the form of porous tungsten materials used as a source of cesium ions for ionic propulsion. At the tube exit neutrals flow away along the surface in a radial direction and can evaporate as ions.¹³⁻¹⁸ The second flux mode creates a plasma at the tube exit.

The second fact is that, to the extent that the volume flux is dominant, neutral density decreases linearly from the entrance to the exit of the tube, except at the ends where the density is non-linear over a length comparable to the tube diameter.

For the remainder of the investigation, a linear decrease of the density along the tube was assumed, this being the condition for the transport of neutrals along a tube by the molecular flux mode, or Knudsen mode. To make the model of a linear decrease of density compatible with the Knudsen flux, the relation expressed by Equation (33) must exist between the neutral densities on the tube surface, at the exit, $n_{gs}(L)$, and at the entrance, $n_{gs}(0)$. The number of neutrals leaving the tube in unit time (Knudsen's Γ flux) is given by Equation (34), which is identical with the known formula for Knudsen's flux, Equation (35), when the pressures at the entrance and exit of the tube are expressed by relations given in Equations (36) and (37).



$$\frac{n_{gs}(L)}{n_{gs}(O)} = \frac{1}{1 + \frac{3}{4} \frac{L}{R}} \quad (33)$$

$$r_1 = \pi R^2 \frac{n_{gs}(O) \left(\frac{k T}{2 \pi m} \right)^{1/2}}{1 + \frac{3}{8} \frac{L}{R}} \quad (34)$$

$$r_2 = \frac{8\sqrt{\pi}}{3} (2 m k T)^{-1/2} \frac{R^3}{L} \left[P(O) - P(L) \right] \quad (35)$$

$$P(O) = k T \cdot n_{gs}(O) \quad (36)$$

$$P(L) = \frac{P(O)}{1 + \frac{3}{8} \frac{L}{R}} \quad (37)$$

Simplified Model for the Determination of Particle Density Along the Tube

To obtain an initial estimate of the charges inside the tube, the model of the linear decrease of neutral density along the tube is combined with the model of plasma in an isothermal cavity. For this calculation the tube is divided into a number of sections with decreasing neutral density; this can be viewed as a series of cesium reservoirs with decreasing temperatures.

Knowing the density of the cesium vapor in each section, it is possible to determine for each section (see Figure 144):

1. The work function, ϕ , of the inner surface (Nottingham-Houston chart)²⁰

2. The density, n_{-s} , of the electrons on the surface, from Richardson-Dushman, Equation (24)

3. The density, n_{+s} , of the ions on the surface, from Saha-Langmuir, Equation (25)
4. The density, $n_{\pm p}$, of the plasma, from Saha, Equation (23)
5. The plasma potential, $\mu_p = \phi_0$, Equation (27), which with ϕ gives the height of the sheath $(\phi - \mu_p)$
6. The thickness of the sheath, g

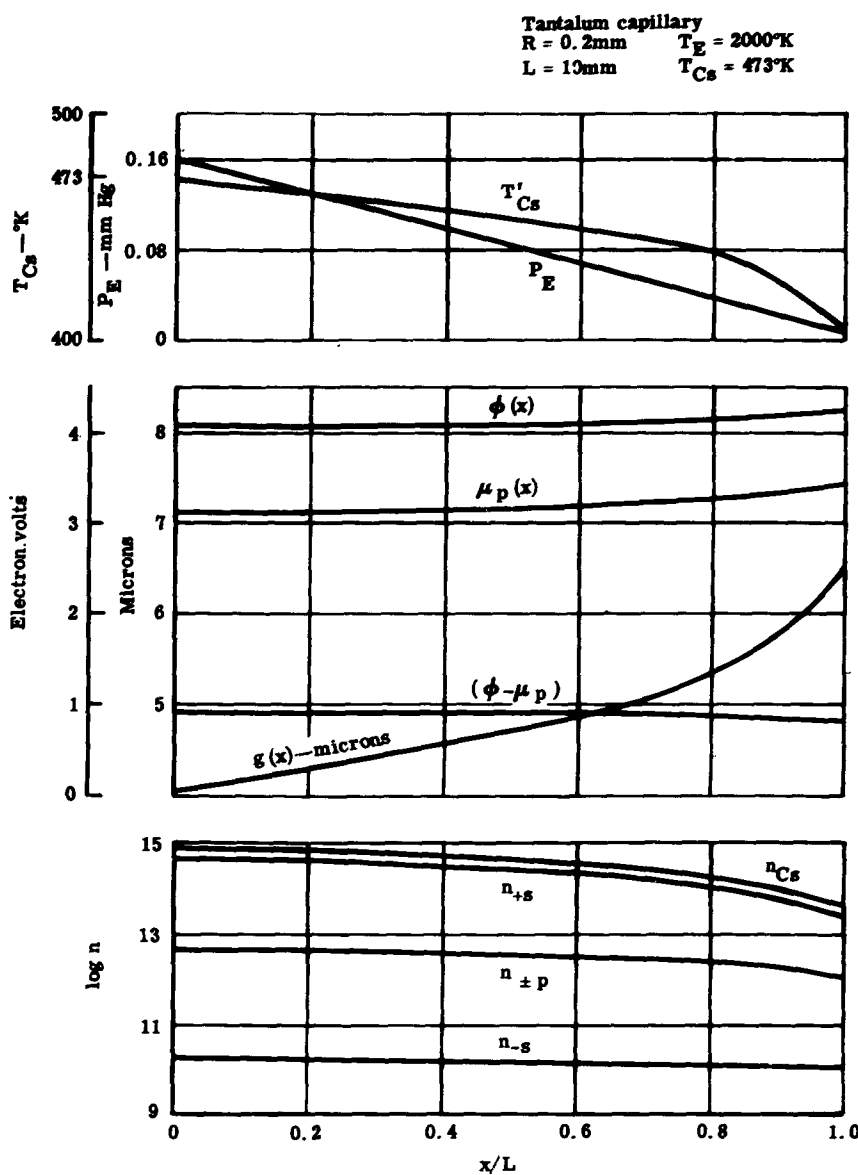


Figure 144. Pressure, Density, and Potential Quantities as a Function of Capillary Length

Curves have been drawn for various values of the temperature, T_E , of the capillaries and of the cesium reservoir temperature, T_{Cs} . A few are given in Figure 145 to show how the relative and absolute levels of electron and ion densities vary when the tube temperature T_E changes. The useful condition (with an ion sheath) is obtained by increasing the tube temperature, T_E , for a given temperature, T_{Cs} , of the cesium bath, or decreasing the temperature of the cesium bath for a given tube temperature, T_E .

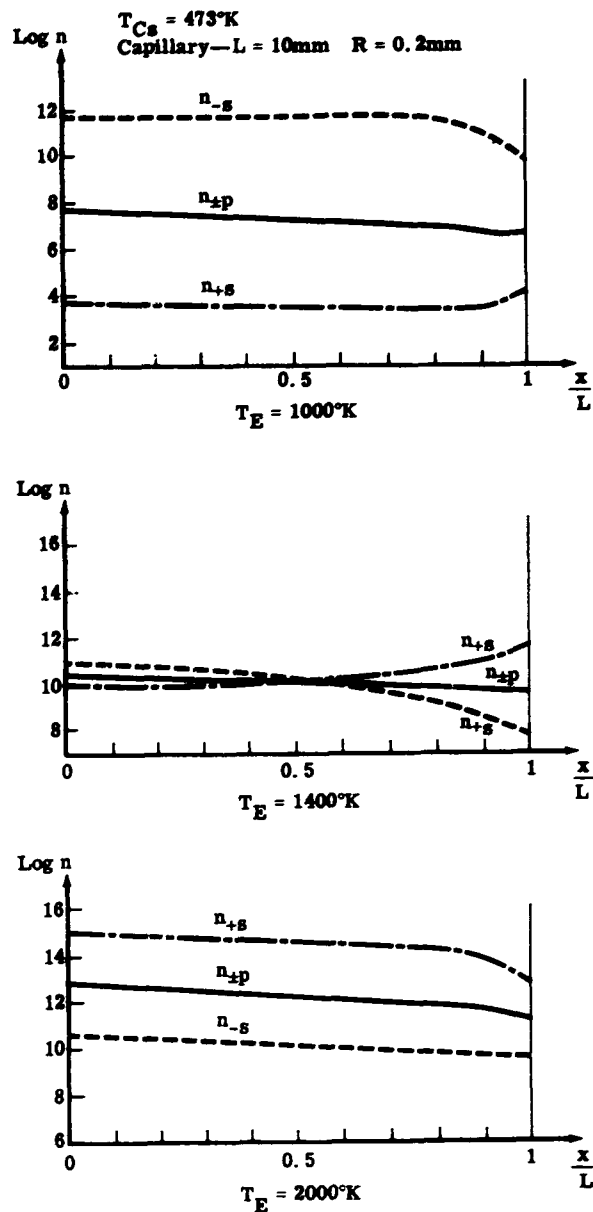


Figure 145. Density Functions for Three Emitter Temperatures at a Constant Cesium Temperature of 473°K

When predicting from this model the emission of electrons and ions at the tube exit, only charges at the end of the tube are considered.*

Extraction of Charged Particles

In the previous section the available electron and ion current densities were considered. Now to be determined is whether the available currents can be extracted. It will be necessary to consider the equipotential surfaces, as shown qualitatively in Figure 146, for the condition where an ion sheath exists between the plasma and the tube.

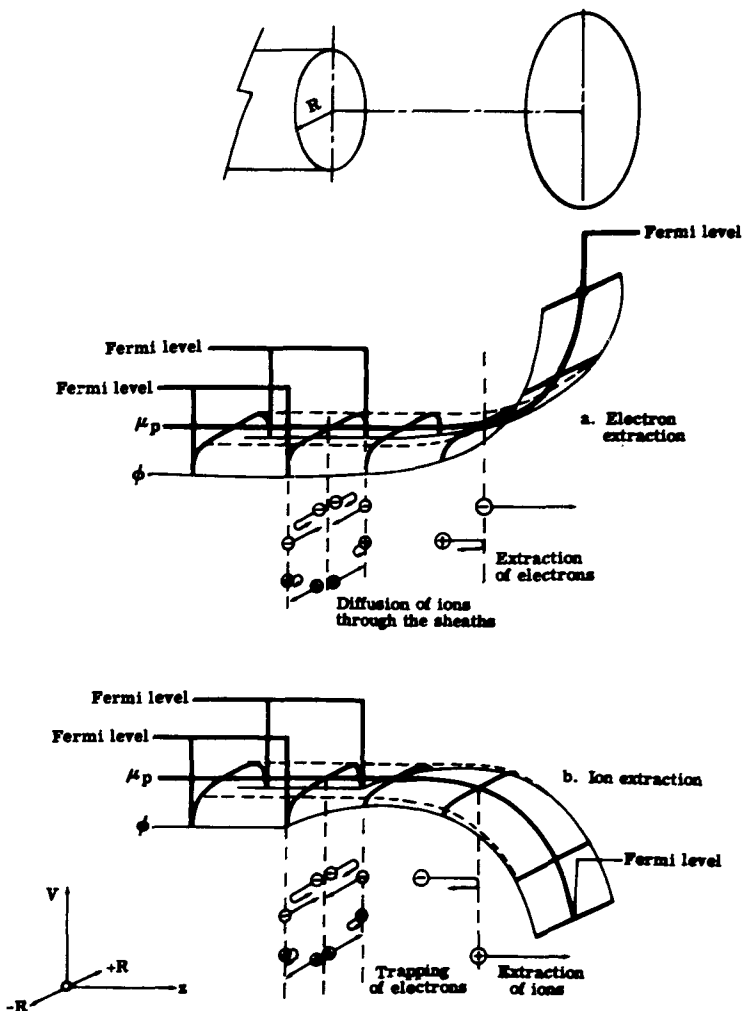


Figure 146. Sketch Depicting Extraction of Charged Particles from Tube

*This highly simplified model does not account for interactions between the various sections. In practice, there would be interactions between the sections especially when the pressure is so high that collisions between electrons and neutrals cannot be neglected.

Electron Extraction

In this case the exit end of the tube is opposite an electron collector electrode (positive potential); the potential increases from the tube exit to the surface of the collector (see Figure 146 a). The random electron flux is thus attracted by the electrode, the flow being fed from electrons trapped on the tube axis by the radial potential wall. Ions tend to be eliminated by diffusion under the influence of the potential gradients present. From this model it is seen that there is no difficulty in extracting the total random electron current from the plasma, provided that the inner surface area of the tube is sufficiently large to supply this current by summation of the relatively low emission per unit area of the inner surface of the tube. If the surface area is too small, saturation will occur.

It can be expected that, in the limit, the current extracted at the open section S_o would be equal to the current emitted by the surface of area S_s .

$$v_{-p} \cdot S_o = v_{-s} \cdot S_s$$

It is actually found in certain measurements that the density of the electron current extracted is much greater than that supplied per square centimeter of inner surface area, but no current greater than that emitted by the whole inner surface of the capillary tube has ever been measured. Eichenbaum made the same observation in the case of a hollow structure in the form of a cylindrical cavity.²¹

Ion Extraction

In this case the tube exit is opposite an ion collector electrode (negative potential). The potential decreases from the tube exit to the collector (see Figure 146 b). The condition for electrons is thus different from that for ions in the case of electron extraction—namely, the electrons are trapped both by the radial potential sheath and the longitudinal potential gradient. The trapping phenomena of minority charges in a charge flux are a problem already considered in the focusing of electron beams.²²⁻²⁴ Although this is the inverse case, it would appear legitimate to consider that the trapping of electrons could increase their density and would compensate, at least in part, for the majority of the ion charges in the sheath. Hence, there is a possibility for extracting a larger ion current than that corresponding to the density of the random ion flux in the plasma. If the charge in the ion sheath were fully compensated, the density of the ion current would be that corresponding to the density of the n_{+s} ions on the surface. If, moreover, the degree of ionization, Equation (23), is equal to one, the ion current should be equal to the Knudsen flux, expressed as an electric current.

EXPERIMENTAL WORK

It has been shown that the production in a tube of a dense plasma surrounded by an ion sheath can be useful as a source of electrons or ions. The experiments described in this section were performed to compare experimental results with theory based on such a model. Also, the capillary emitter was examined for possible application in a thermo-ionic converter.

MONOCAPILLARY WITH AN ELECTRODE PROBE

Arrangement and Method of Measurement

In this measurement arrangement, a probe (or collector) with a guard ring is placed opposite the exit of a capillary at a distance variable from 0.5 to 1.5 mm. Two variations of the device shown in Figure 147 were investigated. One had a tantalum capillary and the other a molybdenum. Cesium vapor from a reservoir raised to temperature T_{Cs} is passed through the capillary at temperature T_E . It is then trapped at -15°C by cold pumping to avoid a high pressure at the capillary exit. The monocapillary with the probe and cesium reservoir is placed in a bell jar, as shown in Figure 148. The cesium leaving the capillary is condensed at the top of the bell jar.

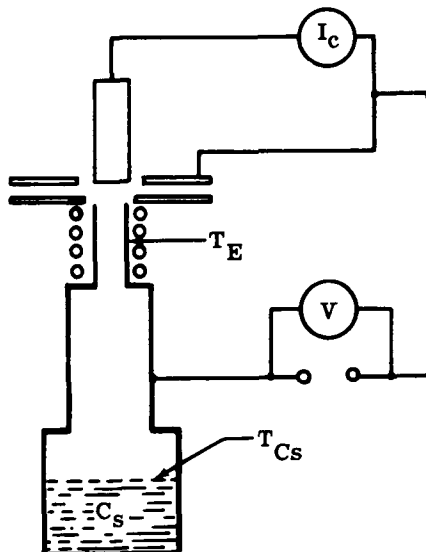


Figure 147. Arrangement of
Electrode-Probe Monocapillary System

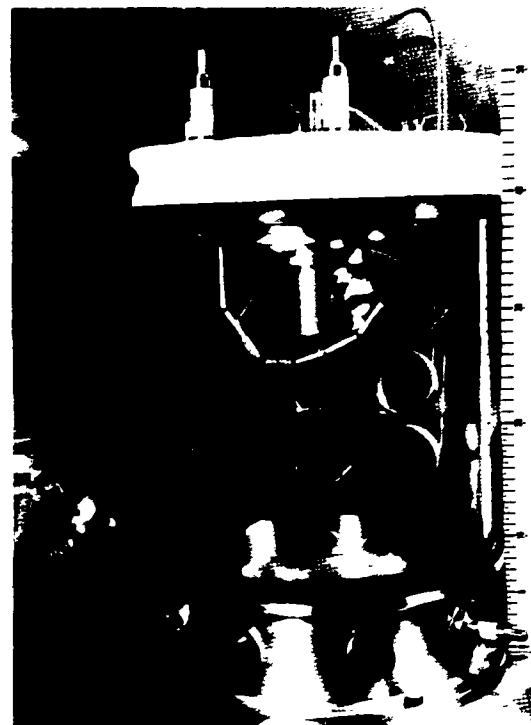


Figure 148. Photograph of Electrode-Probe
Monocapillary System

The $I_c(V)$ characteristics of the electron probe were drawn for a potential difference between the collector and the emitter varying from -10 v to +6 v. Figure 149 shows the shape of the characteristics measured. The electron current is above the abscissa and the ion current below. The electron and ion currents at the capillary exit were taken as the currents measured at ± 3 v from V_o on an $I_c(V)$ curve.* These electron current densities were compared with those obtained by Houston for tantalum (Figure 150) and for molybdenum (Figure 151).²⁵ These figures show that the shape of the curve obtained for a capillary is totally different from that obtained from a cesiated planar surface. The density of the electron current supplied by the capillary, for a given value of T_{Cs} , is greater than that obtained from a planar surface, when the emitter temperature exceeds a certain value. Conversely, it is below the planar value when the emitter temperature is below this value. For the emitter temperatures used in thermo-ionic converters, the electron emission from the capillary is higher than from the planar surface.

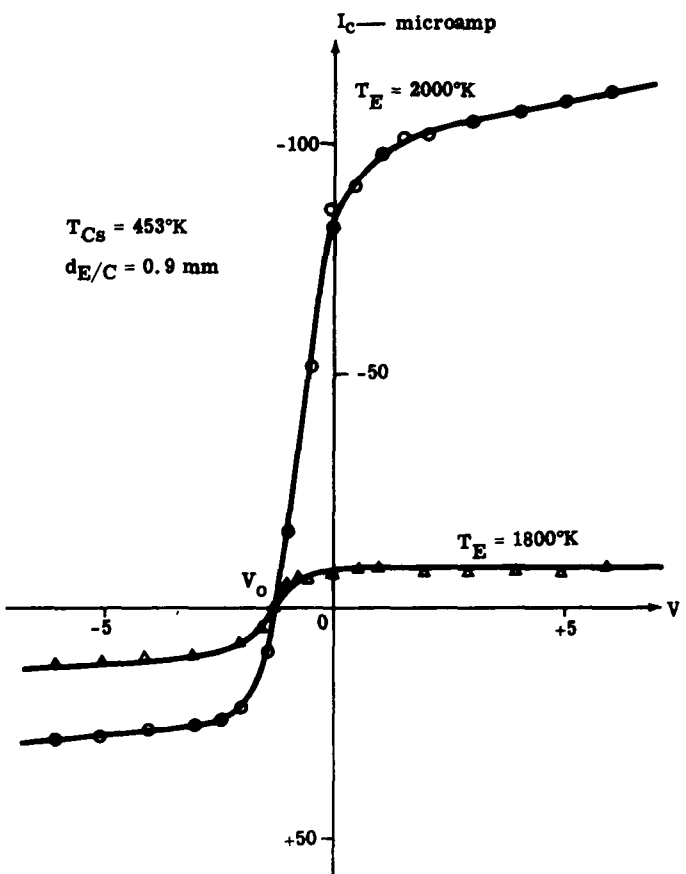


Figure 149. Example of I_c (-V) Characteristic Measured with the Electrode-Probe Monocapillary System

* V_o is the potential for zero current.

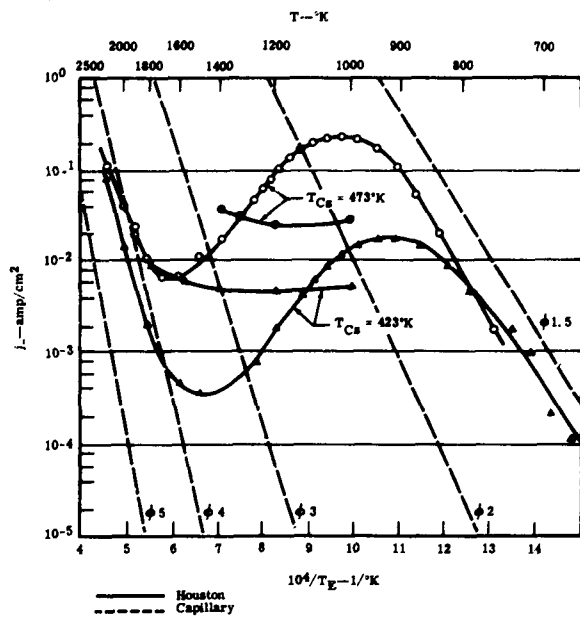


Figure 150. Comparison of Curves Showing the Density of the Electron Current Against the Reciprocal of the Temperature. Data Were Obtained with an Electrode-Probe Capillary Emitter and Tantalum Emitter in the Plasma

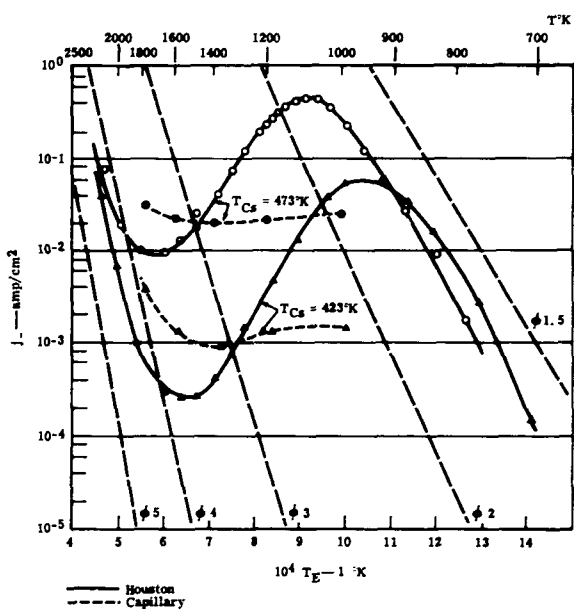


Figure 151. Comparison of Curves Showing the Density of the Electron-Current Against the Reciprocal of the Temperature. Data were Obtained with an Electrode-Probe Capillary Emitter and a Molybdenum Emitter in the Plasma

Electron Current

It is noted that the temperature at which the electron emission of the monocapillary exceeds that of the planar surface corresponds to the region of change from the electron sheath to the ion sheath inside the capillary (see Figure 145).

The measured electron currents are compared with theory in Figure 152. The theoretical curves shown include the electron emission from a tantalum and molybdenum surface and the plasma random electron current. In the latter case, three types of plasma have been considered:

- The plasma for which the concentration of neutral atoms at the capillary exit is equal to that at the capillary entrance:

$$n'_{gs \text{ entrance}} = n_{Cs} \left(\frac{T_{Cs}}{T_E} \right)^{1/2}$$

- The plasma in which the exit density of neutral atoms is equal to only 1/40 of the density n'_{gs} of the neutral atoms at the capillary entrance, from Equation (33)
- The plasma density $n_{\pm p}(L)$ at the capillary exit corresponds to 1/20 of the plasma density at the capillary entrance. The 1/20 ratio was chosen because if a flux of neutral atoms is taken through a capillary of diameter $2R$ and length L , then:

$$\frac{n_g(L)}{n_g(O)} = \frac{1}{1 + \frac{3}{8} \frac{L}{R}}$$

or, in the case of a capillary of 0.4 mm and length 10 mm:

$$n_g(L) \approx \frac{1}{20} n_g(O)$$

As was to be expected, the experimental values do not correspond to the electron emission from the metal. The shape of the experimental curve is the same as that of the curves corresponding to the plasma currents. The models in which the plasma has a neutral density at the exit equal to one-fortieth of the capillary entrance show an electron current density from three to six times greater than the measured value. However, there is fairly good agreement between the experimental values and the density of the electron current corresponding to the model in which

$$n_{\pm p}(L) = \frac{1}{20} n_{\pm p}(O)$$

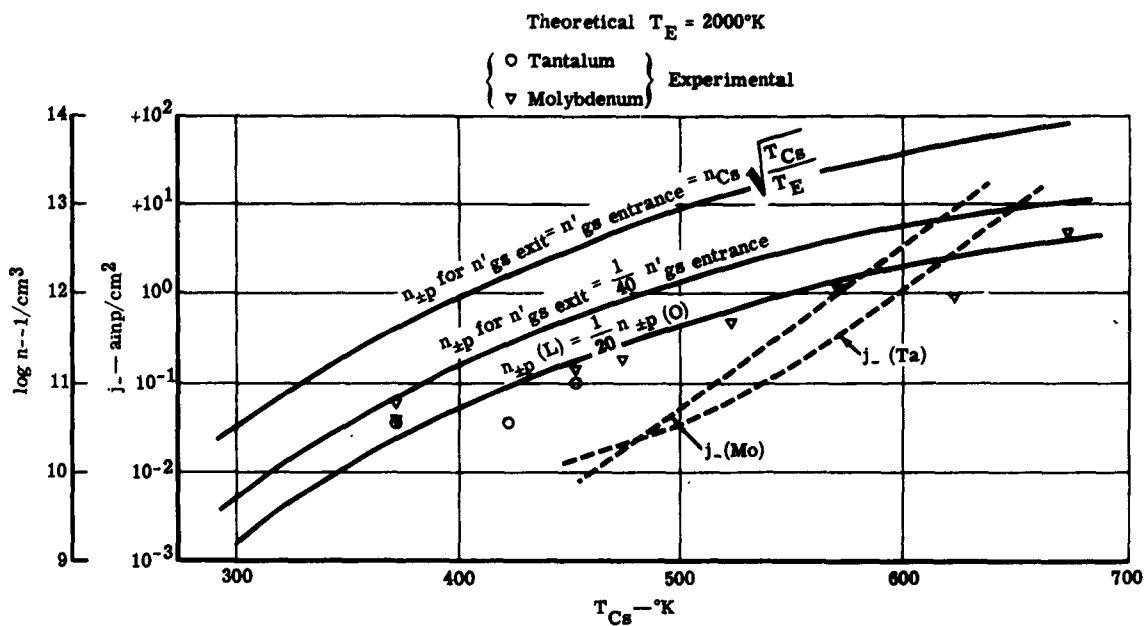


Figure 152. Theoretical and Experimental Comparison of Electron Current Densities Measured with the Electrode-Probe Monocapillary System

The model which appears to conform best with experiment is one in which the plasma flux inside the capillary may be treated as a flux of neutral atoms with an atom density of $n_{\pm p}(\text{O})$ at the capillary entrance. The electron current is determined by applying Knudsen's flux formula to find the plasma concentration at the capillary exit.

Ion Current

The measured densities of ion current are compared with theory in Figure 153. Three theoretical curves are plotted. Two of these curves show the random plasma current at the capillary exit. The first curve corresponds to the case for which the concentration n'_{gs} of neutral atoms at the capillary exit is equal to that at the entrance:

$$n'_{\text{gs entrance}} = n_{\text{Cs}} \left(\frac{T_{\text{Cs}}}{T_E} \right)^{1/2}$$

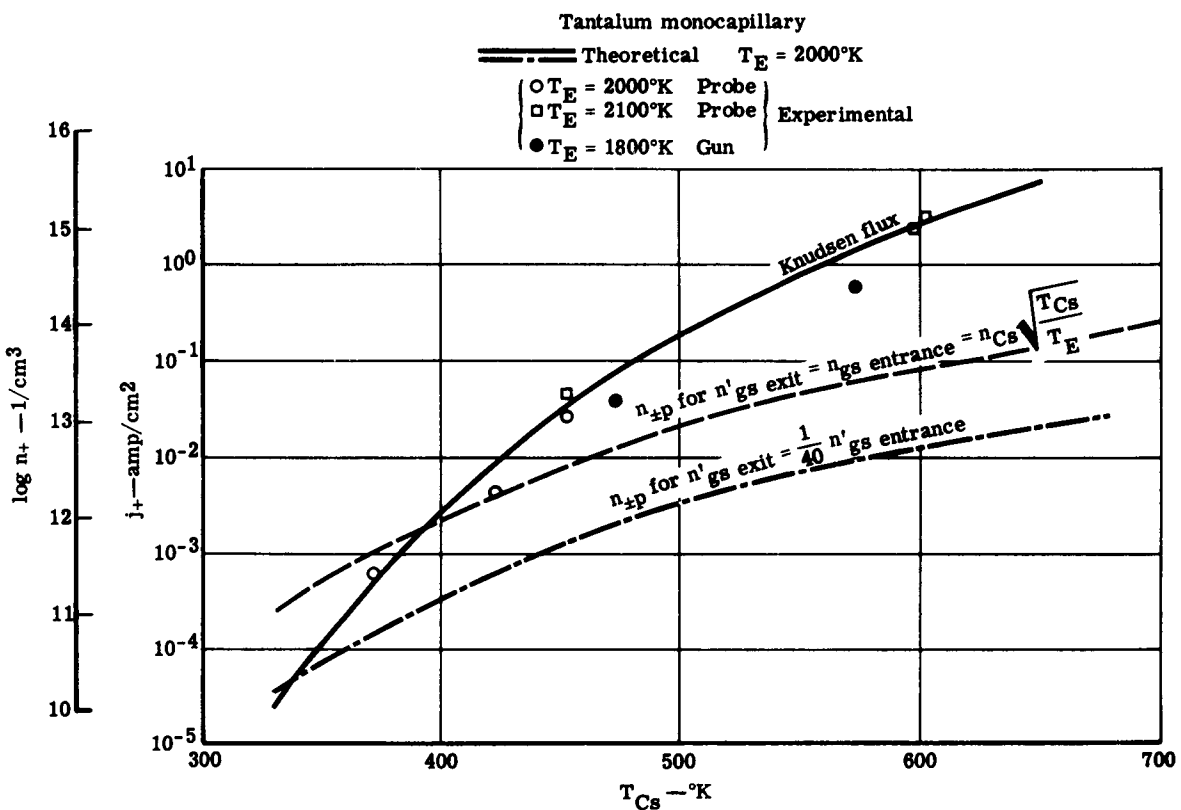


Figure 153. Theoretical and Experimental Comparison of Ion-Current Densities Measured with Electrode-Probe and Ion-Extraction Electrode Monocapillaries

For the second curve, the density n'_{gs} of the neutral atoms at the capillary exit is equal to one-fortieth of the entrance density. It is seen that the measured values for the ion current follow a curve with a greater slope than predicted by these first two theoretical curves. In general, the ion current is greater than the random ion current in the plasma. The third theoretical curve shows the ion current corresponding to the Knudsen flux expressed as an electric current for the case where the degree of ionization is nearly equal to one. The agreement between this theoretical curve and the experimental data is satisfactory.

MONOCAPILLARY WITH EXTRACTION ELECTRODES

Current measurements made with extraction electrodes were compared with previous measurements made with the electrode probe. Two tantalum monocapillaries (length $L = 10$ mm, diameter $2R = 0.4$ mm) were constructed; one of the structures was designed for electron extraction tests, and the other was used for tests on the extraction of ions. The extraction systems were Pierce electrodes.

Experimental Work on the Monocapillary for Electron Extraction

Figure 154 shows diagrammatically the electron extraction system. The extractor and collector combination are raised to a positive accelerating voltage, variable from 0 to 2 kv with respect to the emitter. The grid is negatively biased with respect to the collector in order to eliminate the perturbing effect of secondary emission. As in the case of the monocapillary with an electrode probe, cesium from a reservoir heated at temperature T_{Cs} passes through the capillary raised to temperature T_E and is trapped by cold pumping.

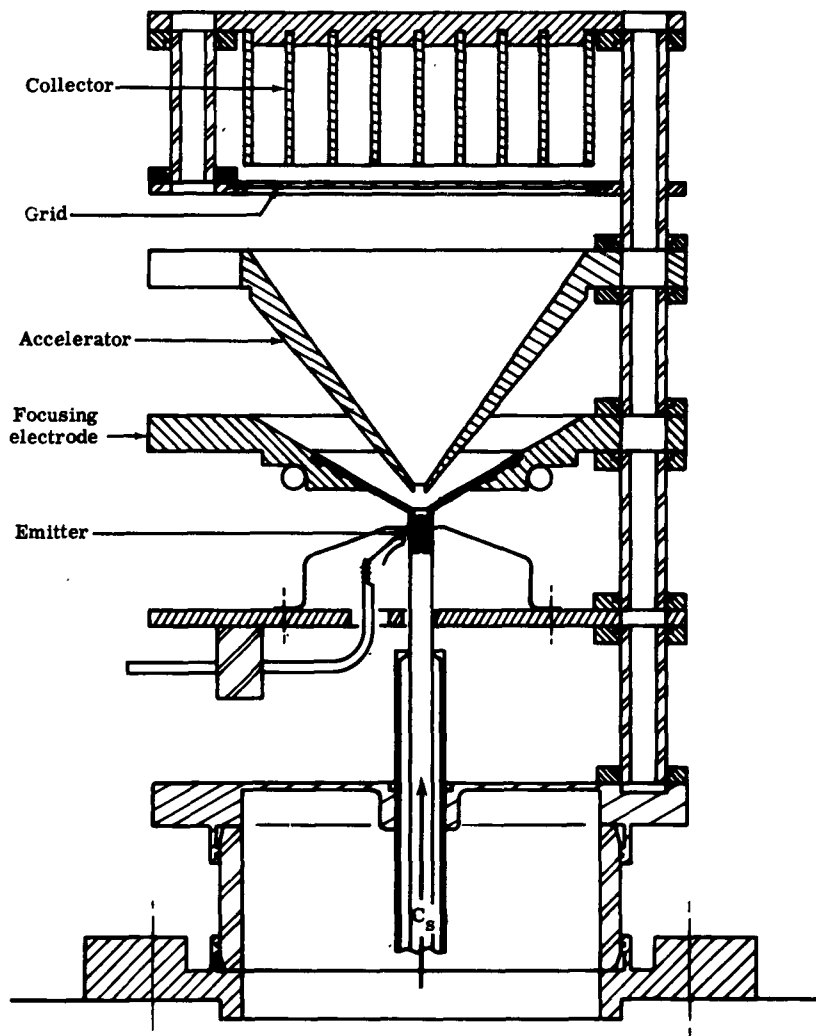


Figure 154. Sketch of the Electron Extraction Monocapillary

With this arrangement, $I_-(V_{acc})$ characteristics were obtained for the collector current as a function of extraction voltage. Figure 155 shows the curves obtained by varying T_E from 1800 to 2000°K for $T_{Cs} = 561^\circ\text{K}$, $V_G - V_{acc} = -60$ v, with the control grid at emitter potential. An electron current density of 8 amp/cm² was obtained for $T_E = 2200^\circ\text{K}$, $T_{Cs} = 561^\circ\text{K}$.

The electron currents obtained were compared against the theoretical values. Figure 156 shows the comparison at $T_E = 2000^\circ\text{K}$. The theoretical curves shown are electron emission from a tantalum surface in the presence of cesium vapor and the plasma random electron current density.

Comparison between theory and experiment confirm the results obtained for the capillary with the electrode probe—i. e., the model in which the plasma has a density of neutral atoms

$n'_{gs\ exit} = \frac{1}{40} n'_{gs\ entrance}$ gives a current density from three to six times greater than the measured value; the agreement between the experimental values and the theoretical model, in which $n_{\pm p}(L) = \frac{1}{20} n_{\pm p}(O)$, is satisfactory. The experimental points for T_{Cs} less than 400°K are higher than predicted from the model; this may be due to the fact that the cesium pressure at the capillary exit is nearly equal to the entrance pressure.

Experimental Work on the Monocapillary for Ion Extraction

Figure 157 shows diagrammatically the arrangement used for extracting ions from the monocapillary. The extractor-collector combination is raised to a negative voltage, variable from 0 to -10 kv with respect to the potential of the capillary emitter. The influence of secondary emission is eliminated by applying positive bias on the collector with respect to the extractor. The cesium circuit is the same as for the electron extraction capillary.

Figure 158 shows the ion current, I_+ , characteristic as a function of the accelerating voltage, V_{acc} . The ion current densities measured at saturation are plotted in Figure 153 in order to compare them with the theoretical curves. Taking into consideration the fact that $T_E = 1800^\circ\text{K}$ instead of 2000°K, there is satisfactory confirmation of the result obtained with the electrode probe capillary.

MULTICAPILLARY CONSTITUTING THE EMITTER IN THERMO-IONIC CONVERTERS

Arrangement and Measurements

The application of the multicapillary emitter in a thermo-ionic converter was investigated. In order to obtain measurements from a tantalum multicapillary emitter and a tungsten multicapillary emitter, several converters were fabricated. Figure 159 shows the emitter-collector space; the distance between these two electrodes could be varied from 0.3 to 2 mm. Figure 160 is a microphotograph of such a multicapillary emitter obtained by stacking alternately

plane foils and corrugated foils of tantalum or tungsten. The thickness of the foils is 15 microns and their length is 10 mm. The front surface area of the emitter is 0.3 cm^2 and includes about 320 capillaries.

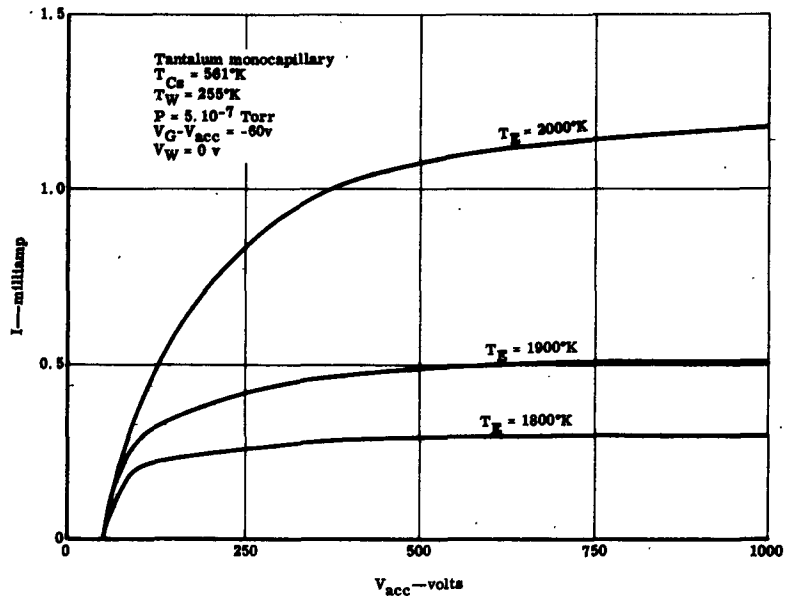


Figure 155. Example of Characteristic of Extracted Electron Current (I) Against Accelerating Potential (V_{acc}) Measured with the Electron Extraction Monocapillary

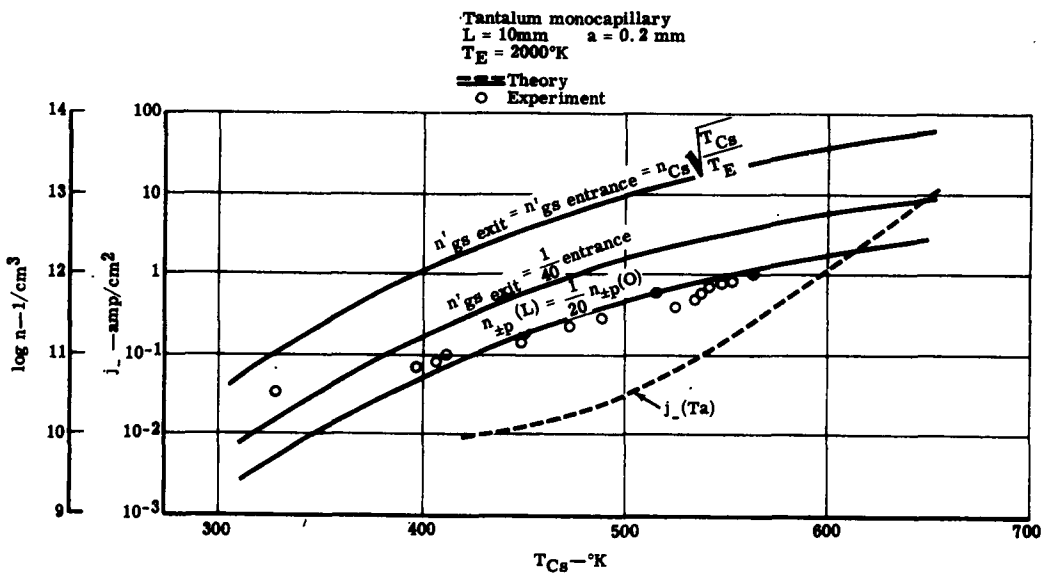


Figure 156. Theoretical and Experimental Comparison of Electron Current Measured with the Electron-Gun Extraction Monocapillary System

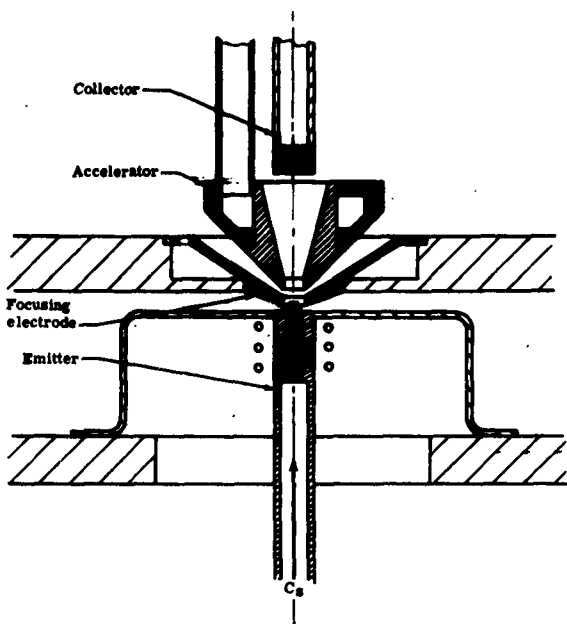


Figure 157. Arrangement of Ion Extraction Monocapillary System

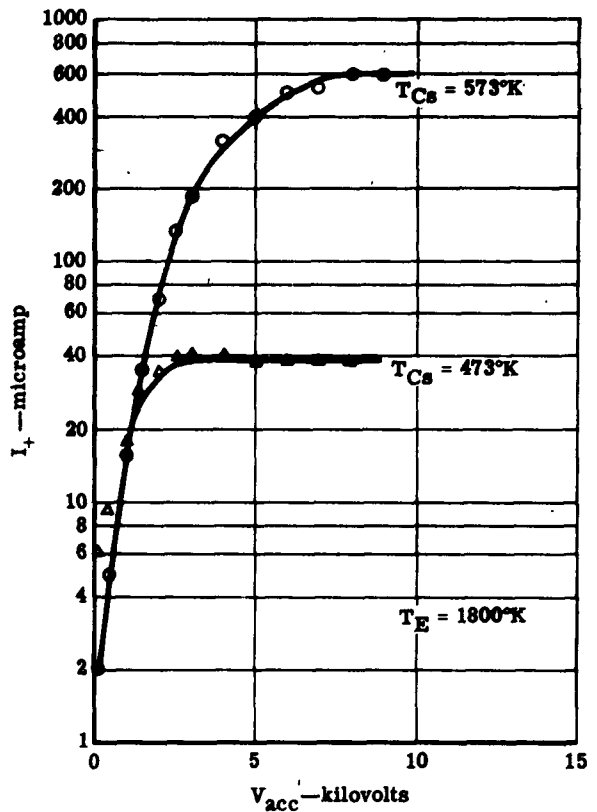


Figure 158. Example of Characteristic of Extracted Ion-Current (I_+) Against Accelerating Potential (V_{acc}) Measured with the Ion Extraction Monocapillary System

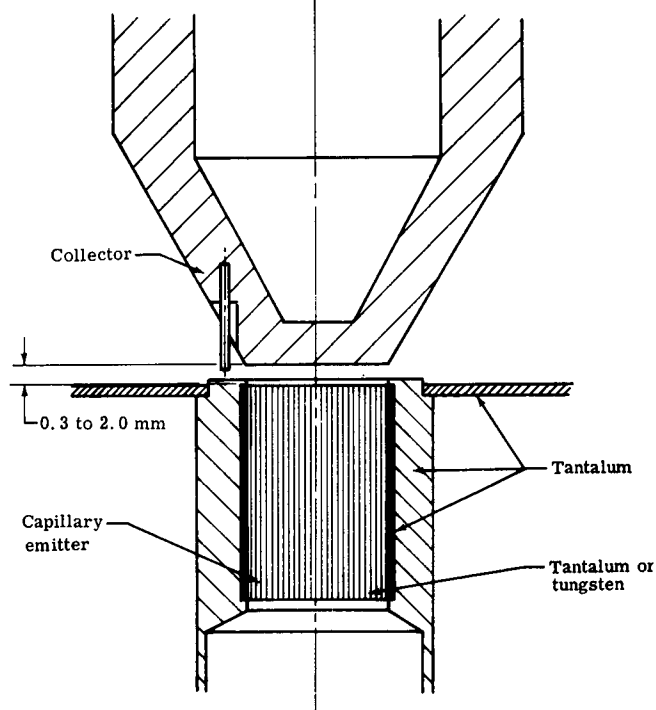


Figure 159. Magnified Diagram of the Multicapillary Emitter and Collector

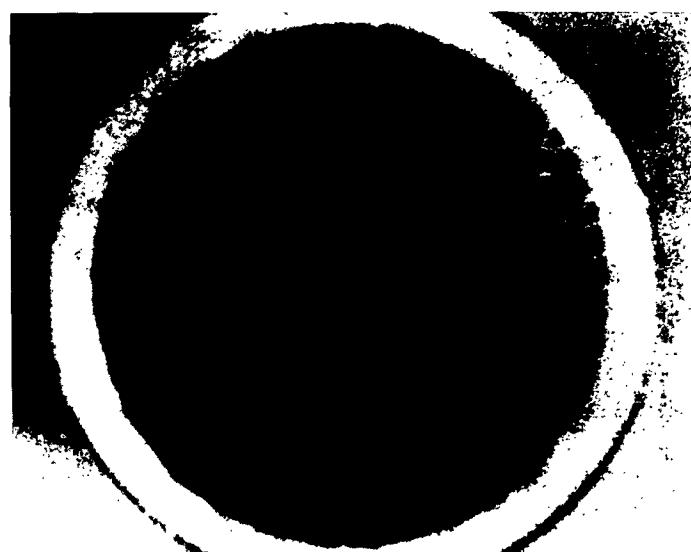


Figure 160. Microphotograph of a Multicapillary Emitter

The arrangement of the multicapillary converter is shown in Figure 161. The multicapillary emitter is heated by electron bombardment; the temperature, T_E , is measured optically through a sapphire window. Cesium vapor from the reservoir, heated to temperature T_{Cs} , passes through the emitter and flows radially outward through the interelectrode space; it condenses on the cooled surfaces surrounding the collector and returns to the reservoir by gravity. Figure 162 is a photograph of a multicapillary converter.

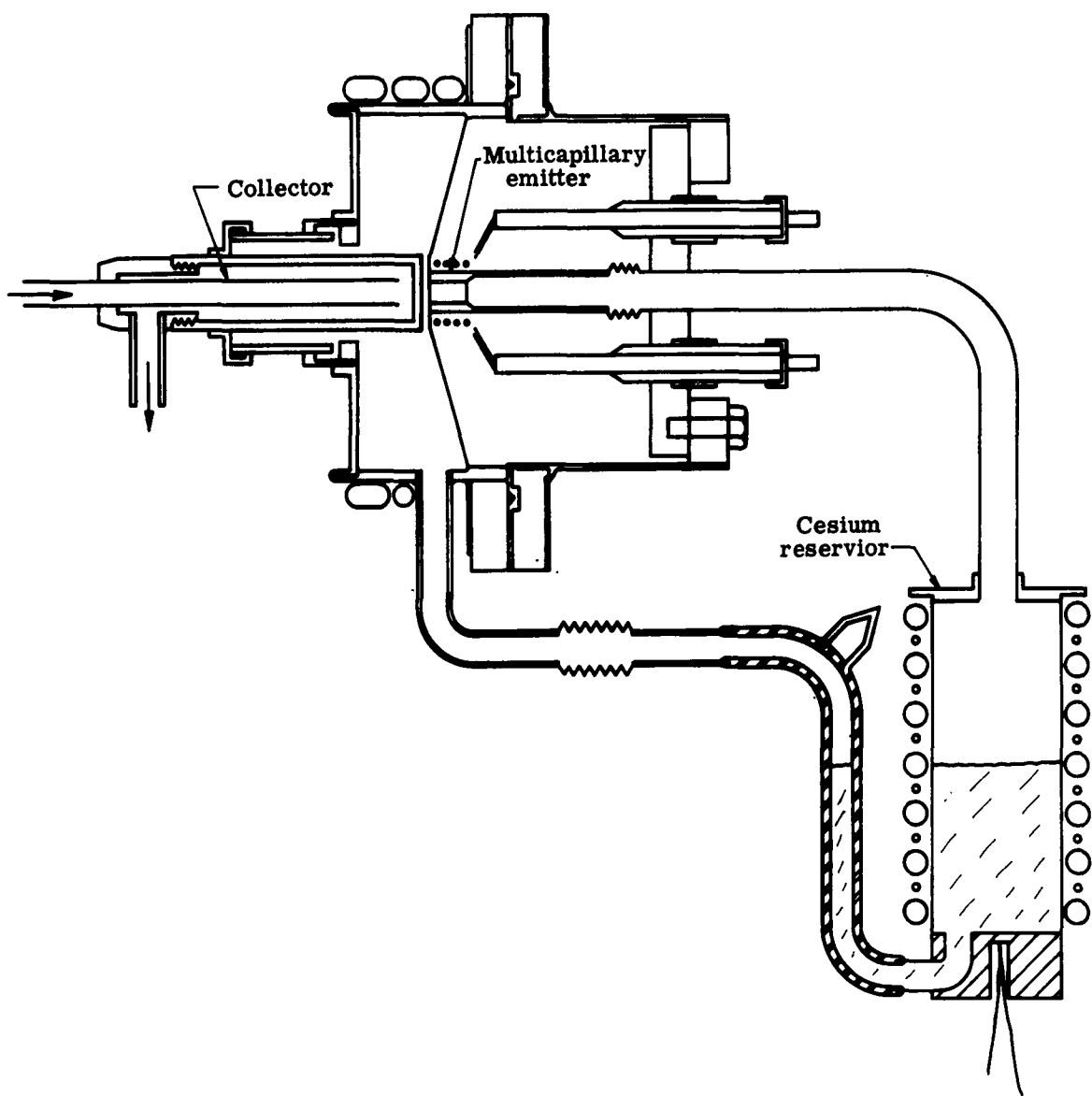


Figure 161. Design Concept of Multicapillary Emitter Converter



Figure 162. Photograph of Experimental Multicapillary Emitter Converter Setup

In the multicapillary converter the pressure at the exit of each capillary is higher than that in the monocapillary systems described. In order to determine the pressure at the capillary exit, calculations were made on the conditions for a continuous flux through the emitter consisting of 320 capillaries and the emitter-collector space.¹⁹ The results of these calculations show that (1) the pressure at the exit of a capillary varies with the distance from the emitter axis and (2) the mean cesium pressure in the interelectrode space varies from 10 to 55% of the pressure at the capillary entrance when the emitter-collector distance decreases from 2.0 to 0.3 mm.

The shapes of the current-voltage characteristics measured on multicapillary converters were similar to those observed on converters with conventional cesiated surface emitters. The $I_c(V_c)$ characteristics were obtained over the following ranges:

T_E from 1400 to 2100°K

T_{Cs} from 423 to 673°K

$d_{E/C}$ from 0.3 to 2.0 mm

Figure 163 shows the $I_c(V_c)$ curves obtained when varying the emitter-collector distance, $d_{E/C}$. Small facts are evident:

- There is a relatively slight influence of the interelectrode distance on the passive mode when changing from 0.5 mm to 2 mm.

- The arc mode appears first for the smallest values of $d_{E/C}$.

This phenomenon can be explained as follows. When $d_{E/C}$ decreases, the pressure in the emitter-collector space increases so that the mean free path, λ , decreases more rapidly than $d_{E/C}$.

Electron Current

Comparison between theory and experiment can be made in the same manner as for the mono-capillary, after accounting for the fact that the pressure at the capillary exit is much higher than in the former case. For electron currents, comparisons can be made with the following theoretical models:

- Case where n'_{gs} exit = n'_{gs} entrance
- Case where n'_{gs} exit is equal to a fraction of n'_{gs} at the entrance

The fraction would be determined by the mean pressure in the emitter-collector space. Fairly good agreement was obtained between theory and experiment when the density ratio, n'_{gs} exit = $\frac{1}{10}$ n'_{gs} entrance, was used.¹⁸

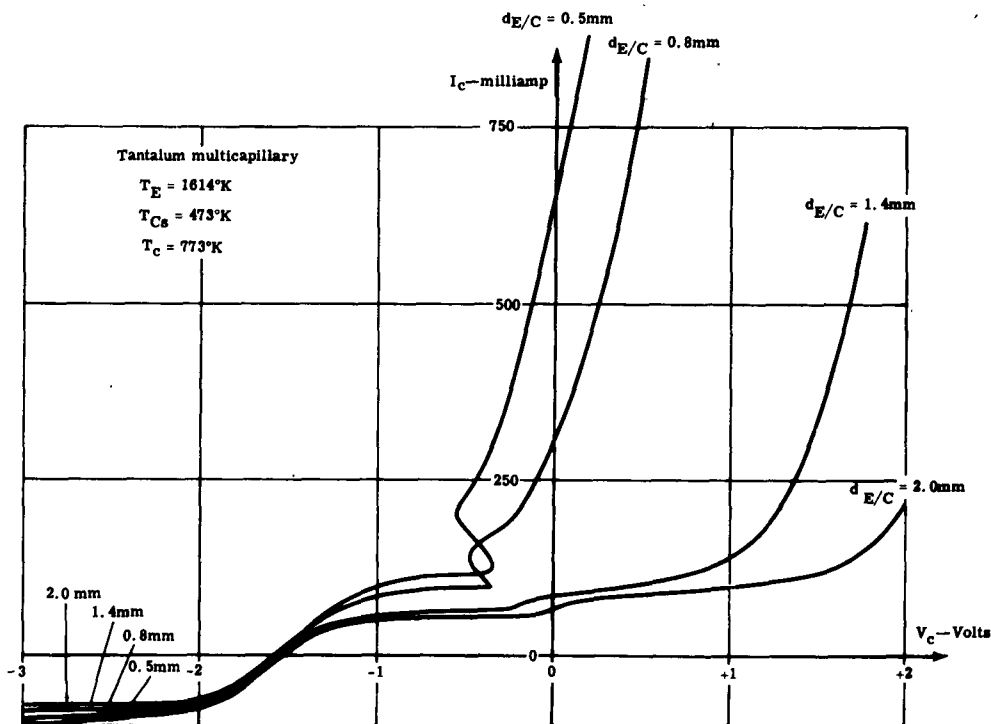


Figure 163. I_c (V_c) Characteristic for Various Interelectrode Distances Measured with the Tantalum Multicapillary Emitter Converter

Ion Current

The collector temperature had a marked effect on the measured ion current. When T_C decreases from 616°C to 60°C, the ion current decreases by a factor of about 100. The ion currents measured for small values of T_C were compared with theory, using the random ion current in the plasma at the capillary exit when $n'_{\text{gs exit}} = \frac{1}{20}$ entrance.¹⁸ The slope of the experimental curve was much greater than that predicted from the plasma random ion current. The model described previously for ion extraction should apply here. It was shown for the monocapillary in Figure 153 that the slope of the curve corresponding to this model is much greater than for the other two models.

Generally, measurements made on the multicapillary have shown the existence of an electron current/ion current ratio much lower than 500.¹⁹ This result cannot be explained when only the random current in a given plasma is measured. However, such behavior is not contradictory to the model for ion extraction.

Comparison Between a Tungsten Multicapillary and a Sintered Tungsten Emitter

At the output of a capillary tube, the volume flux is dominant rather than the surface flux. On the other hand, the converse is true in the case of porous materials used as a source of cesium ions for ionic propulsion. In order to show the difference between the modes of operation of the two devices, a sintered tungsten emitter converter with pores of a few microns diameter was investigated. The thickness of the pressed material was 2 mm. This emitter replaced a multicapillary in a converter of exactly the same design described previously.

A typical example of comparison between the $I_C(V_C)$ curves obtained with the two converters is shown in Figure 164. For the same parameter values, the curves are different and the saturation electron current in the passive mode from the multicapillary is 15 to 20 times higher than that from the sintered material; the same ratio is found for the ion currents. When the cesium reservoir temperature is raised 100°K in the case of the sintered emitter converter, the currents measured are still lower than those measured with the multicapillary emitter converter. The existence of the arc mode in the multicapillary emitter converter (Figure 164) and its absence in the case of the converter with the porous emitter seem to be due to a greater atom density in the emitter-collector space of the multicapillary emitter converter.

Figure 165 shows the optimum power obtained with the multicapillary emitter converters. The same figure shows the maximum power densities obtained, over the same ranges of T_{Cs} , with the sintered tungsten emitter converter. These densities are much lower.

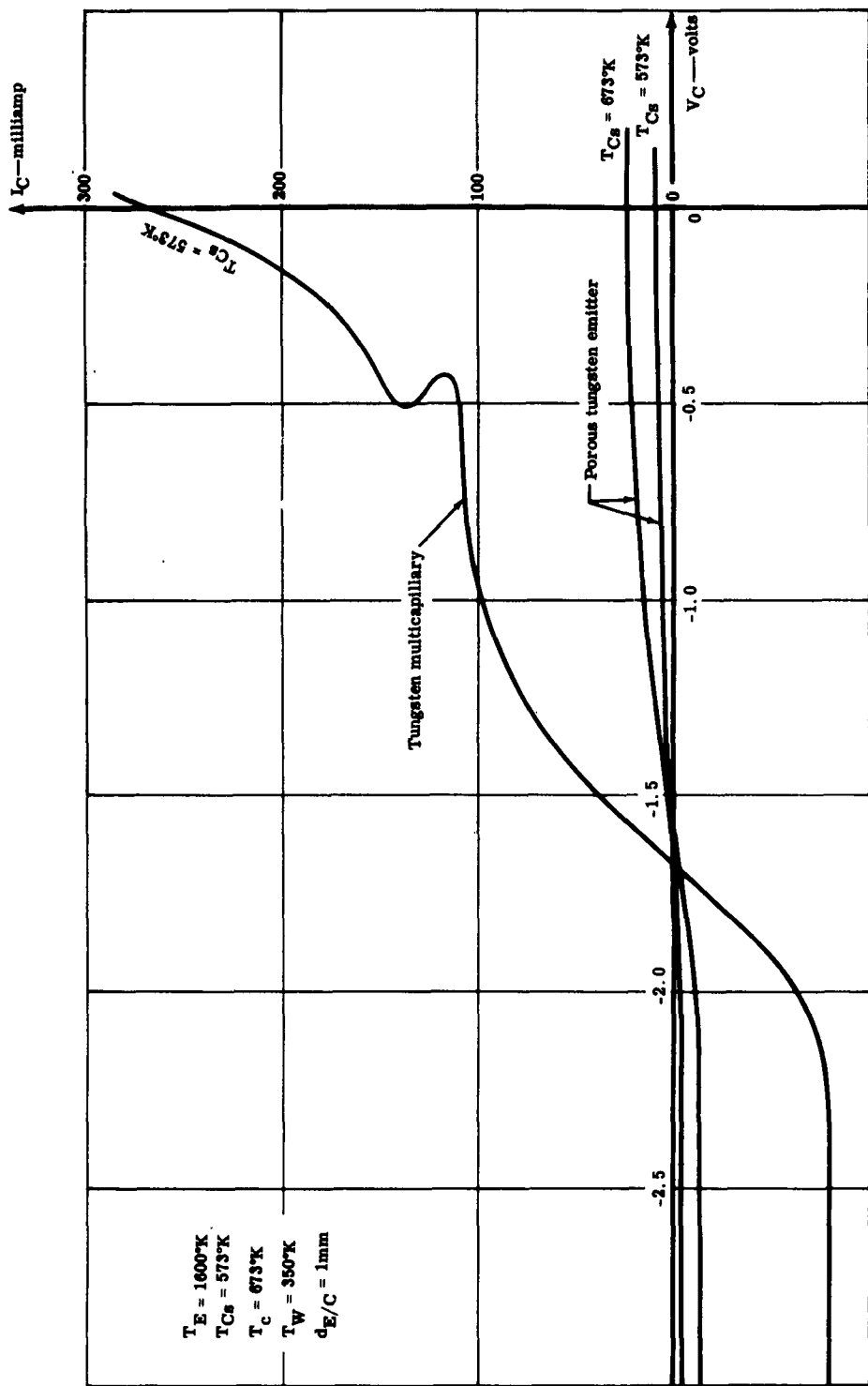


Figure 164. $I_C(V_C)$ Characteristics. Comparison of a Tungsten Multicapillary Emitter Converter with a Sintered Porous Tungsten Emitter Converter

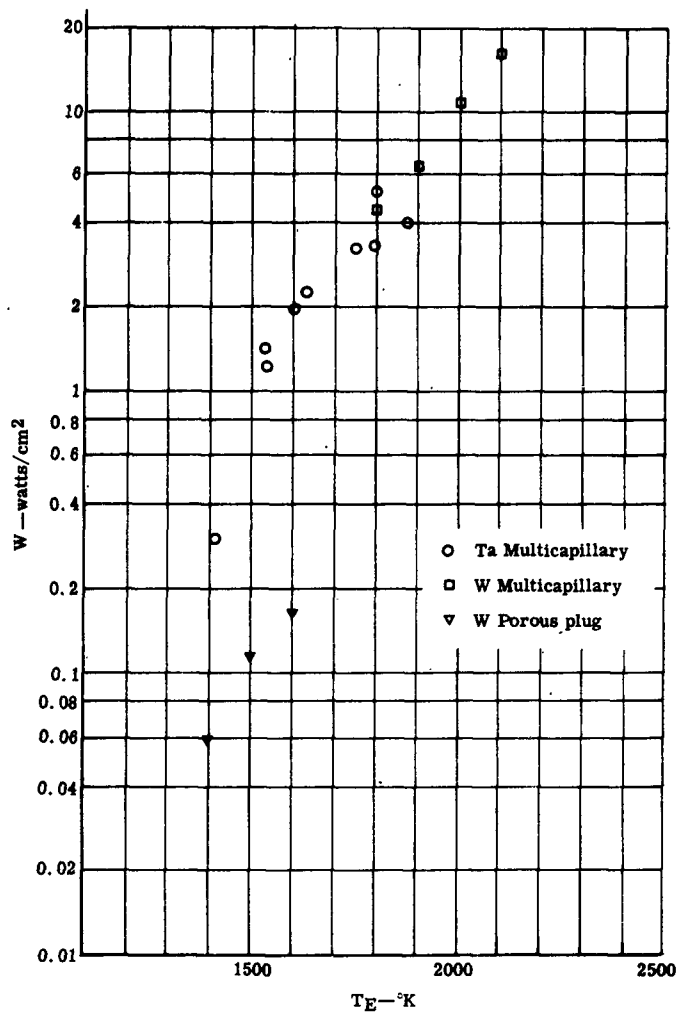


Figure 165. Preliminary Values of Measured Power Densities

CONCLUSION

Although the theoretical models so far developed are quite simplified, they are in relatively good agreement with the experimental results.

In the case of the electron currents, the experimental values are from three to six times less than those expected from the model with a 1/40 neutral density ratio. Better agreement is obtained by assuming plasma density ratio of 1/20 (fraction corresponding to that of neutrals in the Knudsen flux).

In the case of ion currents, satisfactory agreement is found between measurements and the model in which the space charge in the ion sheath is compensated by trapping of the electrons reflected in the interelectrode space.

As regards the technical value of the capillary emitter, this emitter could find application as:

- A source of electrons with a current density greater than 10 amp/cm^2 in electron tubes
- A source of cesium ions with a current density of the order of 1 amp/cm^2
- A source of cesium plasma
- A dual emitter of electrons and ions in a thermo-ionic converter

As regards the last-mentioned application, the best performances from the power density point of view are comparable with those obtained with conventional converters (compact electrodes in cesium vapor). The multicapillary emitter is better, from the power density point of view, for low cesium bath temperatures—i.e., under conditions for which the level of power density is lowest. However, experiments so far carried out with this type of converter show that power densities up to 5 to 15 watts/cm² can be obtained at 1900 to 2100°K, with the further advantage of a lower cesium pressure; hence, the advantages of a greater interelectrode distance and greater reliability in operation are possible.

BIBLIOGRAPHY

1. Jain, S. C. and Krishnan, K. S. in Proc. Roy. Soc. A 213, 143 (1952); A 215, 431 (1952); A 217, 451 (1952).
2. Babcock, M. L., Holshouser, D. F., and Von Foerster, H. M. in Phys. Rev. 91, 755 (1953).
3. Mueller, G. E. in Trans. IRE P G E D. 4, 33 (1953).
4. Brett, H. and Kumpfner, B. D. in Convention Record IRE, 2 part 3, 66 (1954).
5. Poole, K. M. in J. A. P. 26, 1176 (1955).
6. Veith, W. Naturwiss. 42, 40 (1955).
7. Brunn, K. R. University of Illinois, ASTIA No. AFCRC-TV-57-195 and A.D. 117036 (April 1956).
8. Chin, T. N. in J. A. P. 28, 744 (1957).
9. Dubinina, E. M. and Pyt'eva, M. B. Radio Eng. and Electronics. 5, 100 (1960).
10. Fincke, G. C. Fifth Nat. Conf. Tube Techniques (September 1960).
11. Brodie, I. and Niewold, A. in J. A. P. 33, 3328 (November 1962).
12. Kotnik, J. T. NASA-Technical Note D-1187 (February 1962).
13. Nazarian, G. M. and Shelton, H. ARS 1386-60 (November 1960).
14. Zuccaro, D., Speiser, R. C., and Teem, J. H. ARS 1387-60 (November 1960).
15. Husmann, O. K. ARS 1396-60 (November 1960).
16. Dulgeroff, C. R., Speiser, R. C., and Forrester, A. T. ARS 926-59 (November 1959).
17. Edwards, R. N., Jasper, P. B., Kuskevics, G., and Scheffer, P. A. ARS 1127-60 (May 1960).
18. Cybulski, R. J. and Kotnik, J. T. in AIAA Journal. 1, 1293 (June 1963).

19. Dresser, D. L., Laurita, W. G., and Dunlop, J. D.; Huber, H. and LeBihan, R. AIAA 63-156 (June 1963).
20. Nottingham, W. B. TEECO-Report No. 4-62 (October 1962).
21. Eichenbaum, A. L. RCA Review. 23, 230 (June 1962).
22. Field, L. M., Spangenberg, K., and Helm, R. in Electrical Comm. 24, 108 (1947).
23. Linder, E. G. L. and Hernqvist, K. G. in J. A. P. 21, 1088 (1950).
24. Ginzton, E. L. and Wadia, B. H. PIRE, 42, 1548 (1954).
25. Houston, J. M. Proceedings of the Second Government-Industry Thermionic Roundtable Discussion, P.I.C. - E.L.E.-Ti 3/3, 1961.

DISTRIBUTION LIST

No. of Copies

Activities at WPAFB

1

ASAPRL

1

ASNXR

1

ASNXR (Mr. Daniels)

2

APP

2

APIP

19

APIP-2 (Mr. G. H. Miller)

1

ASRNE4

1

ASRCEM-1

3

ASYF

Department of Defense Activities

Army

1

U. S. Army Signal R&D Lab

Attention: SIGRA/SL-PS (Dr. Kittl)

Fort Monmouth, New Jersey

Navy

1

Office of Naval Research

Power Branch, Code 429

Attention: CDR J. J. Connelly

Washington 25, D. C.

1

U.S. Naval Research Lab

Technical Information Division

Washington 25, D. C.

1

Chief, Bureau of Ships

Department of the Navy

Attention: Code 342B, Mr. Rosenbaum

Washington 25, D. C.

No. of Copies

Air Force

1

SSD (SSTRE, Major Iller)
AF Unit Post Office
Los Angeles 45, California

1

AFCRL (CRZAP)
L G Hanscom Field
Bedford, Massachusetts

40

Defense Documentation Center
Arlington Hall Station
Arlington 12, Virginia

Other U. S. Government Agencies

1

Institute for Defense Analysis
Attention: Dr. R. Hamilton
1825 Connecticut NW
Washington 25, D.C.

1

Direct ARPA
The Pentagon
Attention: Dr. J. Huth
Washington 25, D.C.

1

National Aeronautical and Space Administration
Attention: Dr. Walter Scott
1520 H Street NW
Washington 25, D.C.

1

NASA Lewis Research Center
Attention: Library
21000 Brookpark Road
Cleveland 25, Ohio

1

NASA Manned Spacecraft Center
SEDD (Attention: J. D. Murrell)
Houston, Texas

1

Jet Propulsion Laboratory
Spacecraft Secondary Power Section
Attention: Mr. Paul Goldsmith
4800 Oak Park Drive
Pasadena, California

<u>No. of Copies</u>	<u>Other U. S. Government Agencies</u>
1	U. S. Atomic Energy Commission Division of Reactor Development Attention: Lt Cmdr J. Prosser Washington 25, D.C.
1	U. S. Atomic Energy Commission San Francisco Operations Office Attention: Reactor Division 2111 Bancroft Way Berkeley 4, California
1	U. S. Atomic Energy Commission Office of Technical Information Extension P. O. Box 62 Oak Ridge, Tennessee
100	OTS STOCK 1200 South Eads Street Arlington, Virginia
1	Aerospace Corporation Attention: Library Technical Document Group Post Office Box 95085 Los Angeles 45, California
1	Power Information Center University of Pennsylvania Moore School Building 200 South 33rd Street Philadelphia 4, Pennsylvania
1	Aerojet-General Nucleonics Attention: K. E. Buck Box 77 San Ramon, California
1	Atomics International Attention: Dr. R. C. Allen P.O. Box 309 Canoga Park, California

<u>No. of Copies</u>	<u>Other U. S. Government Agencies</u>
1	Ford Instrument Company Attention: T. Jarvis 3110 Thomson Avenue Long Island City, New York
1	General Atomic Attention: Dr. W. Pidd P. O. Box 608 San Diego 12, California
1	The Martin Corporation Attention: Dr. M. Talaat Baltimore 3, Maryland
1	General Electric Company Research Laboratory Attention: W. Grattidge P. O. Box 1088 Schenectady, New York
1	General Electric Company Attention: Mr. D. L. Shaefer Power Tube Division 1 River Road Schenectady 5, New York
1	General Electric Company Valley Forge Space Technology Center Attention: Dr. J. C. Danko P. O. Box 8555 Philadelphia 1, Pennsylvania
1	International Telephone & Telegraph ITT Industrial Laboratories Attention: Dr. D. K. Coles 3700 East Pontiac Street Fort Wayne, Indiana
1	Thermal Electron Engineering Corporation Attention: Dr. G. Hatsopoulos 85 First Avenue Waltham 54, Massachusetts

<u>No. of Copies</u>	<u>Other U. S. Government Agencies</u>
----------------------	--

1	Thompson Ramo Wooldridge Inc. New Products Research Attention: W. J. Leovic 23555 Euclid Avenue Cleveland 17, Ohio
1	The Bendix Corporation Research Laboratory Attention: George Burton Southfield, Michigan
1	Union Carbide Corporation Parma Research Laboratory 12900 Snow Road Parma, Ohio
1	Pratt and Whitney Aircraft United Aircraft Corporation 400 Main Street East Hartford, Connecticut Attention: W. H. Podolny

Research and Technology Division, AF Aero-Propulsion Lab, Wright-Patterson AFB, Ohio. Rpt. No. ASD-TDR-63-865. INVESTIGATION OF CAPILLARY Emitter THERMIONIC CONVERTERS. Final report, Sept 63, 190 pp; incl. illus., tables, 26 refs. Unclassified Report

A random current theoretical model is formulated to describe the emission of ions and electrons from a capillary thermionic emitter. Extensive experimental results from monocapillary and multicapillary devices are shown to be in good agreement with the theory. Practical power densities of 5 to 15 watts/cm² were obtained between 1900 and 2100°K. A modified capillary emitter in which no cesium flow is required

1. Theory of ion emission
2. Thermionic emission on cesium vapor
I. AFSC Project 8173,
Task 817305-11
II. Contract AF33(616)-8299
III. Allison Division, General Motors Corporation, Indianapolis, Indiana
IV. D. L. Dresser, et al.
V. Allison Division EDR 3532
VI. Aval fr OTS
VII. In DDC (formerly ASTIA) collection

Research and Technology Division, AF Aero-Propulsion Lab, Wright-Patterson AFB, Ohio. Rpt. No. ASD-TDR-63-865. INVESTIGATION OF CAPILLARY Emitter THERMIONIC CONVERTERS. Final report, Sept 63, 190 pp; incl. illus., tables, 26 refs. Unclassified Report

A random current theoretical model is formulated to describe the emission of ions and electrons from a capillary thermionic emitter. Extensive experimental results from monocapillary and multicapillary devices are shown to be in good agreement with the theory. Practical power densities of 5 to 15 watts/cm² were obtained between 1900 and 2100°K. A modified capillary emitter in which no cesium flow is required

1. Theory of ion emission
2. Thermionic emission on cesium vapor
I. AFSC Project 8173,
Task 817305-11
II. Contract AF33(616)-8299
III. Allison Division, General Motors Corporation, Indianapolis, Indiana
IV. D. L. Dresser, et al.
V. Allison Division EDR 3532
VI. Aval fr OTS
VII. In DDC (formerly ASTIA) collection

Research and Technology Division, AF Aero-Propulsion Lab, Wright-Patterson AFB, Ohio. Rpt. No. ASD-TDR-63-865. INVESTIGATION OF CAPILLARY Emitter THERMIONIC CONVERTERS. Final report, Sept 63, 190 pp; incl. illus., tables, 26 refs. Unclassified Report

A random current theoretical model is formulated to describe the emission of ions and electrons from a capillary thermionic emitter. Extensive experimental results from monocapillary and multicapillary devices are shown to be in good agreement with the theory. Practical power densities of 5 to 15 watts/cm² were obtained between 1900 and 2100°K. A modified capillary emitter in which no cesium flow is required

1. Theory of ion emission
2. Thermionic emission on cesium vapor
I. AFSC Project 8173,
Task 817305-11
II. Contract AF33(616)-8299
III. Allison Division, General Motors Corporation, Indianapolis, Indiana
IV. D. L. Dresser, et al.
V. Allison Division EDR 3532
VI. Aval fr OTS
VII. In DDC (formerly ASTIA) collection

Research and Technology Division, AF Aero-Propulsion Lab, Wright-Patterson AFB, Ohio. Rpt. No. ASD-TDR-63-865. INVESTIGATION OF CAPILLARY Emitter THERMIONIC CONVERTERS. Final report, Sept 63, 190 pp; incl. illus., tables, 26 refs. Unclassified Report

A random current theoretical model is formulated to describe the emission of ions and electrons from a capillary thermionic emitter. Extensive experimental results from monocapillary and multicapillary devices are shown to be in good agreement with the theory. Practical power densities of 5 to 15 watts/cm² were obtained between 1900 and 2100°K. A modified capillary emitter in which no cesium flow is required

1. Theory of ion emission
2. Thermionic emission on cesium vapor
I. AFSC Project 8173,
Task 817305-11
II. Contract AF33(616)-8299
III. Allison Division, General Motors Corporation, Indianapolis, Indiana
IV. D. L. Dresser, et al.
V. Allison Division EDR 3532
VI. Aval fr OTS
VII. In DDC (formerly ASTIA) collection

Research and Technology Division, AF Aero-Propulsion Lab, Wright-Patterson AFB, Ohio. Rpt. No. ASD-TDR-63-865. INVESTIGATION OF CAPILLARY Emitter THERMIONIC CONVERTERS. Final report, Sept 63, 190 pp; incl. illus., tables, 26 refs. Unclassified Report

A random current theoretical model is formulated to describe the emission of ions and electrons from a capillary thermionic emitter. Extensive experimental results from monocapillary and multicapillary devices are shown to be in good agreement with the theory. Practical power densities of 5 to 15 watts/cm² were obtained between 1900 and 2100°K. A modified capillary emitter in which no cesium flow is required

was also investigated and found to agree with the random current model. Ion current measurements, high frequency oscillations, and spectroscopic data are used to interpret the operating conditions of the capillary emitter. Technical developments are reported on the subjects of emitter fabrication and chemical vapor deposition.

was also investigated and found to agree with the random current model. Ion current measurements, high frequency oscillations, and spectroscopic data are used to interpret the operating conditions of the capillary emitter. Technology developments are reported on the subjects of emitter fabrication and chemical vapor deposition.

was also investigated and found to agree with the random current model. In current measurements, high frequency oscillations, and spectroscopic data are used to interpret the operating conditions of the capillary filament. Technological developments are reported on the subjects of emitter fabrication and chemical vapor deposition.

was also investigated and found to agree with the random current model. Ion current measurements, high frequency oscillations, and spectroscopic data are used to interpret the operating conditions of the capillary emitter. Technology developments are reported on the subjects of emitter fabrication and chemical vapor denotation.